

LOAD RESPONSE OF TOPOLOGICALLY INTERLOCKED MATERIAL
SYSTEMS - ARCHIMEDEAN AND LAVES TILINGS

A Thesis

Submitted to the Faculty

of

Purdue University

by

Andrew J. Williams

In Partial Fulfillment of the

Requirements for the Degree

of

Master of Science in Mechanical Engineering

August 2019

Purdue University

West Lafayette, Indiana

THE PURDUE UNIVERSITY GRADUATE SCHOOL
STATEMENT OF THESIS APPROVAL

Dr. Thomas Siegmund, Chair

School of Mechanical Engineering

Dr. Adrian Buganza Tepole

School of Mechanical Engineering

Dr. Marcial Gonzalez

School of Mechanical Engineering

Approved by:

Dr. Jay Gore

Head of the School of Mechanical Engineering Graduate Program

ACKNOWLEDGMENTS

I would like to give a special thanks to:

- Dr. Siegmund, my advisor
- Kristoffer Sjolund for his help with the disphenoid models
- My lab group for all my random questions
- My family for their support and encouragement

TABLE OF CONTENTS

	Page
LIST OF TABLES	vi
LIST OF FIGURES	vii
SYMBOLS	xvii
ABSTRACT	xviii
1. INTRODUCTION	1
1.1 Load Response	2
1.2 Motivation	5
1.2.1 Chirality	7
1.2.2 Reciprocity of the Load Response	7
1.3 Scope of Research	10
1.4 Thesis Overview	11
2. METHODS	12
2.1 Tile Space	12
2.1.1 Archimedean Tilings	12
2.1.2 Laves Tilings	13
2.1.3 Tilings for the Construction of TIM Systems	14
2.1.4 Boundaries	16
2.2 3D Model	19
2.2.1 Untruncated Blocks	20
2.2.2 Truncated Blocks	20
2.2.3 Frame	24
2.2.4 Assemblies and Configurations	24
2.3 Finite Element Model	29
2.3.1 Displacement Loading	29
2.3.2 Body Force Loading	32
2.3.3 Internal Load Transfer	32
2.4 Finite Element Code	33
2.4.1 Mesh Convergence	34
2.4.2 Energy Balance	34
2.4.3 Mesh Alignment	36
2.4.4 Validation	39
2.5 Python Implementation	42
3. TIM SYSTEMS UNDER APPLIED DISPLACEMENTS	43

	Page
3.1 System Energies, Reaction Force, and Reaction Moment	43
3.2 Analysis of the System Internal Load Transfer	64
4. TIM SYSTEMS UNDER BODY FORCE LOADING	76
4.1 System Energies	76
4.2 Body Force Slip Ratios	82
4.3 Analysis of the System Internal Load Transfer	88
5. DISCUSSION	99
5.1 Cross Property Relationships	99
5.2 Strength Correlations with Architecture	103
5.3 Chirality	108
5.4 Reciprocity of the Load Response	112
5.5 Effects of the Coefficient of Friction	113
5.5.1 Detailed Effects of the Coefficient of Friction	114
5.5.2 Aggregate Effects of the Coefficient of Friction	124
5.6 Expansion of the Material Space	127
6. CONCLUSIONS	130
REFERENCES	132
A. CONVERGENCE	135
B. FALSE ENERGY	145
C. SELECT DATA	150
D. ABAQUS INPUT FILE	152

LIST OF TABLES

Table	Page
2.1 Number of tiles and edges lengths for the set of bounded tilings in this work.	18
C.1 Select data for all configurations with coefficient of friction $\mu = 0.2$	150
C.2 Select architectural aspects for all assemblies.	151

LIST OF FIGURES

Figure	Page
1.1 (a) Flat vault design by Joseph Abeille, 1699 [7]. (b) Prototype "G-Block" assembly, 1984 [8].	2
1.2 Experiment results for a TIM system [10].	3
1.3 Modeling a TIM system as a summation of Mises trusses [10–12]. (a) The locations of thrust lines are depicted on a center loaded TIM system. (b) A vector plot of compressive stresses shows the thrust lines. (c) A cross section of one thrust line shows its truss-like shape. (d) The total force-deflection response modeled as a summation of responses from Mises trusses.	4
1.4 Material property chart of Young's modulus and density [19].	5
1.5 Material property chart of Young's modulus and strength [19].	6
1.6 BMW Vision Next 100 concept car with segmented skin [22].	7
1.7 A spiral is chiral. The two spirals shown here are mirror images of each other. No matter how they are rotated, they can never overlay each other.	8
1.8 Chiral metamaterials have been shown to induce a twist under axial loading [26]. (a) Chiral metamaterial. (b) Structure comprised of chiral metamaterial twisting under axial load.	8
1.9 Example of a non-reciprocal structure. (a) The unloaded structure. (b) Bending is resisted only by the red material. (c) Bending is resisted by both the red and blue materials.	9
2.1 The 11 distinct Archimedean Tilings. The $(3^4.6)$ tiling occurs in left-handed and right-handed forms, both are shown here.	14
2.2 The 11 distinct Laves Tilings. The $[3^4.6]$ tiling occurs in left-handed and right-handed forms, both are shown here.	15
2.3 The set of bounded tilings considered in this work.	17
2.4 (a) Front view of plate with thrust line. (b) Top view of square plate with thrust line. (c) Top view of hexagon plate with thrust line.	19
2.5 The angle θ is the angle between the plane intersecting a tile edge and a plane perpendicular to the tile plane.	21

Figure	Page
2.6 Block construction from a square tile. (a) The intersection of three edge planes defines the first vertex. (b) The intersection of the next three edge planes defines the second vertex. (c) All planes and all vertices. (d) Wire frame of the resulting block.	22
2.7 Truncated block construction from a square tile. (a) The intersection of two edge planes and the top plane defines the first top vertex. (b) The intersection of the next two edge planes and the top plane defines the second top vertex. (c) The intersection of two edge planes and the bottom plane defines the first bottom vertex. (d) The intersection of the next two edge planes and the bottom plane defines the next bottom vertex. (e) All planes and all vertices. (f) Wire frame of the resulting block.	23
2.8 Assembly configurations: (a) [4 ⁴]-A, (b) [4 ⁴]-B.	25
2.9 Assembly configurations: (a) [3.6.3.6]-A, (b) [3.6.3.6]-B.	25
2.10 Assembly configurations: (a) [3.4.6.4]-A, (b) [3.4.6.4]-B, (c) [3.4.6.4]-C. . .	26
2.11 Assembly configurations: (a) [3 ⁶]-A, (b) [3 ⁶]-B.	26
2.12 Assembly configurations: (a) (4.8 ²)-A(-), (b) (4.8 ²)-A(+), (c) (4.8 ²)-B. . .	27
2.13 Assembly configurations: (a) (4.6.12)-A(-), (b) (4.6.12)-A(+), (c) (4.6.12)-B(-), (d) (4.6.12)-B(+), (e) (4.6.12)-C(-), (f) (4.6.12)-C(+).	28
2.14 Displacement load setup with fixed frame and velocity controlled indenter.	30
2.15 Example of displacement loading simulation results, [3.6.3.6]-B, (a) System energies (b) Force-deflection response. (c) Moment-deflection response. . .	31
2.16 Gravity load setup with fixed frame and gravity load applied to all blocks.	32
2.17 Example vector plot of minimum principal stress [MPa], [4 ⁴]-A configuration under displacement load.	33
2.18 Example of mesh convergence for [3.6.3.6]-A. (a) Force-deflection data. (b) Maximum force vs number of elements.	35
2.19 Example of false energies ratios and their sum, [3.6.3.6]-A.	37
2.20 Mesh convergence, [4 ⁴]-A, showing an outlier at Seed = 2.0 mm. (a) Force-deflection data. (b) Maximum force vs number of elements.	37
2.21 Mesh convergence, [4 ⁴]-B, showing an outlier at Seed = 1.6 mm. (a) Force-deflection data. (b) Maximum force vs number of elements.	38
2.22 One side of contact interface for tetrahedron showing interlocked hour-glassing. Blue is protrusion, green/yellow is indentation.	39

Figure	Page
2.23 Finite element model validation for (a) square plate, and (b) hexagon plate.	40
2.24 Vector plot of maximum absolute value principal stresses [MPa] for a square plate transversely loaded to a deflection of 12.5 mm.	40
2.25 Vector plot of maximum absolute value principal stresses [MPa] for a hexagon plate transversely loaded to a deflection of 12.5 mm.	41
3.1 Displacement loading results for [4 ⁴]-A configuration: (a) System energies. (b) Slip ratio ALLFD/ALLSE. (c) Force-deflection response. (d) Moment-deflection response.	46
3.2 Displacement loading results for [4 ⁴]-B configuration: (a) System energies. (b) Slip ratio ALLFD/ALLSE. (c) Force-deflection response. (d) Moment-deflection response.	47
3.3 Displacement loading results for [3.6.3.6]-A configuration: (a) System energies. (b) Slip ratio ALLFD/ALLSE. (c) Force-deflection response. (d) Moment-deflection response.	48
3.4 Displacement loading results for [3.6.3.6]-B configuration: (a) System energies. (b) Slip ratio ALLFD/ALLSE. (c) Force-deflection response. (d) Moment-deflection response.	49
3.5 Displacement loading results for [3.4.6.4]-A configuration: (a) System energies. (b) Slip ratio ALLFD/ALLSE. (c) Force-deflection response. (d) Moment-deflection response.	50
3.6 Displacement loading results for [3.4.6.4]-B configuration: (a) System energies. (b) Slip ratio ALLFD/ALLSE. (c) Force-deflection response. (d) Moment-deflection response.	51
3.7 Displacement loading results for [3.4.6.4]-C configuration: (a) System energies. (b) Slip ratio ALLFD/ALLSE. (c) Force-deflection response. (d) Moment-deflection response.	52
3.8 Displacement loading results for [3 ⁶]-A configuration: (a) System energies. (b) Slip ratio ALLFD/ALLSE. (c) Force-deflection response. (d) Moment-deflection response.	53
3.9 Displacement loading results for [3 ⁶]-B configuration: (a) System energies. (b) Slip ratio ALLFD/ALLSE. (c) Force-deflection response. (d) Moment-deflection response.	54
3.10 Displacement loading results for (4.8 ²)-A(-) configuration: (a) System energies. (b) Slip ratio ALLFD/ALLSE. (c) Force-deflection response. (d) Moment-deflection response.	55

Figure	Page
3.11 Displacement loading results for (4.8 ²)-A(+) configuration: (a) System energies. (b) Slip ratio ALLFD/ALLSE. (c) Force-deflection response. (d) Moment-deflection response.	56
3.12 Displacement loading results for (4.8 ²)-B configuration: (a) System energies. (b) Slip ratio ALLFD/ALLSE. (c) Force-deflection response. (d) Moment-deflection response.	57
3.13 Displacement loading results for (4.6.12)-A(-) configuration: (a) System energies. (b) Slip ratio ALLFD/ALLSE. (c) Force-deflection response. (d) Moment-deflection response.	58
3.14 Displacement loading results for (4.6.12)-A(+) configuration: (a) System energies. (b) Slip ratio ALLFD/ALLSE. (c) Force-deflection response. (d) Moment-deflection response.	59
3.15 Displacement loading results for (4.6.12)-B(-) configuration: (a) System energies. (b) Slip ratio ALLFD/ALLSE. (c) Force-deflection response. (d) Moment-deflection response.	60
3.16 Displacement loading results for (4.6.12)-B(+) configuration: (a) System energies. (b) Slip ratio ALLFD/ALLSE. (c) Force-deflection response. (d) Moment-deflection response.	61
3.17 Displacement loading results for (4.6.12)-C(-) configuration: (a) System energies. (b) Slip ratio ALLFD/ALLSE. (c) Force-deflection response. (d) Moment-deflection response.	62
3.18 Displacement loading results for (4.6.12)-C(+) configuration: (a) System energies. (b) Slip ratio ALLFD/ALLSE. (c) Force-deflection response. (d) Moment-deflection response.	63
3.19 Vector plot of minimum principal stress [MPa] for the [4 ⁴]-A configuration under displacement load. High stress areas of interest are marked in blue.	66
3.20 Vector plot of minimum principal stress [MPa] for the [4 ⁴]-B configuration under displacement load. High stress areas of interest are marked in blue.	67
3.21 Vector plot of minimum principal stress [MPa] for the [3.6.3.6]-A configuration under displacement load. High stress areas of interest are marked in blue.	67
3.22 Vector plot of minimum principal stress [MPa] for the [3.6.3.6]-B configuration under displacement load. High stress areas of interest are marked in blue.	68

Figure	Page
3.23 Vector plot of minimum principal stress [MPa] for the [3.4.6.4]-A configuration under displacement load. High stress areas of interest are marked in blue.	68
3.24 Vector plot of minimum principal stress [MPa] for the [3.4.6.4]-B configuration under displacement load. High stress areas of interest are marked in blue.	69
3.25 Vector plot of minimum principal stress [MPa] for the [3.4.6.4]-C configuration under displacement load. High stress areas of interest are marked in blue.	69
3.26 Vector plot of minimum principal stress [MPa] for the [3 ⁶]-A configuration under displacement load. Thrust lines are depicted.	70
3.27 Vector plot of minimum principal stress [MPa] for the [3 ⁶]-B configuration under displacement load. Thrust lines are depicted.	70
3.28 Vector plot of minimum principal stress [MPa] for the (4.8 ²)-A(-) configuration under displacement load. Thrust lines are depicted.	71
3.29 Vector plot of minimum principal stress [MPa] for the (4.8 ²)-A(+) configuration under displacement load. Thrust lines are depicted.	71
3.30 Vector plot of minimum principal stress [MPa] for the (4.8 ²)-B configuration under displacement load. Thrust lines are depicted.	72
3.31 Vector plot of minimum principal stress [MPa] for the (4.6.12)-A(-) configuration under displacement load. Thrust lines are depicted.	72
3.32 Vector plot of minimum principal stress [MPa] for the (4.6.12)-A(+) configuration under displacement load. Thrust lines are depicted.	73
3.33 Vector plot of minimum principal stress [MPa] for the (4.6.12)-B(-) configuration under displacement load. Thrust lines are depicted.	73
3.34 Vector plot of minimum principal stress [MPa] for the (4.6.12)-B(+) configuration under displacement load. Thrust lines are depicted.	74
3.35 Vector plot of minimum principal stress [MPa] for the (4.6.12)-C(-) configuration under displacement load. Thrust lines are depicted.	74
3.36 Vector plot of minimum principal stress [MPa] for the (4.6.12)-C(+) configuration under displacement load. Thrust lines are depicted.	75
4.1 System energies under gravity loading for (a) [4 ⁴]-A, (b) [4 ⁴]-B.	76
4.2 System energies under gravity loading for (a) [3.6.3.6]-A, (b) [3.6.3.6]-B.	77

Figure	Page
4.3 System energies under gravity loading for (a) [3.4.6.4]-A, (b) [3.4.6.4]-B, (c) [3.4.6.4]-C.	78
4.4 System energies under gravity loading for (a) [3 ⁶]-A, (b) [3 ⁶]-B.	79
4.5 System energies under gravity loading for (a) (4.8 ²)-A(-), (b) (4.8 ²)-A(+), (c) (4.8 ²)-B.	80
4.6 System energies under gravity loading for (a) (4.6.12)-A(-), (b) (4.6.12)-A(+), (c) (4.6.12)-B(-), (d) (4.6.12)-B(+), (e) (4.6.12)-C(-), (f) (4.6.12)-C(+).	81
4.7 Slip ratio under gravity loading for (a) [4 ⁴]-A, (b) [4 ⁴]-B.	82
4.8 Slip ratio under gravity loading for (a) [3.6.3.6]-A, (b) [3.6.3.6]-B.	83
4.9 Slip ratio under gravity loading for (a) [3.4.6.4]-A, (b) [3.4.6.4]-B, (c) [3.4.6.4]-C.	84
4.10 Slip ratio under gravity loading for (a) [3 ⁶]-A, (b) [3 ⁶]-B.	85
4.11 Slip ratio under gravity loading for (a)(4.8 ²)-A(-), (b) (4.8 ²)-A(+), (c) (4.8 ²)-B.	86
4.12 Slip ratio under gravity loading for (a) (4.6.12)-A(-), (b) (4.6.12)-A(+), (c) (4.6.12)-B(-), (d) (4.6.12)-B(+), (e) (4.6.12)-C(-), (f) (4.6.12)-C(+).	87
4.13 Vector plot of minimum principal stress [MPa] for the [4 ⁴]-A configuration under gravity load. The dual tessellation is depicted.	89
4.14 Vector plot of minimum principal stress [MPa] for the [4 ⁴]-B configuration under gravity load. The dual tessellation is depicted.	90
4.15 Vector plot of minimum principal stress [MPa] for the [3.6.3.6]-A configuration under gravity load. The dual tessellation is depicted.	90
4.16 Vector plot of minimum principal stress [MPa] for the [3.6.3.6]-B configuration under gravity load. The dual tessellation is depicted.	91
4.17 Vector plot of minimum principal stress [MPa] for the [3.4.6.4]-A configuration under gravity load. The dual tessellation is depicted.	91
4.18 Vector plot of minimum principal stress [MPa] for the [3.4.6.4]-B configuration under gravity load. The dual tessellation is depicted.	92
4.19 Vector plot of minimum principal stress [MPa] for the [3.4.6.4]-C configuration under gravity load. The dual tessellation is depicted.	92
4.20 Vector plot of minimum principal stress [MPa] for the [3 ⁶]-A configuration under gravity load. The dual tessellation is depicted.	93

Figure	Page
4.21 Vector plot of minimum principal stress [MPa] for the $[3^6]$ -B configuration under gravity load. The dual tessellation is depicted.	93
4.22 Vector plot of minimum principal stress [MPa] for the (4.8^2) -A(-) configuration under gravity load. The dual tessellation is depicted.	94
4.23 Vector plot of minimum principal stress [MPa] for the (4.8^2) -A(+) configuration under gravity load. The dual tessellation is depicted.	94
4.24 Vector plot of minimum principal stress [MPa] for the (4.8^2) -B configuration under gravity load. The dual tessellation is depicted.	95
4.25 Vector plot of minimum principal stress [MPa] for the $(4.6.12)$ -A(-) configuration under gravity load. The dual tessellation is depicted.	95
4.26 Vector plot of minimum principal stress [MPa] for the $(4.6.12)$ -A(+) configuration under gravity load. The dual tessellation is depicted.	96
4.27 Vector plot of minimum principal stress [MPa] for the $(4.6.12)$ -B(-) configuration under gravity load. The dual tessellation is depicted.	96
4.28 Vector plot of minimum principal stress [MPa] for the $(4.6.12)$ -B(+) configuration under gravity load. The dual tessellation is depicted.	97
4.29 Vector plot of minimum principal stress [MPa] for the $(4.6.12)$ -C(-) configuration under gravity load. The dual tessellation is depicted.	97
4.30 Vector plot of minimum principal stress [MPa] for the $(4.6.12)$ -C(+) configuration under gravity load. The dual tessellation is depicted.	98
5.1 Strength and stiffness cross property correlation.	100
5.2 Toughness and stiffness cross property correlation.	101
5.3 Toughness and strength cross property correlation.	101
5.4 Stiffness and onset of slip dominance cross property correlation.	102
5.5 Stiffness and the constant slip ratio value from gravity loading.	102
5.6 Strength vs number of tiles in the base tiling.	105
5.7 Strength vs total contact area between segmented bodies.	105
5.8 Strength vs number of contact interfaces between segmented bodies.	106
5.9 Strength vs area of the largest tile in the base tiling.	106
5.10 Strength vs area of the smallest tile in the base tiling.	107
5.11 Chiral length vs deflection for (a) $[4^4]$ -B, (b) $[3^6]$ -B.	109

Figure	Page
5.12 Chiral length vs deflection for (a) [3.6.3.6]-A, (b) [3.6.3.6]-B.	110
5.13 Chiral length vs deflection for (a) [3.4.6.4]-A, (b) [3.4.6.4]-B, (c) [3.4.6.4]-C.	111
5.14 Reciprocity of force-deflection for assemblies based on the (4.8 ²) tiling. (4.8 ²)-A is non-reciprocal while (4.8 ²)-B exhibits reciprocity. (a) (4.8 ²)-A, (b) (4.8 ²)-B.	112
5.15 Reciprocity of force-deflection for assemblies based on the (4.6.12) tiling. All are non-reciprocal (a) (4.6.12)-A, (b) (4.6.12)-B, (c) (4.6.12)-C.	113
5.16 Effect of friction on [3.4.6.4]-B for (a) force-deflection, (b) moment-deflection, (c) chiral length.	116
5.17 Effect of friction on system energies of [3.4.6.4]-B for (a) $\mu = 0.2$, (b) $\mu = 0.3$, (c) $\mu = 0.4$	117
5.18 Effect of friction on [3 ⁶]-B for (a) force-deflection, (b) moment-deflection, (c) chiral length.	118
5.19 Effect of friction on system energies of [3 ⁶]-B for (a) $\mu = 0.2$, (b) $\mu = 0.3$, (c) $\mu = 0.4$	119
5.20 Effect of friction on (4.8 ²)-B for (a) force-deflection, (b) moment-deflection.	120
5.21 Effect of friction on system energies of (4.8 ²)-B for (a) $\mu = 0.2$, (b) $\mu = 0.3$, (c) $\mu = 0.4$	121
5.22 Effect of friction on (4.6.12)-A(+) for (a) force-deflection, (b) moment- deflection.	122
5.23 Effect of friction on system energies of (4.6.12)-A(+) for (a) $\mu = 0.2$, (b) $\mu = 0.3$, (c) $\mu = 0.4$	123
5.24 Strength and stiffness cross property correlation trends for $\mu = 0.2$, $\mu =$ 0.3 , and $\mu = 0.4$	125
5.25 Toughness and stiffness cross property correlation trends for $\mu = 0.2$, $\mu = 0.3$, and $\mu = 0.4$	125
5.26 Toughness and strength cross property correlation trends for $\mu = 0.2$, $\mu = 0.3$, and $\mu = 0.4$	126
5.27 Material property chart of Young's modulus and density [19] with the- oretical expansions of ceramic and metal material spaces resulting from segmentation. The direction of influence of friction on segmented systems is also marked.	128

Figure	Page
5.28 Material property chart of Young's modulus and strength [19] with a theoretical homogeneous material (magenta) and its corresponding segmented material system (blue). The direction of influence of friction on segmented systems is also marked.	129
A.1 Mesh convergence for [4 ⁴]-A configuration: (a) Force-deflection data. (b) Maximum force vs number of elements.	135
A.2 Mesh convergence for [4 ⁴]-B configuration: (a) Force-deflection data. (b) Maximum force vs number of elements.	136
A.3 Mesh convergence for [3.6.3.6]-A configuration: (a) Force-deflection data. (b) Maximum force vs number of elements.	136
A.4 Mesh convergence for [3.6.3.6]-B configuration: (a) Force-deflection data. (b) Maximum force vs number of elements.	137
A.5 Mesh convergence for [3.4.6.4]-A configuration: (a) Force-deflection data. (b) Maximum force vs number of elements.	137
A.6 Mesh convergence for [3.4.6.4]-B configuration: (a) Force-deflection data. (b) Maximum force vs number of elements.	138
A.7 Mesh convergence for [3.4.6.4]-C configuration: (a) Force-deflection data. (b) Maximum force vs number of elements.	138
A.8 Mesh convergence for [3 ⁶]-A configuration: (a) Force-deflection data. (b) Maximum force vs number of elements.	139
A.9 Mesh convergence for [3 ⁶]-B configuration: (a) Force-deflection data. (b) Maximum force vs number of elements.	139
A.10 Mesh convergence for (4.8 ²)-A(-) configuration: (a) Force-deflection data. (b) Maximum force vs number of elements.	140
A.11 Mesh convergence for (4.8 ²)-A(+) configuration: (a) Force-deflection data. (b) Maximum force vs number of elements.	140
A.12 Mesh convergence for (4.8 ²)-B(-) configuration: (a) Force-deflection data. (b) Maximum force vs number of elements.	141
A.13 Mesh convergence for (4.8 ²)-B(+) configuration: (a) Force-deflection data. (b) Maximum force vs number of elements.	141
A.14 Mesh convergence for (4.6.12)-A(-) configuration: (a) Force-deflection data. (b) Maximum force vs number of elements.	142
A.15 Mesh convergence for (4.6.12)-A(+) configuration: (a) Force-deflection data. (b) Maximum force vs number of elements.	142

Figure	Page
A.16 Mesh convergence for (4.6.12)-B(-) configuration: (a) Force-deflection data. (b) Maximum force vs number of elements.	143
A.17 Mesh convergence for (4.6.12)-B(+) configuration: (a) Force-deflection data. (b) Maximum force vs number of elements.	143
A.18 Mesh convergence for (4.6.12)-C(-) configuration: (a) Force-deflection data. (b) Maximum force vs number of elements.	144
A.19 Mesh convergence for (4.6.12)-C(+) configuration: (a) Force-deflection data. (b) Maximum force vs number of elements.	144
B.1 False energies for (a) [4 ⁴]-A, (b) [4 ⁴]-B.	145
B.2 False energies for (a) [3.6.3.6]-A, (b) [3.6.3.6]-B.	145
B.3 False energies for (a) [3.4.6.4]-A, (b) [3.4.6.4]-B, (c) [3.4.6.4]-C.	146
B.4 False energies for (a) [3 ⁶]-A, (b) [3 ⁶]-B.	147
B.5 False energies for (a) (4.8 ²)-A(-), (b) (4.8 ²)-A(+), (c) (4.8 ²)-B(-), (d) (4.8 ²)-B(+).	148
B.6 False energies for (a) (4.6.12)-A(-), (b) (4.6.12)-A(+), (c) (4.6.12)-B(-), (d) (4.6.12)-B(+), (e) (4.6.12)-C(-), (f) (4.6.12)-C(+).	149

SYMBOLS

a	width of a square plate
b	radius of a circle plate
δ	deflection
D	elastic plate constant
E	Young's modulus
F	force
ν	Poisson's ratio
r'_0	radius of applied distributed load
σ	stress
t	plate thickness

ABSTRACT

Williams, Andrew J. M.S.M.E., Purdue University, August 2019. Load Response of Topologically Interlocked Material Systems - Archimedean and Laves Tilings. Major Professor: Thomas H. Siegmund, School of Mechanical Engineering.

Segmented material systems have been shown to provide advantages over monolithic materials including the potential for combinations of properties such as strength, toughness, and ductility that are not otherwise attainable. One such class of segmented system is that of topologically interlocked material (TIM) systems. These are material systems consisting of one or more repeating unit blocks assembled in a planar configuration. When coupled with a bounding frame, this plate-like structure can withstand transverse loads without the use of adhesive or fasteners between blocks.

One method of generating TIM systems is to start with a 2D tiling and project each edge of the tiles at alternating angles from the tile normal. This work examines 18 unique configurations of TIM systems generated from the Archimedean and the Laves tilings. These systems are constructed as segmented plates having approximately the same number of building blocks and with equivalent overall dimensions so that the effect of the segmentation patterns on the load response of the TIM system can be investigated. Finite element models were utilized to simulate both displacement controlled loading and body force loading of each configuration with various coefficients of friction. The load responses were recorded and the characteristics of chirality and reciprocity of the load response were observed.

The TIM system configurations in this study resulted in a wide variety of performance. Their range of properties is presented, and a mechanism for strength in a TIM system is postulated. The findings of this work enable the material design space

to be expanded by facilitating the creation of material systems with a greater range of properties than is possible with monolithic materials.

1. INTRODUCTION

Topologically interlocked materials (TIMs) are material systems consisting of one or more repeating unit blocks assembled in a planar configuration such that each block is geometrically constrained by its neighbours. The assembly is terminated by a frame that constrains the outermost blocks. The resulting plate-like structure does not use any type of adhesive or fastener between blocks but is capable of carrying transverse loads. These material systems are advantageous due to their potential attractive combination of strength, toughness, and damage tolerance as compared to monolithic plates, especially when using lower strength materials [1–4]. TIMs are damage tolerant due to the fact that cracks in any single block cannot propagate to neighbouring blocks [5].

The first known concept of interlocking structures can be found in segmented lintels of castles, cathedrals, and churches from the Middle Ages [6]. In 1699 the first known interlocked plate-like structure as proposed by Joseph Abeille [7], Figure 1.1(a). This flat vault is essentially an assembly of truncated tetrahedra. It was revisited in 1984 as a concrete paving method [8], Figure 1.1(b), however, the mechanics of such a system were not studied in detail until 2001 when the concept was brought back to light with a mechanical analysis of a tetrahedron assembly [9]. Since then there has been continued interest in the study of TIMs.

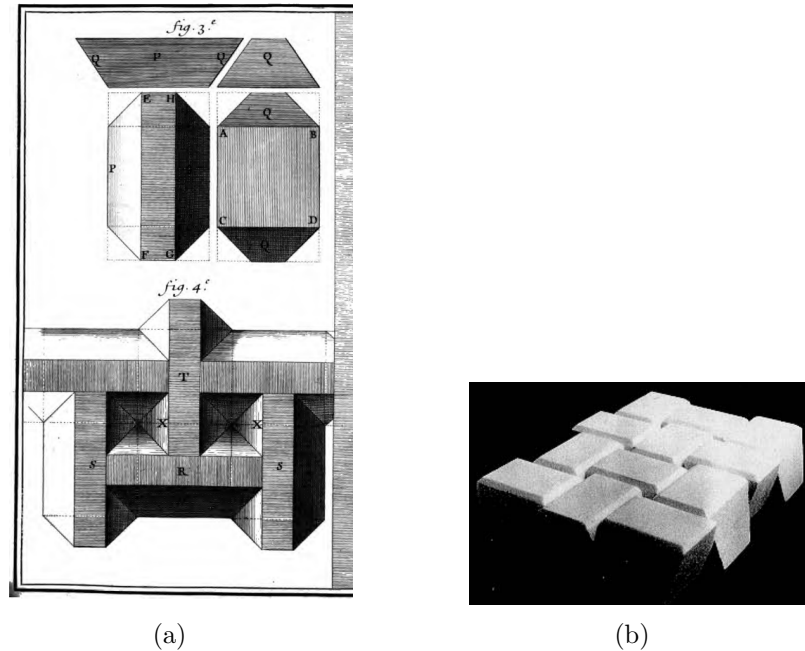


Figure 1.1. (a) Flat vault design by Joseph Abeille, 1699 [7]. (b) Prototype "G-Block" assembly, 1984 [8].

Prior work has focused extensively on the tetrahedron assembly including static loading [10], impact response [3], adaptability [11], scaling [12], and manufacturing [4]. Some work has been done to study the mechanics of assemblies of octahedra [1] and osteomorphic blocks [2], and many additional designs have been proposed and studied to varying degrees [13–15], but there is no unifying theory across the broad spectrum of possible TIMs.

1.1 Load Response

The force-deflection response of a transversely loaded, simply supported monolithic square, Equation (1.1), or circle, Equation (1.2), plate is a linear relationship [16]. These equations are only valid for small deflections such that the plate remains in the elastic region. However, similarly sized plates constructed from TIM systems can far exceed the deflections of a monolithic plate. The force deflection-

response of a TIM system to displacement controlled transverse loading is typically a skewed parabola similar to that of a Mises truss [1, 10, 17, 18], Figure 1.2. After an initial stiffness, the maximum strength is reached and followed by a period of negative stiffness until the reaction force returns to zero. The response is usually skewed so that the period of negative stiffness occurs over a larger deflection than the initial period up to the the maximum strength. Unlike a Mises truss, TIM systems cannot snap through and enter a negative strength regime because they have no mechanism to carry tensile loads. The mode of final failure is disassembly of the system during which the individual blocks separate from each other.

$$F = \frac{7.893\delta Et^3}{a^2} \quad (1.1)$$

$$F = \frac{16\pi\delta D(1 + \nu)}{b^2(3 + \nu)} \quad (1.2)$$

$$D = \frac{Et^3}{12(1 - \nu^2)}$$

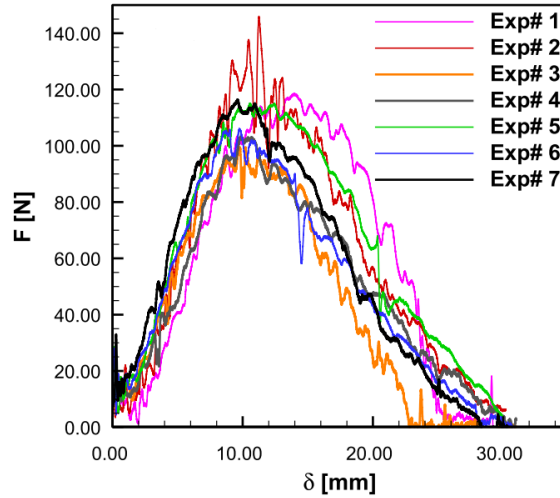


Figure 1.2. Experiment results for a TIM system [10]

The force-deflection response of TIM systems has been modeled as a summation of Mises trusses [10], Figure 1.3. This method accounts for the skewed nature of the parabola response by having trusses that collapse at different deflections, Figure 1.3(d). This truss-like behavior can be visualized in a finite element model by displaying a vector plot of compressive stresses, Figures 1.3(b) and 1.3(c). Concentrations of stress appear as thrust lines through the model indicating truss-like behavior.

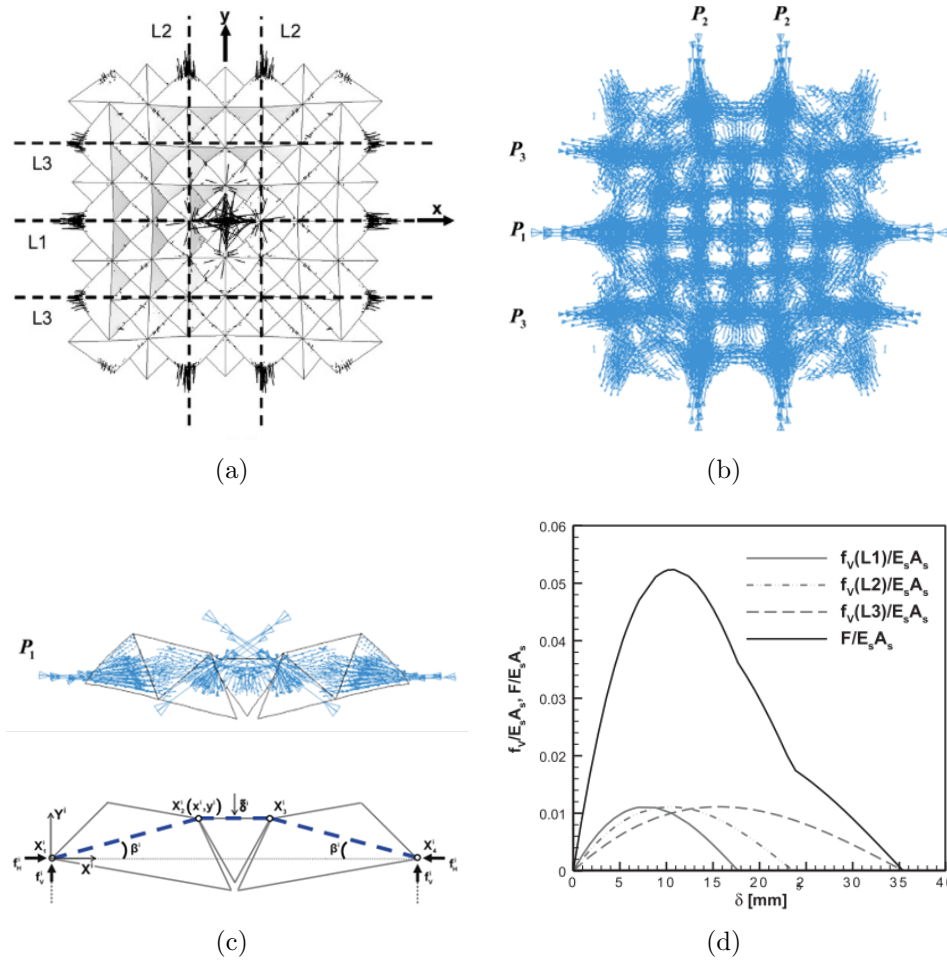


Figure 1.3. Modeling a TIM system as a summation of Mises trusses [10–12]. (a) The locations of thrust lines are depicted on a center loaded TIM system. (b) A vector plot of compressive stresses shows the thrust lines. (c) A cross section of one thrust line shows its truss-like shape. (d) The total force-deflection response modeled as a summation of responses from Mises trusses.

1.2 Motivation

For traditional materials elastic modulus increases with density, but the creation of modern elastomers breaks that trend and widens the available material space by enabling the formulation of materials having a wide range of elastic moduli over similar densities, Figure 1.4. This work seeks to accomplish a similar goal by enabling a range of elastic moduli for any material by altering the global elasticity through the structure of the system. With this approach, the density of the base material would not change, but different segmentation patterns could lead to varying elastic moduli for the system.

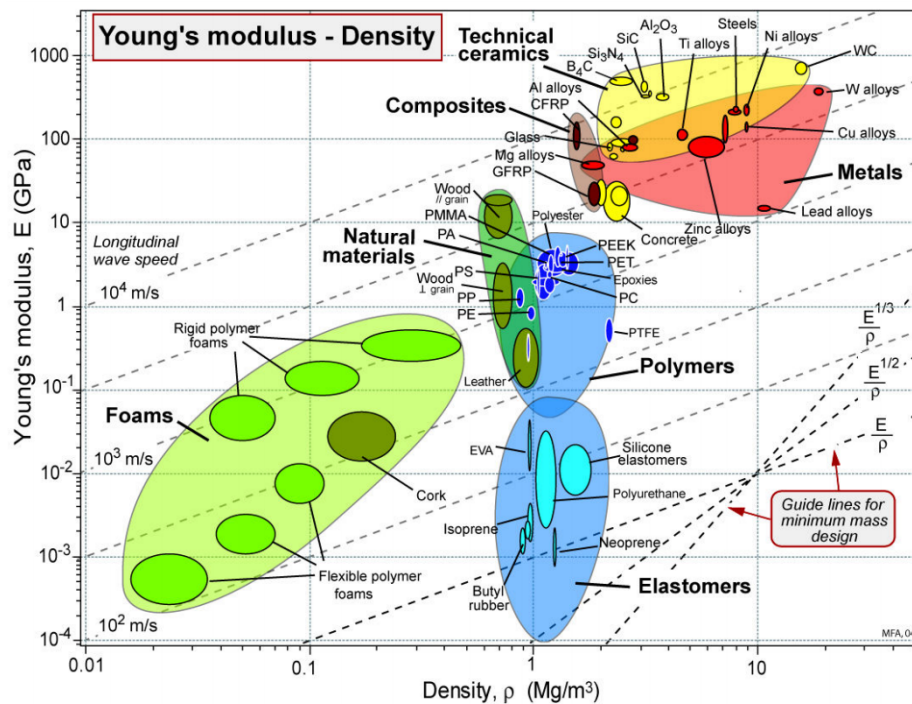


Figure 1.4. Material property chart of Young's modulus and density [19].

Similarly, the elastic modulus generally increases with the material strength, Figure 1.5, but this trend can be problematic if high strength and ductility are required. This problem has been addressed in nature through various methods, such as in a

fish's scales which must be locally strong in order to provide protection but must also be globally flexible to allow the fish to swim [20]. Fish scales have inspired the creation of synthetic materials that are locally strong and globally flexible with the intent of protecting soft materials [21]. Similar approaches have been utilized in engineering applications such as the BMW Vision Next 100 concept car, Figure 1.6. This vehicle has segmented body panels around the front wheel wells that allow the car's exterior to deform with the tires as the vehicle turns. The vehicle's exterior is strong enough to protect the vehicle and flexible enough to deform around the tires. This work seeks to expand the options available for such applications that require strong yet ductile materials by implementing segmentation in the material system to provide local strength and global flexibility.

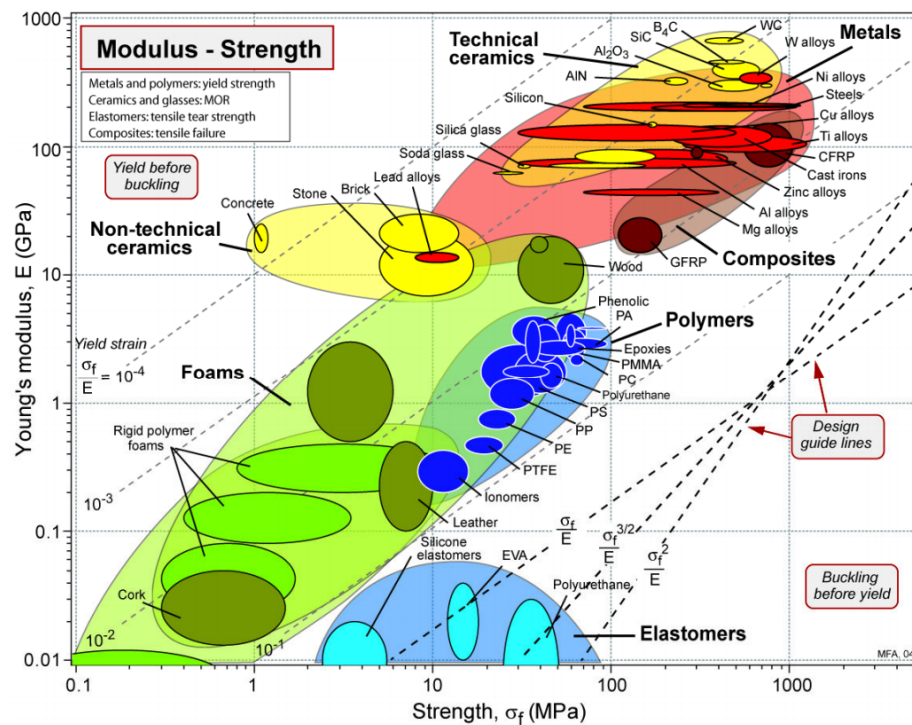


Figure 1.5. Material property chart of Young's modulus and strength [19].



Figure 1.6. BMW Vision Next 100 concept car with segmented skin [22].

In addition to breaking the trends of traditional material properties, segmented systems might exhibit unique characteristics that are not possible with monolithic materials, such as chirality and varying reciprocity of the load response.

1.2.1 Chirality

Chirality is a geometric property indicating that a shape or object cannot be superimposed onto a mirror image of itself, such as the spirals in Figure 1.7. Chirality occurs naturally in biology, a quick look at one's hands will show this, but it also occurs at a cellular level where it is utilized for various objectives [23–25]. Its ability to add functionality to a structure can be advantageous to engineering applications as well [26–28]. In some material systems, chirality has been shown to induce a rotation in the system as a linear load is applied, Figure 1.8 [26].

1.2.2 Reciprocity of the Load Response

Static non-reciprocity has been demonstrated in metamaterials and can be used to add functionality to a structure [29]. TIM systems may also be able to demonstrate a

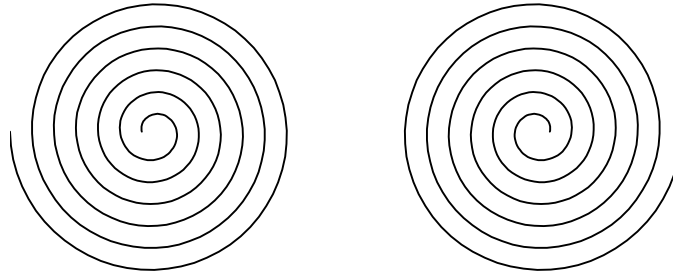


Figure 1.7. A spiral is chiral. The two spirals shown here are mirror images of each other. No matter how they are rotated, they can never overlay each other.

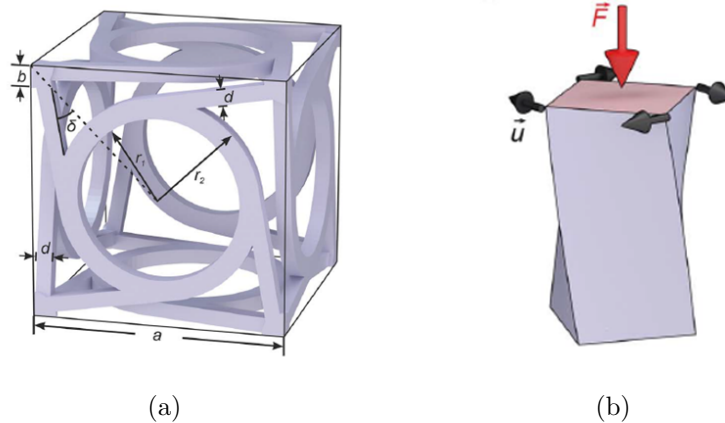


Figure 1.8. Chiral metamaterials have been shown to induce a twist under axial loading [26]. (a) Chiral metamaterial. (b) Structure comprised of chiral metamaterial twisting under axial load.

type of non-reciprocity with regard to the load response. In the context of this work, a structure will be considered reciprocal in the load response if the response is the same regardless of the load direction. For example, consider a traditional monolithic plate oriented such that the transverse direction is aligned with the Z -axis. Assuming the edges of the plate are fixed, its response would be equal in magnitude regardless of whether it were loaded in the $+Z$ or $-Z$ direction. However, a structure such

as in Figure 1.9 is not reciprocal in the load response. If this structure were bent in the plane of this page such that the center moved up relative to the ends, the vertical flanges would angle away from each other and would not significantly affect the response, Figure 1.9(b). But if the structure were bent in the other direction, the vertical flanges would deflect inwards and contact each other resulting in a much stiffer response, Figure 1.9(c). This kind of non-reciprocal behavior could be advantageous in some designs, such as in the BMW Vision Next 100. It would be beneficial to have a lower stiffness when bending the car's exterior outward and a higher stiffness when bending the exterior inwards. This would allow the exterior to more easily bend outward around the tires when the vehicle turns, but it would also enable a stiff response to bending inward so as to protect the vehicle from impact. Some prior work has been done to create a non-reciprocal response in TIM systems by asymmetric truncation or by using multiple materials [4,30]. This work seeks to investigate if TIM systems can exhibit non-reciprocity.

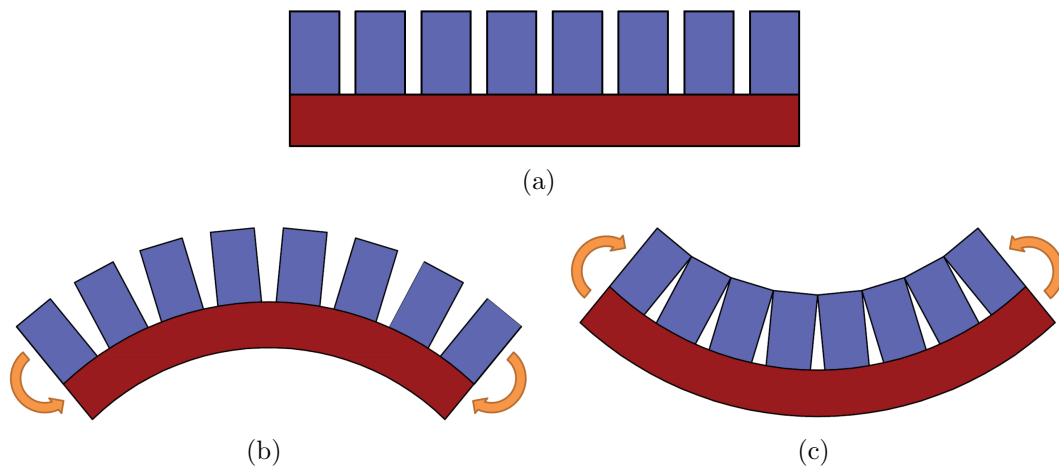


Figure 1.9. Example of a non-reciprocal structure. (a) The unloaded structure. (b) Bending is resisted only by the red material. (c) Bending is resisted by both the red and blue materials.

1.3 Scope of Research

The goal of this research is to increase our understanding of TIM systems originating from a variety of tilings. To this date there has not been a comprehensive study of TIM systems in order to draw conclusions across the various systems. This work will examine TIM systems constructed from six different tilings and formed into 18 configurations. It will address the following goals:

1. Determine the load response of TIM systems emerging from Archimedean and Laves tilings. Some of the configurations presented here have been examined extensively, while others have only been shown in geometric form and have not been the subject of any load testing or simulations. This work will determine the load response of all 18 configurations under two different load types.
2. Find property-architecture relationships across TIM systems. There has been little work to find generalized descriptions for the properties of various TIM systems. This work seeks determine an order to the TIM systems and to draw broad conclusions across them.
3. Identify unique characteristics of some TIM systems, including chirality and non-reciprocity of the load response. Prior work has not reported on chirality or non-reciprocity, but the exploration of these characteristics could expand the potential of TIM systems in future applications. Such characteristics could be advantageous or detrimental to a given design, so it is a goal of this work to describe them.
4. Expand the engineering material design space. Material systems can offer many advantages over monolithic materials. It is a goal of this work to broaden the material design space by using TIM systems to achieve sets of material properties that are unobtainable by monolithic materials.

1.4 Thesis Overview

Chapter 2 will describe the methods that were used to construct the set of TIM systems that were studied in this work. It will also detail the displacement loading and body force loading that the TIM systems were subjected to, and it will outline the modeling and simulation of these systems, as well as describe the data to be collected from the simulations and how that data will be presented in later chapters. Chapter 3 will present the results collected from the displacement load simulations, and Chapter 4 will show the results collected from the body force load simulations. The relative performance and characteristics of the TIM systems will be examined in Chapter 5, and trends across the systems will be described. Additionally, the implications of these findings will be discussed. Finally, Chapter 6 will summarize the important findings of this work and will provide concluding remarks. It will also outline potential areas of future work.

2. METHODS

This chapter describes the tiling selection process, the methods used to generate 3D interlocking geometry from the tiles, the creation of finite element models, and the verification of those models.

2.1 Tile Space

The midplane cross section of a TIM system is a 2D tiling, and this tiling is the basis for the creation of the TIM system [31]. There are an infinite number of possible tilings that could span a planar space [32], but this work focuses on two major tile sets: the Archimedean and the Laves tilings. These tile sets are duals, meaning that for every tiling in one set, there exists a dual tiling in the other set. A dual tiling is one that is obtained by drawing lines between the center points of adjacent tiles in a given tiling. Archimedean tilings consist of regular polygons only and possess one type of vertex [32]. Laves tilings are defined as having an equal angular spacing of all edges at any vertex [32]. There are 11 distinct tilings of each type.

2.1.1 Archimedean Tilings

The 11 distinct Archimedean tilings are shown in Figure 2.1. A naming convention is to use integer numbers with exponents separated by periods and contained within parenthesis. This number sequence describes the common vertex at all tile intersections. Each integer represents the number of sides of a tile that shares the vertex, and the exponent is the number of that type of tile that shares the vertex [32]. For example, each vertex in the (4.8^2) tiling is shared by one square tile, represented by a single “4”, and two octagon tiles, represented by “8²”.

In a TIM system, the sides of each block must alternate between sloping toward and away from the tile normal. Therefore, all tiles must have an even number of sides in order to continuously alternate side angles. This restriction eliminates the (3^6) , $(3^4.6)$, $(3^3.4^2)$, $(3^2.4.3.4)$, $(3.4.6.4)$, $(3.6.3.6)$, and (3.12^2) tilings. The remaining tilings are the (4^4) , (6^3) , $(4.6.12)$, and (4.8^2) tilings. The (4^4) and (6^3) tilings are considered regular tilings due to the fact that they are comprised of a single tile repeated in the same orientation.

2.1.2 Laves Tilings

The 11 distinct Laves tilings are shown in Figure 2.2. A naming convention is to use integer numbers with exponents separated by periods and contained within square braces. This number sequence describes the number of edges sharing each vertex of a single tile [32]. The integer is the number of edges that share a given vertex, and the exponent is the number of times that vertex is repeated moving around a single tile. For example, choose one tile of the $[3.4.6.4]$ tiling and start at its vertex that is shared by a total of 3 edges. Move in either direction around the tile and the next vertex is shared by 4 edges, then the next is shared by 6 edges, and the last vertex is shared by 4 edges. Similarly named Archimedean and Laves tilings are duals to each other, such as $[3^3.4^2]$ and $(3^3.4^2)$

The necessity for tiles with an even number of sides when constructing a TIM system eliminates the $[3^4.6]$, $[3^3.4^2]$, $[3^2.4.3.4]$, $[3.12^2]$, $[4.6.12]$, $[4.8^2]$, and $[6^3]$ tilings. The remaining tilings are the $[3^6]$, $[3.6.3.6]$, $[3.4.6.4]$, and $[4^4]$ tilings. The $[4^4]$ and $[3^6]$ tilings are regular tilings and are equivalent to the (4^4) and (6^3) regular Archimedean tilings. Therefore, only the $[3.6.3.6]$ and $[3.4.6.4]$ tilings are added beyond those from the Archimedean tilings.

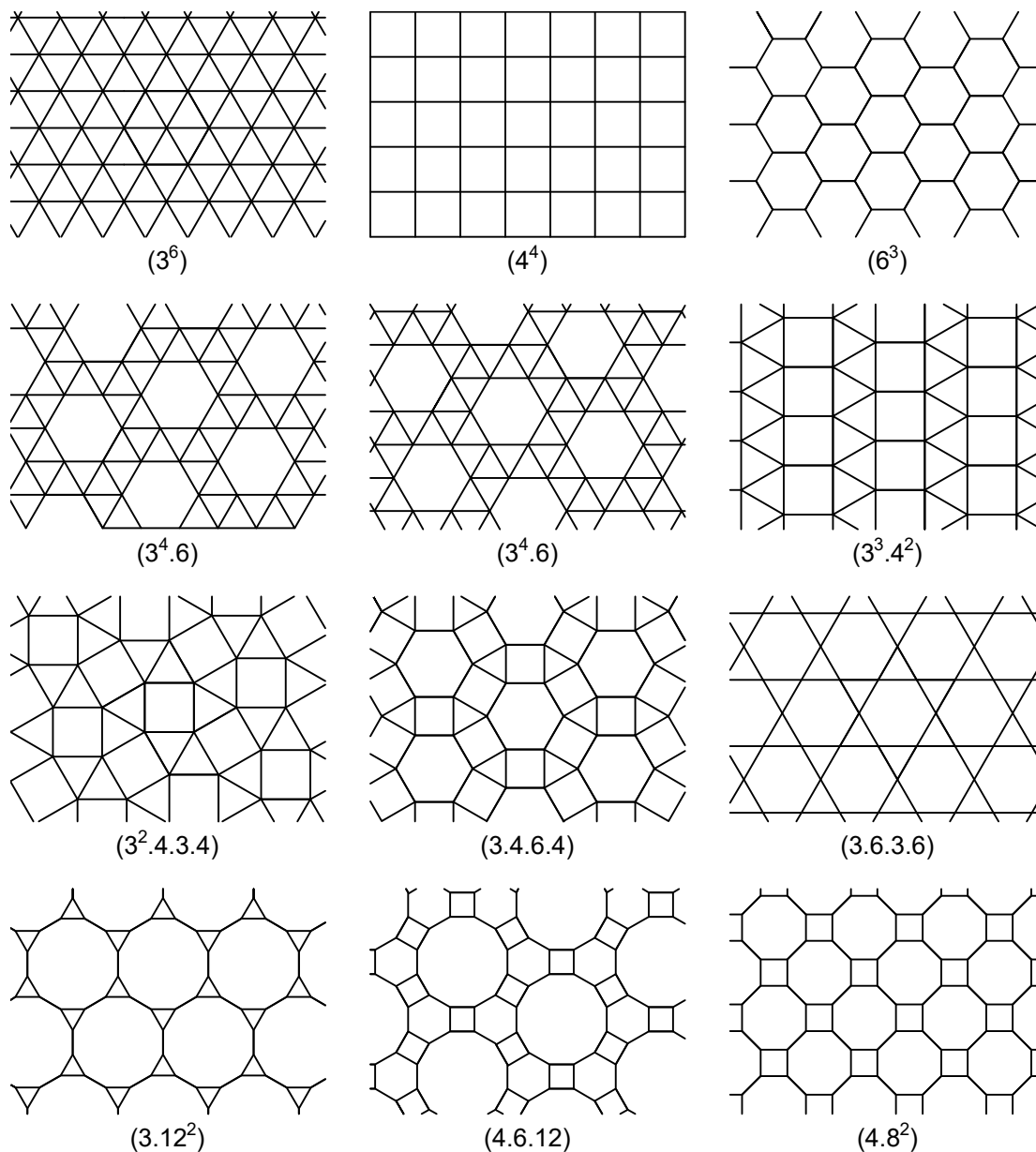


Figure 2.1. The 11 distinct Archimedean Tilings. The $(3^4.6)$ tiling occurs in left-handed and right-handed forms, both are shown here.

2.1.3 Tilings for the Construction of TIM Systems

The tilings considered in this study are the $(4^4)/[4^4]$, $[3.6.3.6]$, $[3.4.6.4]$, $(6^3)/[3^6]$, (4.8^2) , and $(4.6.12)$ tilings. The Laves notation was chosen to denote the $[4^4]$ and

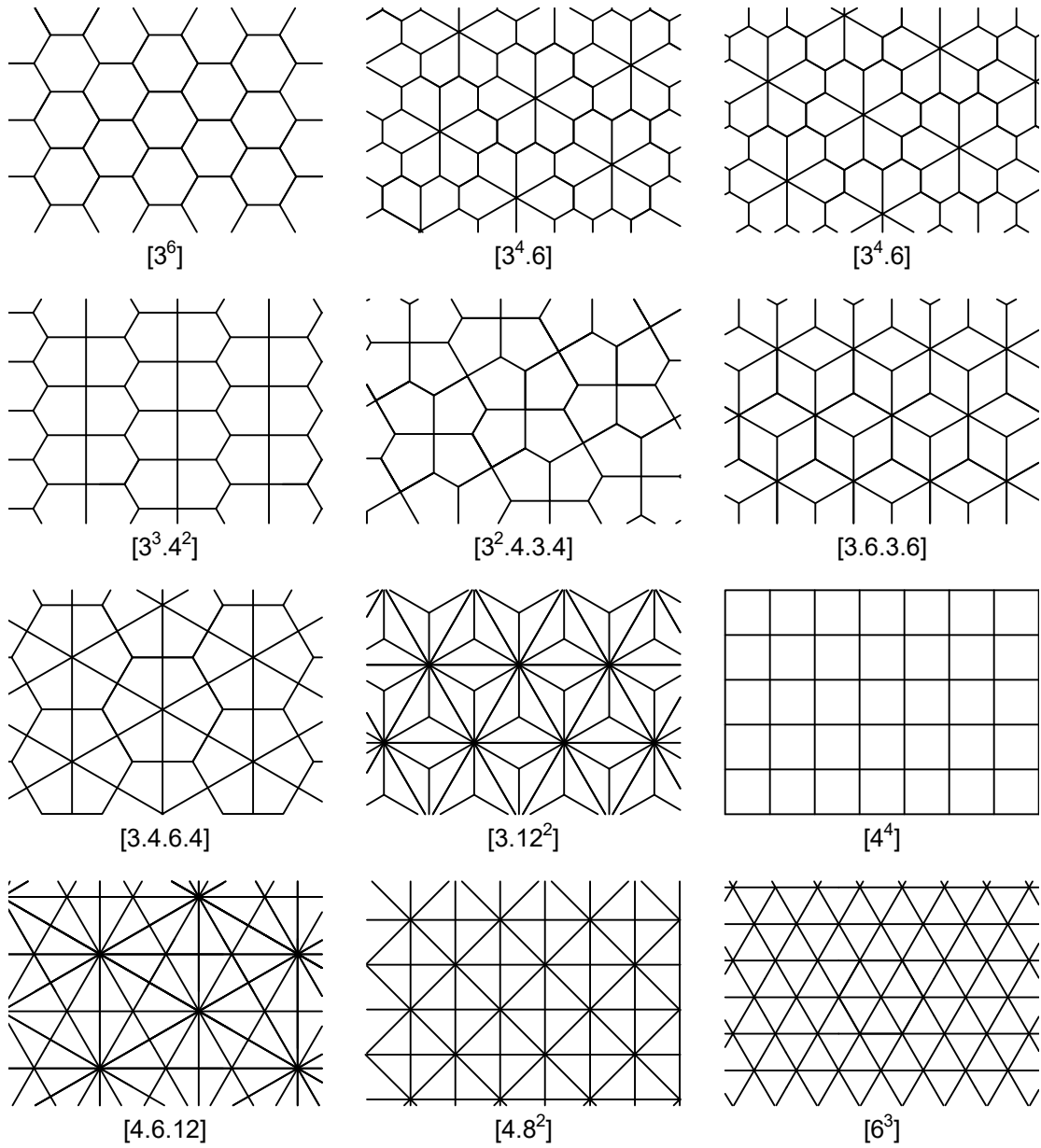


Figure 2.2. The 11 distinct Laves Tilings. The $[3^4.6]$ tiling occurs in left-handed and right-handed forms, both are shown here.

$[3^6]$ tilings instead of the Archimedean notation of (4^4) and (6^3) because these tilings are more similar to the other Laves tilings than to the other Archimedean tilings in this study. The $[4^4]$, $[3.6.3.6]$, $[3.4.6.4]$, and $[3^6]$ tilings each consist of a single tile,

whereas the (4.8^2) tiling consists of two tiles and the $(4.6.12)$ tiling consists of three. The single-tile tilings each possess a four-sided tile, with the exception of the $[3^6]$ tiling which has a six sided tile. It is also worth noting that the $[3.4.6.4]$ tiling is the only tiling considered in this study with more than one edge length.

2.1.4 Boundaries

By their definition, tilings expand infinitely within a plane, but for this work it was necessary to define a tiling domain. It was desired that a boundary in the form of a regular polygon be defined for each tiling, such that the tiling was radially symmetric about its center point within the boundary. It was found that either a square or hexagon could meet this criteria depending on the tiling. However, it was generally not possible to draw such a boundary that did not cross any of the tiles. In such cases, any tiles that were intersected by the border became part of the border. Additionally, it was found that there are multiple possible center points for each tiling, such as centering the border around different vertices or around the centroid of different tiles. These various boundaries will be referred to as A, B, and C variants of a given tiling.

It was desired to have the same number of block in each assembly in order to compare the load response of the TIM systems resulting from each tiling without introducing scaling effects caused by varying numbers of blocks [12], however, there was a natural variance in the number of tiles that could be contained within a border for each tiling, so it was not possible to have the exact number of blocks in all configurations. Bounded tilings with approximately 49 tiles were selected for each configuration following the work of Khandelwal et al. which focused on an assembly of 49 blocks [10]. The resulting bounded tilings ranged from 42 tiles up to 64 tiles, Table 2.1, and are shown in Figure 2.3.

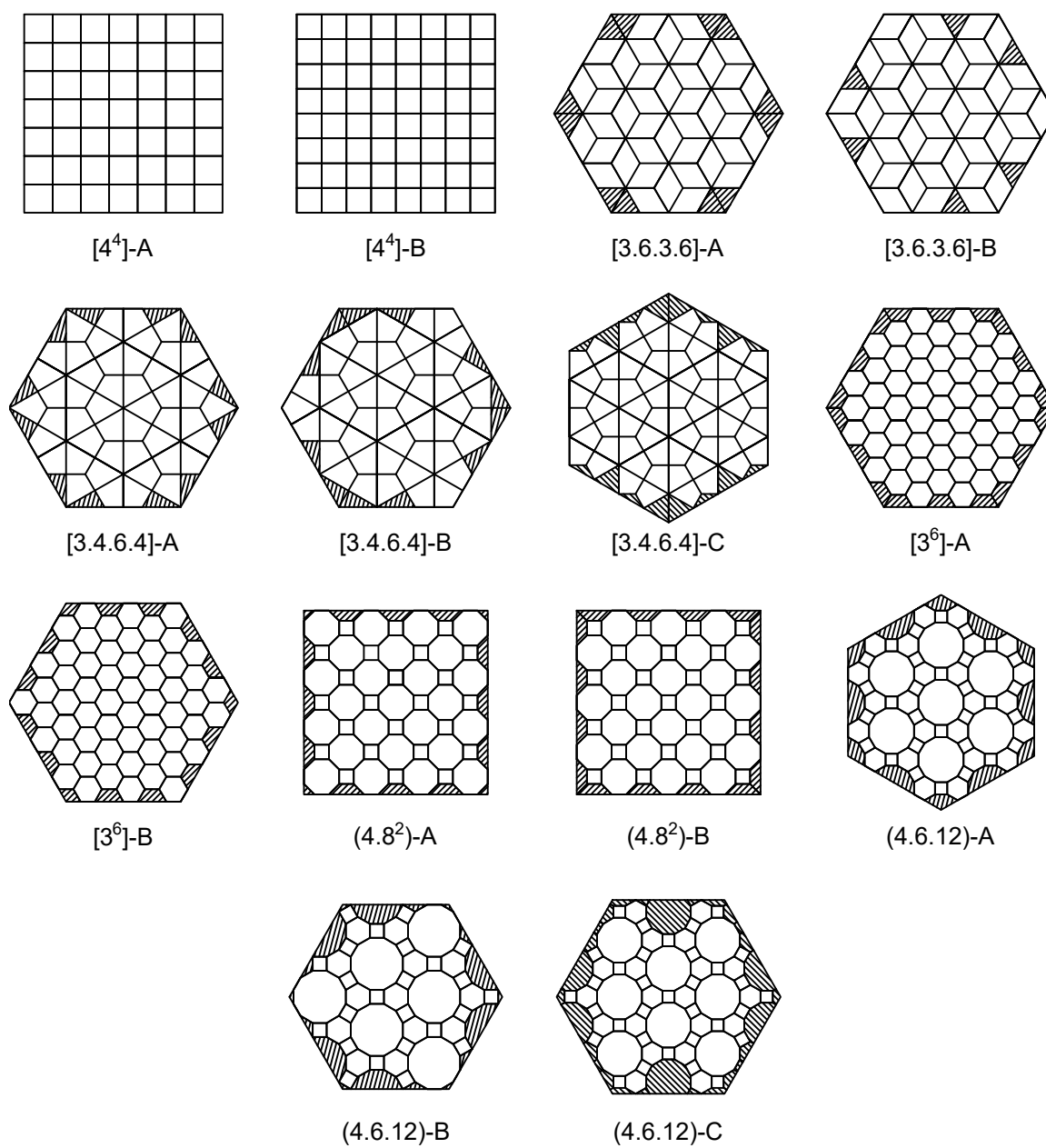


Figure 2.3. The set of bounded tilings considered in this work.

Table 2.1.

Number of tiles and edges lengths for the set of bounded tilings in this work.

Tiling	Tiles	Edge 1 [mm]	Edge 2 [mm]
$[4^4]$ -A	49	29.7	-
$[4^4]$ -B	64	26.0	-
$[3.6.3.6]$ -A	42	30.0	-
$[3.6.3.6]$ -B	46	30.0	-
$[3.4.6.4]$ -A	48	20.0	34.6
$[3.4.6.4]$ -B	48	20.0	34.6
$[3.4.6.4]$ -C	64	17.3	30.0
$[3^6]$ -A	55	15.0	-
$[3^6]$ -B	57	15.0	-
(4.8^2) -A	49	12.2	-
(4.8^2) -B	49	12.2	-
$(4.6.12)$ -A	61	12.7	-
$(4.6.12)$ -B	43	14.6	-
$(4.6.12)$ -C	61	12.6	-

2.2 3D Model

All the tilings were made into TIM systems that formed plates of approximately the same size. It is well known that the length and thickness of a homogeneous plate has a significant effect on its strength under transverse load. Additionally, if a TIM system is modeled as a series of Mises trusses, the performance of such trusses is largely dependent on the length L_0 and height H_0 which they span, Figure 2.4(a). Therefore, L_0 and H_0 were made to be constant across all configurations. L_0 was measured as the radius of the inscribed circle of the tile border in order to have similarity between square and hexagon borders, Figure 2.4.

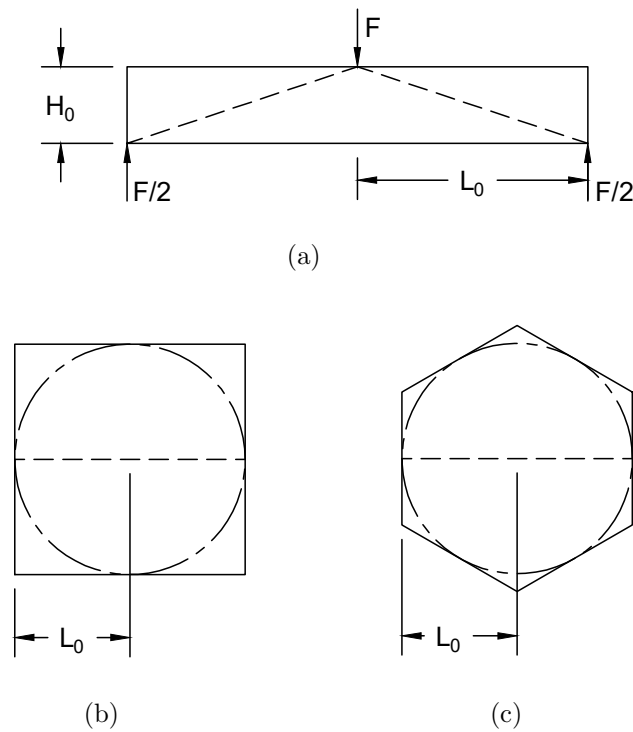


Figure 2.4. (a) Front view of plate with thrust line. (b) Top view of square plate with thrust line. (c) Top view of hexagon plate with thrust line.

The TIM block thickness H_0 was chosen to be 10.0 mm and the length L_0 was derived from the largest assembly. It was necessary to determine the largest assembly

after constructing each assembly such that its thinnest block was 10.0 mm thick after a 10% truncation, discussed in Section 2.2.2. All other assemblies could be scaled up to match the length of the largest assembly and then truncated further to match the thickness, but the larger assemblies could not be scaled down to smaller lengths without sacrificing thickness. The largest assembly was the (4.6.12)-C assembly with 61 blocks, from which L_0 was determined to be 103.9 mm.

2.2.1 Untruncated Blocks

A 3D block is constructed from a 2D tile by first projecting planes from each edge of the tile at alternating angles θ from the normal [31], Figure 2.5. The magnitude of the edge projection angle θ must be the same for all edges, but its direction will alternate between angling toward the tile center and away from the tile center for each edge. The projection angle for all configurations in this study was $\theta = 17^\circ$. Within an assembly, the blocks must be oriented such that their edge projection angles are complimentary; if the edge of one tile is angled toward the tile center, the abutting edge of the adjacent tile must be angled away from its center. Once the projection angles are specified, the vertices of the block can be determined. Each block formed from an n -sided tile will have n vertices. The intersection of the planes projected from any three consecutive tile edges locates one vertex, Figure 2.6(a). Computing the intersection of planes from all sets of three consecutive edges will locate all vertices of the block, Figure 2.6(c). Finally, edges can be drawn between the vertices to enclose the 3D volume, Figure 2.6(d). If the tile is a regular polygon, a uniform antiprism block will be formed. In any case, the midplane cross section of the block will retain the tile from which it was formed.

2.2.2 Truncated Blocks

Blocks constructed from tiles of different sizes and shapes naturally have differing overall dimensions. In order to maintain a constant thickness across all configurations

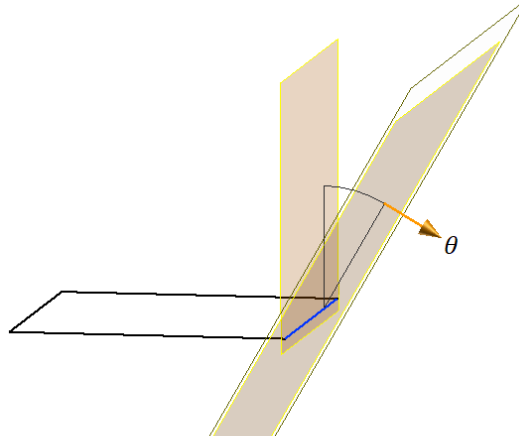


Figure 2.5. The angle θ is the angle between the plane intersecting a tile edge and a plane perpendicular to the tile plane.

of TIM systems in this study, it was necessary to truncate many of the larger blocks to match the thickness of the smaller blocks. This created a scenario where the thinnest block could be untruncated, but the all the other blocks would be truncated to match the thinnest block, however, it was decided to truncated even the thinnest blocks for continuity and to reduce the potential for point contact issues that might arise in a finite element model. Therefore, the thinnest blocks were truncated to 10% of their original thickness, and all other blocks were truncated to match the thickness of the thinnest blocks.

In order to construct a truncated block, a similar method to the untruncated blocks is used, but in this case each block formed from an n -sided tile will have $2n$ vertices. Two additional planes must be defined that are parallel and equidistant from the tile plane. These are the top and bottom planes, and they must be closer to the tile plane than all of the vertices of the untruncated block. Every set of planes projecting from two consecutive tile edges will yield two vertices, one by computing their intersection with the top plane, Figure 2.7(a), and the other by computing their intersection with the bottom plane, Figure 2.7(c). Computing the intersection of all sets of planes projecting from two consecutive edges and the top or bottom planes

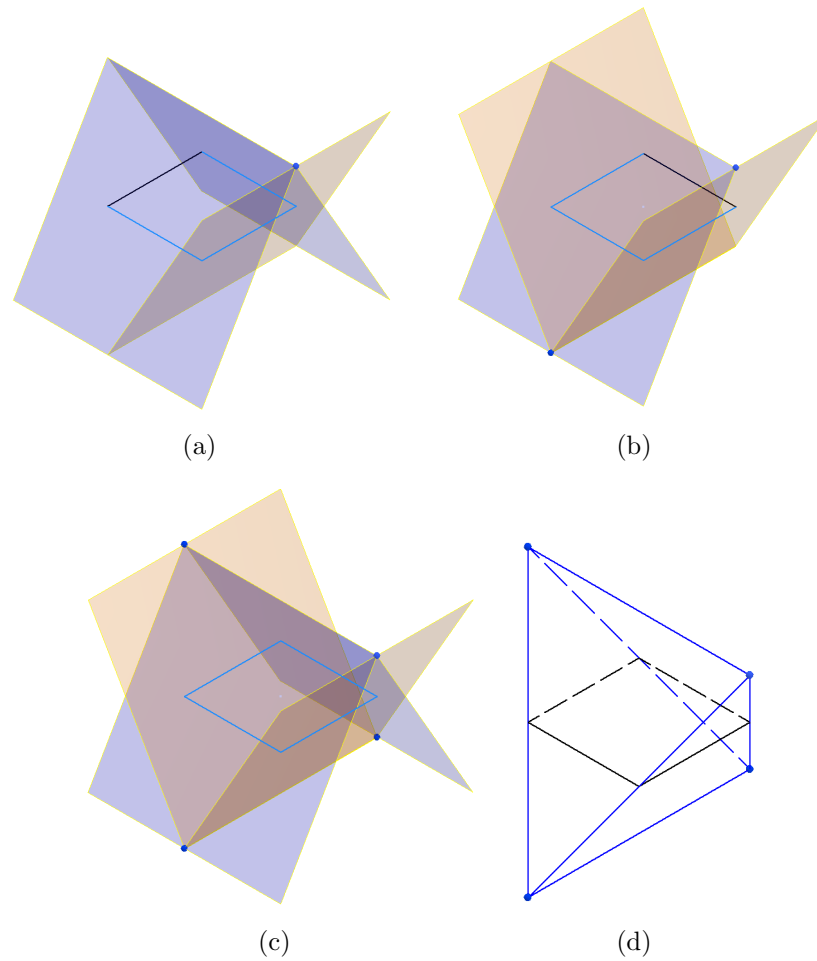


Figure 2.6. Block construction from a square tile. (a) The intersection of three edge planes defines the first vertex. (b) The intersection of the next three edge planes defines the second vertex. (c) All planes and all vertices. (d) Wire frame of the resulting block.

will locate all the vertices of the block, Figure 2.7(e). Edges are then drawn between the vertices to construct the block, Figure 2.7(f).

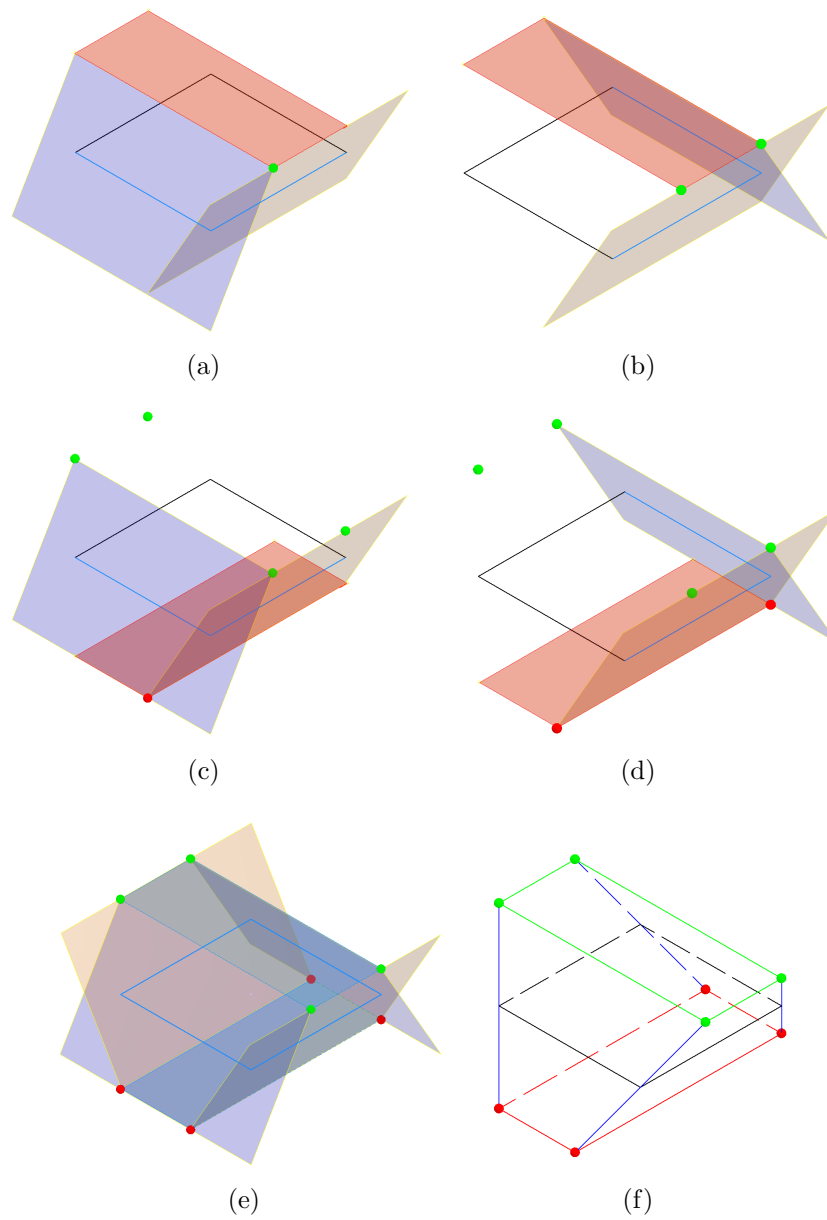


Figure 2.7. Truncated block construction from a square tile. (a) The intersection of two edge planes and the top plane defines the first top vertex. (b) The intersection of the next two edge planes and the top plane defines the second top vertex. (c) The intersection of two edge planes and the bottom plane defines the first bottom vertex. (d) The intersection of the next two edge planes and the bottom plane defines the next bottom vertex. (e) All planes and all vertices. (f) Wire frame of the resulting block.

2.2.3 Frame

TIM systems require a bounding frame to constrain the blocks in plane. These were constructed by expanding each tiling beyond the boundaries drawn in Figure 2.3 so that there was a tile adjacent to every side of the outer tiles in the bounded set. Blocks were generated on the additional tiles such that the blocks formed from the bounded tiling were completely surrounded by this additional set of blocks. The set of surrounding blocks were fused into a single part to serve as a frame for the assembly. The outer profile of this conglomerate frame was cut into either a square or hexagon shape as appropriate. Frames are shown in blue in Figures 2.8 - 2.13.

2.2.4 Assemblies and Configurations

The TIM systems in this study were constructed such that the tile plane lies on the XY-plane, therefore, the Z-axis is the transverse direction. The geometry of the single-tile systems is such that they can be flipped over and rotated to exactly overlay their original position. This means that their transverse load response is the same for loads in the -Z and +Z directions. However, the multi-tile systems do not typically share this property, so their transverse load response is often dependent on the load direction. The TIM system configurations used in this study are named after the bounded tiling from which they were created, and if the assembly is direction dependent, the load direction will be indicated. For example, the $[4^4]$ -A assembly is not direction dependent, but the $[4.8^2]$ -A assembly is, therefore it will be denoted as two separate configurations $[4.8^2]$ -A(-) and $[4.8^2]$ -A(+). The complete set of TIM system configurations in this study is shown in Figures 2.8 - 2.13.

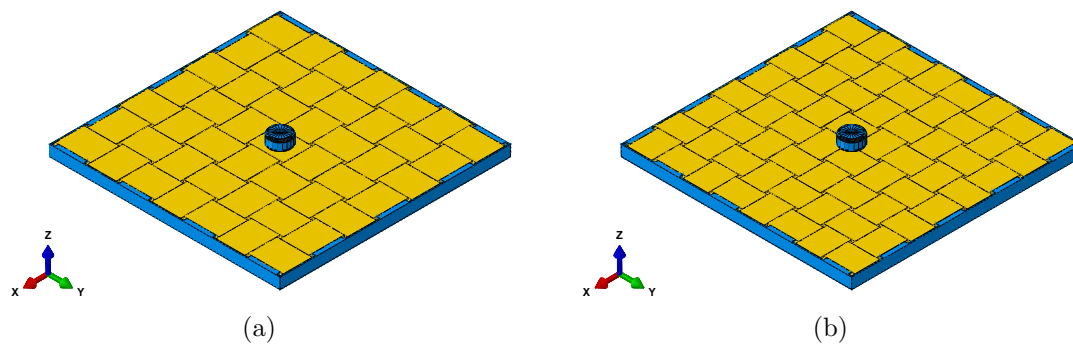


Figure 2.8. Assembly configurations: (a) $[4^4]$ -A, (b) $[4^4]$ -B.

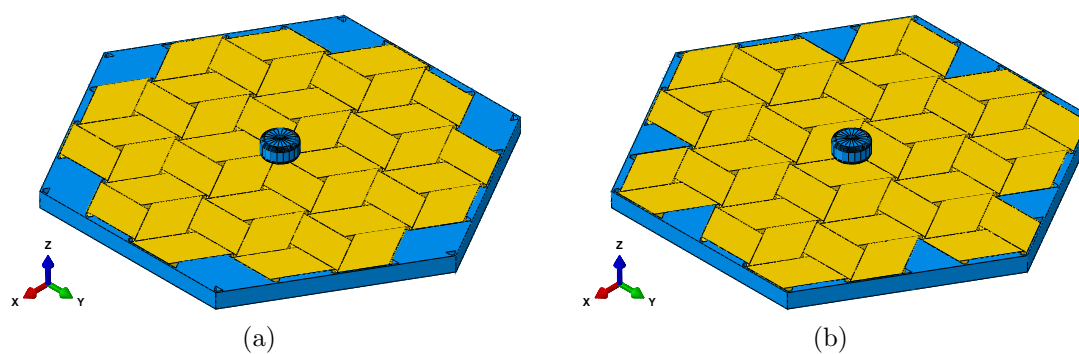


Figure 2.9. Assembly configurations: (a) $[3.6.3.6]$ -A, (b) $[3.6.3.6]$ -B.

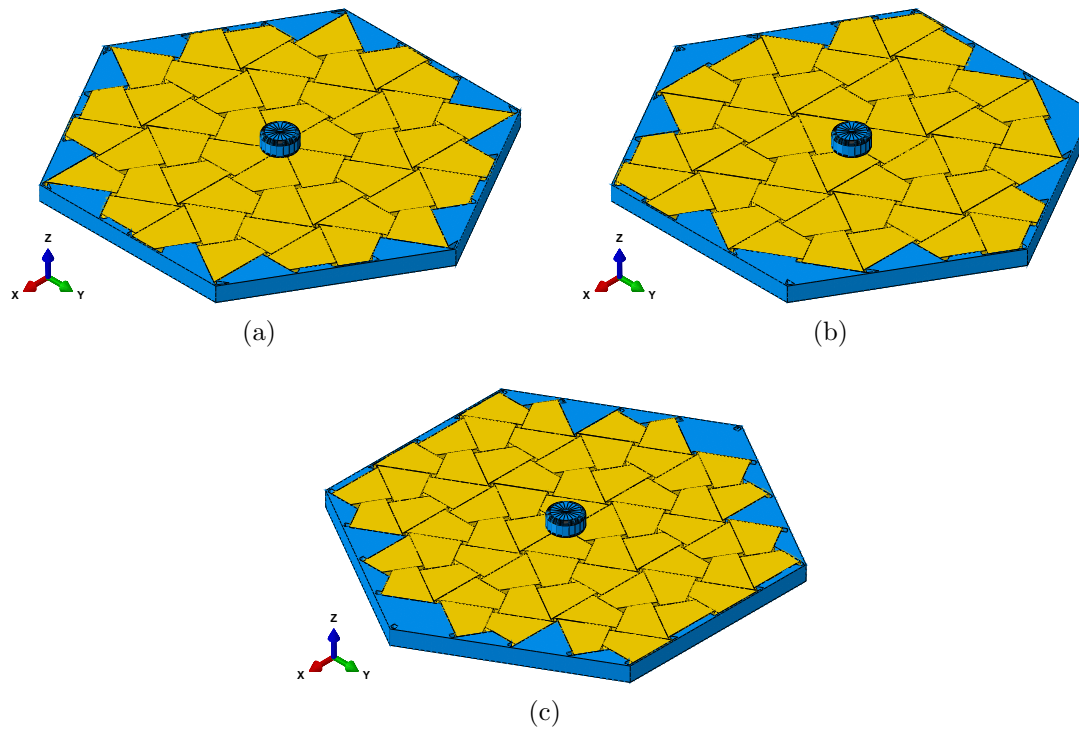


Figure 2.10. Assembly configurations: (a) [3.4.6.4]-A, (b) [3.4.6.4]-B, (c) [3.4.6.4]-C.

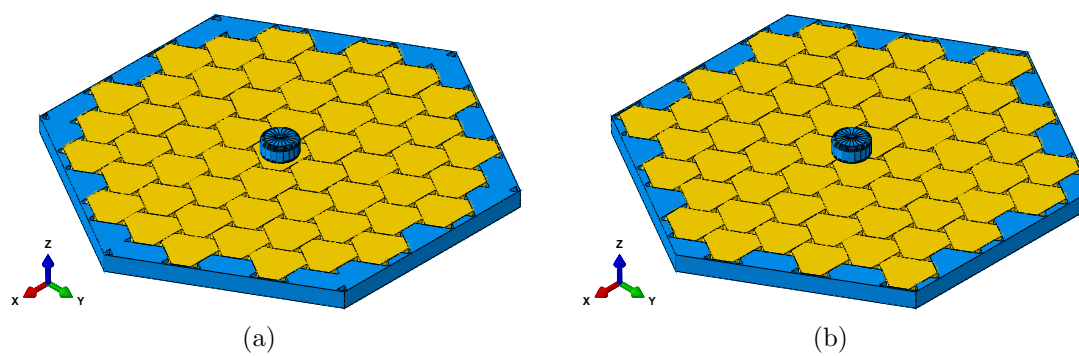


Figure 2.11. Assembly configurations: (a) [3⁶]-A, (b) [3⁶]-B.

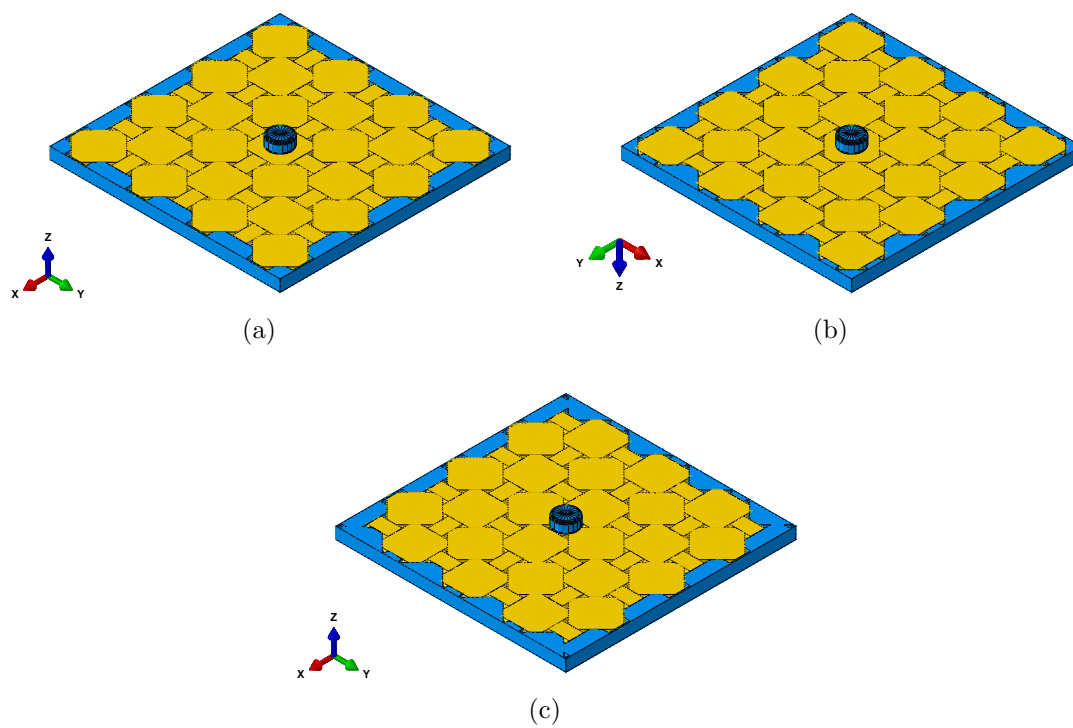


Figure 2.12. Assembly configurations: (a) (4.8^2) -A(-), (b) (4.8^2) -A(+), (c) (4.8^2) -B.

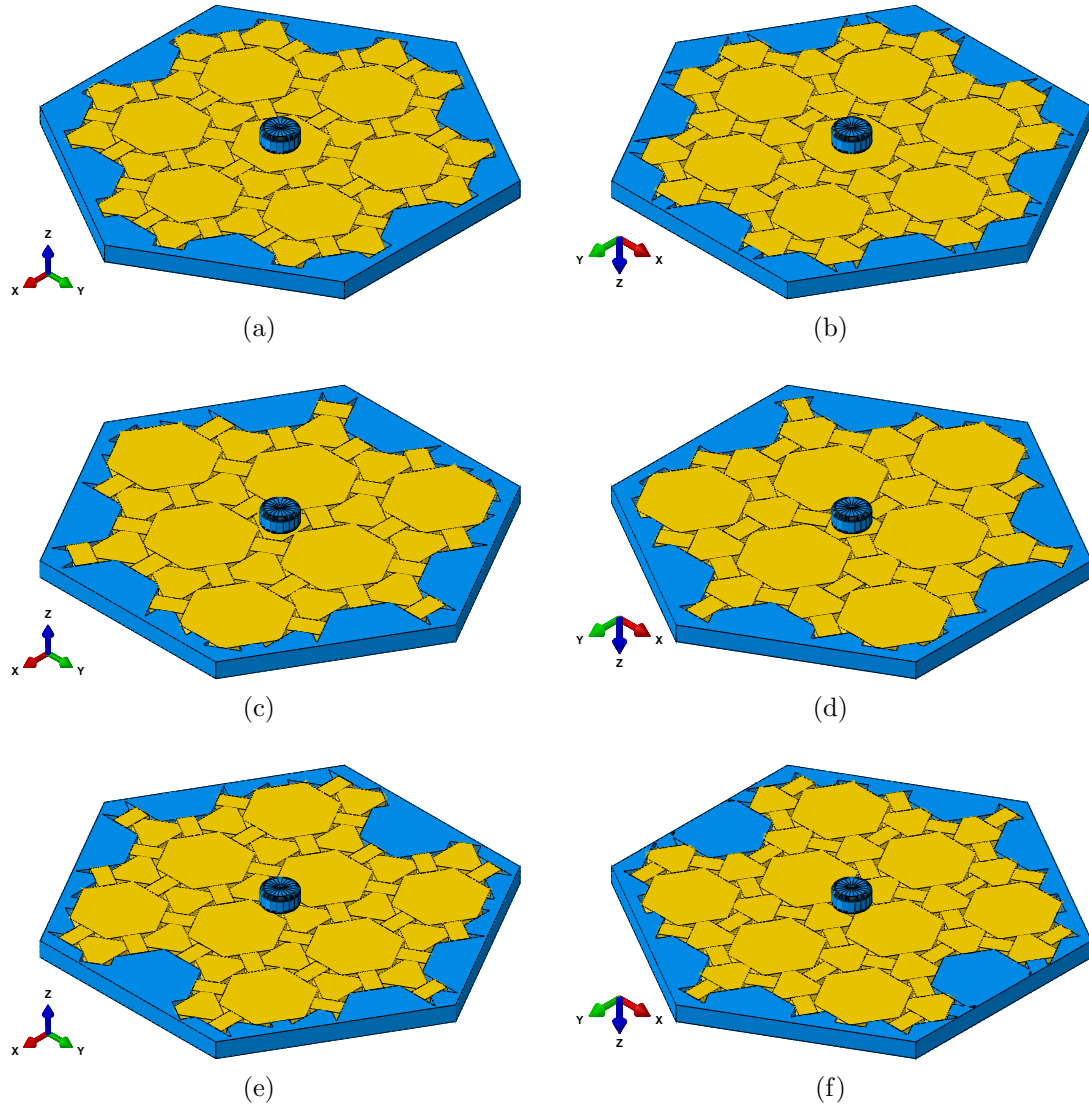


Figure 2.13. Assembly configurations: (a) (4.6.12)-A(-), (b) (4.6.12)-A(+), (c) (4.6.12)-B(-), (d) (4.6.12)-B(+), (e) (4.6.12)-C(-), (f) (4.6.12)-C(+).

2.3 Finite Element Model

Finite element models were used to simulate the performance of each configuration under quasi-static transverse loading from both a controlled displacement and a gravity load. In both cases the frame was made to be undeformable and fixed in space while the load was applied. The blocks were individual deformable bodies with mechanical properties similar to the VeroWhite 3D print polymer by Stratasys having a modulus of elasticity $E = 1.83$ GPa, Poisson ratio $\nu = 0.35$, and density $\rho = 0.95$ g/cm³. Contact was defined between all bodies with a stiff linear pressure-overclosure relationship and a coefficient of friction of $\mu = 0.2$. See Section 2.4.2 for more details on the contact formulation. The displacement loading simulations were also conducted with the coefficient of friction increased to $\mu = 0.3$ and $\mu = 0.4$. The ABAQUS Explicit finite element code was used to solve these models.

2.3.1 Displacement Loading

Displacement loading was achieved through the use of an undeformable cylinder with a radius of 10 mm, referred to as an indenter, which was placed in contact with the model and displaced at a rate of 50 mm/s into the assembly for 0.5 seconds resulting in a total displacement of 25 mm, Figure 2.14. The indenter was constrained such that it could only move along the Z-axis. No lateral motion or rotations were possible. The reaction force in the Z-direction, Figure 2.15(b), and reaction moment about the Z-axis, Figure 2.15(c), were recorded at a reference point on the indenter throughout the simulation as well as several energy measures for the entire system, Figure 2.15(a), including kinetic energy (ALLKE), strain energy (ALLSE), friction dissipation (ALLFD), work input (ALLWK), and a few energies specific to the finite element code which will be discussed in Section 2.4.2. Quasi-static conditions were maintained by ensuring that the indenter moved at a suitably slow speed such that the kinetic energy of the system was negligible compared to the work energy input.

A small initial spike in reaction force was typically observed at the start of the simulation but was considered acceptable.

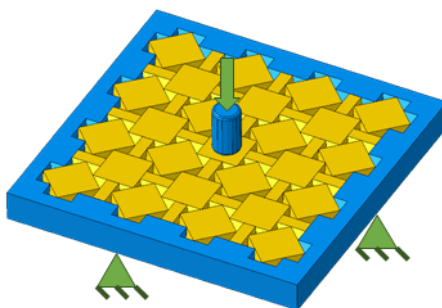


Figure 2.14. Displacement load setup with fixed frame and velocity controlled indenter.

The reaction force and reaction moment were filtered using a second order Butterworth filter with a cutoff frequency of 50 Hz. Both the raw and filtered data are depicted. It should be noted that the absolute value of the reaction force is presented, so it is always positive regardless of the load direction, but the reaction moment is presented as recorded so that a chiral direction can be specified.

The chiral assemblies in this study have a tendency to rotate as they are displaced along the Z -axis. This is indicated by the reaction moment on the indenter which is attempting to resist the assembly's rotation. For the purpose of this study, a TIM system configuration will be considered positively chiral if its assembly rotates in a positive direction about a vector aligned with the load direction. If the assembly rotates in a negative direction about the same vector, it will be considered negatively chiral. Therefore, if the load is applied in the $-Z$ direction (it is for all configurations in this study that exhibit chirality) and a positive reaction moment is recorded on the indenter, then the configuration is positively chiral.

In addition to the raw and filtered data, the point of maximum force is also marked on the force plot, Figure 2.15(b), and a corresponding point is marked on the moment plot, Figure 2.15(b), that occurs at the same deflection as the maximum

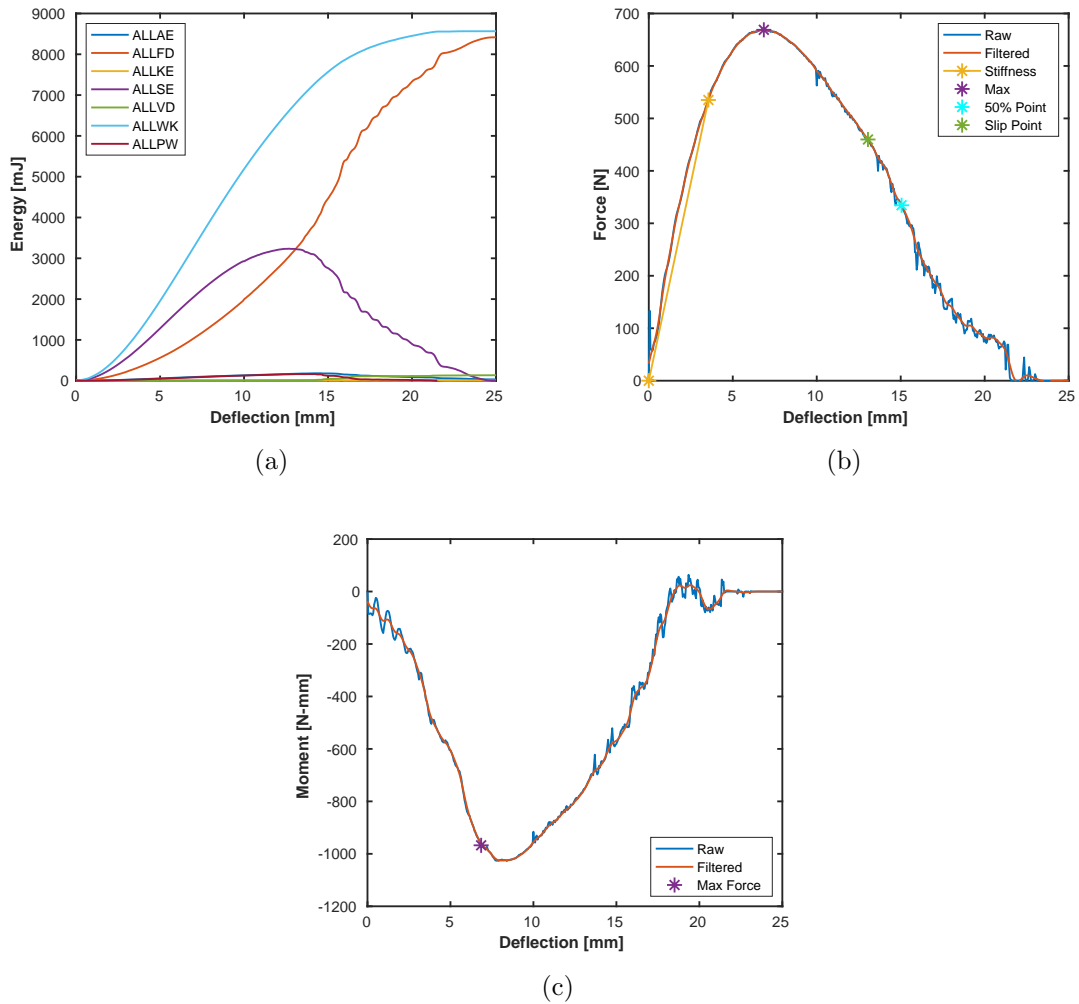


Figure 2.15. Example of displacement loading simulation results, [3.6.3.6]-B, (a) System energies (b) Force-deflection response. (c) Moment-deflection response.

force. The stiffness, the point of “50% strength degradation”, and the “slip point” are also marked on the force-deflection plot. The following definitions will be used when discussing the results for each configuration: (1) Strength is the maximum force recorded during the simulation. (2) Stiffness is computed as the slope of the straight line from the origin to the point at 80% of the strength. (3) Toughness is defined as the integral of the force-deflection response up to the point of 50%

strength degradation. (4) The onset of slip dominance is the deflection at which the slip point occurs, which is when the magnitude of ALLFD becomes greater than ALLSE. It represents transition from deflection being dominated by elastic strain to being dominated by sliding between blocks. (5) The “slip ratio” is the ratio of ALLFD to ALLSE at any given point.

2.3.2 Body Force Loading

Gravity loading was used as a means to apply a distributed load across the system, Figure 2.16, in order to avoid the disturbances in the stress field caused by the indenter and determine the behavior of the system under uniform load. The gravity load started at a magnitude of zero and increased as a smooth ramp function to $20,000 \text{ m/s}^2$ over 0.5 seconds. This ensured collapse for all configurations. Due to the force loading condition, final failure occurred rapidly and catastrophically. System energies were recorded throughout the simulation.

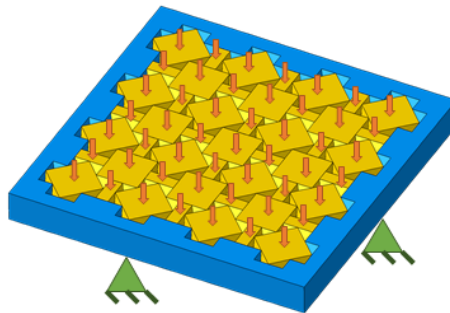


Figure 2.16. Gravity load setup with fixed frame and gravity load applied to all blocks.

2.3.3 Internal Load Transfer

For both displacement loading and gravity loading, vector plots of the minimum principal stress will be presented, such as Figure 2.17. These plots show the compres-

sive stresses throughout the assembly and can be used to illustrate the presence, or lack of, well defined thrust lines in the assembly. They may also reveal stress patterns, such as a tendency for stresses to align with the dual tessellation. Such plots can also be used to visualize the chirality of the system. For displacement loading, the vector plots are shown at a deflection of 2.5 mm. This was a sufficient loading condition for thrust lines to develop without displacing the assembly so far as to cause excessive distortion. For gravity loading the vector plots are shown at a gravity magnitude of 5,000 m/s² which was shortly before the failure load of the weakest assembly.

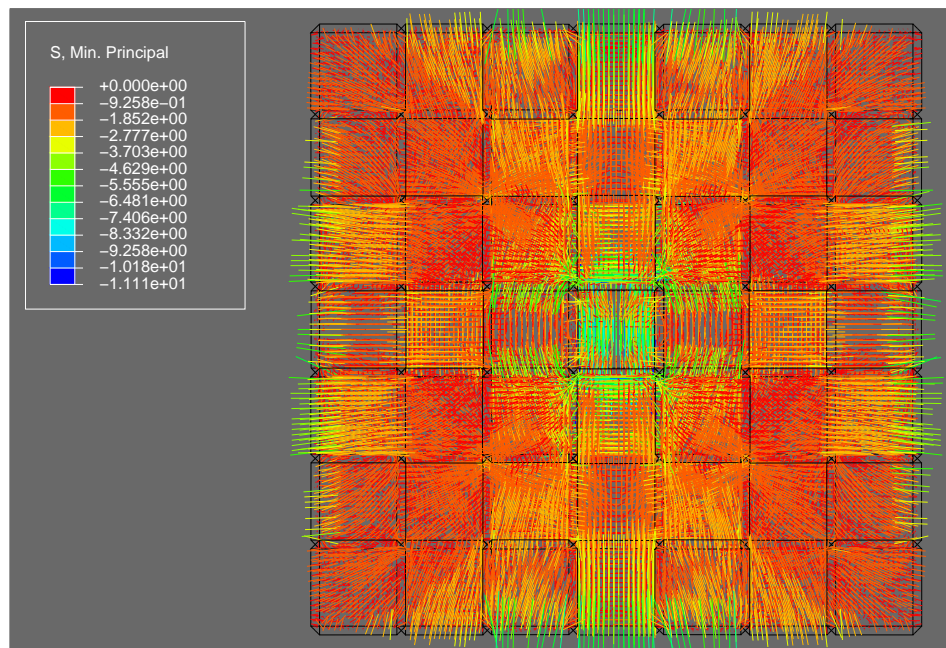


Figure 2.17. Example vector plot of minimum principal stress [MPa], [4⁴]-A configuration under displacement load.

2.4 Finite Element Code

The ABAQUS Explicit finite element code was used to evaluate the models. This code was chosen for its robustness in solving models with a large number of contact interfaces. Solid 8-node reduced integration hexahedral elements (C3D8R) were used

to mesh the blocks, while solid 4-node tetrahedral elements (C3D4) were used for the frame due to its geometric complexity. Enhanced hourglass control was used on the hexahedral elements to reduce an observed tendency for hourglassing with default hourglass control. Mass scaling by a factor of 100 was employed to reduce computation time. Key lines from the input file are included in Appendix D.

2.4.1 Mesh Convergence

Mesh convergence was checked using the force-deflection data from displacement loading. The mesh density of the blocks was controlled by varying the global seed size over a range from 1.5 mm to 2.1 mm by increments of 0.1 mm. The resulting meshes varied in total elements in the assembly by a factor of approximately 3. The force-deflection curves were overlaid for each configuration to check for any significant variance, Figure 2.18(a). Additionally, the maximum force from each mesh was plotted against the number of elements in the assembly, Figure 2.18(b). It was found that all configurations were well converged by a seed size of 1.6 mm with the exception of the [4⁴]-A and [4⁴]-B configurations which will be discussed in Section 2.4.3. A seed size of 1.7 mm was used for the tetrahedron models and 1.6 mm was used for all other configurations. The convergence plots for all configurations are shown in Appendix A.

The seed size of the frame was 3.0 mm for all models. This size was determined such that a reasonable number of elements spanned the contour of the frame. It was not necessary to check convergence for the frame because it was a rigid part and the surface based contact formulation is not mesh sensitive on flat surfaces.

2.4.2 Energy Balance

In addition to the kinetic energy (ALLKE), strain energy (ALLSE), friction dissipation (ALLFD), and work input (ALLWK) presented in Figure 2.15(a), the ABAQUS Explicit finite element code also reports the artificial strain energy (ALLAE), viscous

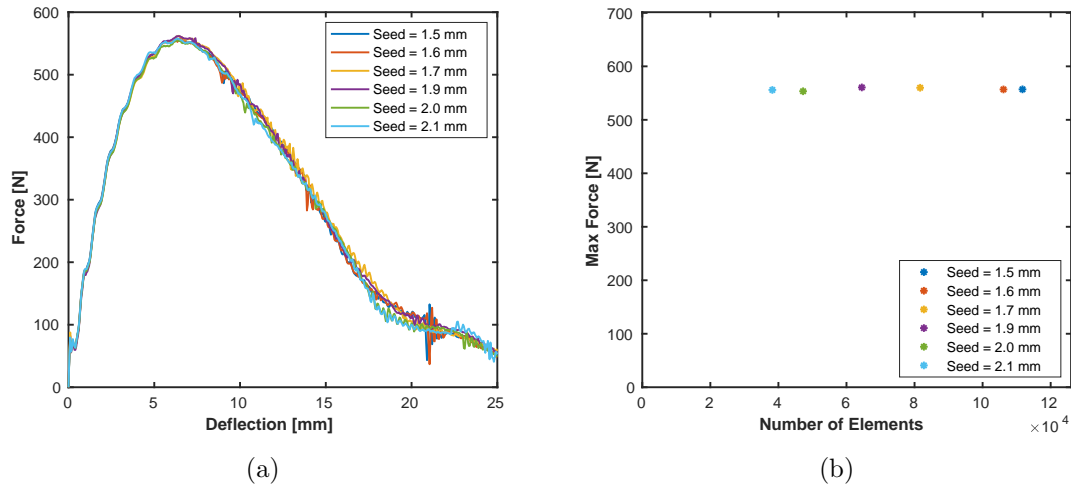


Figure 2.18. Example of mesh convergence for [3.6.3.6]-A. (a) Force-deflection data. (b) Maximum force vs number of elements.

dissipation (ALLVD), and penalty work (ALLPW)¹. These are referred to as false energies meaning that they do not represent a physical phenomenon. It is the nature of an explicit finite element code that these energies will typically be present in at least small amounts. They are the result of various processes that allow the solver to efficiently and/or accurately reach a solution. The goal is to minimize the false energies without incapacitating the solver.

Artificial strain energy occurs as a result of using reduced integration elements. It can be eliminated with the use of full integration elements, but this results in an overly stiff model and increases computation costs. Penalty work is the energy absorbed in the overclosure of softened contact interfaces as a result of the penalty contact formulation. It is essentially potential energy stored in a contact spring. ABAQUS “hard contact” was specified for the simulation which uses a penalty contact formulation with a linear pressure-overclosure relationship. The contact stiffness is

¹The ABAQUS Explicit finite element code reports penalty work as an input, but for the purpose of this study it made more sense to treat it as an energy absorption, so the value of ALLPW was multiplied by -1.

internally computed based on a representative underlying element stiffness. The ABAQUS Explicit code allows for a scale factor to be specified that is included in its underlying calculation. The default scale factor of 1 resulted in a contact stiffness that was too soft causing a significant amount of energy to be absorbed in the contact interfaces as penalty work. Increasing the scale factor to 5 reduced the penalty work to a reasonable level. Viscous dissipation occurs as a result of numerical damping that is employed in order to smooth the simulation. It can be eliminated by disabling the numerical damping, but this resulted in excessive oscillations and produced poor results. It was determined that increasing the variable for critical damping fraction by a factor of 10 from the default value of 0.03 to 0.30 reduced the viscous dissipation to an acceptable level.

Work energy is the only input to the system, so the value of ALLWK should be equal to the sum of the other energies, offset by the initial kinetic energy of the indenter due to its velocity boundary condition. The false energies should account for only a small portion of the total energy if the model is to be accepted. To this end, false energy ratios were computed as the ratio of each false energy to ALLWK over the duration of the simulation, Figure 2.19, and a model was considered acceptable if the sum of the false energy ratios was less than 10%. This target was met for all models. The false energy ratios for each configuration are shown in Appendix B.

2.4.3 Mesh Alignment

It was found that the mesh alignment between blocks played a significant role in the performance of the model. Variations in the load response for different mesh densities were observed in some models that did not agree with the converged solution, instead there was some scatter in the data that could only be described by mesh alignment, Figure 2.20.

The [4⁴]-A and [4⁴]-B configurations were particularly susceptible to mesh alignment issues and exhibited nontraditional hourglassing across contact interfaces in

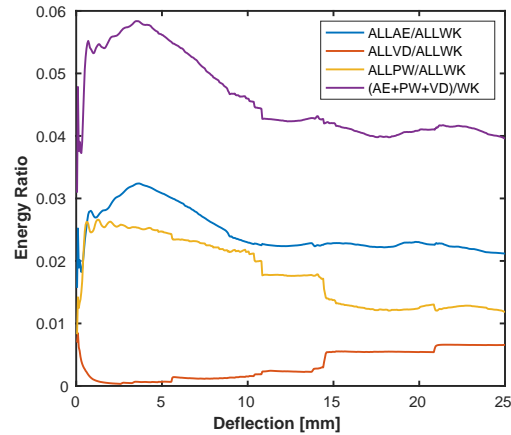


Figure 2.19. Example of false energies ratios and their sum, [3.6.3.6]-A.

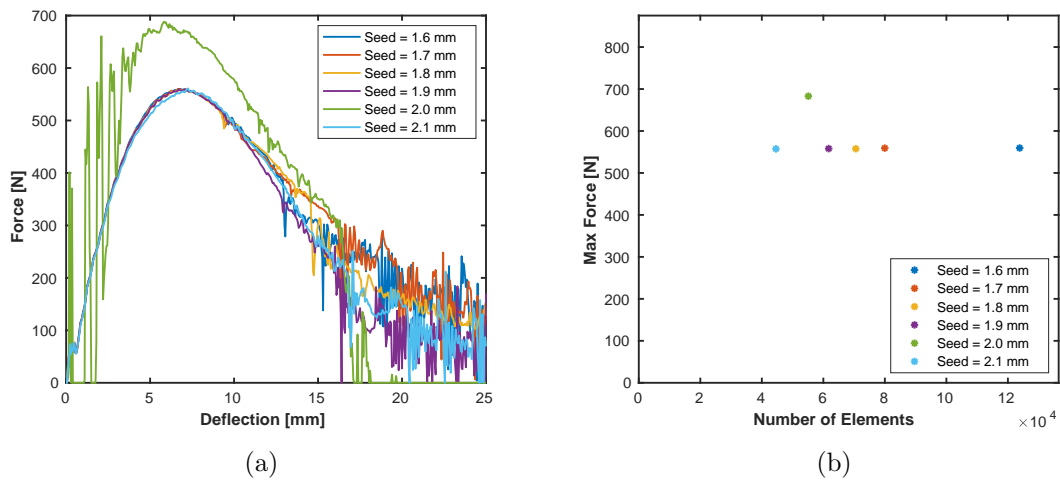


Figure 2.20. Mesh convergence, [4¹]-A, showing an outlier at Seed = 2.0 mm. (a) Force-deflection data. (b) Maximum force vs number of elements.

situations where the nodes were exactly aligned on both sides of the contact interface. The cross contact hourglassing would create an interlocking feature between the blocks and prevent sliding, Figure 2.22. This was remedied for the most part by eliminating features from the finite element model that would force exact mesh

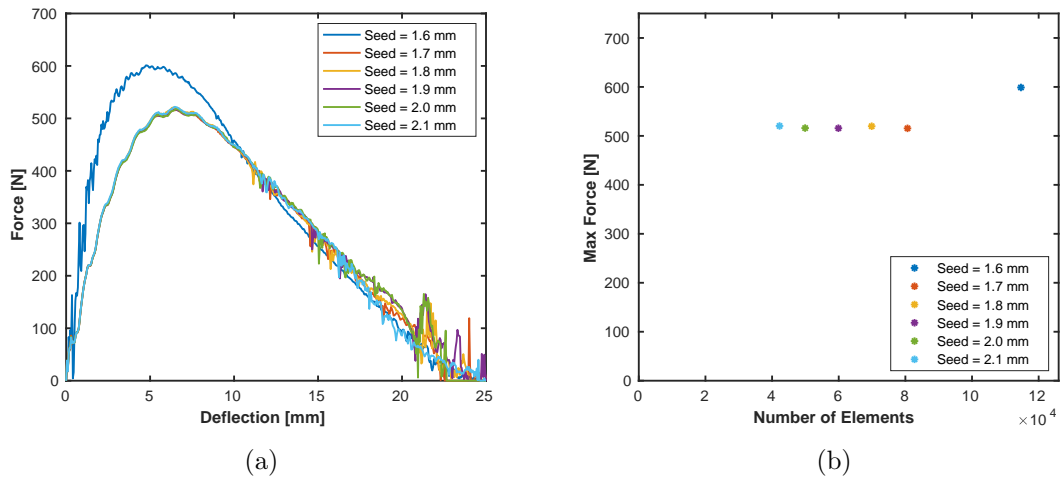


Figure 2.21. Mesh convergence, [4⁴]-B, showing an outlier at Seed = 1.6 mm. (a) Force-deflection data. (b) Maximum force vs number of elements.

alignment, such as partitions at the midplane of a block. In the initial assembly state, such partitions would be exactly aligned and lead to interlocking of the blocks. However, this did not resolve the issue for all meshes, leading to the use of a 1.7 mm seed size for the [4⁴]-A and [4⁴]-B configurations which had some issue at the 1.6 mm seed size, Figure 2.21.

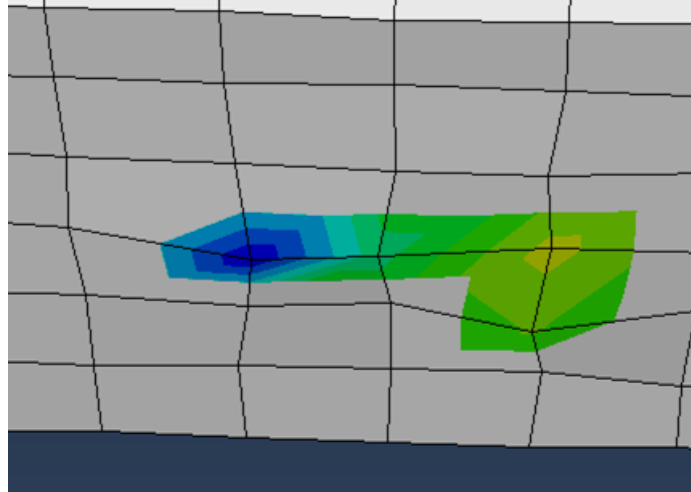


Figure 2.22. One side of contact interface for tetrahedron showing interlocked hourglassing. Blue is protrusion, green/yellow is indentation.

2.4.4 Validation

Finite element models of monolithic square and hexagon plates were created to validate the models. These plates were constructed with the same overall dimensions as the TIM systems, and the same mesh density and properties were applied. They were given simply supported boundary conditions on all sides and were transversely loaded using the same indenter to a deflection of 12.5 mm. The square plate was compared to the square plate equation, Equation (1.1), Figure 2.23(a), and the hexagon plate was compared to a the circle plate equation, Equation (1.2), Figure 2.23(b). The models agree well with the equations for small deflections, but diverge as the deflection increases. This was expected because the plate equations are only valid for small deflections. Additionally, plasticity was not accounted for in the finite element models, but the stresses in the plates at 12.5 mm deflection would have exceeded the yield strength of a material with this modulus, Figures 2.24 and 2.25.

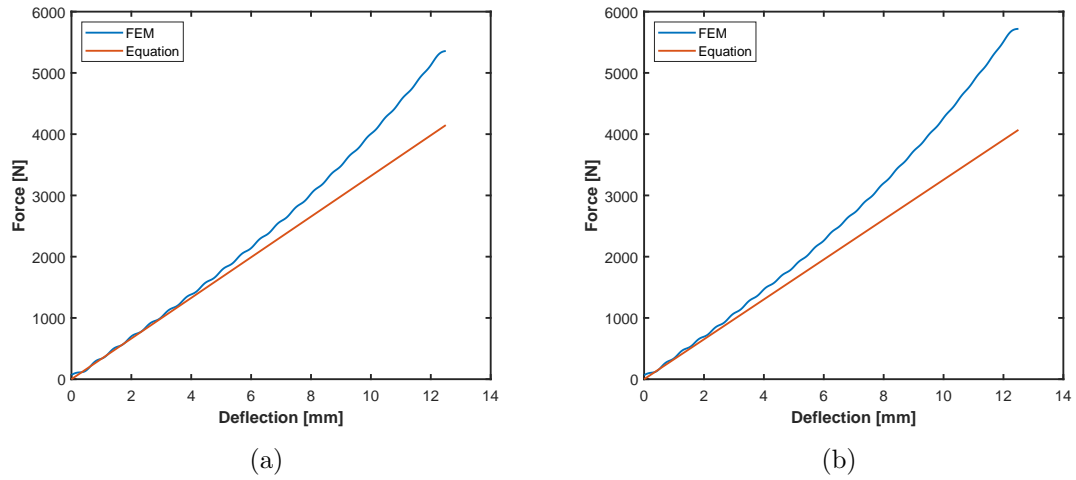


Figure 2.23. Finite element model validation for (a) square plate, and (b) hexagon plate.

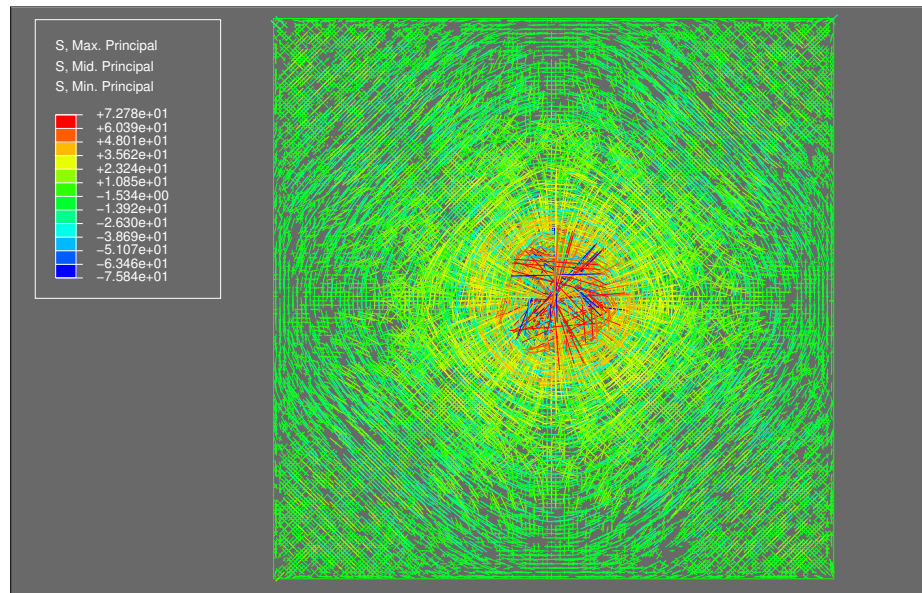


Figure 2.24. Vector plot of maximum absolute value principal stresses [MPa] for a square plate transversely loaded to a deflection of 12.5 mm.

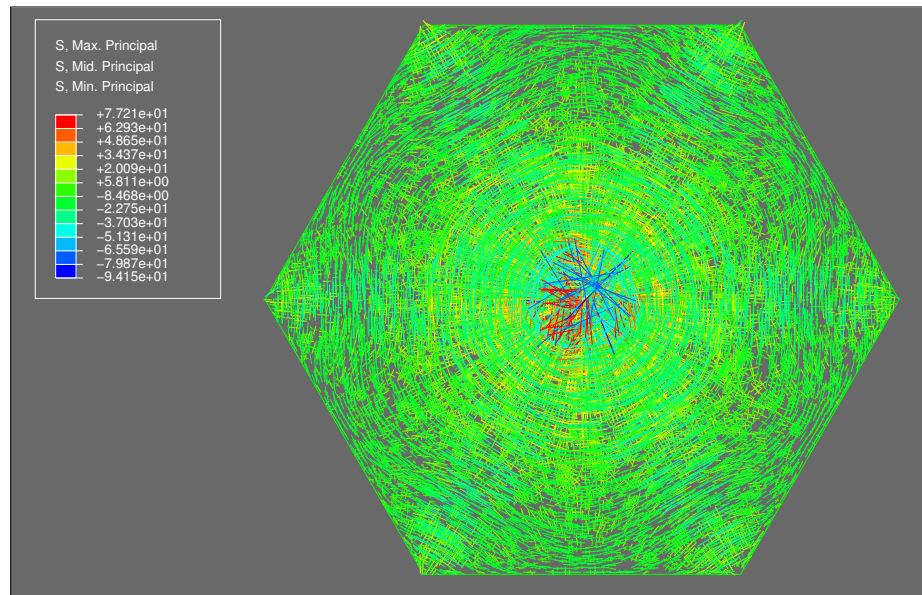


Figure 2.25. Vector plot of maximum absolute value principal stresses [MPa] for a hexagon plate transversely loaded to a deflection of 12.5 mm.

2.5 Python Implementation

ABAQUS CAE has built-in Python programming libraries that enable nearly any function that can be completed within the ABAQUS CAE environment to be written and implemented as Python code. This was very useful due to the repetitive and systematic nature of TIM systems. Python scripts were created for each tiling that parametrically generate the finite element model. Parameters can be altered to specify the assembly configuration, load condition, and block dimensions. Additionally, there are parameters for the material properties, mesh details, and all simulation settings discussed in this chapter. These scripts compute the geometry, construct the assembly, and build the entire finite element model based on the parameters that were input. They are available from the Purdue University Research Repository [33].

3. TIM SYSTEMS UNDER APPLIED DISPLACEMENTS

This chapter contains the data collected from the displacement loading simulations including the system energies, the force-deflection response, the moment-deflection response, and vector plots of the compressive stress fields. The results shown here were computed with the coefficient of friction $\mu = 0.2$.

3.1 System Energies, Reaction Force, and Reaction Moment

The responses of the [4⁴]-A and [4⁴]-B configurations are given in Figures 3.1 and 3.2. The force-deflection response computed for these cases is that of a well developed, skewed parabola type response common to TIM systems. Both cases have similar stiffness, strength, and toughness and exhibit a smooth transition from strain dominance to sliding dominance with slip points that occur after the maximum force and before the 50% point, but the [4⁴]-B configuration has a strong moment response demonstrating positive chirality which peaks shortly after the maximum strength is achieved, whereas the moment response is negligible for the [4⁴]-A configuration.

The [3.6.3.6]-A and [3.6.3.6]-B configurations also resulted in skewed parabola force-deflection responses with similar stiffness, strength, and toughness and exhibited a smooth transition from strain dominance to sliding dominance with slip points that occurred after the maximum force and before the 50% point, however, both configurations had strong moment responses, Figures 3.3 and 3.4. The [3.6.3.6]-A configuration was positively chiral and its moment-deflection response was nearly a scaled replica of its force-deflection response. The [3.6.3.6]-B configuration, on the other hand, was negatively chiral and its moment-deflection response was a little skewed from being a scaled replica of its force-deflection response.

The responses of the [3.4.6.4]-A, [3.4.6.4]-B, and [3.4.6.4]-C configurations are shown in Figures 3.5 - 3.7. The force-deflection response of [3.4.6.4]-A is a skewed parabola similar to the previous configurations. It also has a smooth transition from strain dominance to sliding dominance with a slip point that occurs nearly midway between the maximum force and the 50% point, but its moment response indicates both positive and negative chirality. The reaction moment initially fluctuates before rising to a relatively small positive peak occurring just after the point of maximum force. It then switched directions and approached a negative peak of a much larger magnitude before trending back towards zero as the simulation continued. The [3.4.6.4]-B configuration had a slip ratio very near unity from the beginning of the simulation and was slip dominated after only a few millimeters of deflection. The high tendency to slip is also evident in its force deflection curve where two significant drops in force can be seen at about 8 mm and 14 mm deflection, each followed by a recovery period of positive stiffness before a final drop to complete failure, Figure 3.6(c). This configuration was negatively chiral and its moment-deflection response was nearly a scaled inverse replica of its force-deflection response. The [3.4.6.4]-C configuration had a high slip ratio throughout the simulation, similar to [3.4.6.4]-B, but its slip point did not occur quite as early and its force-deflection response was a skewed parabola without any significant drops, though the raw data does show a greater frequency of small drops that were mostly filtered out. However, its moment-deflection response was not as clean. After rising to an initial peak of about 300 N-mm, the reaction moment falls to a local valley just under 100 N-mm occurring at the same deflection as the maximum force. The reaction moment then rises rapidly to a maximum of about 500 N-mm before trending back toward zero as the simulation progressed.

The [3⁶]-A and [3⁶]-B configurations both have low initial slip ratios and late slip points, Figures 3.8 and 3.9. The slip points occur at or just before a sudden rapid slip leading to complete failure of the system. Only one of these systems is chiral. The moment-deflection response is negligible for the [3⁶]-A configuration, but the [3⁶]-B

configuration has a strong positive reaction moment which peaks somewhat later than the reaction force does.

The results in the following are those of the (4.8^2) -A(-), (4.8^2) -A(+), and (4.8^2) -B configurations, Figures 3.10 - 3.12. The (4.8^2) -A assembly is direction dependent so the responses to loads in both the -Z and +Z directions are presented here. The (4.8^2) -B assembly, however, is not dependent on the load direction. Similar to all the single-tile assemblies, if this assembly is flipped over and then rotated, it can be made to exactly overlay its starting position, therefore its responses to loads in either direction are identical. Both the (4.8^2) -A(-) and (4.8^2) -B configurations have an inflection point in the tail of the force-deflection response where the slope becomes much less steep, while both the (4.8^2) -A(+) and (4.8^2) -B configurations have slip points that occur late in the simulation. The (4.8^2) -A(+) configuration slips rapidly to complete failure after its slip point. None of these configurations are chiral.

The responses of the $(4.6.12)$ -A, $(4.6.12)$ -B, and $(4.6.12)$ -C assemblies are direction dependent, so their responses in both the -Z and +Z directions are shown here, Figures 3.13 - 3.18. All these configurations have slip points occurring after the 50% point, though the slip point of the $(4.6.12)$ -B(-) configuration occurs nearly at the 50% point. The $(4.6.12)$ -A(-), $(4.6.12)$ -A(+), and $(4.6.12)$ -B(-) configurations all have a period of rapid sliding leading to failure, whereas the $(4.6.12)$ -B(+), $(4.6.12)$ -C(-), and $(4.6.12)$ -C(+) configurations approach failure more smoothly. None of these configurations are chiral.

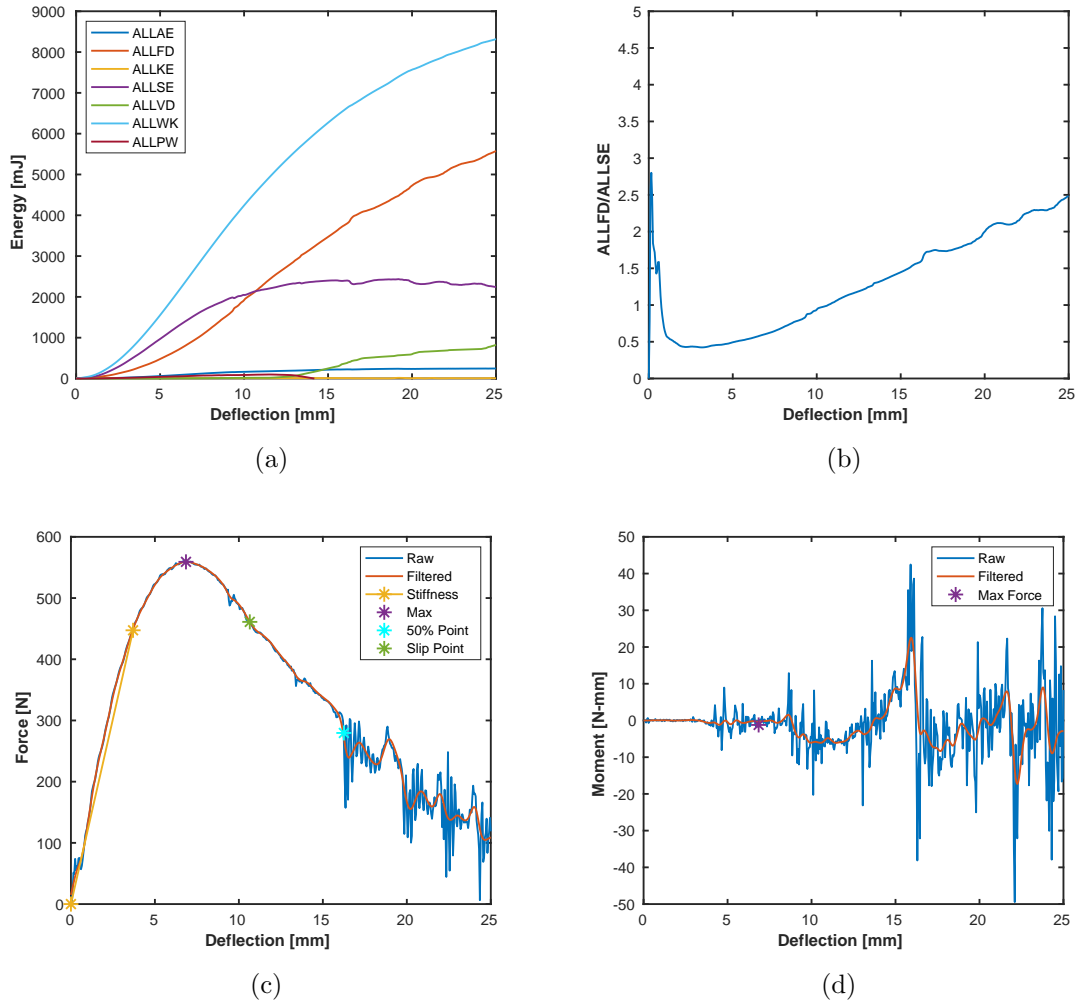


Figure 3.1. Displacement loading results for $[4^4]$ -A configuration: (a) System energies. (b) Slip ratio ALLFD/ALLSE. (c) Force-deflection response. (d) Moment-deflection response.

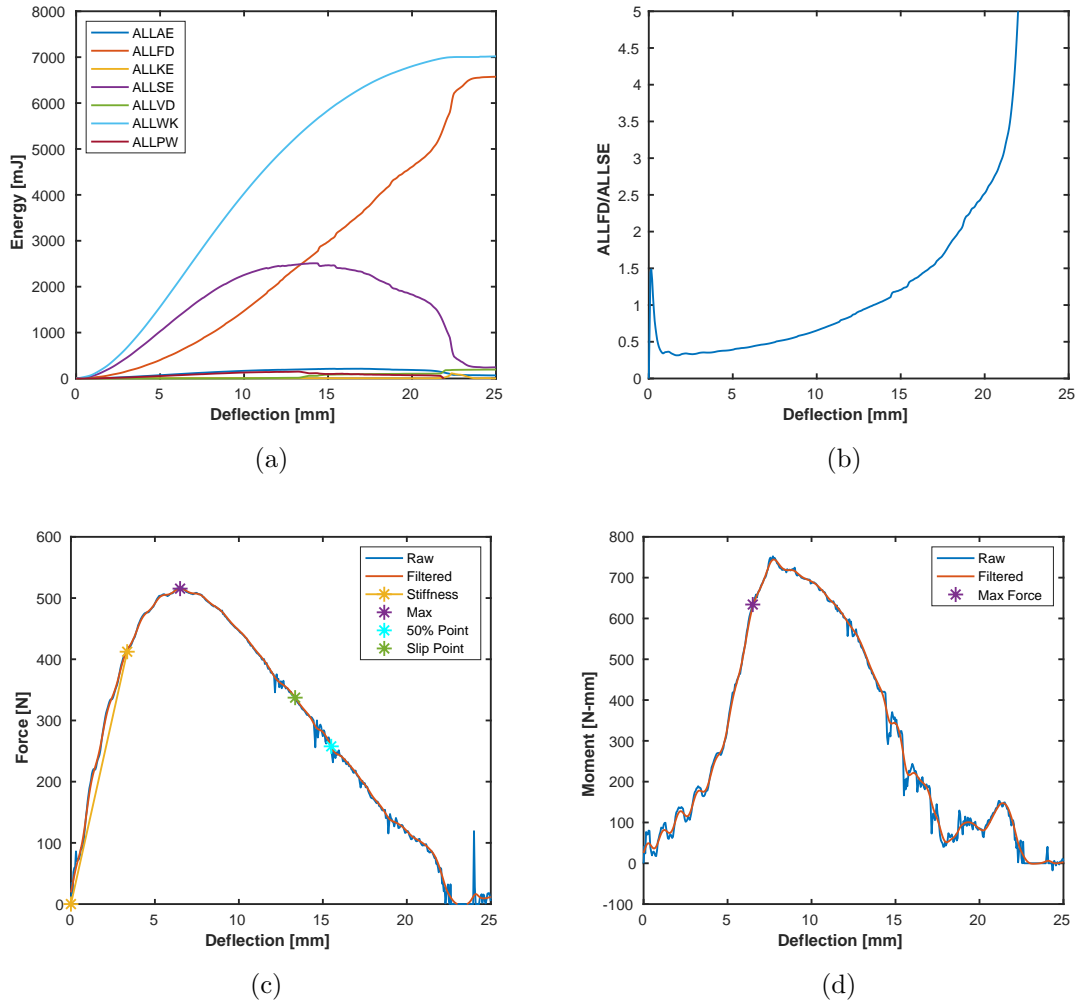


Figure 3.2. Displacement loading results for $[4^4]$ -B configuration: (a) System energies. (b) Slip ratio ALLFD/ALLSE. (c) Force-deflection response. (d) Moment-deflection response.

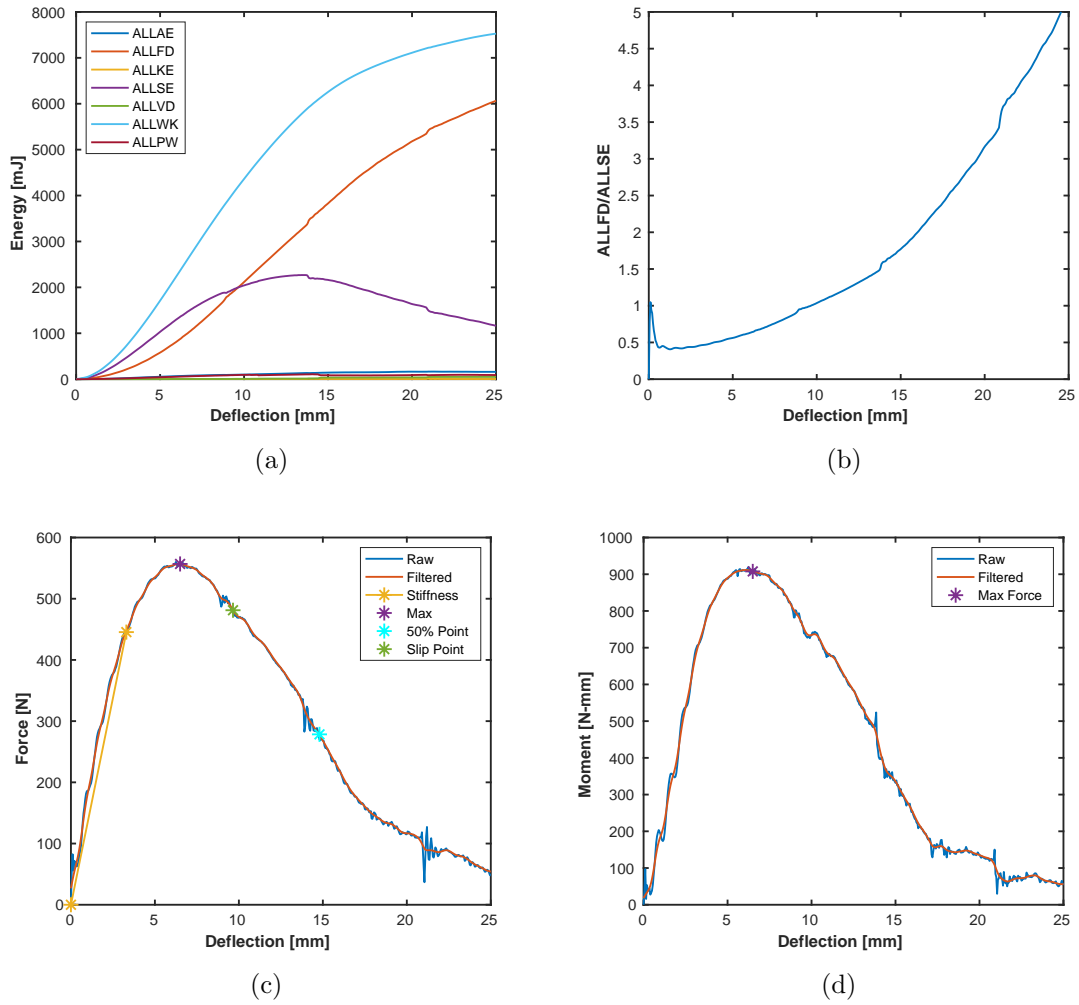


Figure 3.3. Displacement loading results for [3.6.3.6]-A configuration: (a) System energies. (b) Slip ratio ALLFD/ALLSE. (c) Force-deflection response. (d) Moment-deflection response.

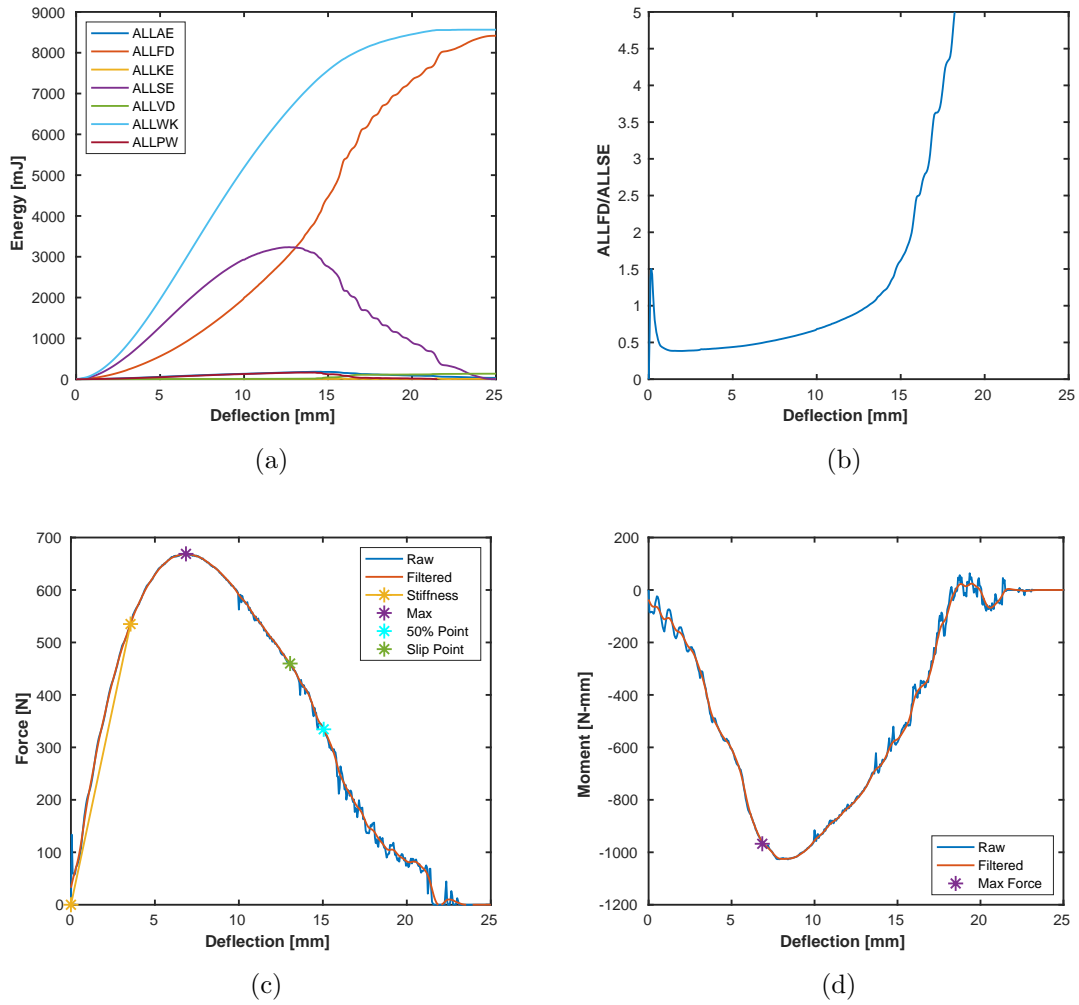


Figure 3.4. Displacement loading results for [3.6.3.6]-B configuration: (a) System energies. (b) Slip ratio ALLFD/ALLSE. (c) Force-deflection response. (d) Moment-deflection response.

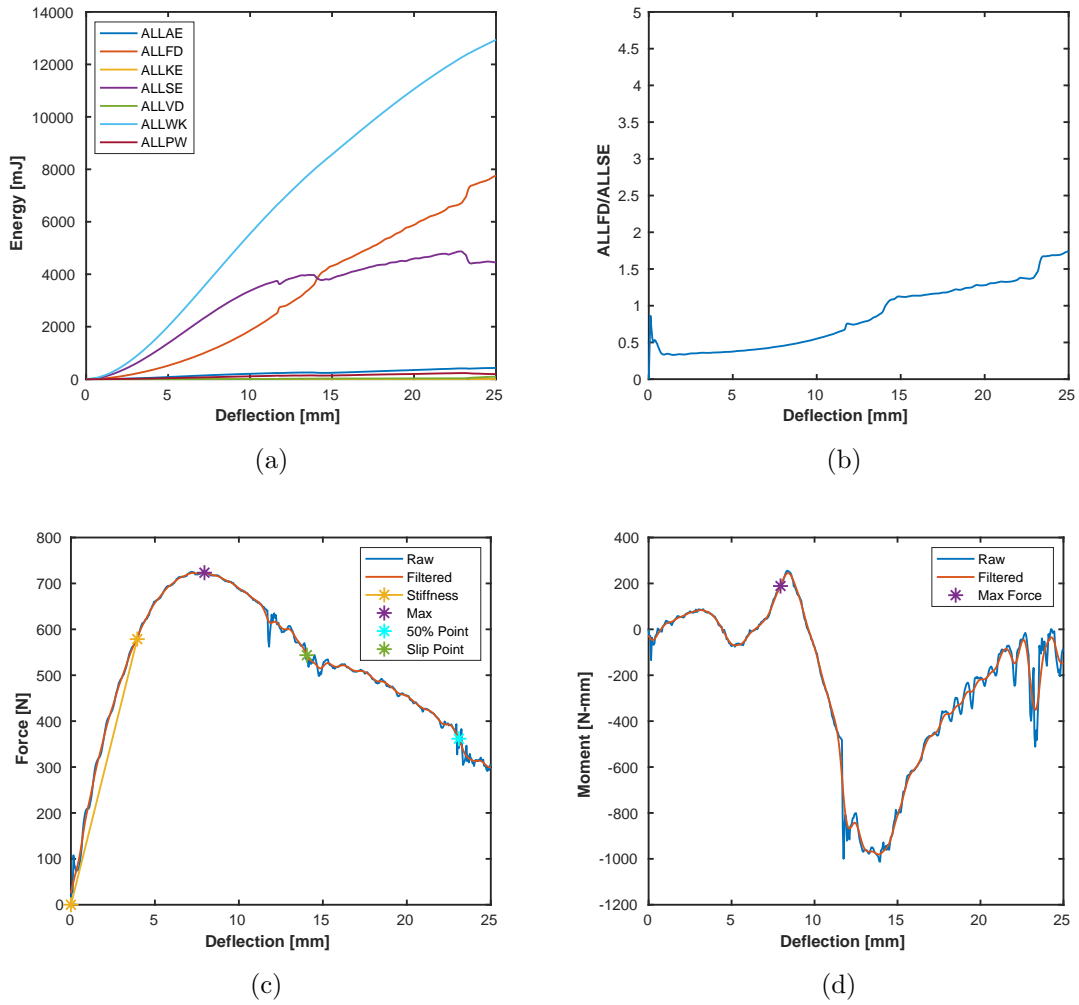


Figure 3.5. Displacement loading results for [3.4.6.4]-A configuration: (a) System energies. (b) Slip ratio ALLFD/ALLSE. (c) Force-deflection response. (d) Moment-deflection response.

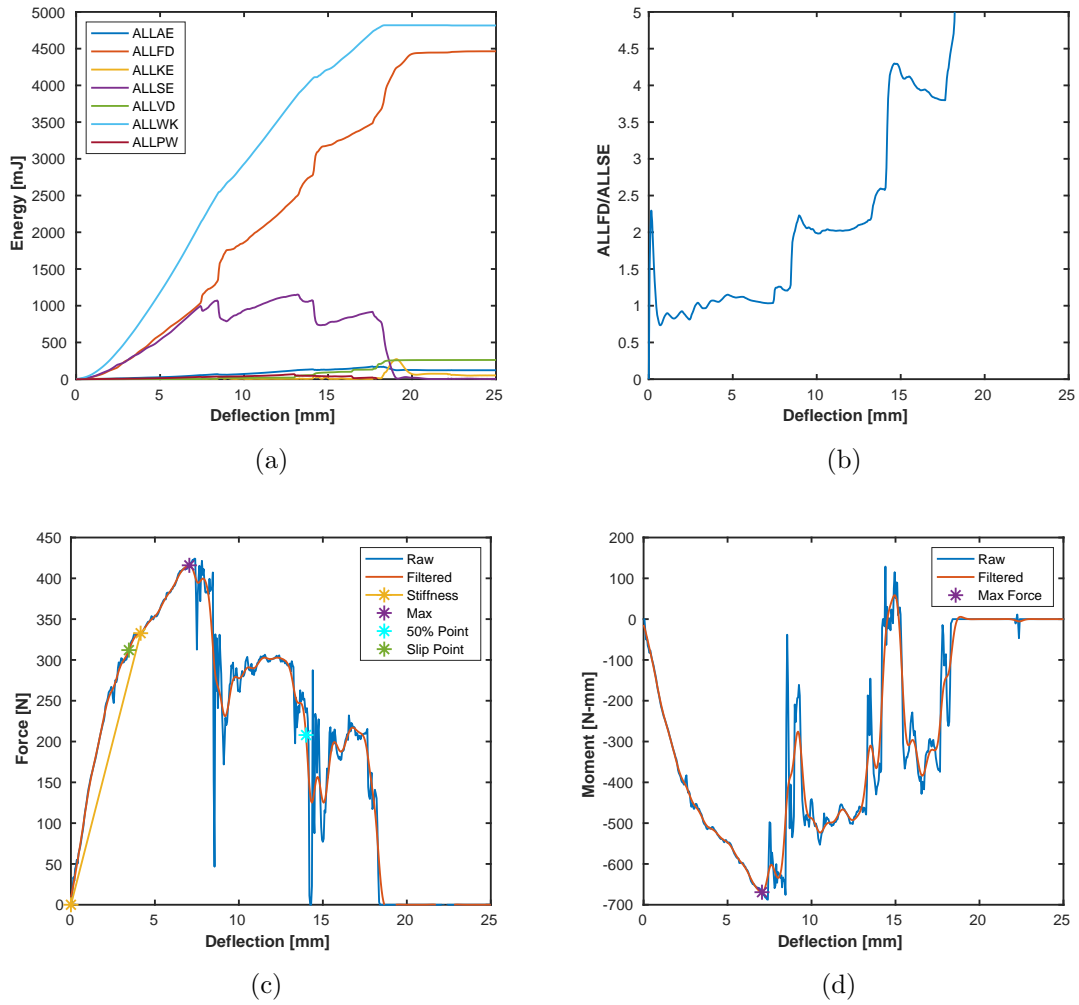


Figure 3.6. Displacement loading results for [3.4.6.4]-B configuration: (a) System energies. (b) Slip ratio ALLFD/ALLSE. (c) Force-deflection response. (d) Moment-deflection response.

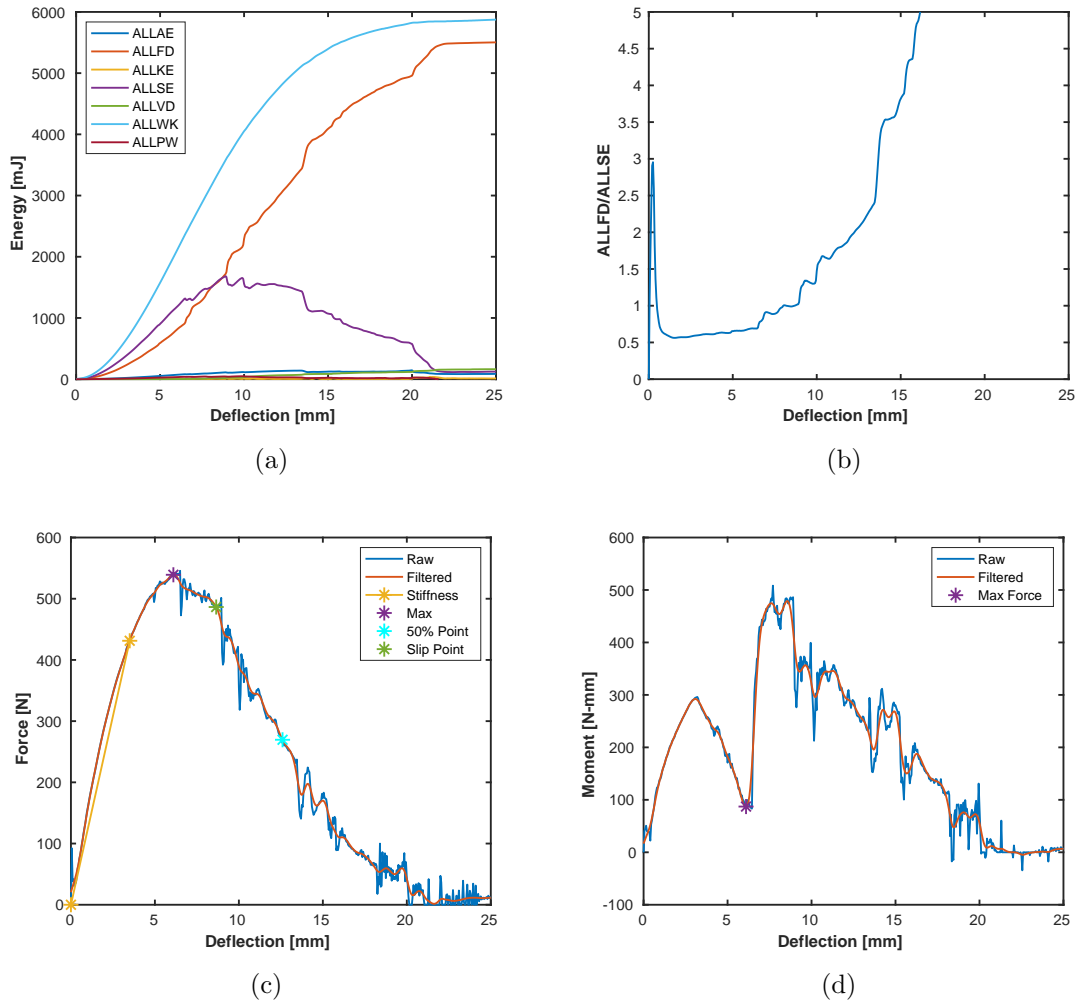


Figure 3.7. Displacement loading results for [3.4.6.4]-C configuration: (a) System energies. (b) Slip ratio ALLFD/ALLSE. (c) Force-deflection response. (d) Moment-deflection response.

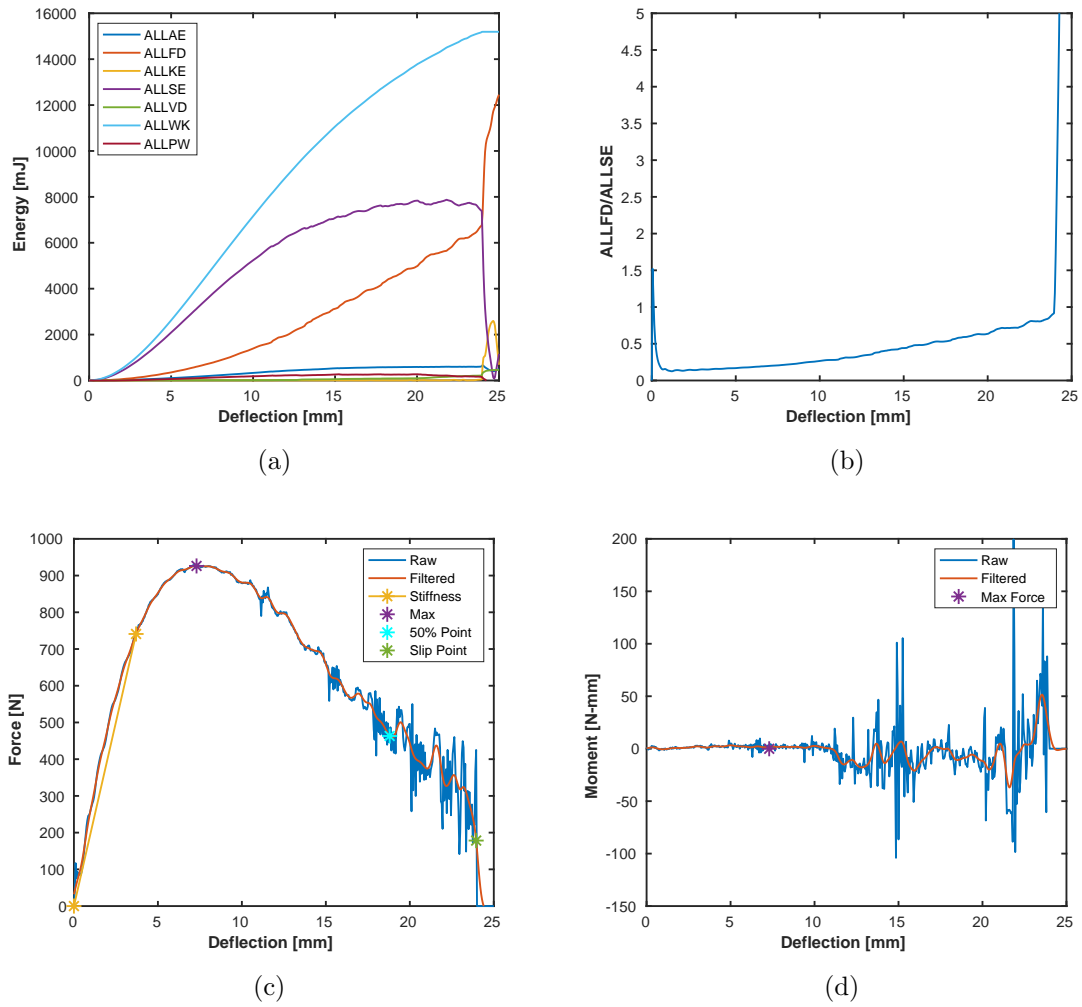


Figure 3.8. Displacement loading results for $[3^6]$ -A configuration: (a) System energies. (b) Slip ratio ALLFD/ALLSE. (c) Force-deflection response. (d) Moment-deflection response.

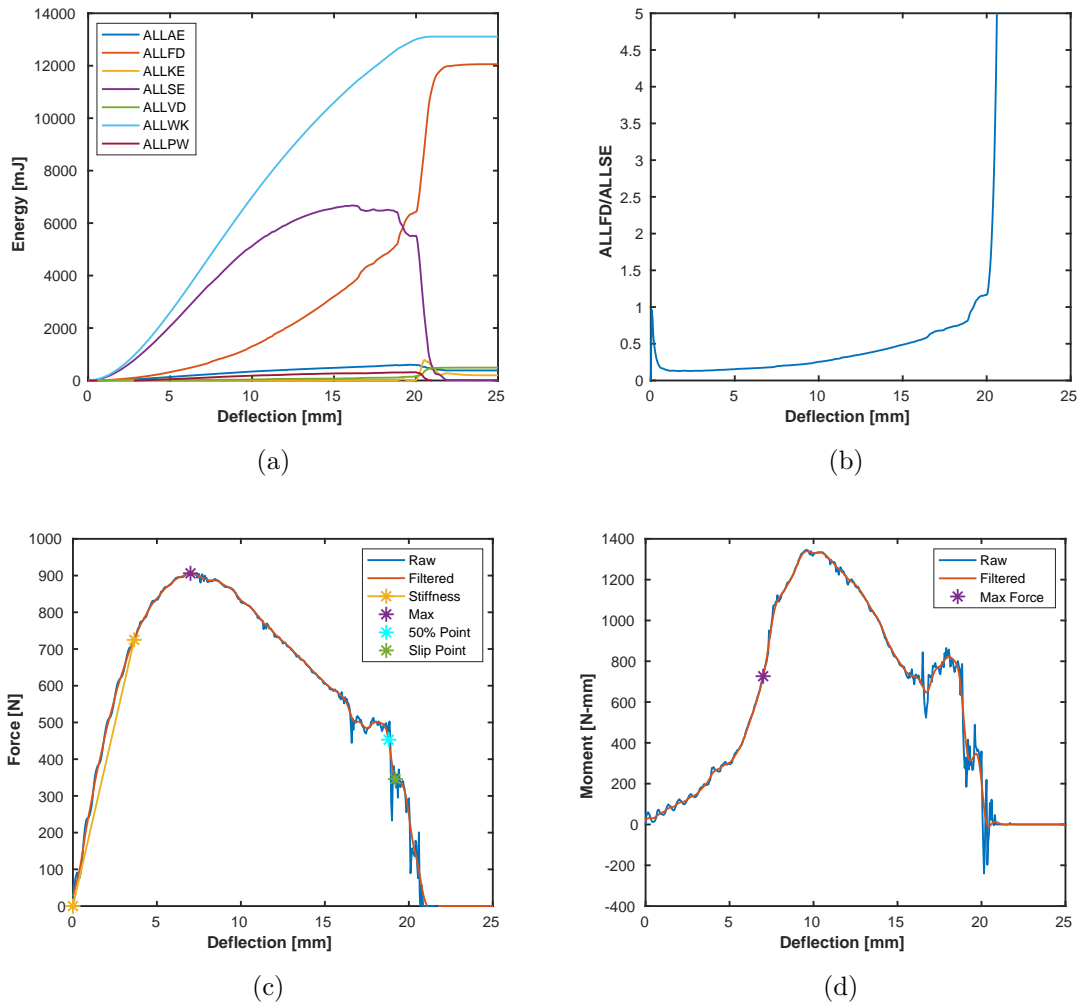


Figure 3.9. Displacement loading results for $[3^6]$ -B configuration: (a) System energies. (b) Slip ratio ALLFD/ALLSE. (c) Force-deflection response. (d) Moment-deflection response.

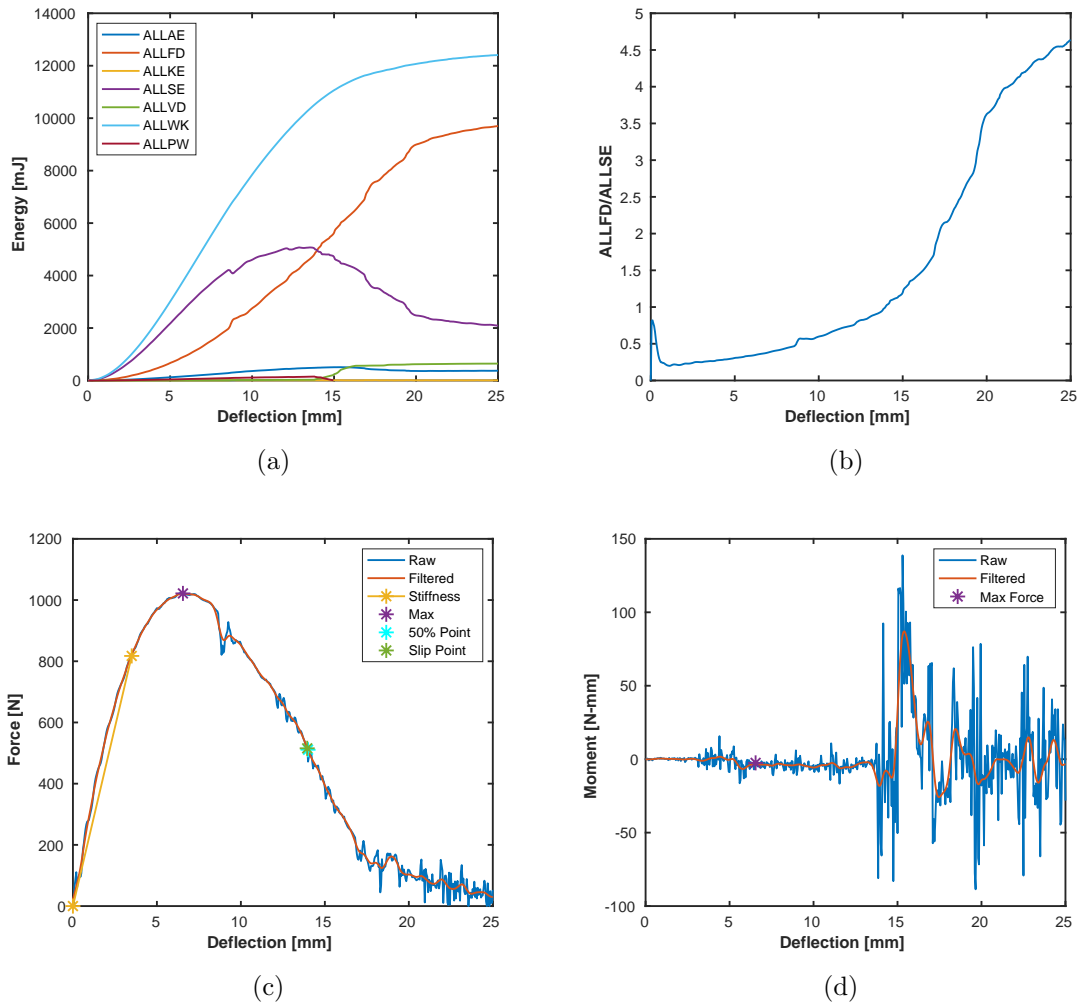


Figure 3.10. Displacement loading results for (4.8²)-A(-) configuration: (a) System energies. (b) Slip ratio ALLFD/ALLSE. (c) Force-deflection response. (d) Moment-deflection response.

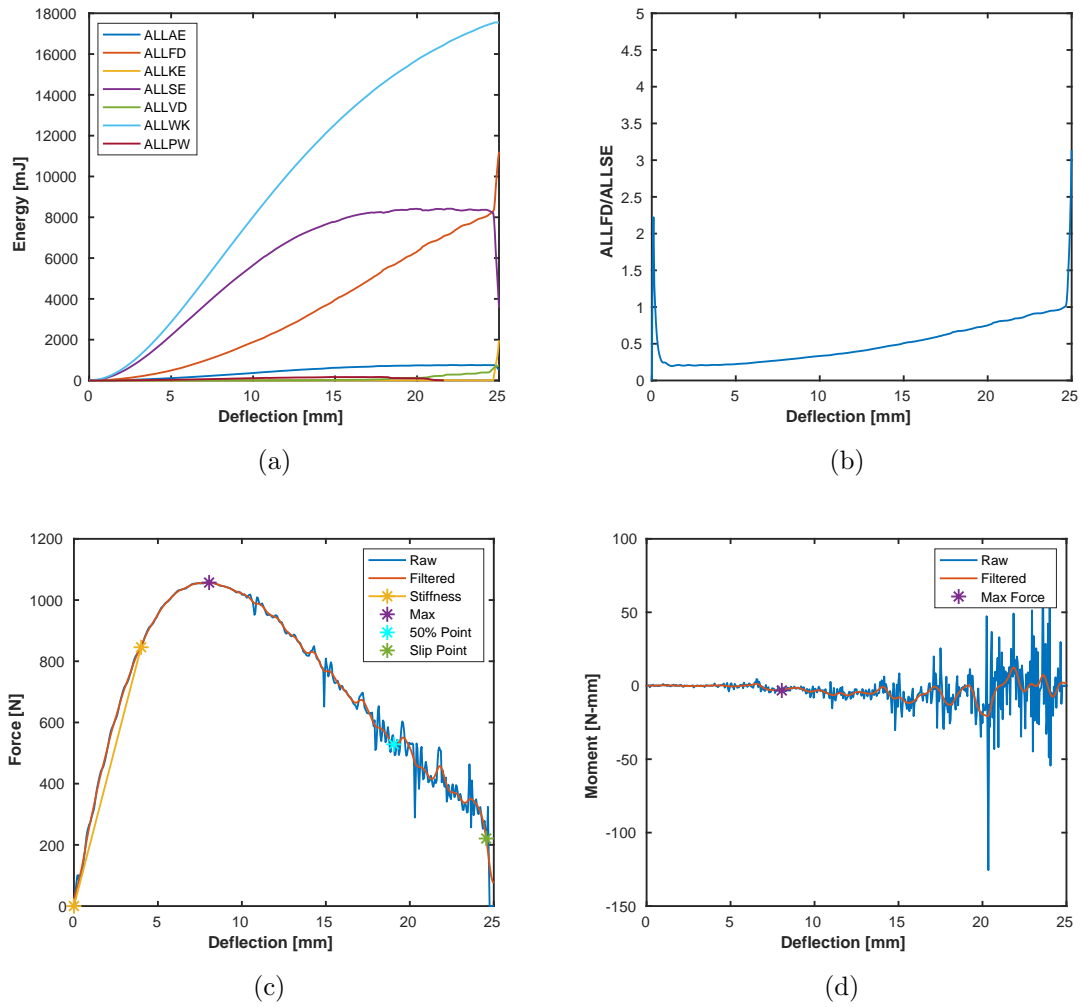


Figure 3.11. Displacement loading results for (4.8²)-A(+) configuration: (a) System energies. (b) Slip ratio ALLFD/ALLSE. (c) Force-deflection response. (d) Moment-deflection response.

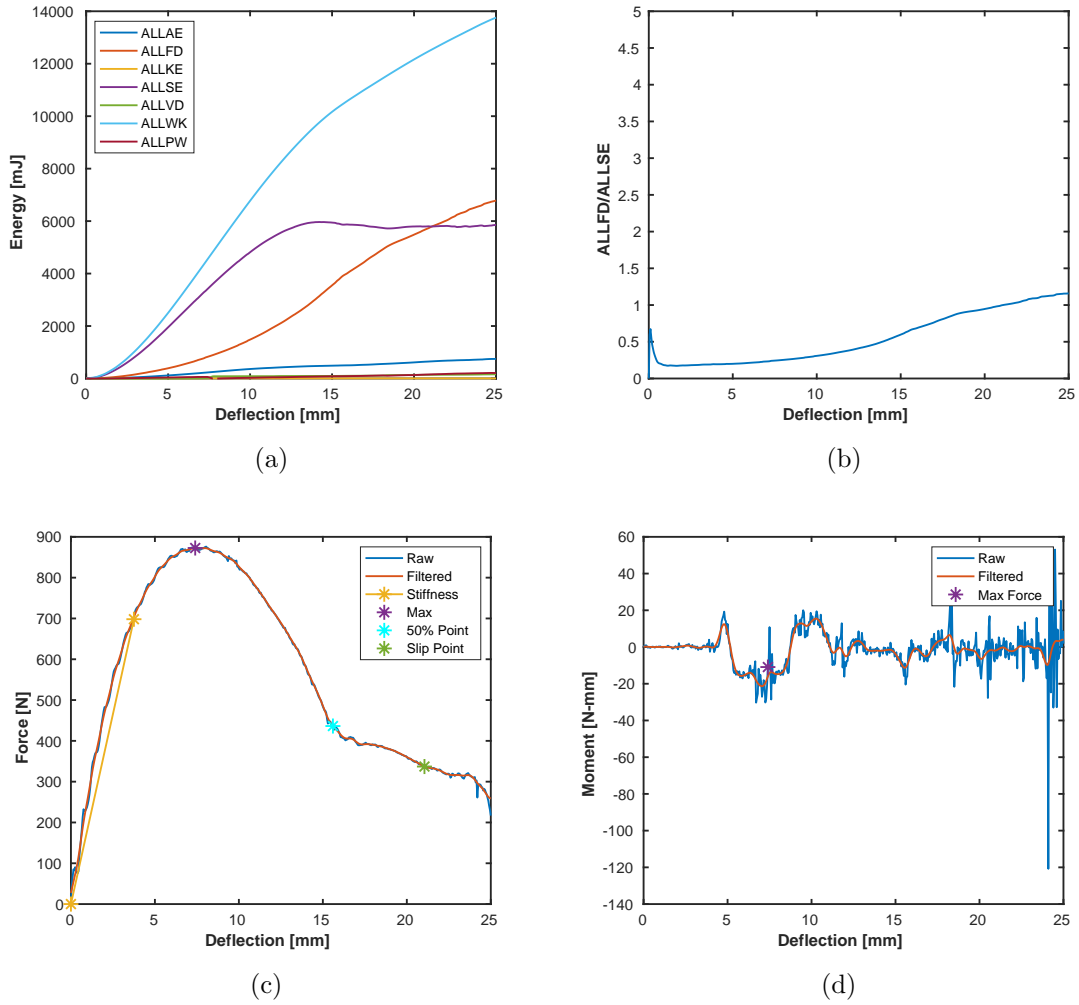


Figure 3.12. Displacement loading results for (4.8²)-B configuration: (a) System energies. (b) Slip ratio ALLFD/ALLSE. (c) Force-deflection response. (d) Moment-deflection response.

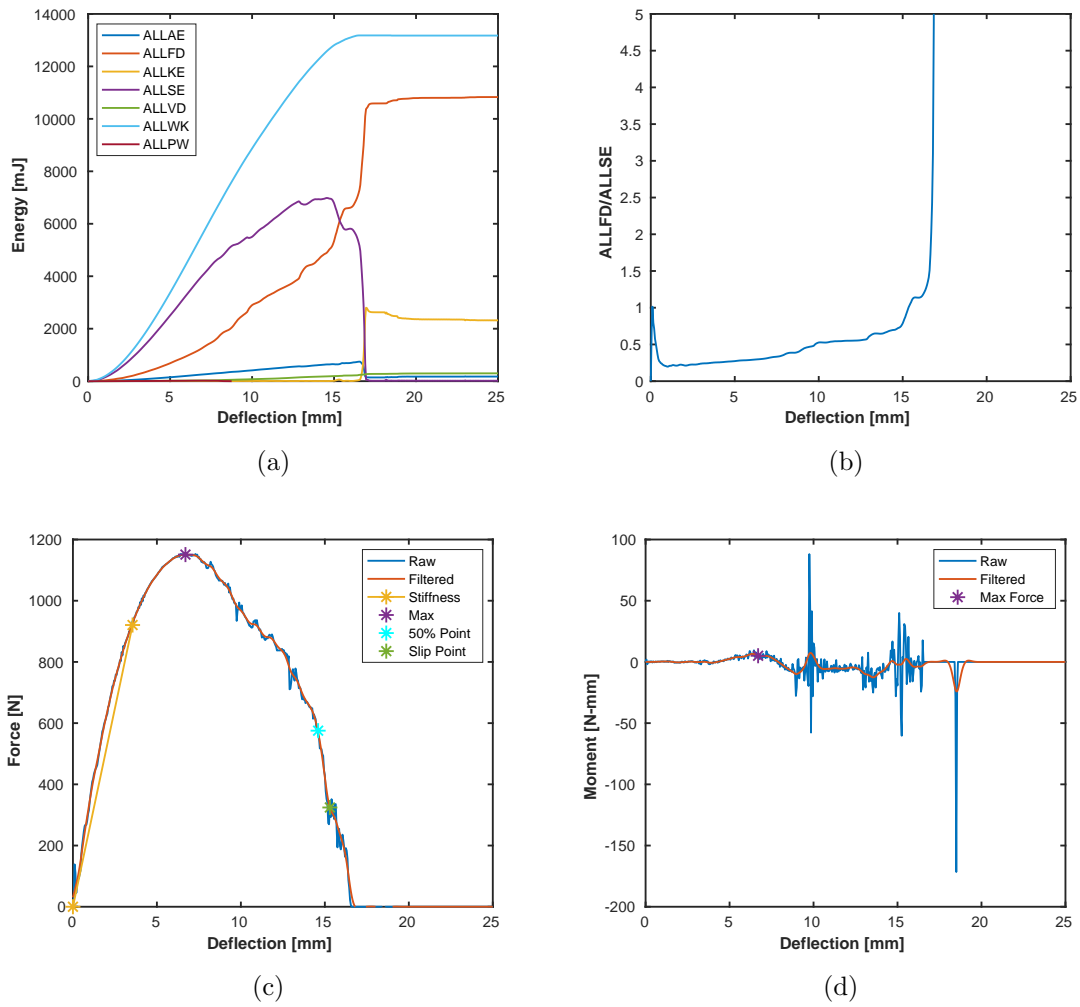


Figure 3.13. Displacement loading results for (4.6.12)-A(-) configuration: (a) System energies. (b) Slip ratio ALLFD/ALLSE. (c) Force-deflection response. (d) Moment-deflection response.

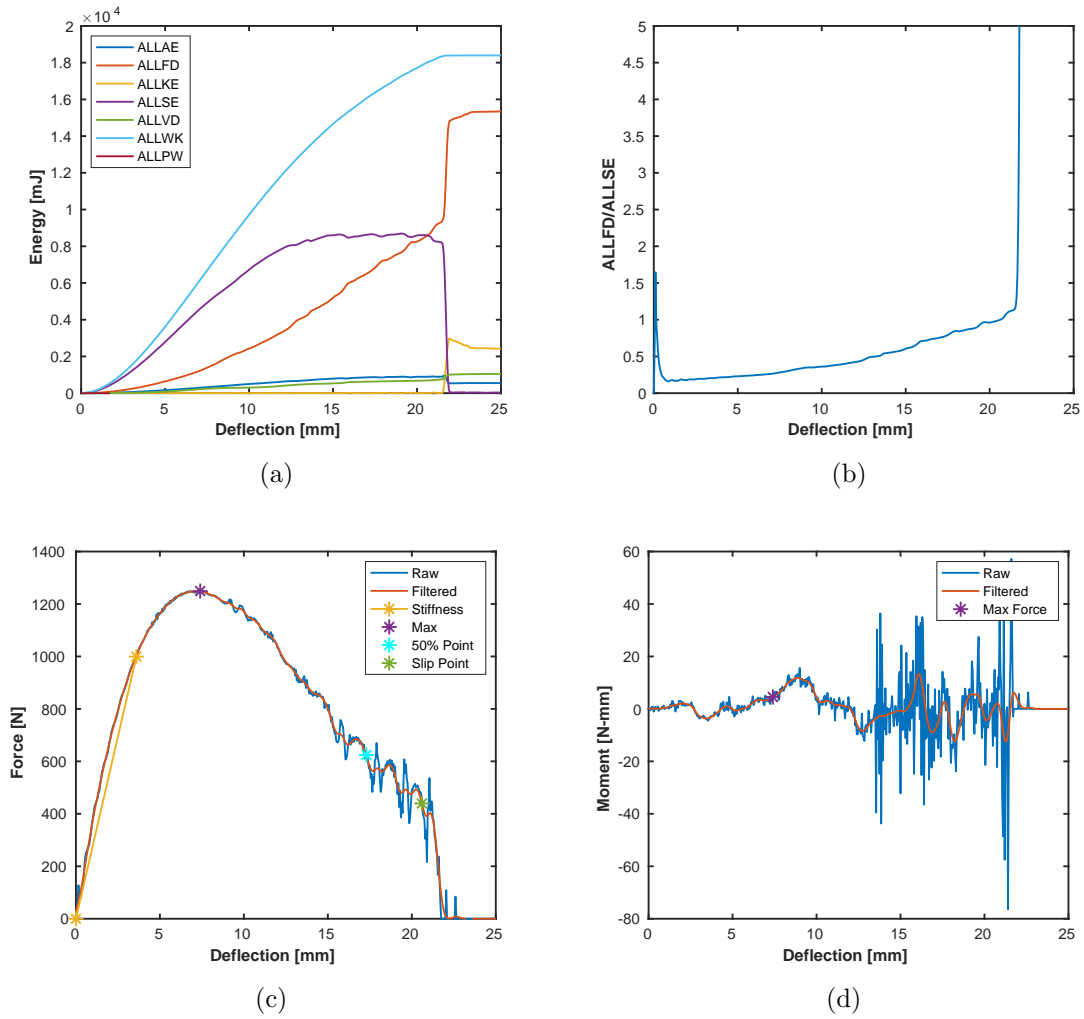


Figure 3.14. Displacement loading results for (4.6.12)-A(+) configuration: (a) System energies. (b) Slip ratio ALLFD/ALLSE. (c) Force-deflection response. (d) Moment-deflection response.

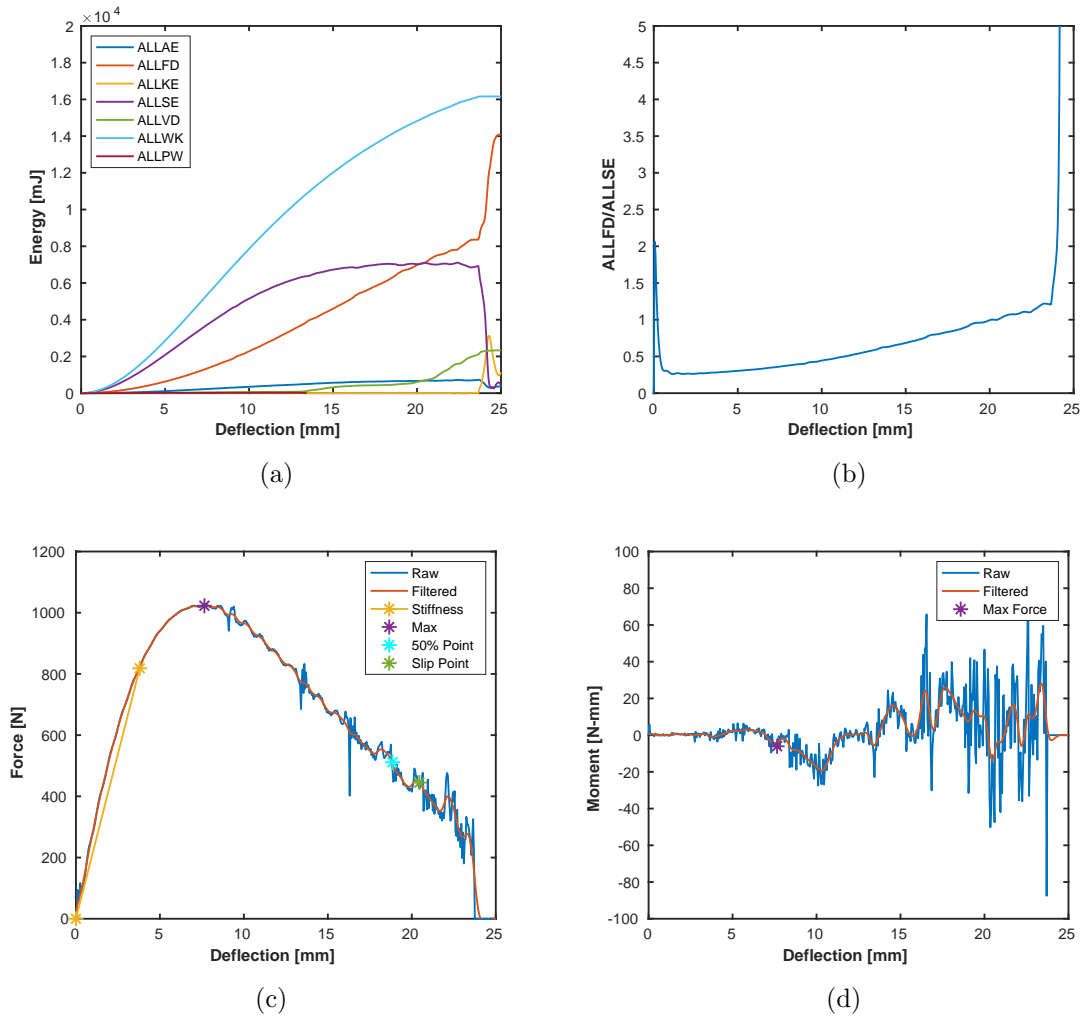


Figure 3.15. Displacement loading results for (4.6.12)-B(-) configuration: (a) System energies. (b) Slip ratio ALLFD/ALLSE. (c) Force-deflection response. (d) Moment-deflection response.

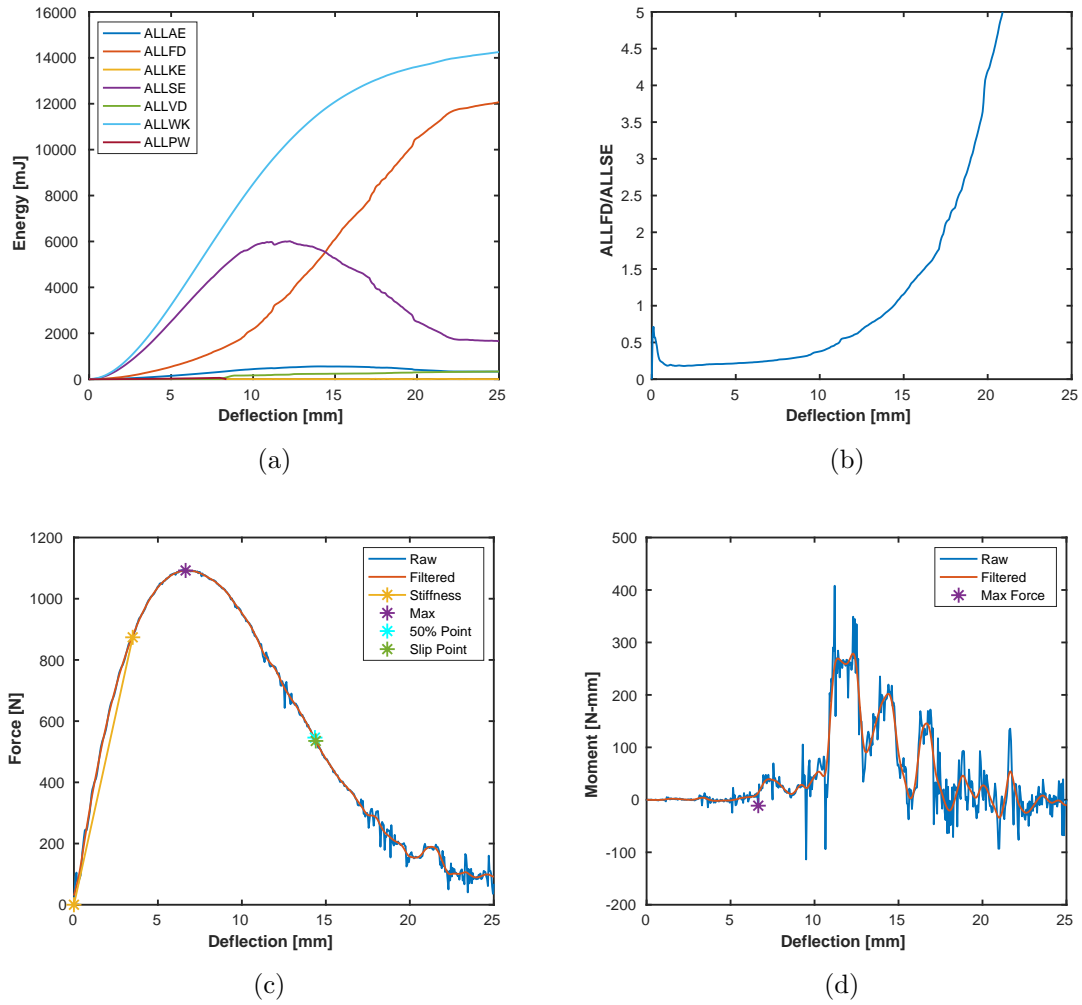


Figure 3.16. Displacement loading results for (4.6.12)-B(+) configuration: (a) System energies. (b) Slip ratio ALLFD/ALLSE. (c) Force-deflection response. (d) Moment-deflection response.

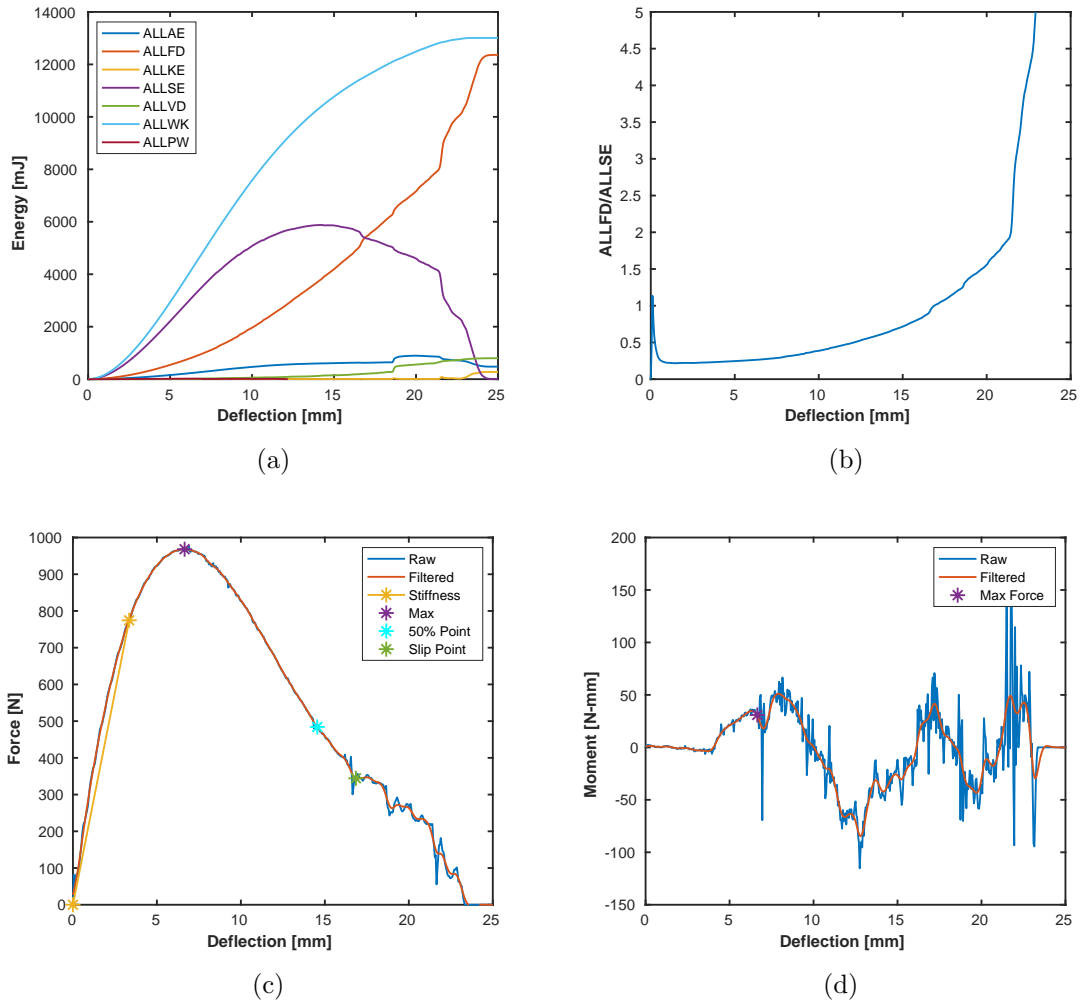


Figure 3.17. Displacement loading results for (4.6.12)-C(-) configuration: (a) System energies. (b) Slip ratio ALLFD/ALLSE. (c) Force-deflection response. (d) Moment-deflection response.

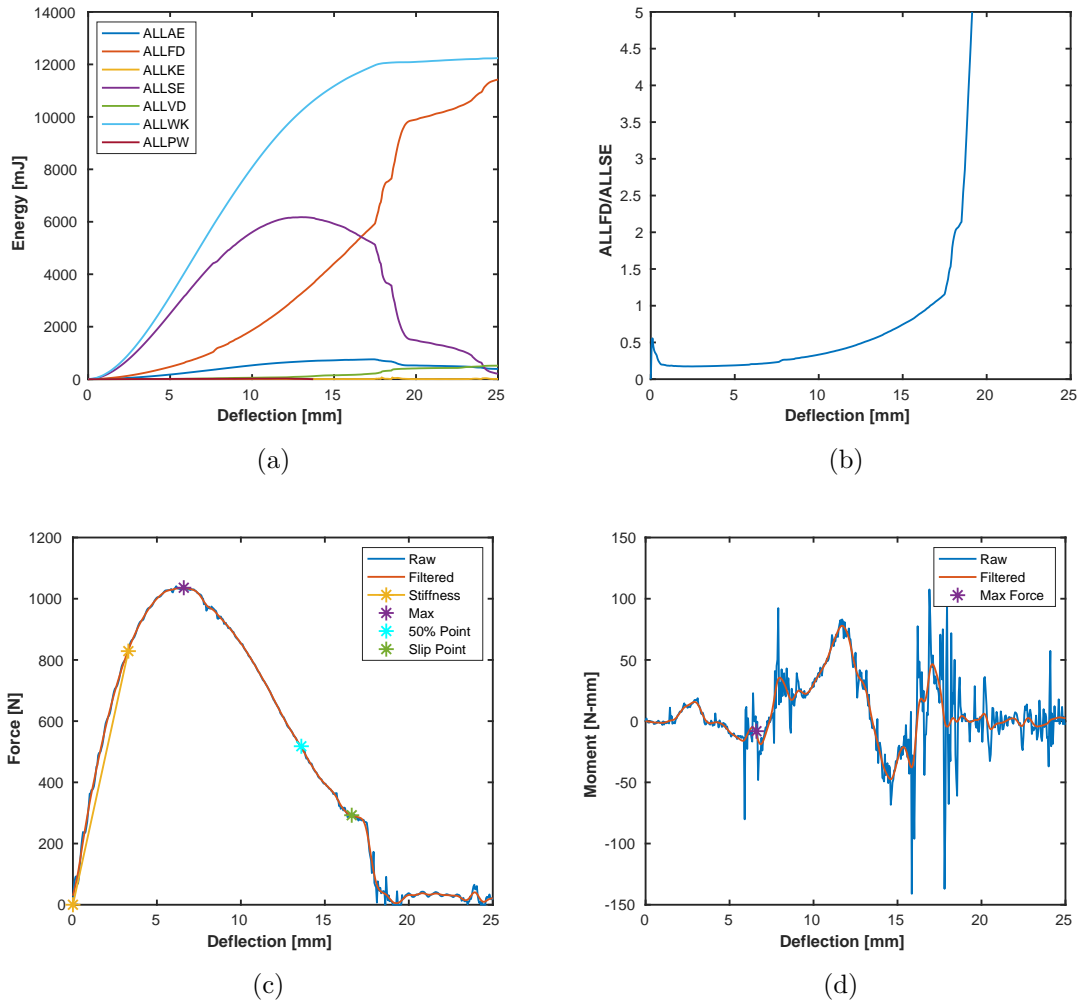


Figure 3.18. Displacement loading results for (4.6.12)-C(+) configuration: (a) System energies. (b) Slip ratio ALLFD/ALLSE. (c) Force-deflection response. (d) Moment-deflection response.

3.2 Analysis of the System Internal Load Transfer

Vector plots of the compressive stresses throughout each assembly at a deflection of 2.5 mm are presented in this section, Figures 3.19 - 3.36. Note that the frames and indentors are not shown in these images. The patterns did not vary significantly with the coefficient of friction, so only the results for $\mu = 0.2$ are presented.

The [4⁴]-A configuration is a truncated variant of the assembly studied by Khandelwal et al. [10], Figure 3.19. Here we can see similar results to those that were found previously. There are strong concentrations of stress perpendicular to the frame in the blocks located in the top/bottom center as well as on the sides just off center as indicated. This is consistent with the proposed truss pattern [10]. Additionally, there are stress concentrations forming triangles at the top and bottom which point to the center as depicted. It can be seen that this configuration is not chiral and that it has rotational symmetry of 180°. The [4⁴]-B configuration also has concentrations of stress perpendicular to the frame, but these concentrations are shaped like offset triangles as outlined in the image, Figure 3.20. The chirality is clearly visible here, and it can be seen that this configuration has rotational symmetry of 90°.

The [3.6.3.6]-A and [3.6.3.6]-B configurations are shown in Figures 3.21 and 3.22. They do not have any clearly defined thrust lines or stress patterns. The stress vectors are generally aligned with the dual tessellation except for near the center where the indenter caused some disturbance. These configurations are chiral, and this can be seen by the outlined blocks which have higher stresses than their neighbors. The [3.6.3.6]-A configuration has rotational symmetry of 60° and the [3.6.3.6]-B configuration has rotational symmetry of 120°.

Like the [3.6.3.6]-A and [3.6.3.6]-B configurations, the [3.4.6.4]-A, [3.4.6.4]-B, and [3.4.6.4]-C configurations lack any well defined thrust lines or stress patterns, Figures 3.23 - 3.25. The stress vectors are generally aligned with the dual tessellation except near the indenter, which causes a disturbance in the stress field, and near the frame where the stresses tend to align perpendicular to the frame. These configura-

tions are also all chiral. Select blocks with higher stresses than their neighbors have been outlined for each configuration to illustrate the chirality. The [3.4.6.4]-A configuration has rotational symmetry of 60° , the [3.4.6.4]-B configuration has rotational symmetry of 120° , and the [3.4.6.4]-C configuration has rotational symmetry of 180° .

The $[3^6]$ -A and $[3^6]$ -B configurations are shown in Figures 3.26 and 3.27. These configurations have well developed thrust lines. The $[3^6]$ -A configuration has six thrust lines aligned radially from the center. It can be seen that three of these lines are more developed than the others. Stress rings around the center are also visible as in traditional plate loading. The stress vectors elsewhere are generally aligned with the dual tessellation. This configuration is not chiral, and it has rotational symmetry of 120° . The $[3^6]$ -B configuration also has six thrust lines, but these are offset from the center, showing chirality. It has rotational symmetry of 120° .

The (4.8^2) -A(-), (4.8^2) -A(+), and (4.8^2) -B configurations are presented in Figures 3.28 and 3.30. From the center block, load is primarily transferred diagonally into the adjacent decahedron blocks in the (4.8^2) -A(-) configuration. Along the frame, the stress concentrations are highest in the hexahedron blocks located at the center of each edge. In the (4.8^2) -A(+) configuration, load is primarily transferred horizontally and vertically from the center block into the adjacent hexahedron blocks, and the stress concentrations along the frame are highest in the two decahedron blocks and one hexahedron block located at the center of each border. Both the (4.8^2) -A(-) and (4.8^2) -A(+) configurations have rotational symmetry of 90° . The (4.8^2) -B configuration has rotational symmetry of 180° . In this configuration load is primarily transferred horizontally from the center block into the decahedron blocks to the left and right. Thrust lines can be seen oriented perpendicularly to the frame from the centermost decahedron blocks to the middle decahedron blocks on each side. None of these configurations are chiral.

The $(4.6.12)$ -A(-), $(4.6.12)$ -A(+), $(4.6.12)$ -B(-), $(4.6.12)$ -B(+), $(4.6.12)$ -C(-), and $(4.6.12)$ -C(+) configurations are shown in Figures 3.31 - 3.36. Both the $(4.6.12)$ -A(-) and $(4.6.12)$ -A(+) configurations have rotational symmetry of 60° , and they both

share a general pattern of radial thrust lines connecting to a hexagon in the middle, but they differ in how the load is transferred from the center block into the adjacent blocks. Similarly, the (4.6.12)-B(-) and (4.6.12)-B(+) configurations also share a general thrust line pattern but differ in the load transfer at the center. These configurations have rotational symmetry of 120° . The (4.6.12)-C(-) and (4.6.12)-C(+) configurations have the greatest stress concentrations aligned generally horizontally toward the two large indentations of the frame on the sides. Like the previous pairs, these two also differ in the load transfer pattern from the center block. These configurations have rotational symmetry of 180° . None of these configurations are chiral.

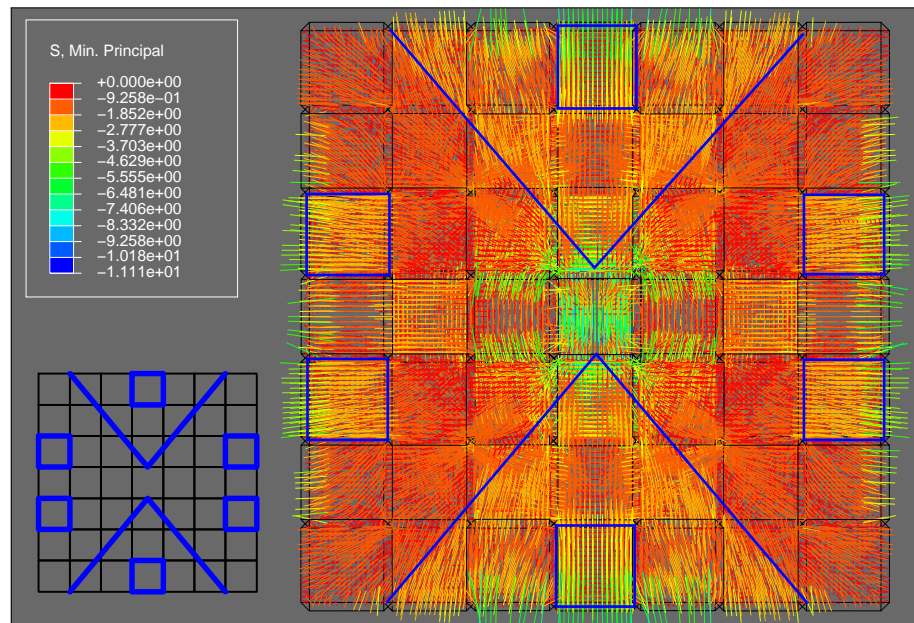


Figure 3.19. Vector plot of minimum principal stress [MPa] for the $[4^4]$ -A configuration under displacement load. High stress areas of interest are marked in blue.

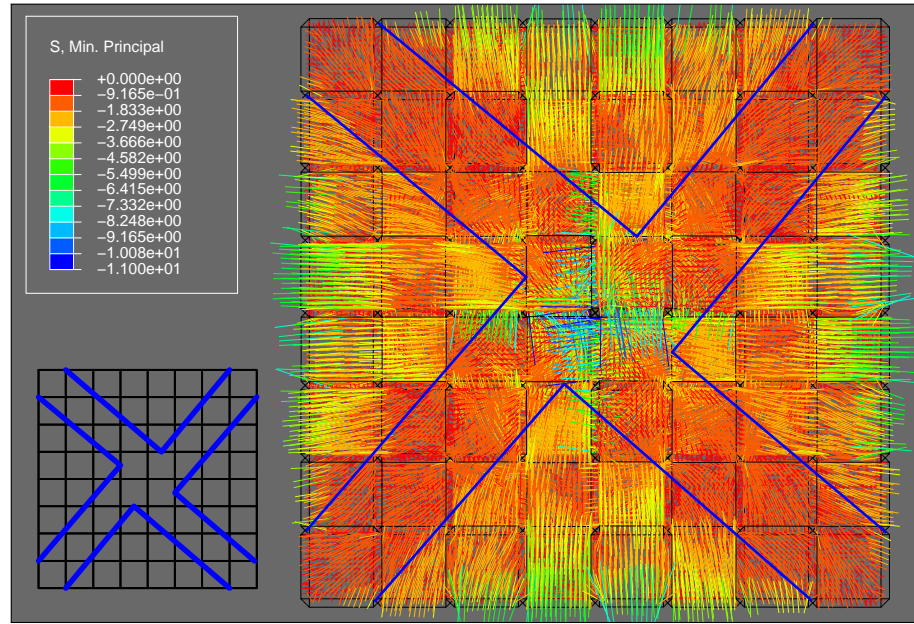


Figure 3.20. Vector plot of minimum principal stress [MPa] for the $[4^4]$ -B configuration under displacement load. High stress areas of interest are marked in blue.

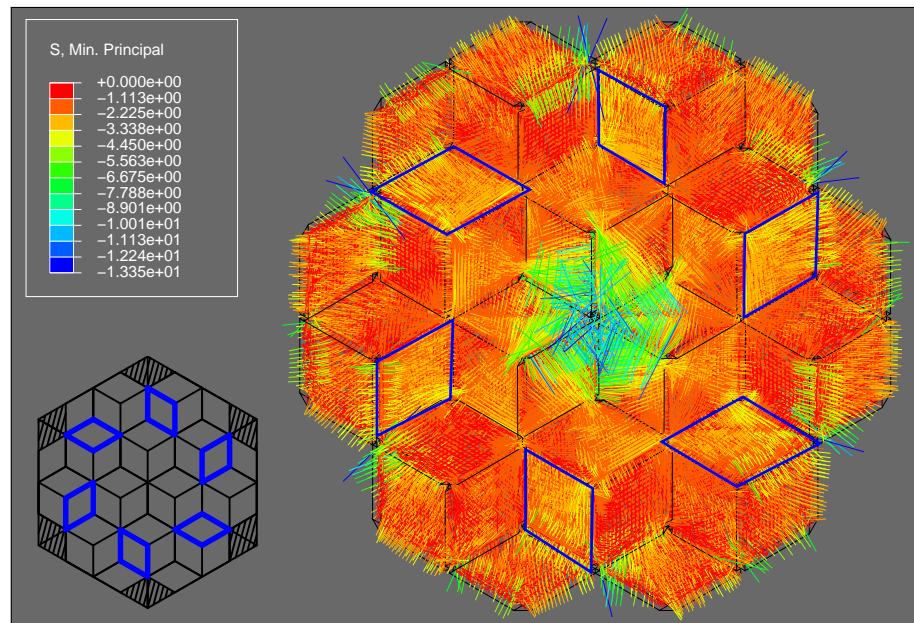


Figure 3.21. Vector plot of minimum principal stress [MPa] for the $[3.6.3.6]$ -A configuration under displacement load. High stress areas of interest are marked in blue.

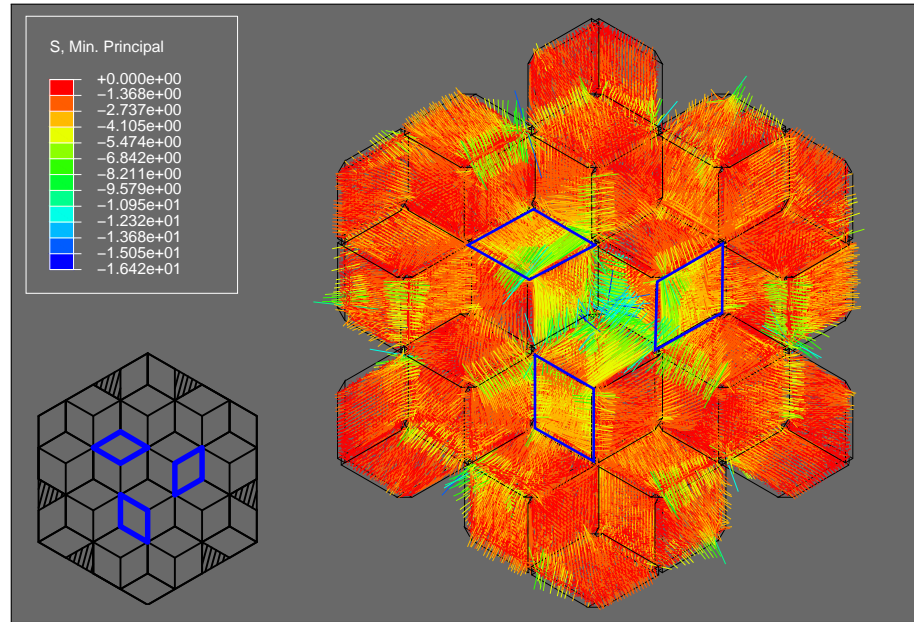


Figure 3.22. Vector plot of minimum principal stress [MPa] for the [3.6.3.6]-B configuration under displacement load. High stress areas of interest are marked in blue.

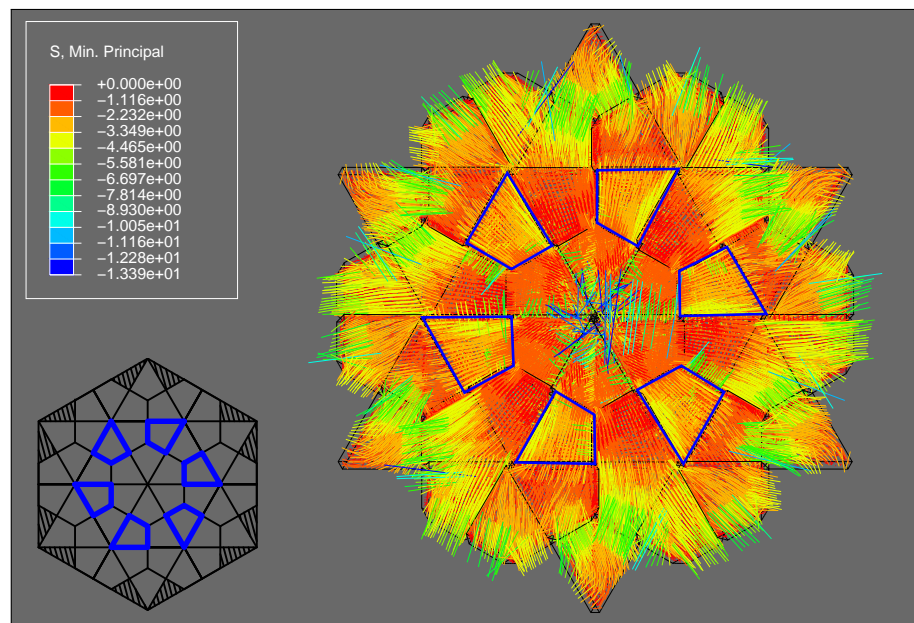


Figure 3.23. Vector plot of minimum principal stress [MPa] for the [3.4.6.4]-A configuration under displacement load. High stress areas of interest are marked in blue.

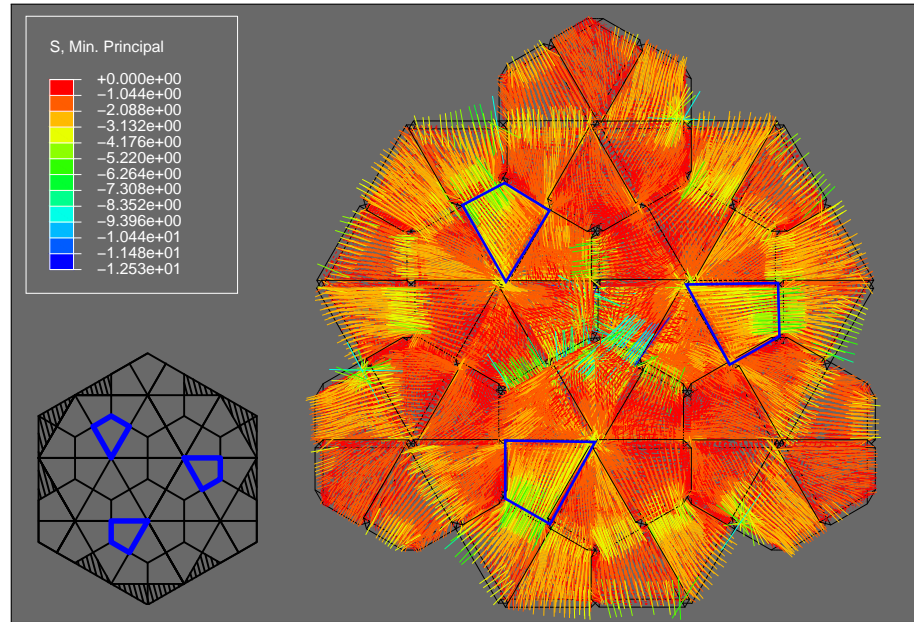


Figure 3.24. Vector plot of minimum principal stress [MPa] for the [3.4.6.4]-B configuration under displacement load. High stress areas of interest are marked in blue.

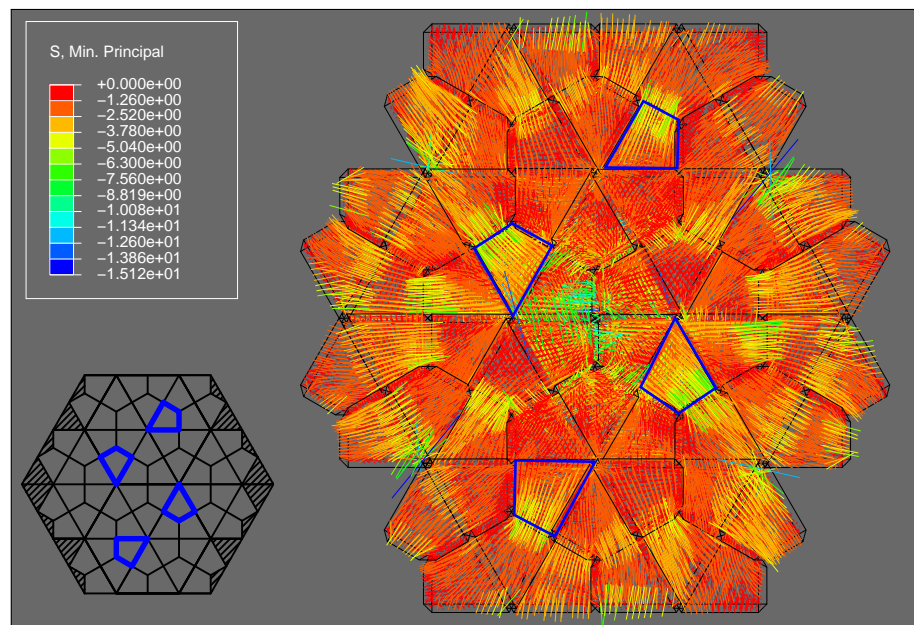


Figure 3.25. Vector plot of minimum principal stress [MPa] for the [3.4.6.4]-C configuration under displacement load. High stress areas of interest are marked in blue.

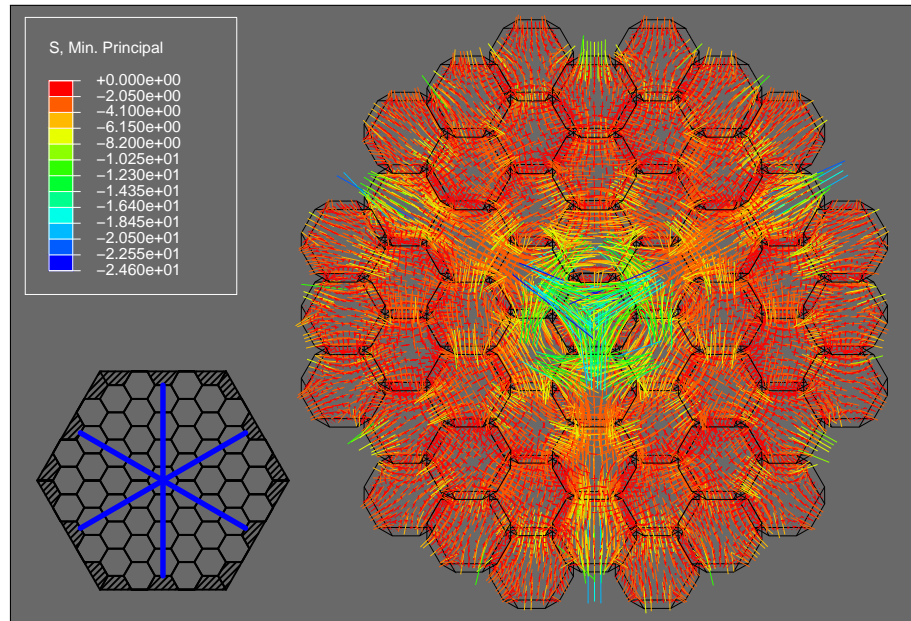


Figure 3.26. Vector plot of minimum principal stress [MPa] for the $[3^6]$ -A configuration under displacement load. Thrust lines are depicted.

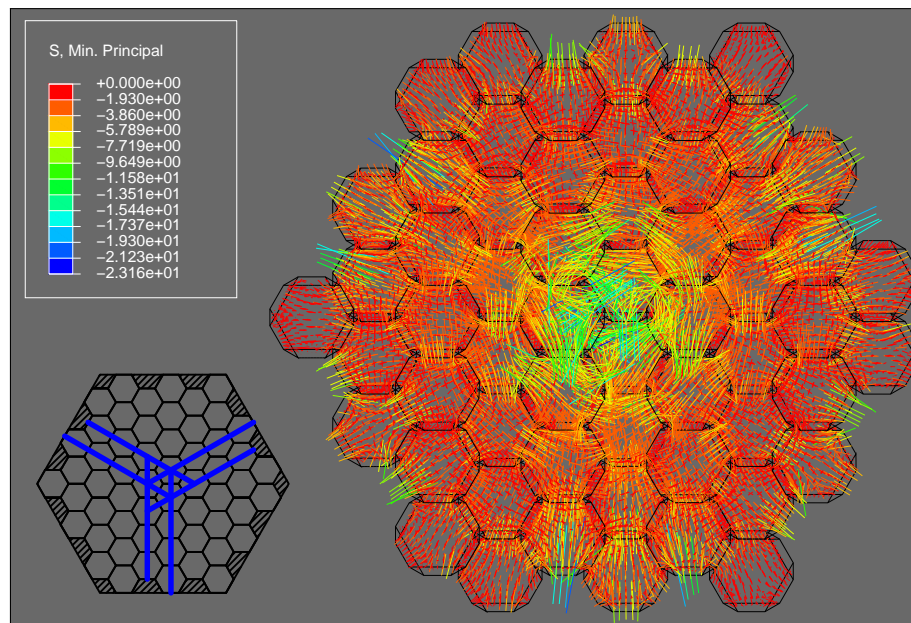


Figure 3.27. Vector plot of minimum principal stress [MPa] for the $[3^6]$ -B configuration under displacement load. Thrust lines are depicted.

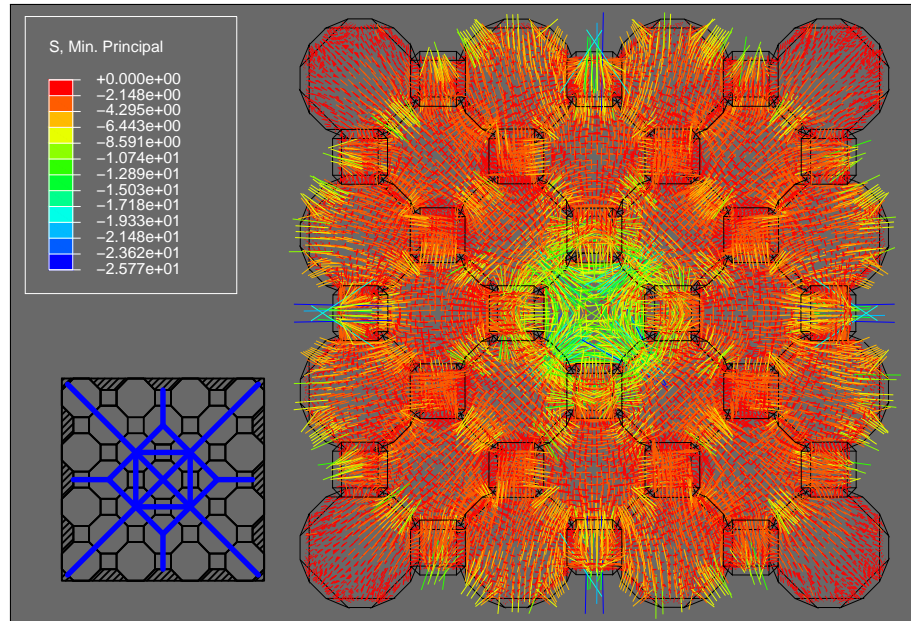


Figure 3.28. Vector plot of minimum principal stress [MPa] for the (4.8^2) -A(-) configuration under displacement load. Thrust lines are depicted.

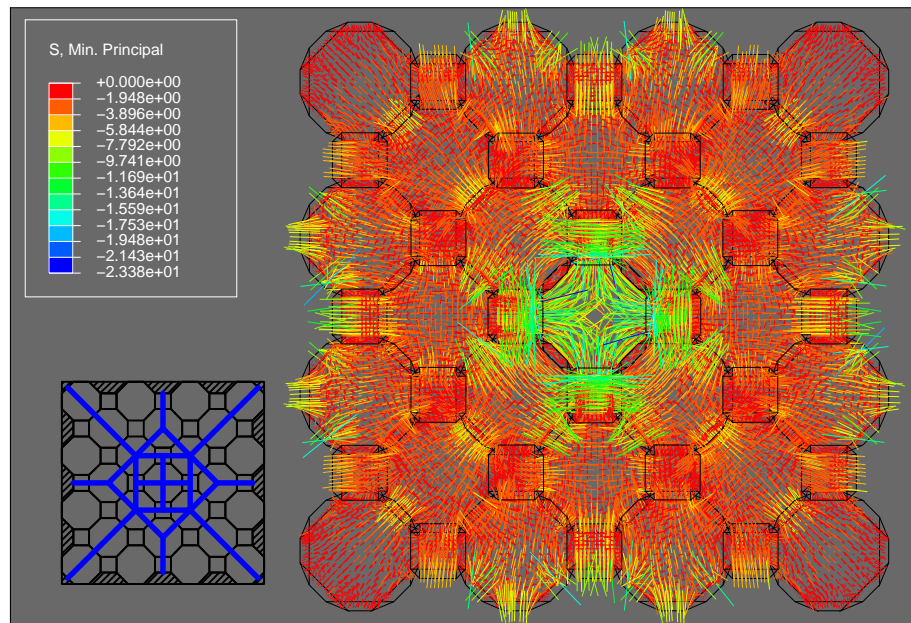


Figure 3.29. Vector plot of minimum principal stress [MPa] for the (4.8^2) -A(+) configuration under displacement load. Thrust lines are depicted.

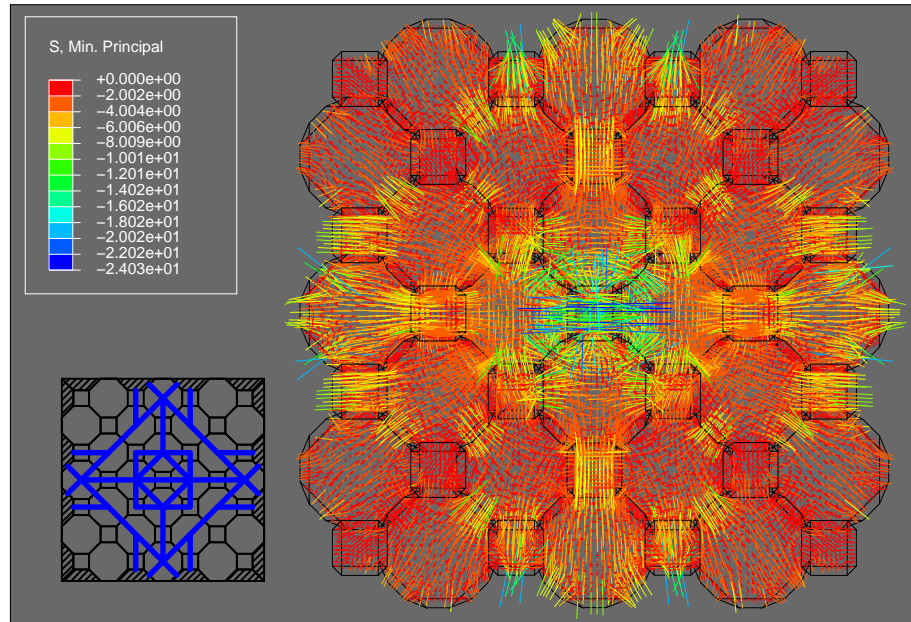


Figure 3.30. Vector plot of minimum principal stress [MPa] for the (4.8^2) -B configuration under displacement load. Thrust lines are depicted.

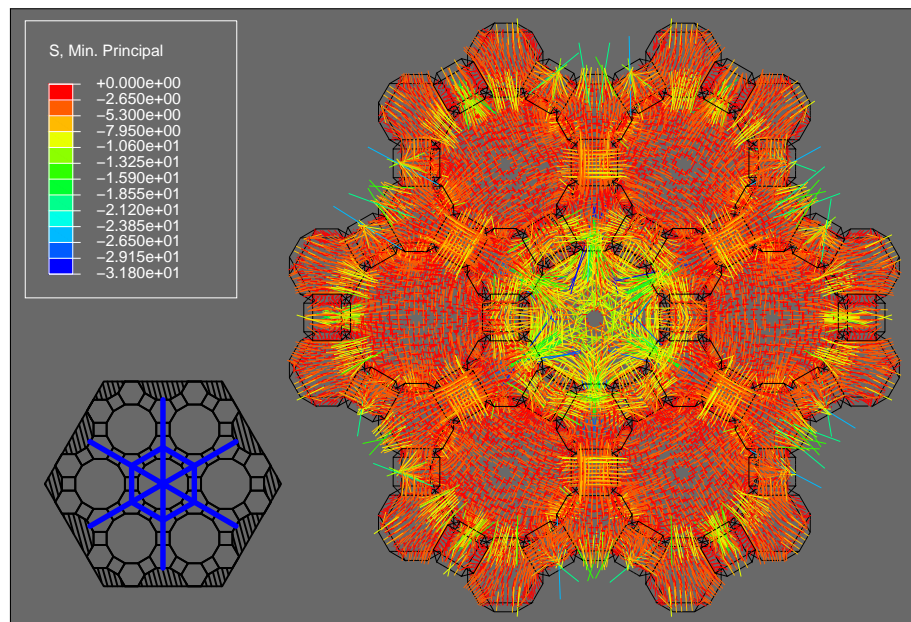


Figure 3.31. Vector plot of minimum principal stress [MPa] for the $(4.6.12)$ -A(-) configuration under displacement load. Thrust lines are depicted.

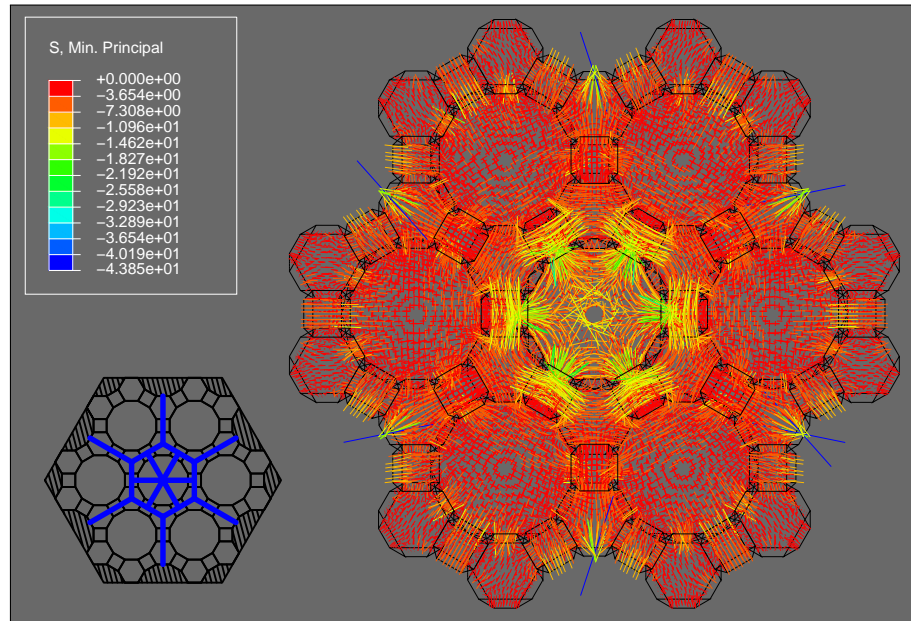


Figure 3.32. Vector plot of minimum principal stress [MPa] for the (4.6.12)-A(+) configuration under displacement load. Thrust lines are depicted.

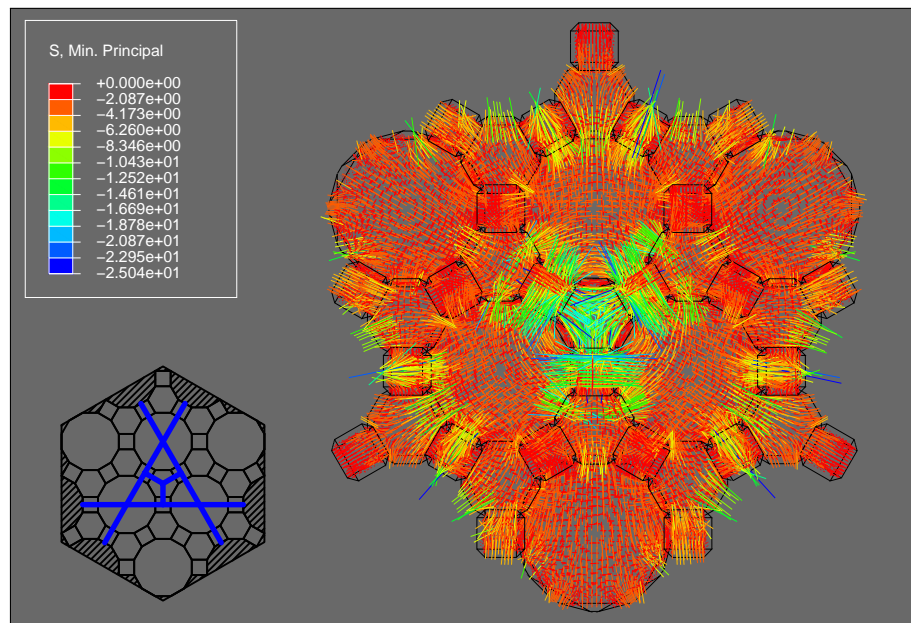


Figure 3.33. Vector plot of minimum principal stress [MPa] for the (4.6.12)-B(-) configuration under displacement load. Thrust lines are depicted.

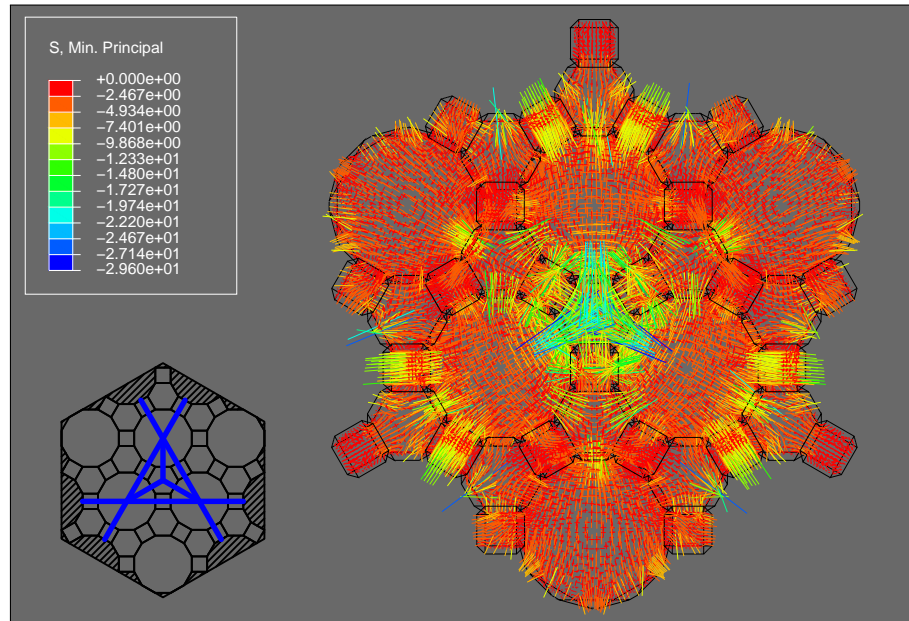


Figure 3.34. Vector plot of minimum principal stress [MPa] for the (4.6.12)-B(+) configuration under displacement load. Thrust lines are depicted.

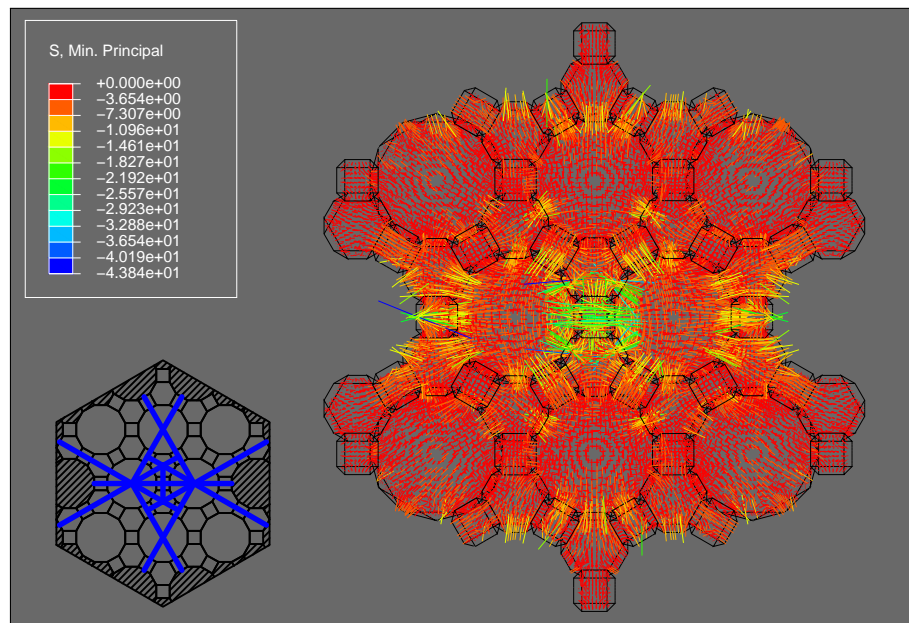


Figure 3.35. Vector plot of minimum principal stress [MPa] for the (4.6.12)-C(-) configuration under displacement load. Thrust lines are depicted.

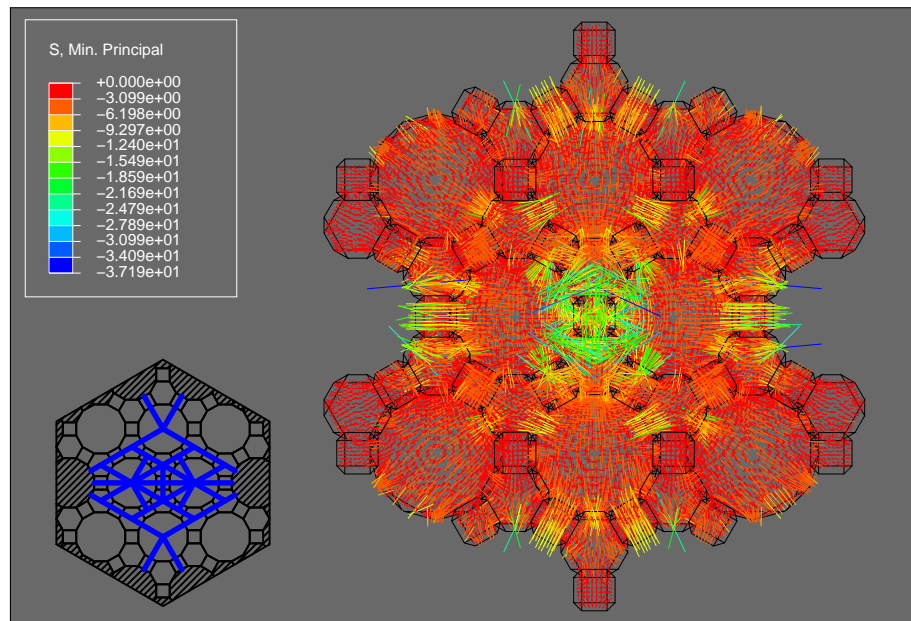


Figure 3.36. Vector plot of minimum principal stress [MPa] for the (4.6.12)-C(+) configuration under displacement load. Thrust lines are depicted.

4. TIM SYSTEMS UNDER BODY FORCE LOADING

This chapter contains the data collected from the body force loading simulations including the system energies and vector plots of the compressive stress fields. The results shown here were computed with the coefficient of friction $\mu = 0.2$.

4.1 System Energies

The system energies for all configurations are shown in Figures 4.1 - 4.6. In all cases the work input increased exponentially as the gravity magnitude was increased. The configurations were strain dominant until a critical point when significant sliding began to occur leading to rapid failure as indicated by a sudden drop in strain energy and a sudden increase in kinetic energy caused by the blocks falling from the assembly.

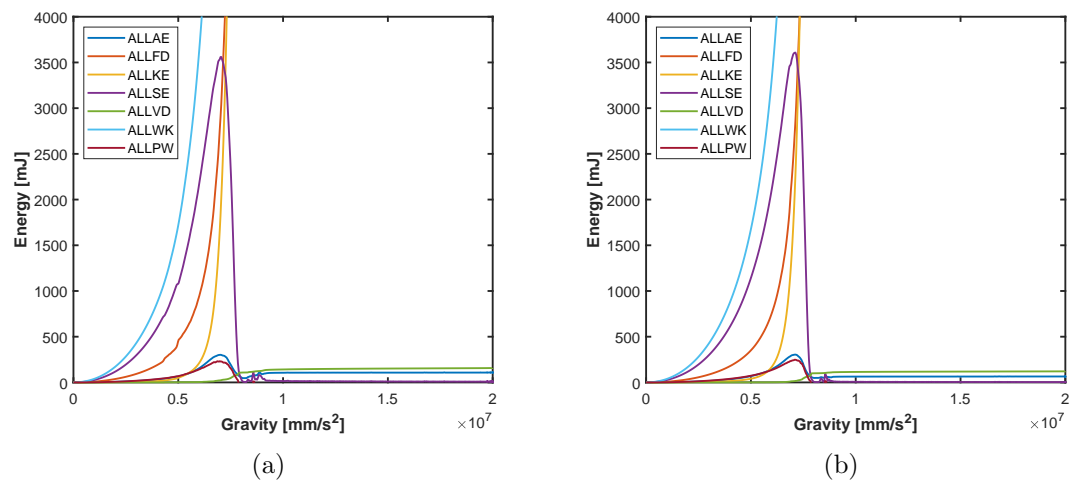


Figure 4.1. System energies under gravity loading for (a) $[4^4]$ -A, (b) $[4^4]$ -B.

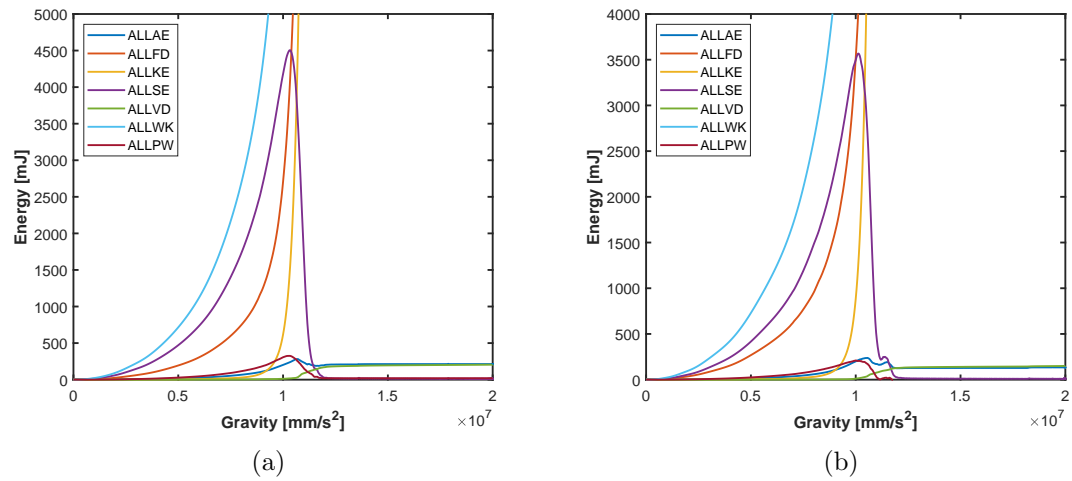


Figure 4.2. System energies under gravity loading for (a) [3.6.3.6]-A, (b) [3.6.3.6]-B.

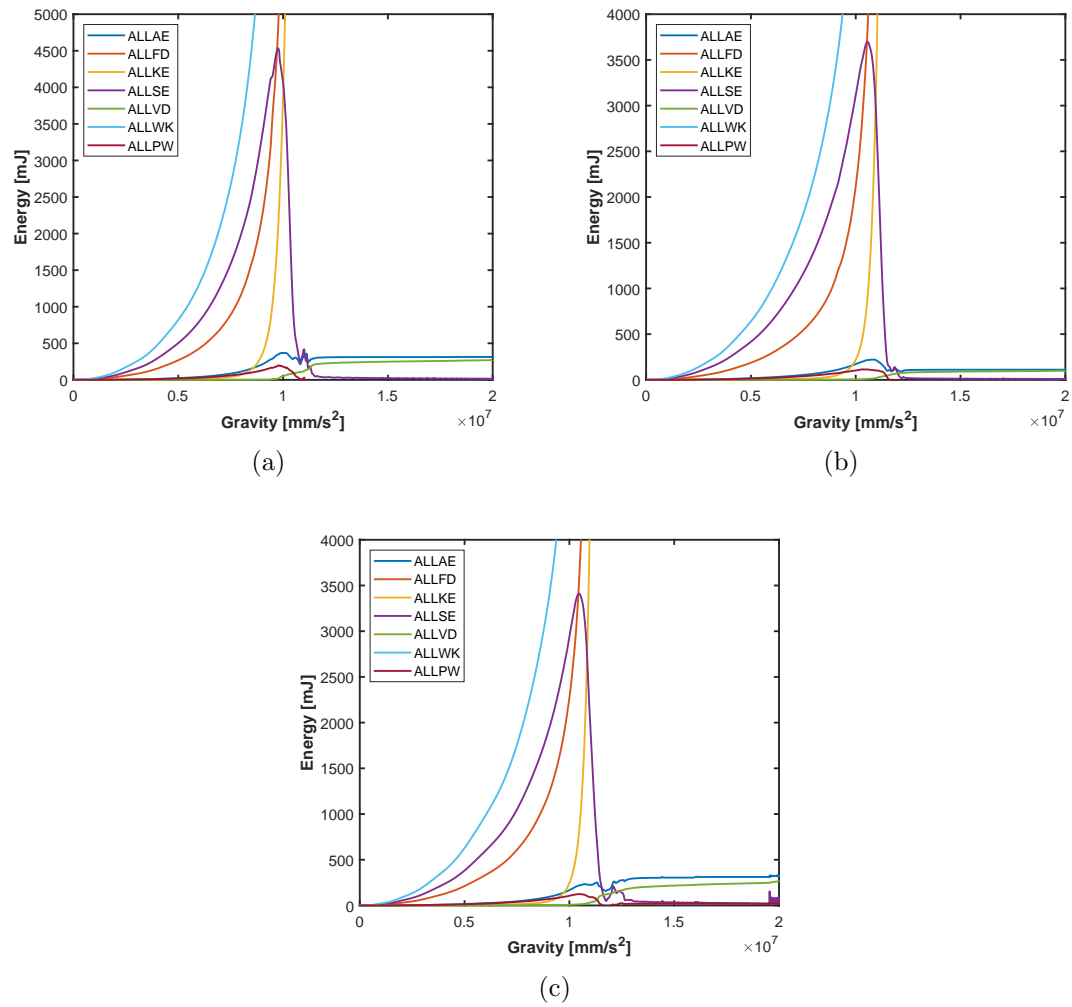


Figure 4.3. System energies under gravity loading for (a) [3.4.6.4]-A, (b) [3.4.6.4]-B, (c) [3.4.6.4]-C.

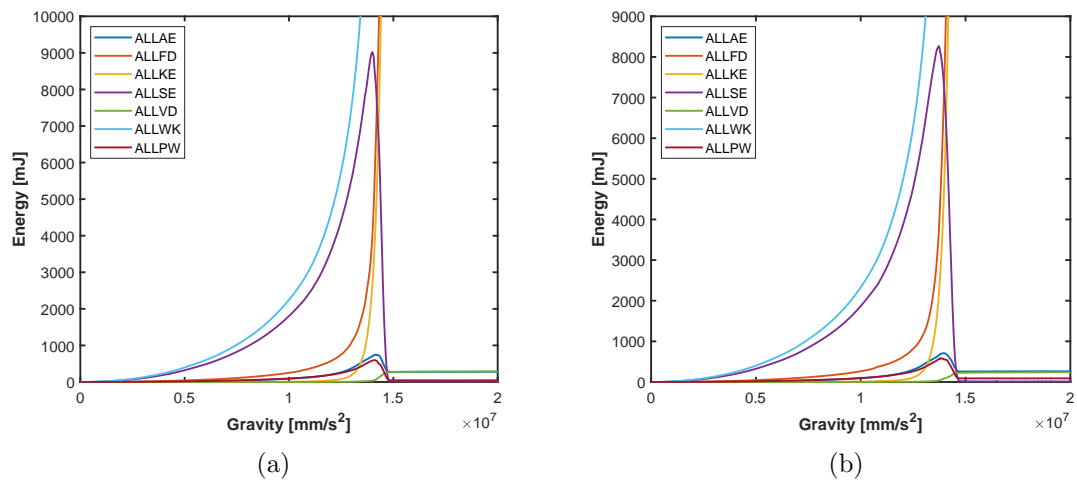


Figure 4.4. System energies under gravity loading for (a) [3⁶]-A, (b) [3⁶]-B.

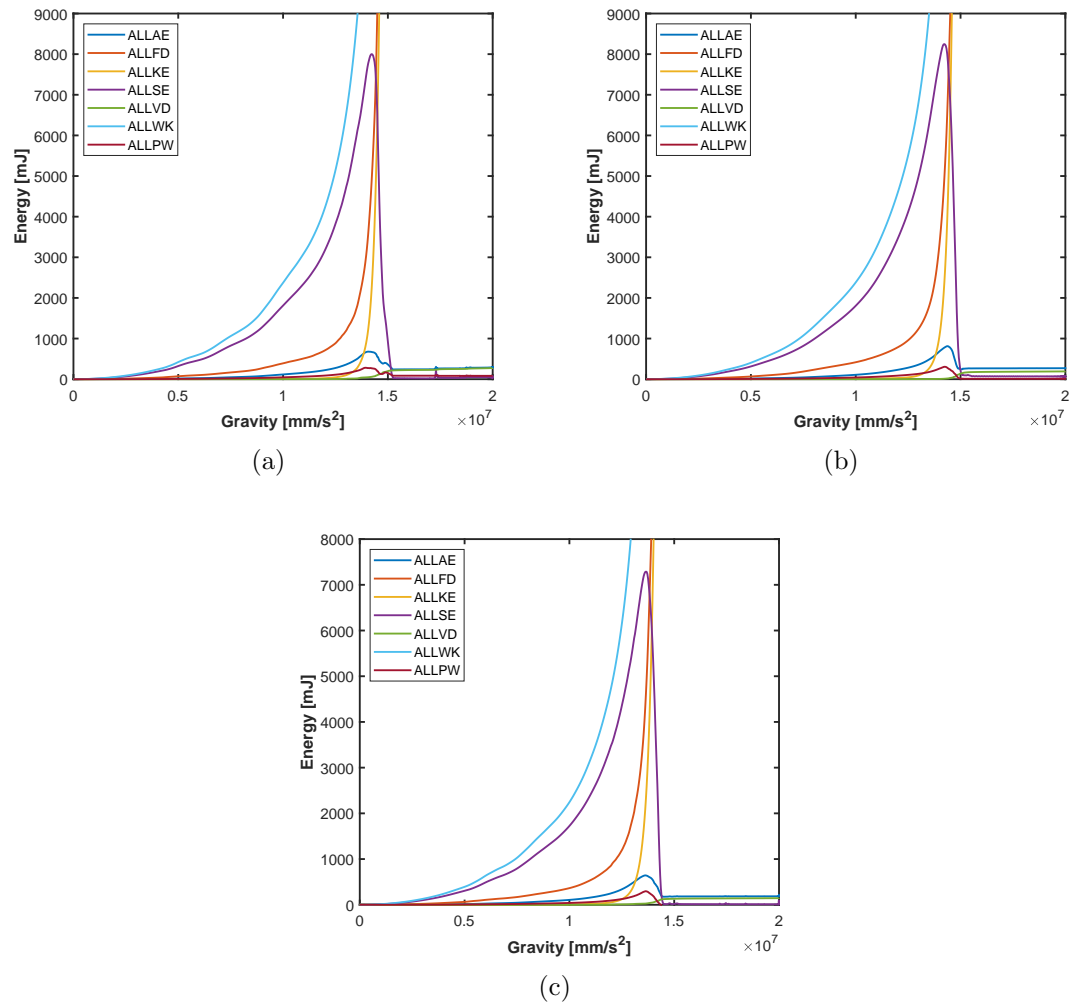


Figure 4.5. System energies under gravity loading for (a) (4.8^2) -A(-), (b) (4.8^2) -A(+), (c) (4.8^2) -B.

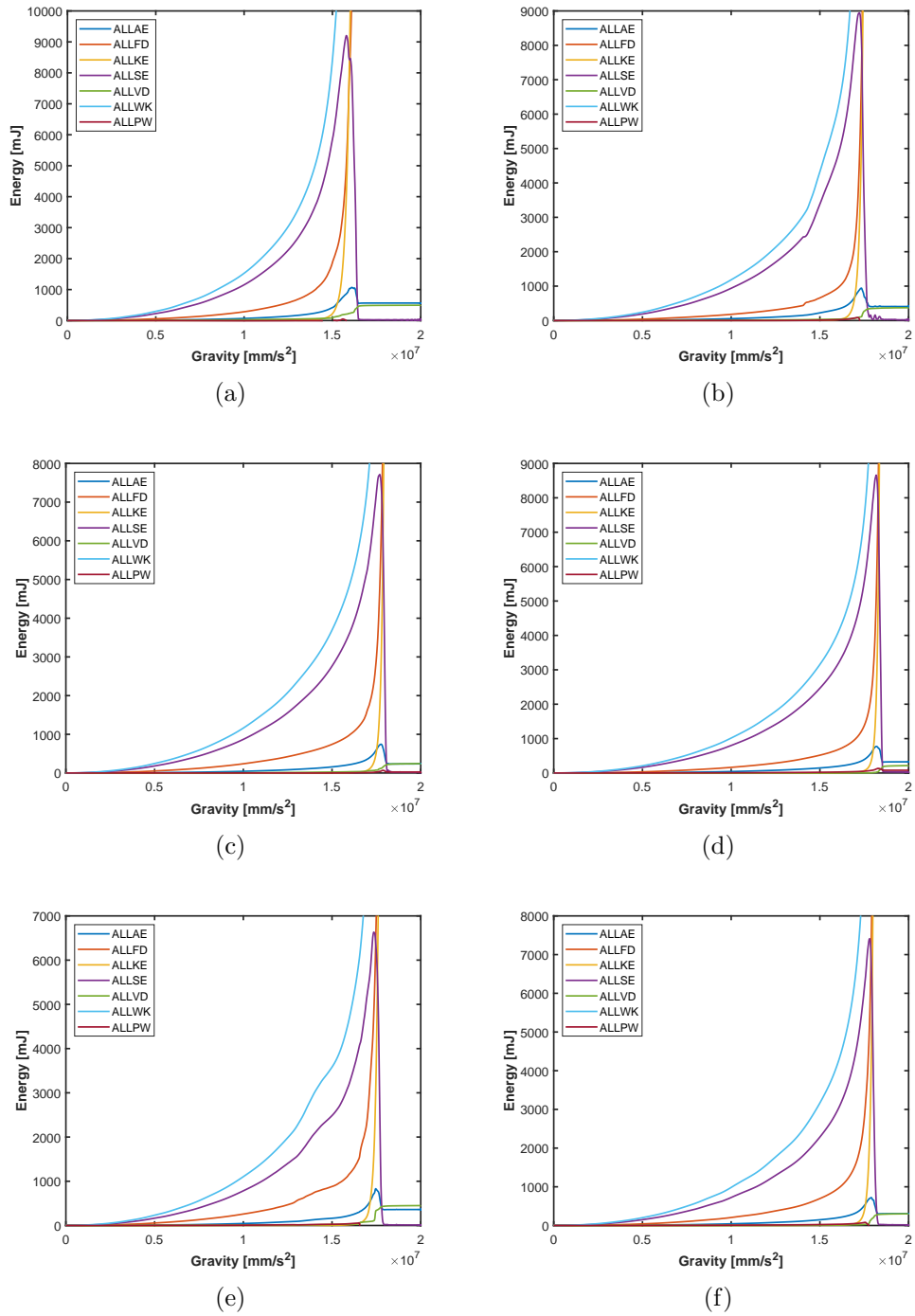


Figure 4.6. System energies under gravity loading for (a) (4.6.12)-A(-), (b) (4.6.12)-A(+), (c) (4.6.12)-B(-), (d) (4.6.12)-B(+), (e) (4.6.12)-C(-), (f) (4.6.12)-C(+).

4.2 Body Force Slip Ratios

The slip ratios for all configurations are presented in Figures 4.7 - 4.12. These are characterized by a constant slip ratio as the gravity magnitude was increased and then a rapid spike when the system failed.

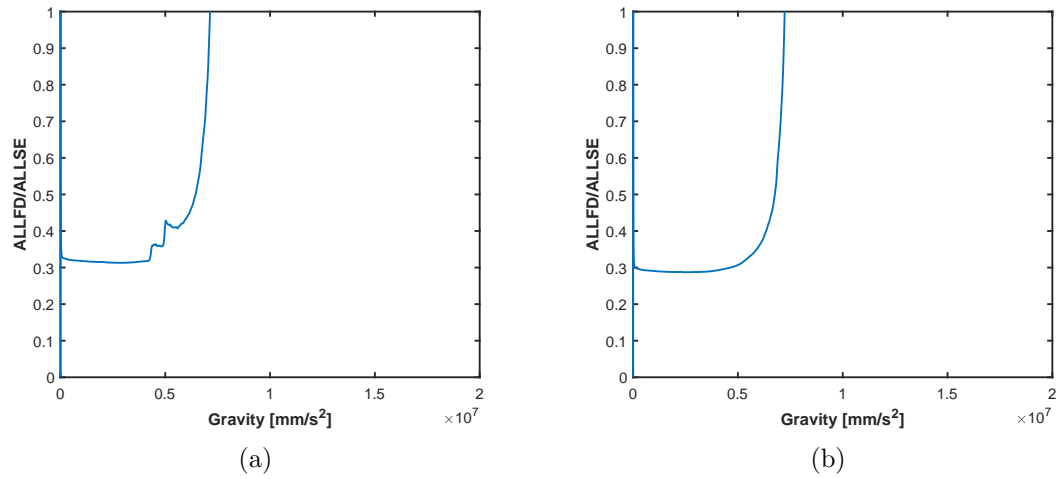


Figure 4.7. Slip ratio under gravity loading for (a) [4⁴]-A, (b) [4⁴]-B.

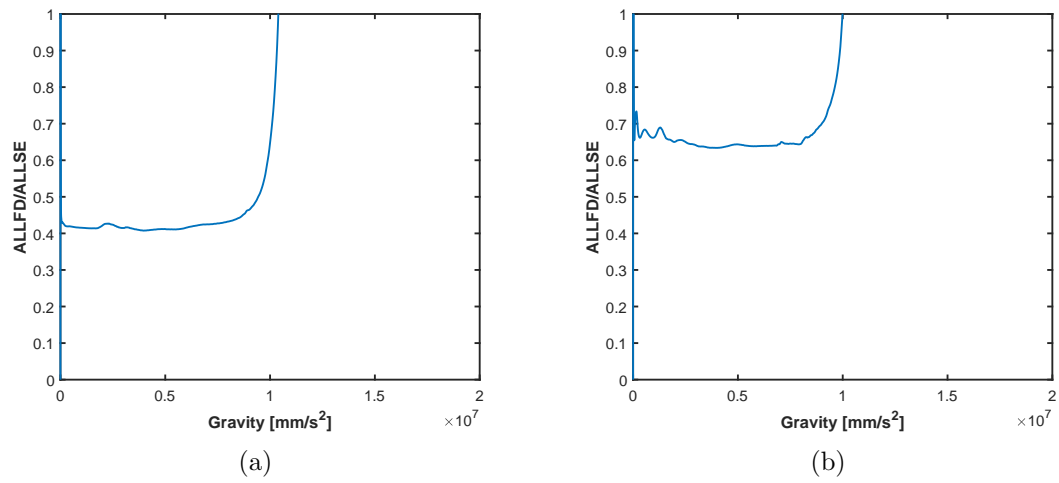


Figure 4.8. Slip ratio under gravity loading for (a) [3.6.3.6]-A, (b) [3.6.3.6]-B.

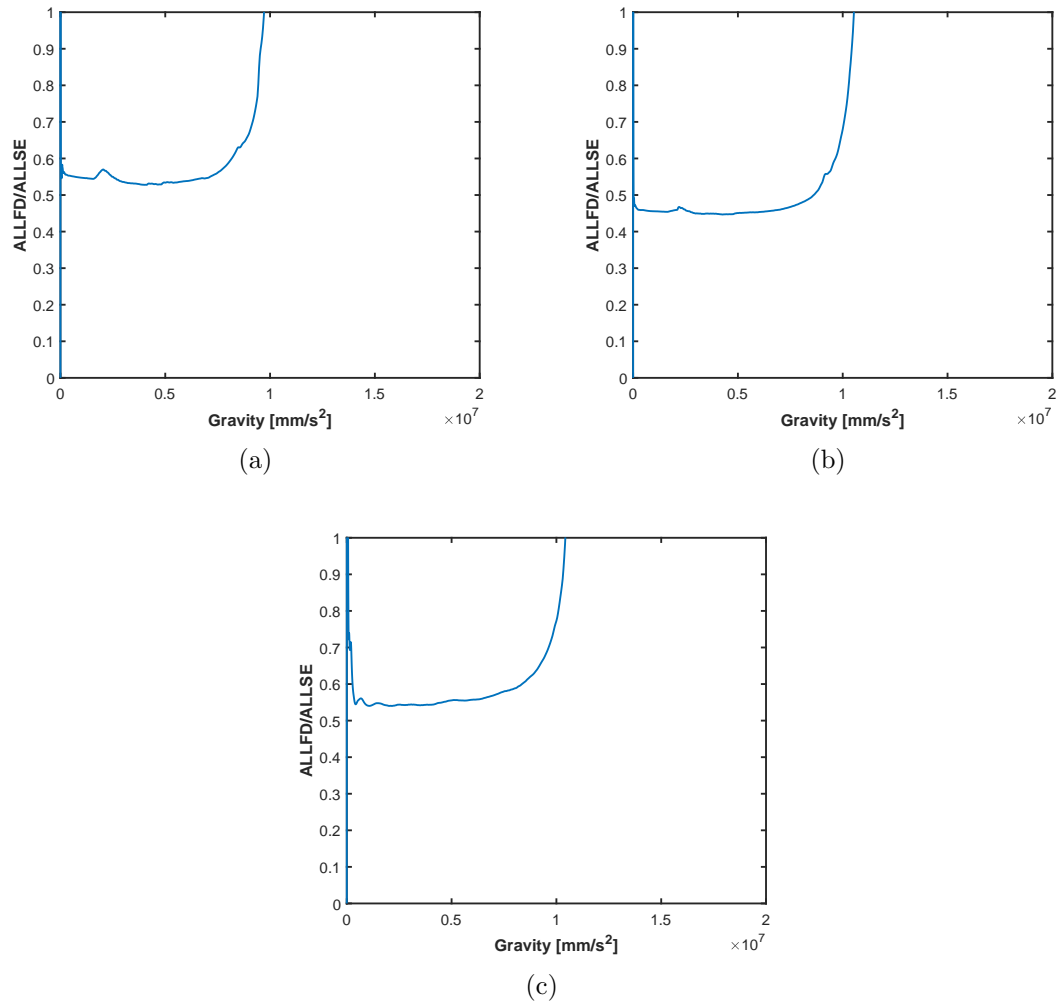


Figure 4.9. Slip ratio under gravity loading for (a) [3.4.6.4]-A, (b) [3.4.6.4]-B, (c) [3.4.6.4]-C.

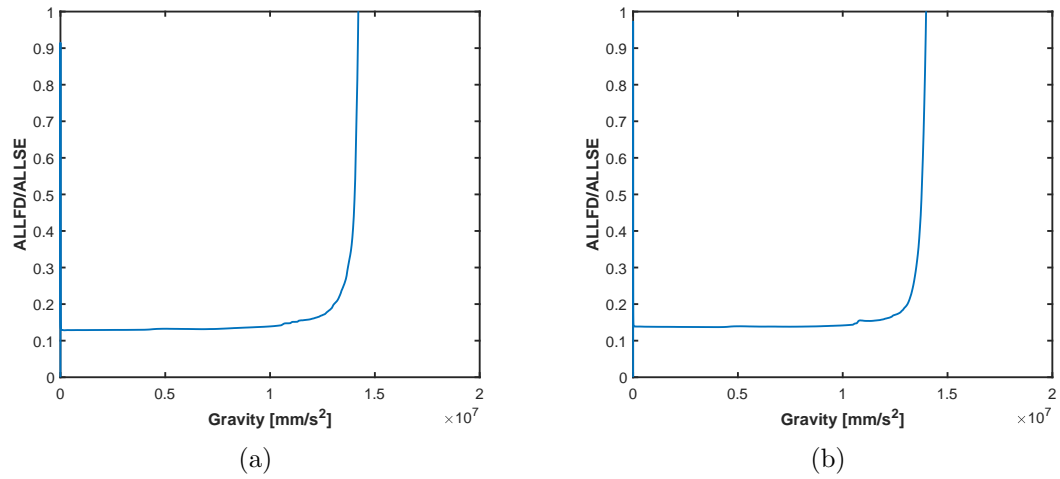


Figure 4.10. Slip ratio under gravity loading for (a) $[3^6]$ -A, (b) $[3^6]$ -B.

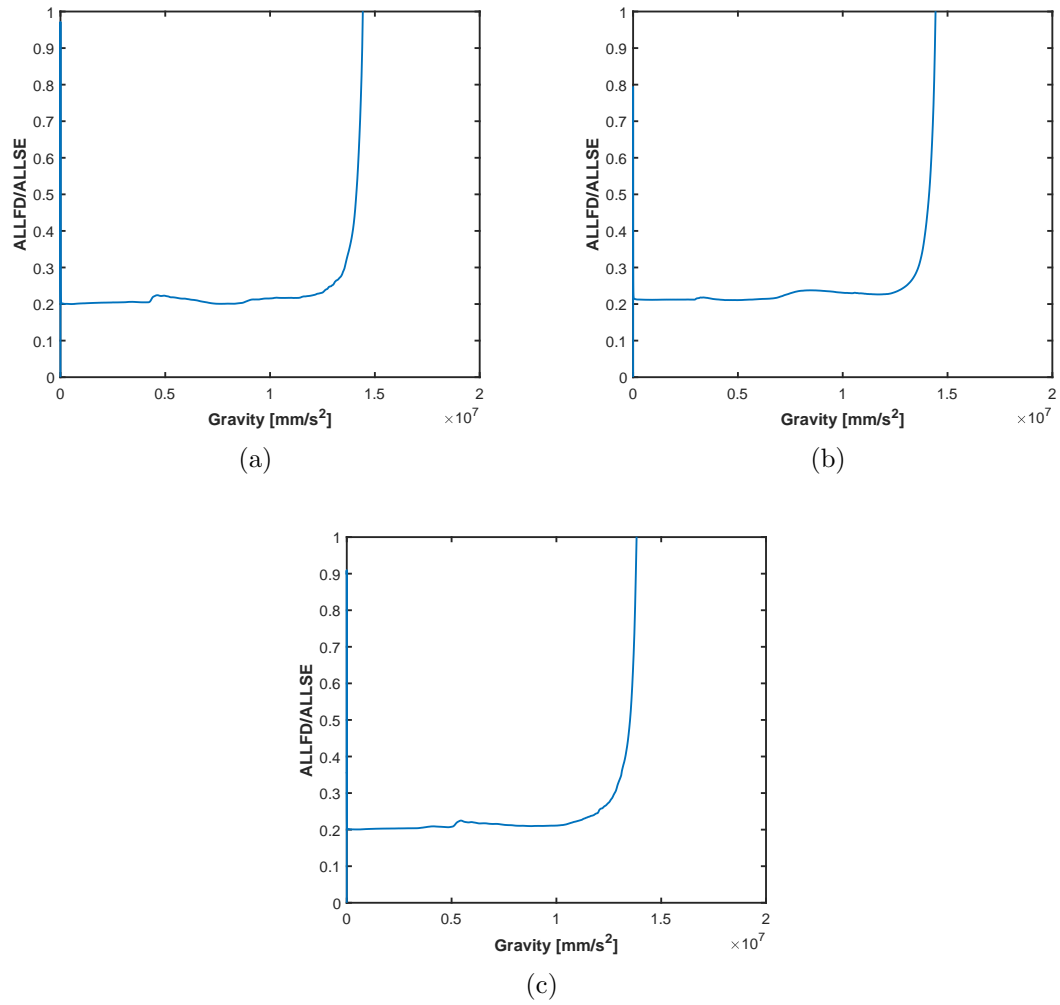


Figure 4.11. Slip ratio under gravity loading for (a)(4.8²)-A(-), (b) (4.8²)-A(+), (c) (4.8²)-B.

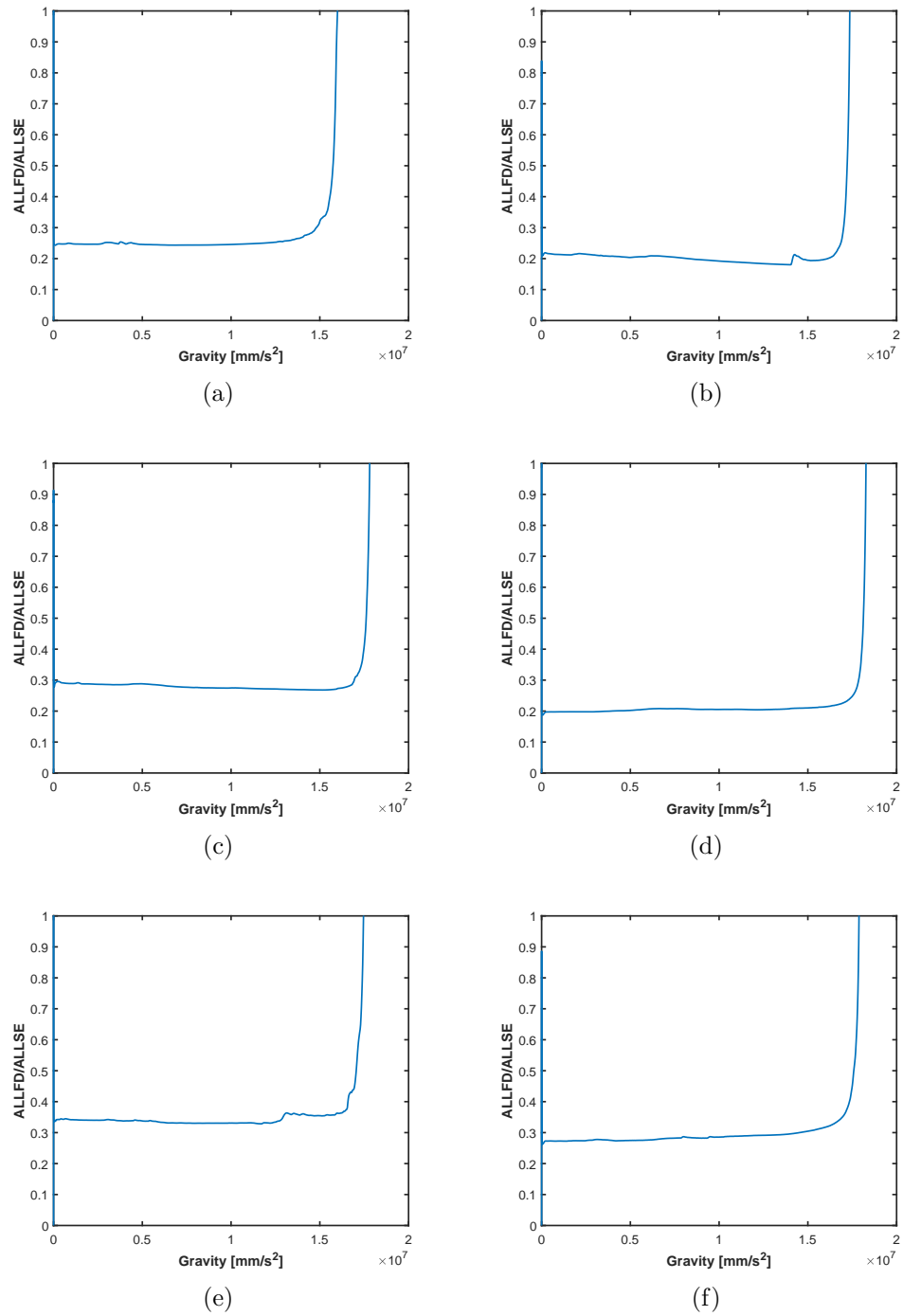


Figure 4.12. Slip ratio under gravity loading for (a) (4.6.12)-A(-), (b) (4.6.12)-A(+), (c) (4.6.12)-B(-), (d) (4.6.12)-B(+), (e) (4.6.12)-C(-), (f) (4.6.12)-C(+).

4.3 Analysis of the System Internal Load Transfer

Vector plots of the compressive stresses throughout each assembly under a gravity load of $5,000 \text{ m/s}^2$ are presented in this section, Figures 4.13 - 4.30.

The $[4^4]$ -A and $[4^4]$ -B configurations are shown in Figures 4.13 and 4.14. The stress fields are of more uniform magnitude than the displacement loading, and the triangle patterns of higher stress are no longer visible, but the select tiles along the frame still have higher stress than their neighbors. The chirality of the $[4^4]$ -B configuration can be seen in the higher stress tiles at the frame. In both configurations the stress vectors appear randomly aligned except at near the frame in which case they are perpendicular to it.

The $[3.6.3.6]$ -A and $[3.6.3.6]$ -B configurations are shown in Figures 4.15 and 4.16. These still do not have any well defined thrust lines. The tendency for stress vectors to follow the dual tessellation is more clearly evident here with the vectors generally being perpendicular to the nearest tile edge. This trend is made more clear by the increase in higher magnitude stresses occurring at the tile edges, particularly in the center of the assemblies that was previously obscured by the indenter. Chirality is still evident but is not as strongly indicated.

Vector plots for the $[3.4.6.4]$ -A, $[3.4.6.4]$ -B, and $[3.4.6.4]$ -C configurations are presented in Figures 4.17 - 4.19. Similar to the $[3.6.3.6]$ -A and $[3.6.3.6]$ -B configurations, these show a higher tendency for the stress vectors to align perpendicular to the nearest tile edge following the dual tessellation, while no well defined thrust lines have developed. The chirality in these configurations is more clearly evident from the increased stress in certain blocks along the frame, rather than by the patterns of blocks within the assembly for the displacement loading cases.

The stress fields for the $[3^6]$ -A and $[3^6]$ -B configurations under gravity load, Figures 4.20 and 4.21, are very similar to those under displacement loading, but there is more tendency for the stresses to align with the dual tessellation around the center of the assembly which was previously distorted by the indenter. Additionally the

stress rings around the center are less prominent. The major thrust lines in both configuration are visible, but the minor thrust lines from displacement loading are less not as noticeable, if even present.

Like the $[3^6]$ -A and $[3^6]$ -B configurations, the (4.8^2) -A(-), (4.8^2) -A(+), and (4.8^2) -B configurations, Figures 4.22 - 4.24, resemble their displacement loading counterparts with less distortion at the center of the assembly. The greatest differences from the displacement loading occur in the (4.8^2) -B configuration which lacks many of the local stress increases occurring at the tile edges throughout the assembly, however, the stress patterns at tiles along the frame are consistent.

The $(4.6.12)$ -A(-), $(4.6.12)$ -A(+), $(4.6.12)$ -B(-), $(4.6.12)$ -B(+), $(4.6.12)$ -C(-), and $(4.6.12)$ -C(+) configurations are shown in Figures 4.25 - 4.30. These also bear a strong resemblance to their displacement loading counterparts, with less distortion occurring near the center. In fact, there are so few apparent differences that it is not worth discussing here.

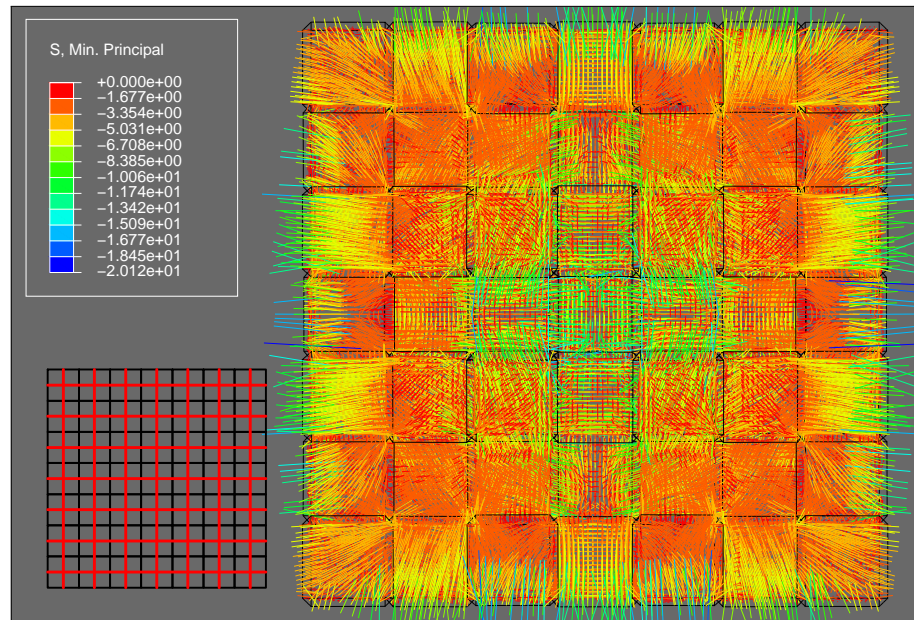


Figure 4.13. Vector plot of minimum principal stress [MPa] for the $[4^4]$ -A configuration under gravity load. The dual tessellation is depicted.

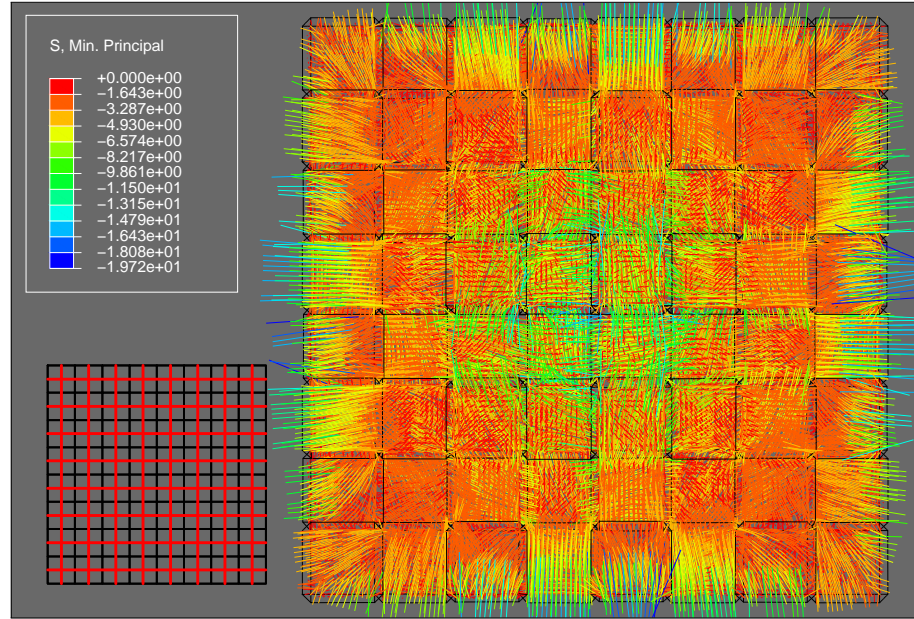


Figure 4.14. Vector plot of minimum principal stress [MPa] for the [4⁴]-B configuration under gravity load. The dual tessellation is depicted.

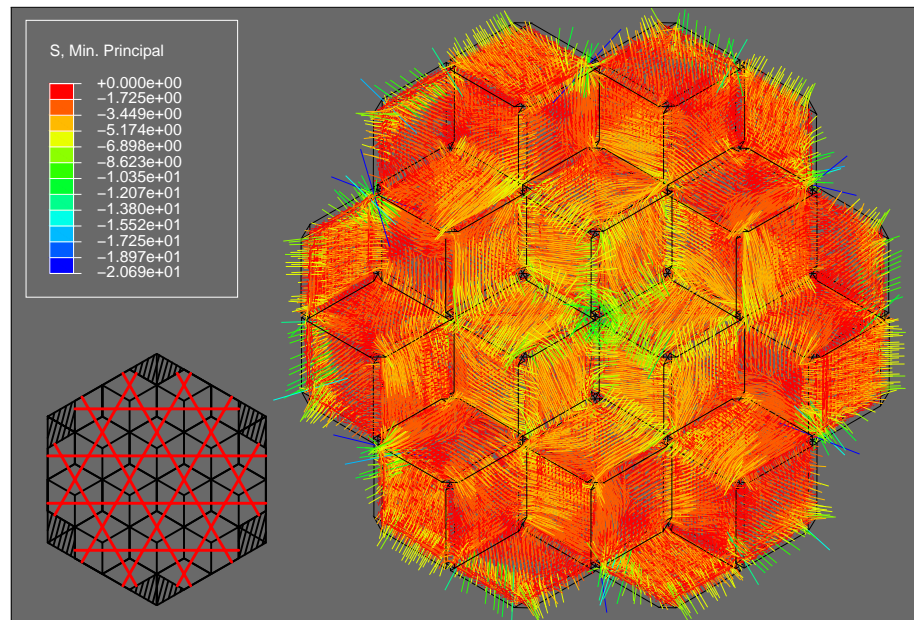


Figure 4.15. Vector plot of minimum principal stress [MPa] for the [3.6.3.6]-A configuration under gravity load. The dual tessellation is depicted.

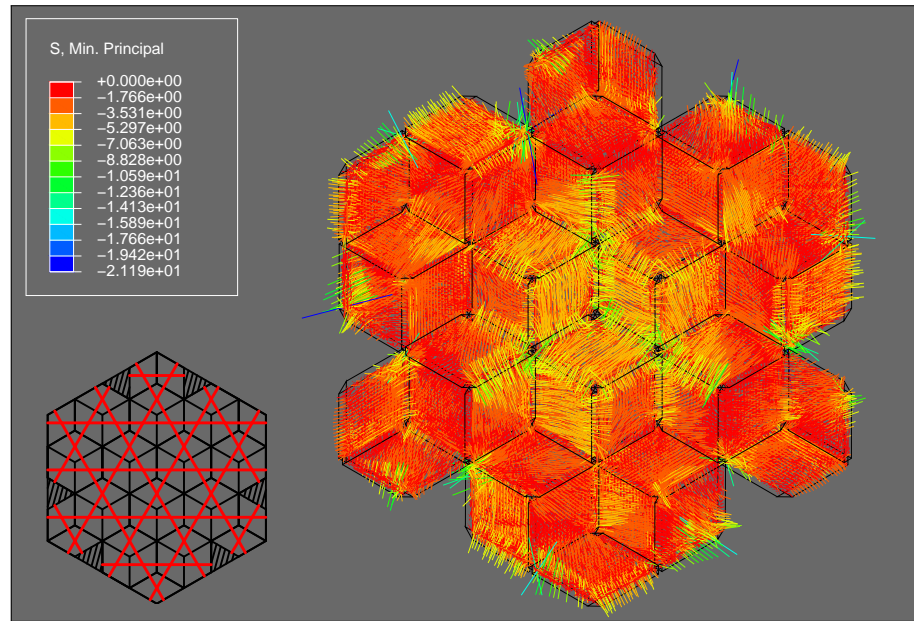


Figure 4.16. Vector plot of minimum principal stress [MPa] for the [3.6.3.6]-B configuration under gravity load. The dual tessellation is depicted.

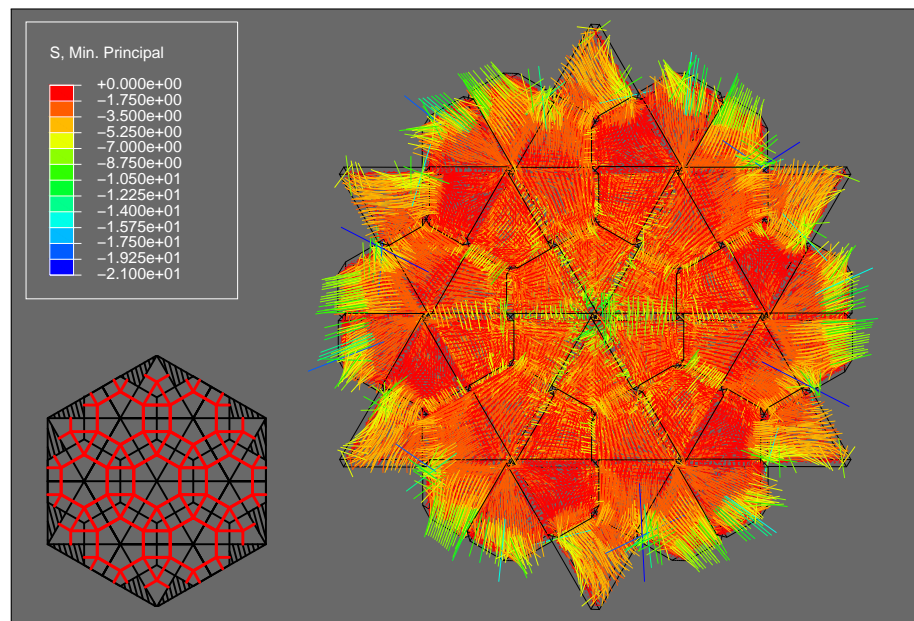


Figure 4.17. Vector plot of minimum principal stress [MPa] for the [3.4.6.4]-A configuration under gravity load. The dual tessellation is depicted.

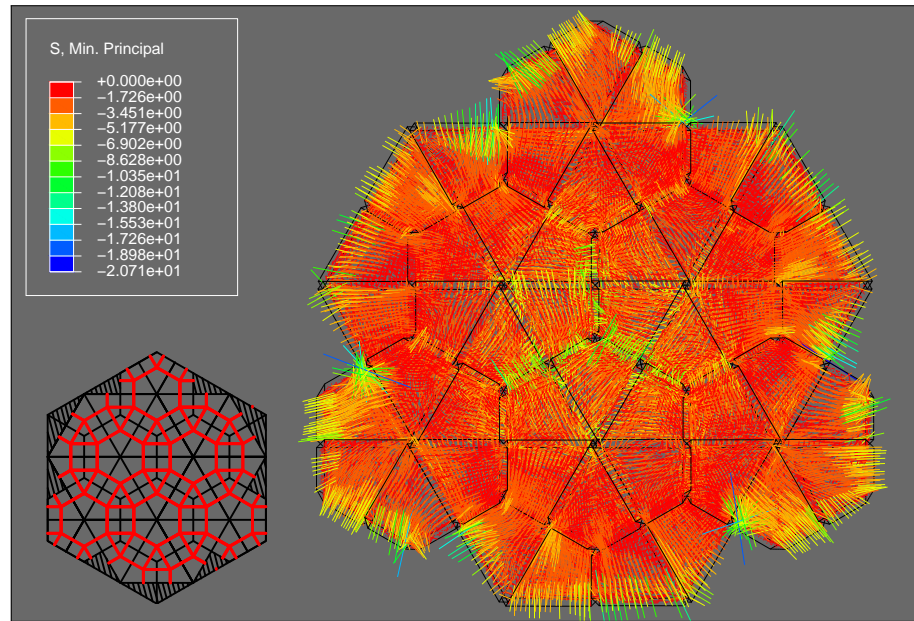


Figure 4.18. Vector plot of minimum principal stress [MPa] for the [3.4.6.4]-B configuration under gravity load. The dual tessellation is depicted.

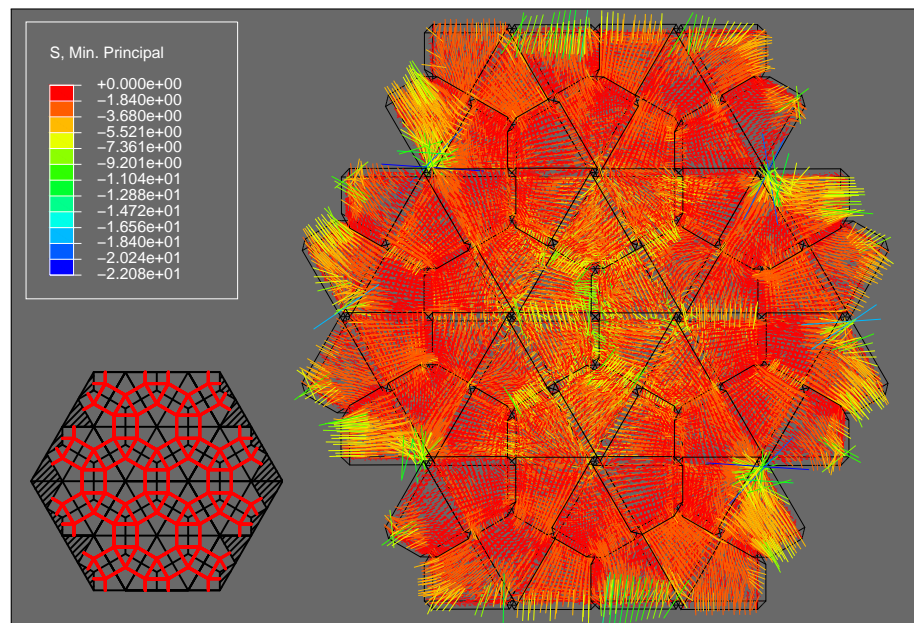


Figure 4.19. Vector plot of minimum principal stress [MPa] for the [3.4.6.4]-C configuration under gravity load. The dual tessellation is depicted.

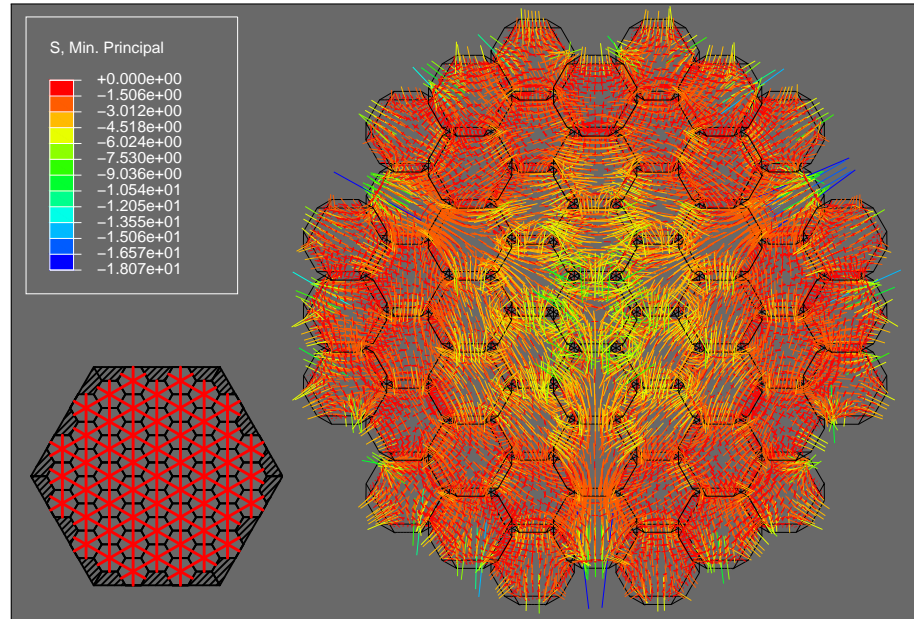


Figure 4.20. Vector plot of minimum principal stress [MPa] for the $[3^6]$ -A configuration under gravity load. The dual tessellation is depicted.

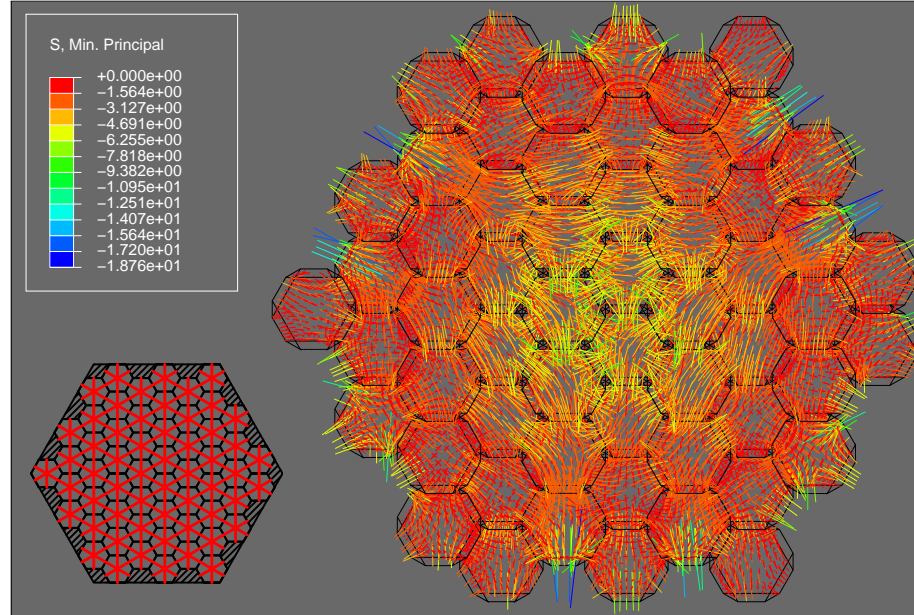


Figure 4.21. Vector plot of minimum principal stress [MPa] for the $[3^6]$ -B configuration under gravity load. The dual tessellation is depicted.

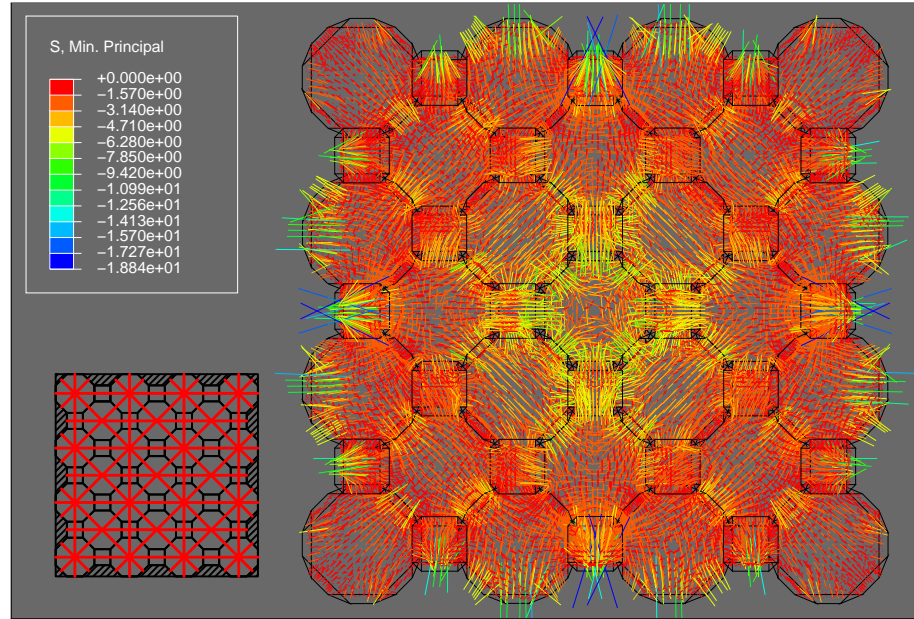


Figure 4.22. Vector plot of minimum principal stress [MPa] for the (4.8^2) -A(-) configuration under gravity load. The dual tessellation is depicted.

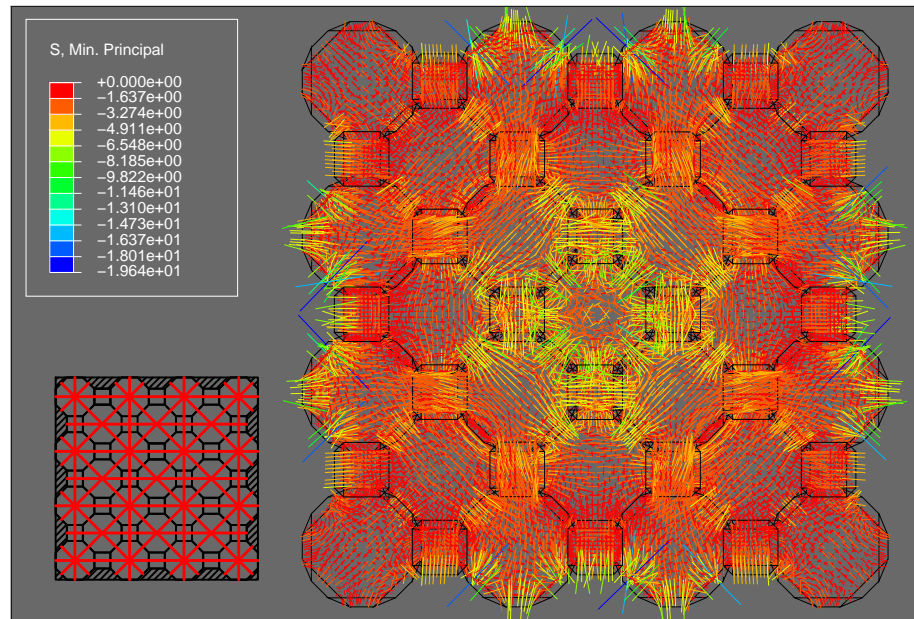


Figure 4.23. Vector plot of minimum principal stress [MPa] for the (4.8^2) -A(+) configuration under gravity load. The dual tessellation is depicted.

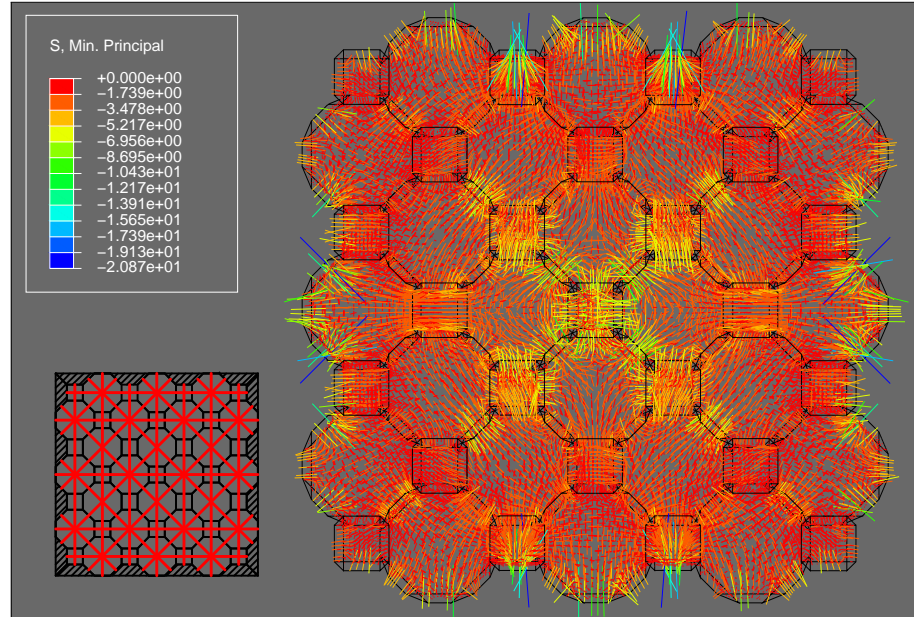


Figure 4.24. Vector plot of minimum principal stress [MPa] for the (4.8^2) -B configuration under gravity load. The dual tessellation is depicted.

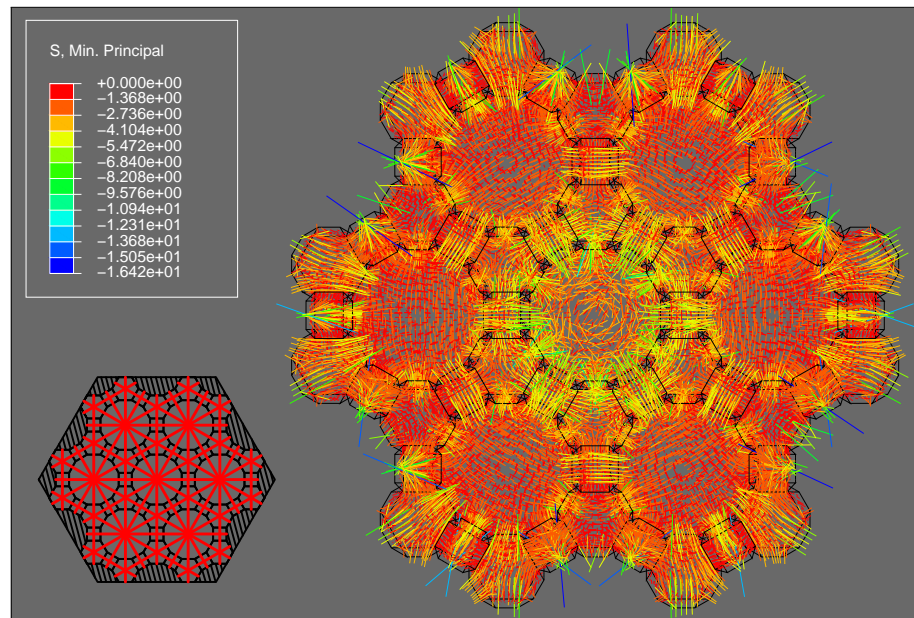


Figure 4.25. Vector plot of minimum principal stress [MPa] for the $(4.6.12)$ -A(-) configuration under gravity load. The dual tessellation is depicted.

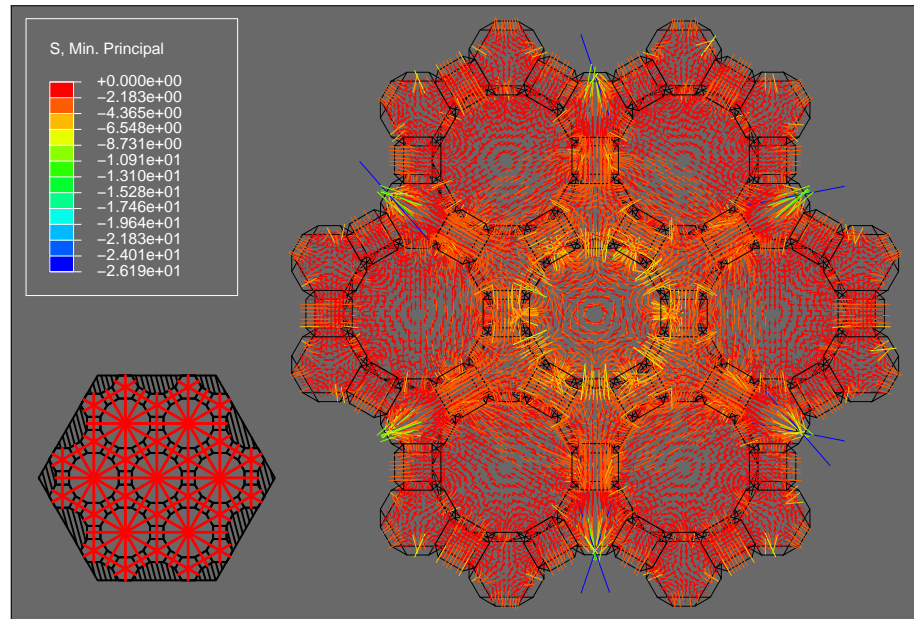


Figure 4.26. Vector plot of minimum principal stress [MPa] for the (4.6.12)-A(+) configuration under gravity load. The dual tessellation is depicted.

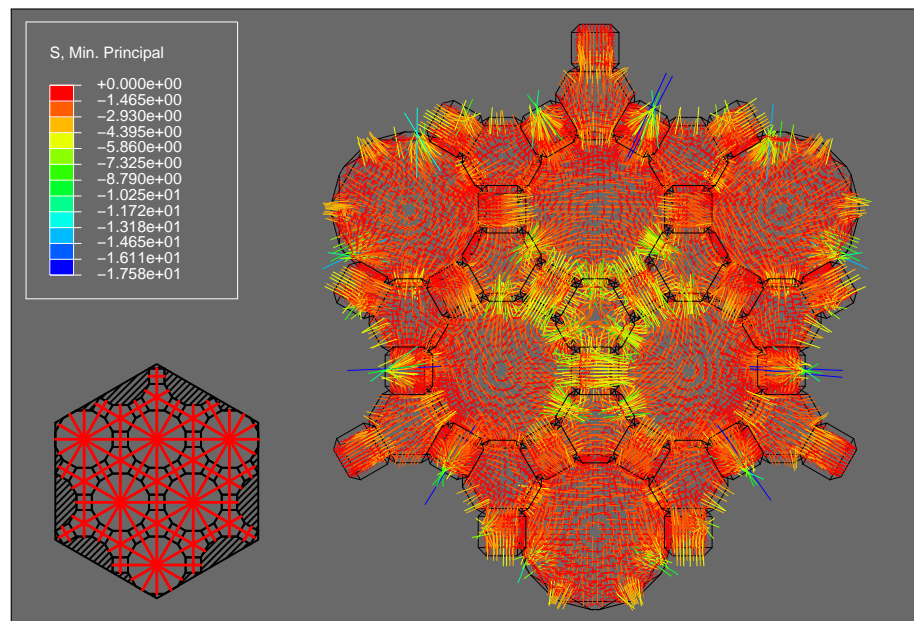


Figure 4.27. Vector plot of minimum principal stress [MPa] for the (4.6.12)-B(-) configuration under gravity load. The dual tessellation is depicted.

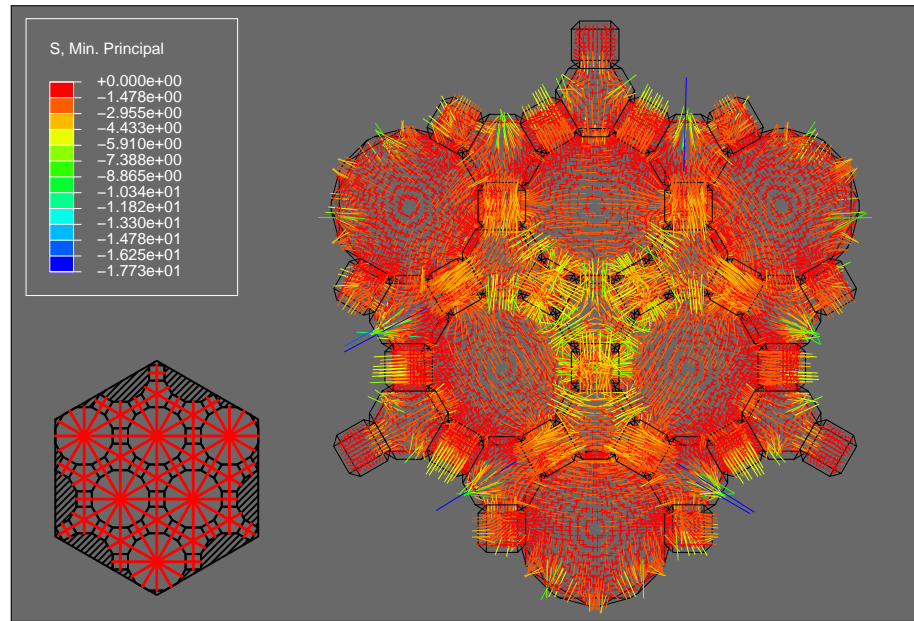


Figure 4.28. Vector plot of minimum principal stress [MPa] for the (4.6.12)-B(+) configuration under gravity load. The dual tessellation is depicted.

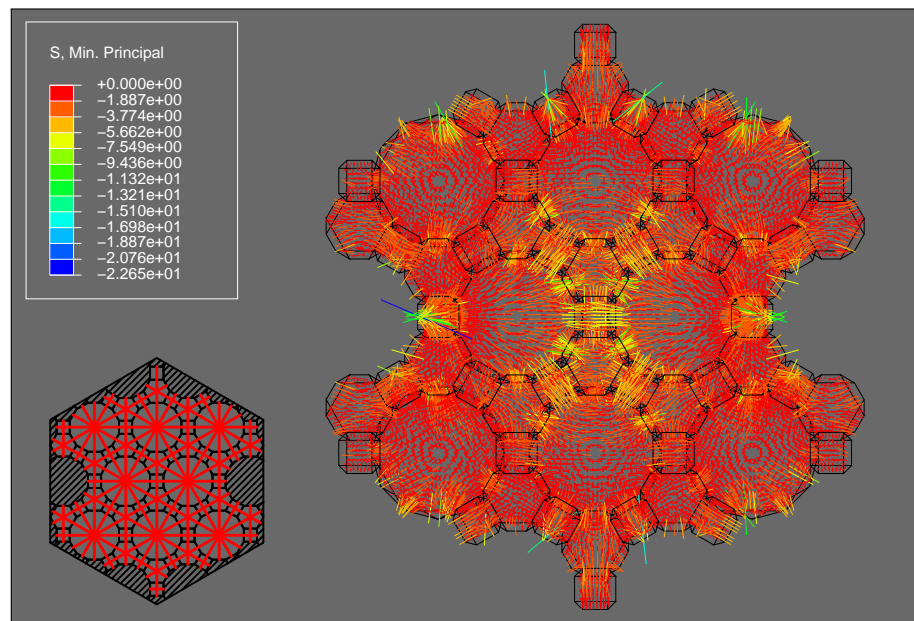


Figure 4.29. Vector plot of minimum principal stress [MPa] for the (4.6.12)-C(-) configuration under gravity load. The dual tessellation is depicted.

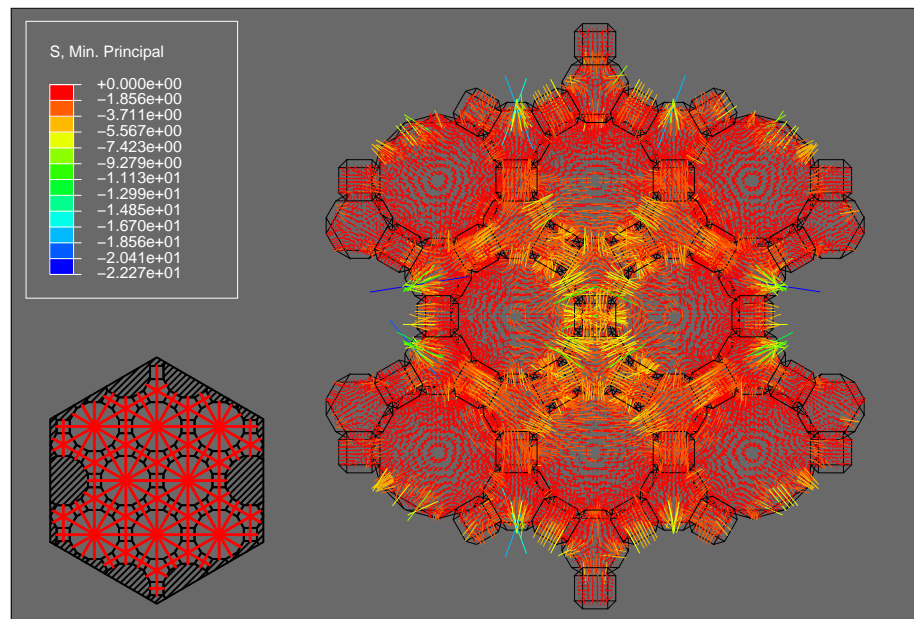


Figure 4.30. Vector plot of minimum principal stress [MPa] for the (4.6.12)-C(+) configuration under gravity load. The dual tessellation is depicted.

5. DISCUSSION

There was a wide range in performance of the TIM system configurations in this study. This chapter will discuss the order of performance of the TIM systems and investigate possible influences on their performance.

5.1 Cross Property Relationships

This section contains cross property plots containing data from all configurations considered. A consistent legend notation is used in all correlation plots, Figure 5.1. The coefficient of determination R^2 of the linear best fit line computed for the data set is given, and a unique symbol for each configuration is used. All configurations based on the same tiling have the same color symbol, and all configurations exhibiting chirality are denoted by an unfilled symbol. Both load directions are shown for non-reciprocal assemblies. Select data is provided in Table C.1.

Strength and stiffness were very well correlated, Figure 5.1. This is consistent with monolithic materials, in which strength and the elastic modulus are well correlated [19], and with Mises trusses, in which strength and stiffness are related. It is also intuitive given that there was not as large a variation in the displacement at failure as in the strength. Final failure for most configurations occurred at a deflection of 2.0 - 2.5 times the assembly thickness, but the strengths varied threefold from about 400 to 1200 N. This results in a vertical scaling of the skewed parabola force-deflection response in which the stiffness and strength vary while the deflection does not. This is consistent with the response of a Mises truss having fixed dimensions and varying stiffness.

Toughness and stiffness were positively correlated, Figure 5.2, as were toughness and strength, Figure 5.3. These positive correlations are some of the desirable char-

acteristics of TIM systems. Traditional monolithic materials decrease in toughness as their strength and elastic modulus are increased [19], but TIM systems allow these properties to be coupled.

It was hypothesized that the onset of slip dominance in a TIM system would be an indicator of the performance of the system on the basis that if a system could more readily slide it would have a lower stiffness. This turned out to be partially true. Configurations in which the onset of slip dominance occurred at greater deflections did in general have higher stiffness, but it was a weak correlation having a coefficient of determination of only $R^2 = 0.43$, Figure 5.4.

Under gravity loading, the slip ratio ALLFD/ALLSE was approximately constant up to the point of failure. This was an interesting finding, and it was hypothesized that this would be an intrinsic property of each system indicating its dependence on sliding. However, this also failed to accurately predict the stiffness of a system, Figure 5.5

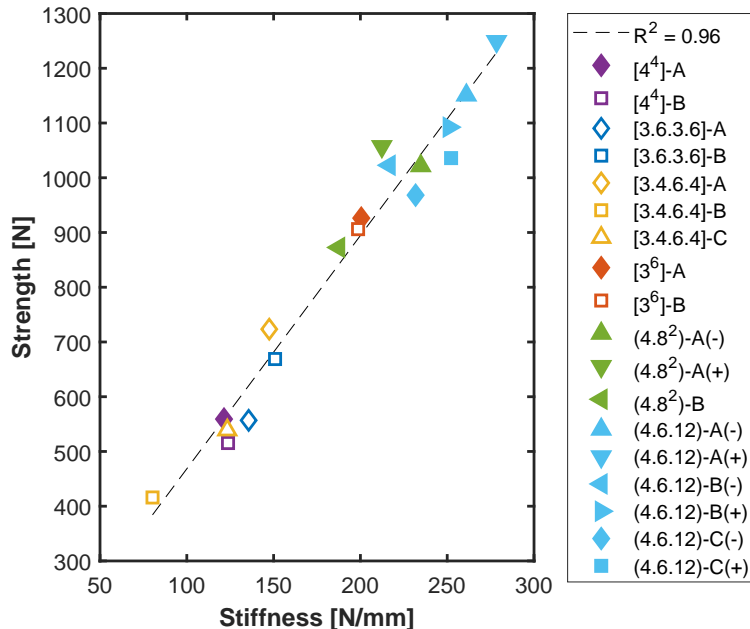


Figure 5.1. Strength and stiffness cross property correlation.

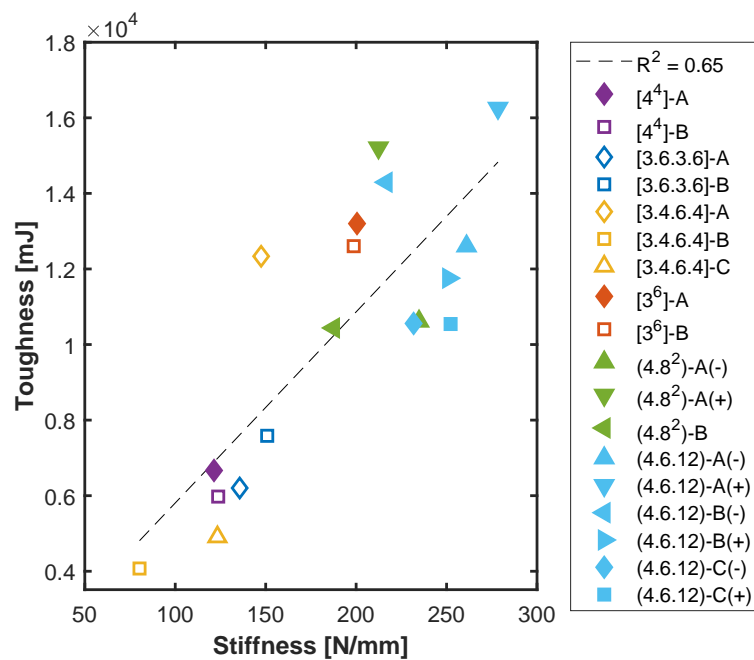


Figure 5.2. Toughness and stiffness cross property correlation.

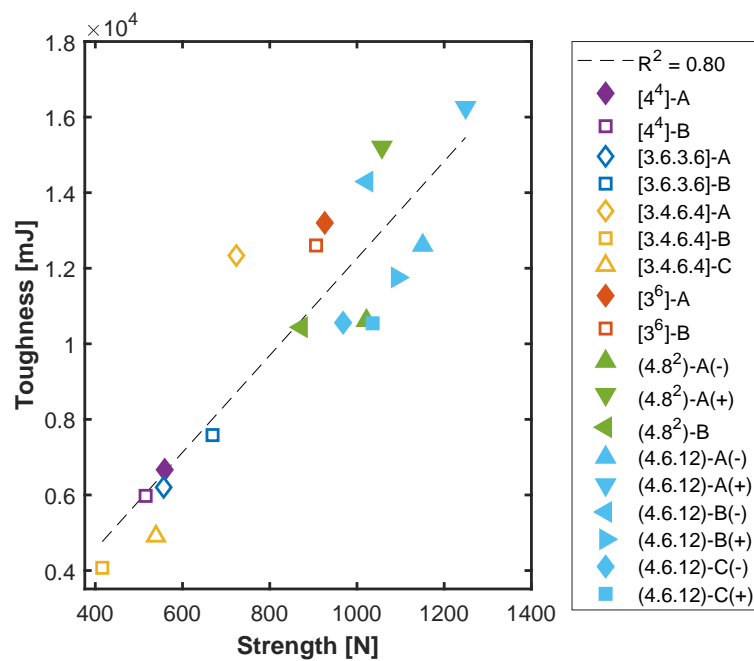


Figure 5.3. Toughness and strength cross property correlation.

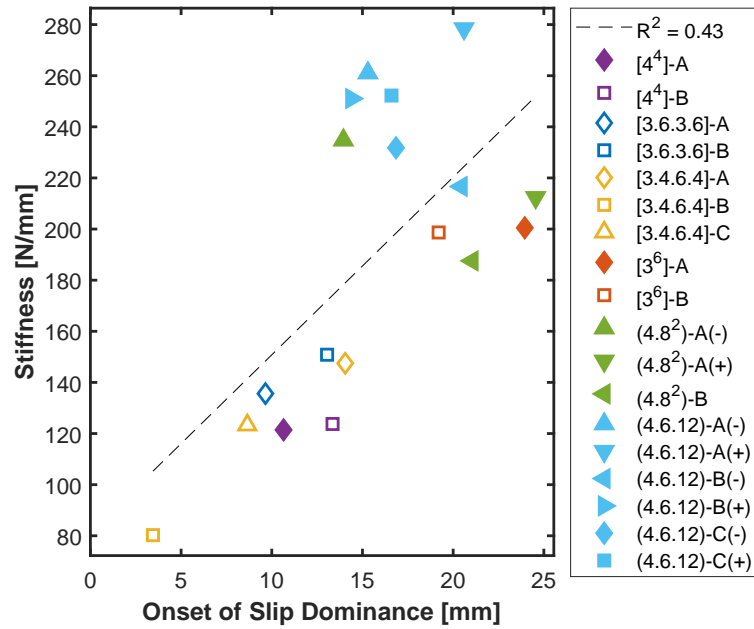


Figure 5.4. Stiffness and onset of slip dominance cross property correlation.

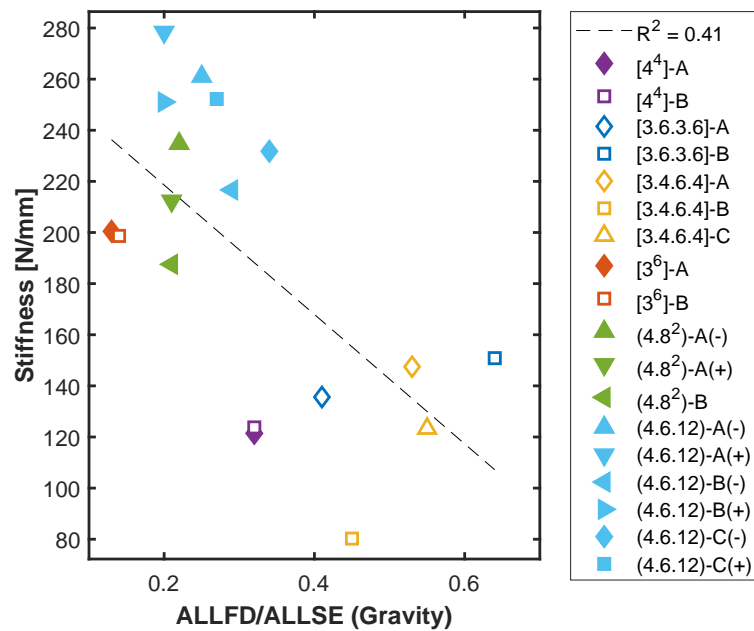


Figure 5.5. Stiffness and the constant slip ratio value from gravity loading.

5.2 Strength Correlations with Architecture

The configuration strength was correlated against a number of architectural aspects in order to find predictors of the performance of the various TIM systems, Figures 5.6 - 5.10, Table C.2. Strength was well correlated with both stiffness and toughness, so if a strength predictor could be found it would also predict stiffness and toughness. To start, the strength was correlated against the number of tiles in the tiling from which each TIM system was constructed, Figure 5.6. It was desired that there not be a correlation here so that scaling effects based on the number of tiles would not be an influence. With a coefficient of determination $R^2 = 0.02$, this goal was met.

The strongest predictor of strength was the total contact area between all segmented bodies in the assembly, Figure 5.7. This value was computed in the assembly's initial position before any displacement had occurred. Smaller values of total contact area predicted higher strength. This suggests that the less segmented a structure is, the greater its strength will be which agrees with the fact that a monolithic plate is generally stronger than its segmented counterparts.

Following the above finding, the strength was correlated against the number of contact interfaces, Figure 5.8, where a contact interface is defined as a state of contact between any two bodies in the segmented assembly. This correlation shows a trend that increasing the number of contact interfaces increases the strength. This would appear to suggest, in disagreement with the previous finding, that increasing the amount of segmentation would increase the strength. However, the total contact area and number of contact interfaces are not equivalent measures of segmentation. This suggests a greater dependence on how the system is segmented rather than how much it is segmented. One way to increase the number of contact interfaces is to increase the number of blocks, but the TIM systems in this study all had approximately the same number of blocks. Therefore, the number of contact interfaces must be altered without changing the number of blocks. This can be done by utilizing blocks with a greater

number of sides, which would increase the number of contact interfaces. This might describe the gap in strength that is seen between the weakest configurations, which are all based on tessellations with a single four-sided tile, and the other configurations which have larger tiles with more sides.

The strength is correlated against the area of the largest tile in the tiling from which each TIM system was constructed in Figure 5.9. The strength is positively correlated with the largest tile area which does support the previous conjecture that TIM systems with larger blocks would be stronger, but with a coefficient of determination $R^2 = 0.52$ it is not a strong correlation. Given that the bounded tilings in this study all have approximately the same number of tiles and about the same total area, if there are larger tiles in a tiling, it must also have some smaller tiles. The strength is correlated against the area of the smallest tile in the tiling from which each TIM system was constructed in Figure 5.10. This is a stronger correlation with a coefficient of determination $R^2 = 0.73$ and suggests that the smallest tile size is a better predictor of strength than the largest tile size.

Clearly the strength of a TIM system is a complicated matter and is likely a function of many factors, but the findings here suggest that the strongest TIM systems are the ones with the least total contact area, the greatest number of contact interfaces, and the smallest tiles. This combination of characteristics leads to the conclusion that TIM system configurations having architectures that constrict load transfer into well defined thrust lines have the greatest strength. This is supported by the finding that the TIM configurations based on the $[3^6]$, (4.8^2) , and $(4.6.12)$ tilings were the strongest and all had well defined thrust lines visible in their compressive stress vector plots.

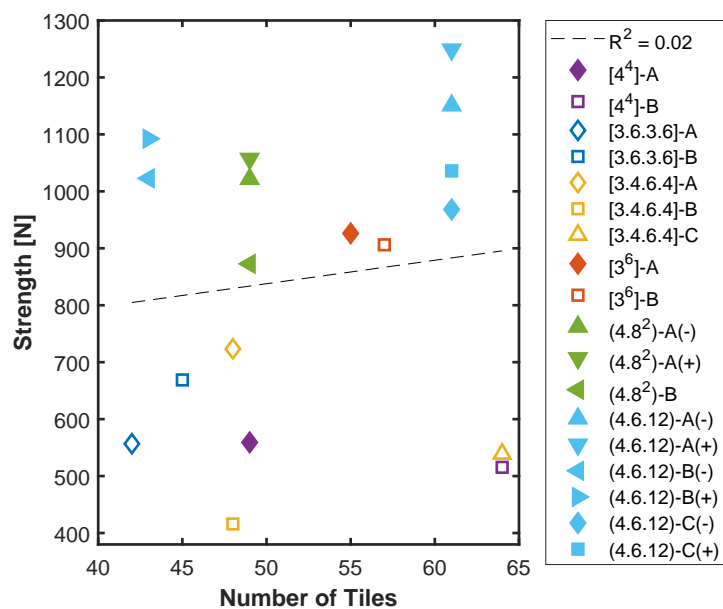


Figure 5.6. Strength vs number of tiles in the base tiling.

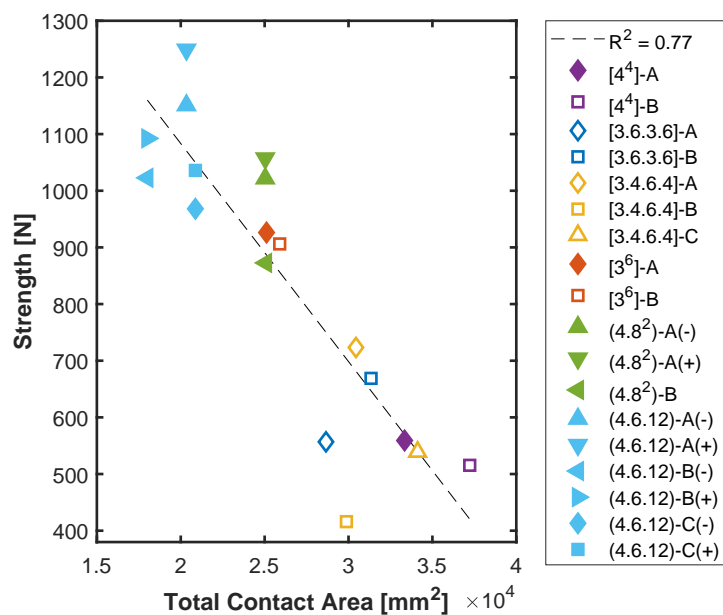


Figure 5.7. Strength vs total contact area between segmented bodies.

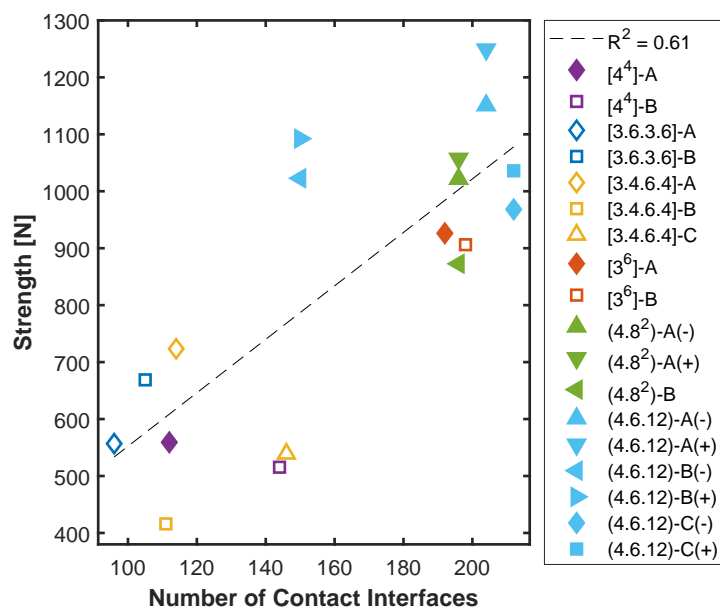


Figure 5.8. Strength vs number of contact interfaces between segmented bodies.

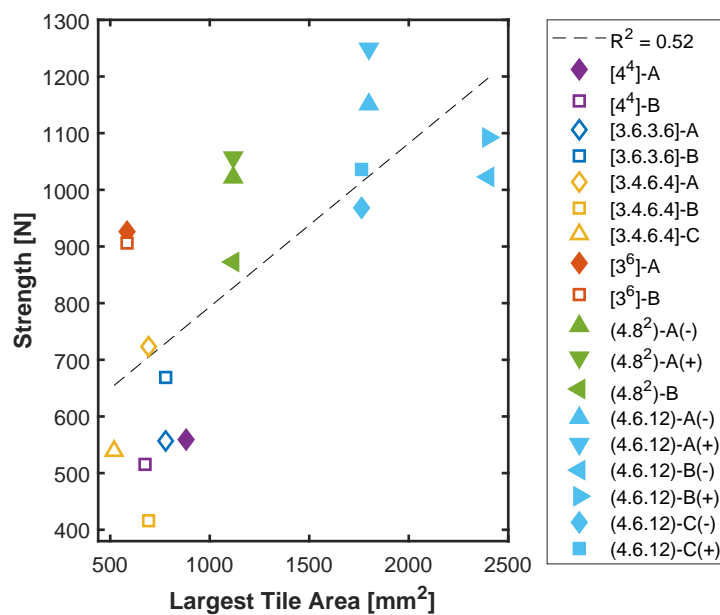


Figure 5.9. Strength vs area of the largest tile in the base tiling.

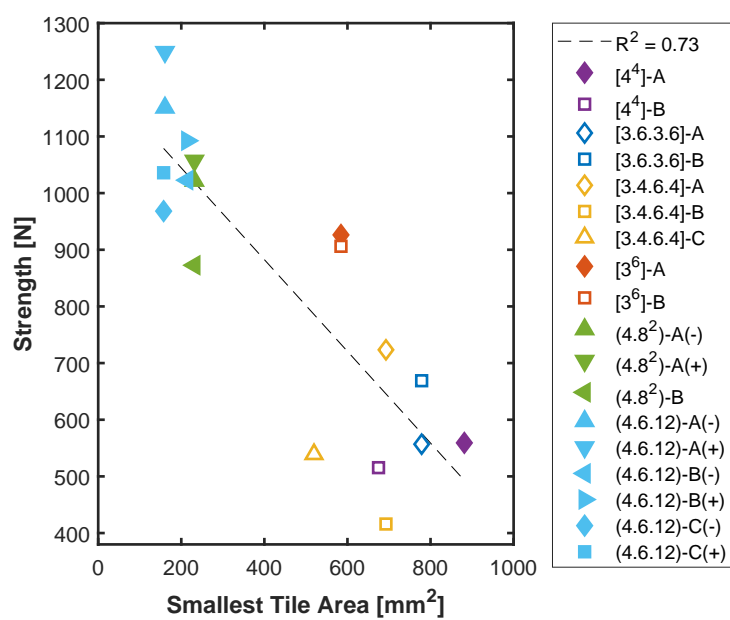


Figure 5.10. Strength vs area of the smallest tile in the base tiling.

5.3 Chirality

Chiral lengths, defined as the reaction moment divided by the reaction force, are shown for all configurations exhibiting chirality, Figures 5.11 - 5.13. This includes the $[4^4]$ -B, $[3.6.3.6]$ -A, $[3.6.3.6]$ -B, $[3.4.6.4]$ -A, $[3.4.6.4]$ -B, $[3.4.6.4]$ -C, and $[3^6]$ -B configurations. The $[4^4]$ -A, $[3^6]$ -A, (4.8^2) -A(-), (4.8^2) -A(+), (4.8^2) -B, $(4.6.12)$ -A(-), $(4.6.12)$ -A(+), $(4.6.12)$ -B(-), $(4.6.12)$ -B(+), $(4.6.12)$ -C(-), and $(4.6.12)$ -C(+) configurations did not exhibit chirality. The magnitude of the chiral length peaked at about 1.5 mm for all chiral configurations. This suggests that its maximum magnitude is independent of the tiling and perhaps dependent on factors.

It was determined that all configurations which were centered on a tile vertex, rather than in the middle of a tile were chiral. As such, the $[4^4]$ and $[3^6]$ based configurations both had one configuration that was chiral, and one configuration that was non-chiral. This begs the question of how would a configuration such as $[4^4]$ -A respond if it was loaded off center on a tile vertex, or if the $[4^4]$ -B configuration was loaded on off center on the middle of a tile? This question is not answered in this work, but there is potential for an assembly to be selectively chiral depending on where it is loaded.

The $[3.6.3.6]$ and $[3.4.6.4]$ based configurations showed the capability for the chirality to change direction based on the specific configuration. The definition of chirality is that an object cannot be overlaid on its mirror image. It follows that for any configuration exhibiting chirality in one direction, its mirror image would be chiral in the other direction. It is therefore trivial to design a particular configuration with a particular chiral direction. However, the configurations in this study, such as the $[3.6.3.6]$ -A and $[3.6.3.6]$ -B configurations, are not mirrors of each other, they have the same block orientations but are bounded differently. This leads to the question of how one such configuration would respond if it were loaded off center on the other tile vertex? Would the chirality change direction? And is chirality caused more by the position of the indenter or the frame? In the gravity loading cases, which have no

indenter, chirality can be seen in the stress fields as offset stress groupings along the frame, Figure 4.17, which would indicate that chirality is caused by the positioning of the frame, but when the indenter is used, there is also strong indication of chirality in tiles that are closer to the center of the assembly, Figure 3.23, which indicates that the indenter also plays a role. Further investigation is required to fully understand this phenomenon.

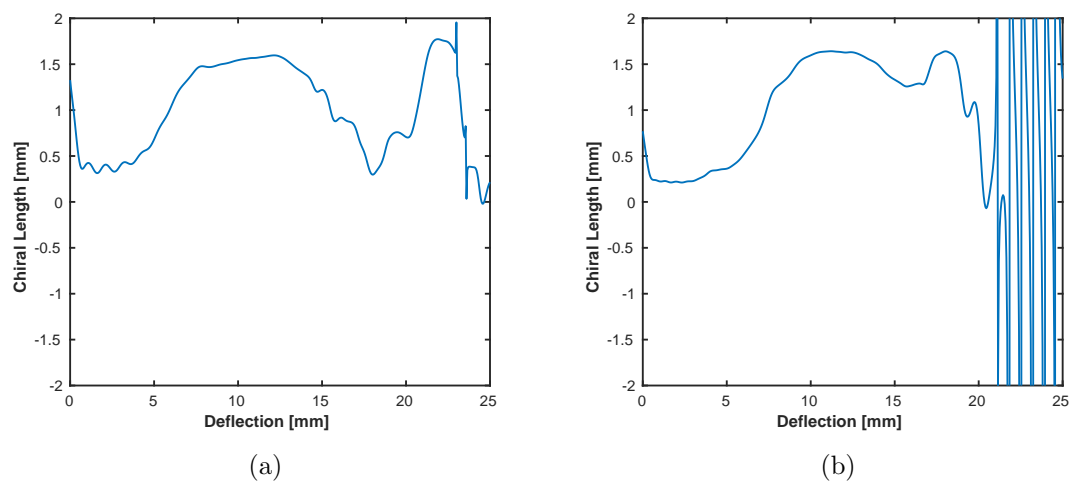


Figure 5.11. Chiral length vs deflection for (a) $[4^4]$ -B, (b) $[3^6]$ -B.

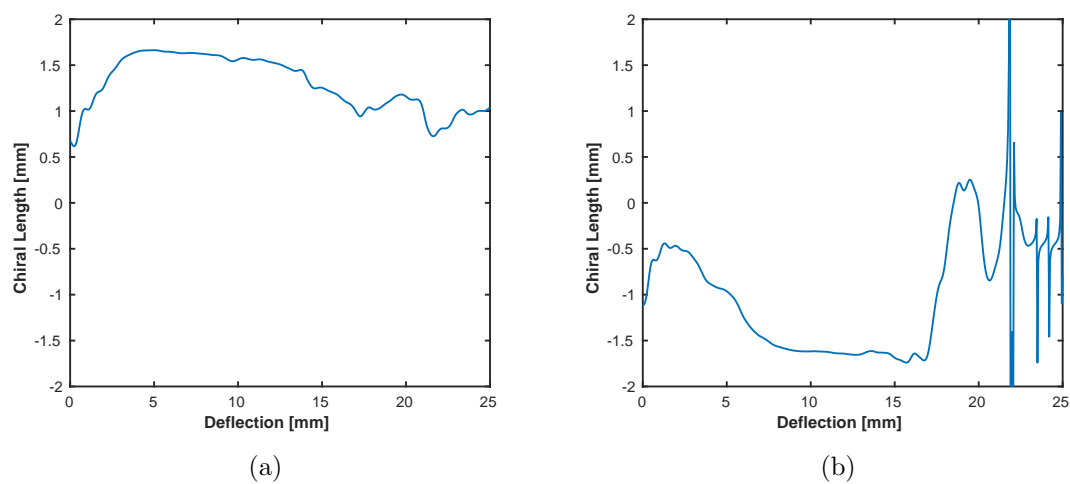


Figure 5.12. Chiral length vs deflection for (a) [3.6.3.6]-A, (b) [3.6.3.6]-B.

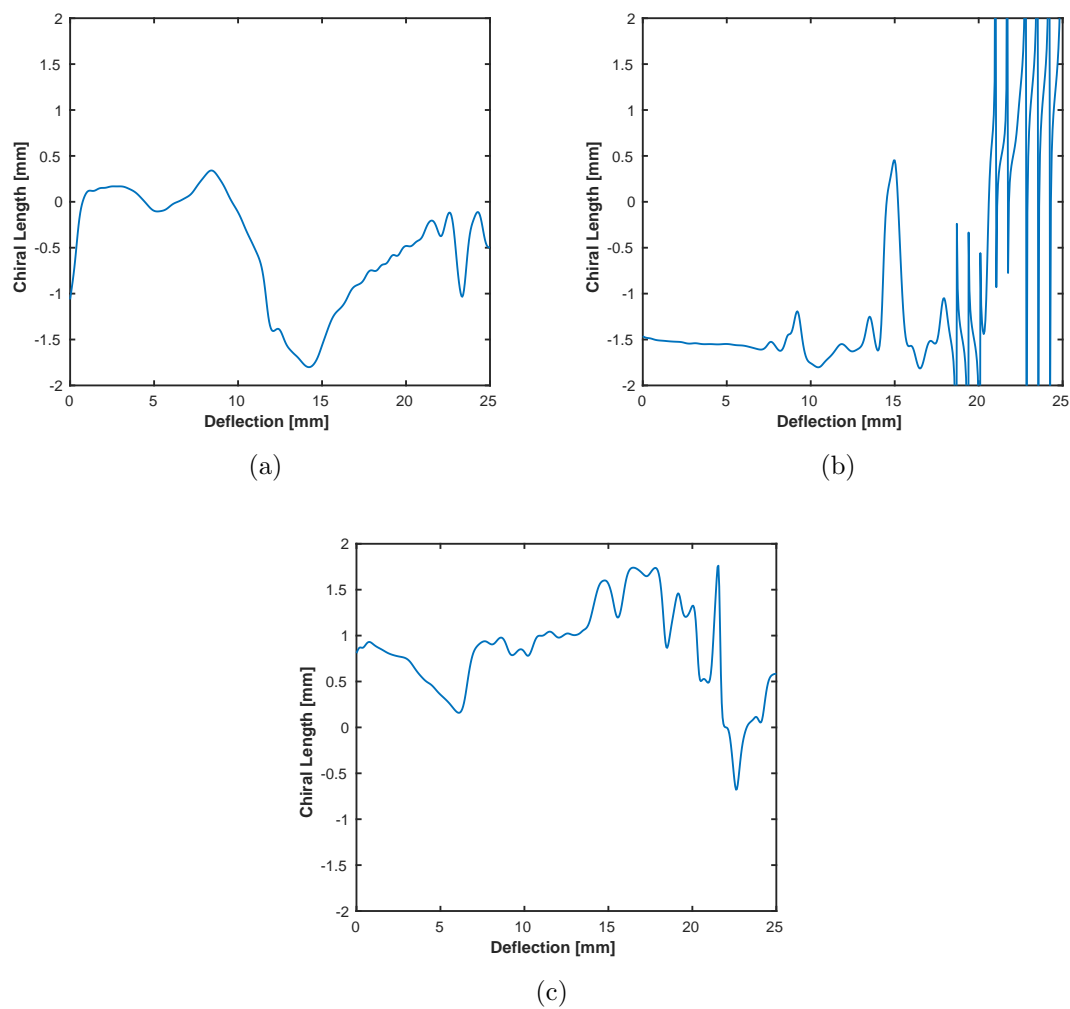


Figure 5.13. Chiral length vs deflection for (a) [3.4.6.4]-A, (b) [3.4.6.4]-B, (c) [3.4.6.4]-C.

5.4 Reciprocity of the Load Response

The force-deflection responses of the four non-reciprocal assemblies, (4.8^2) -A, $(4.6.12)$ -A, $(4.6.12)$ -B, and $(4.6.12)$ -C, are shown in Figures 5.14 and 5.15 with both load directions overlaid. The differences in the load response for each direction are not drastic, but they are significant. The (4.8^2) -B assembly is an example of an assembly that exhibits reciprocity, Figure 5.14(b). It has some negligible differences between the responses of the two load directions which are the result numerical variations. The largest difference is in the $(4.6.12)$ -A assembly in which the response to the $+Z$ load direction completely encompasses the response to the $-Z$ load direction, Figure 5.15(a). If greater asymmetry in the load response was required, the effect could be enhanced by methods such as using multiple materials or asymmetric truncation.

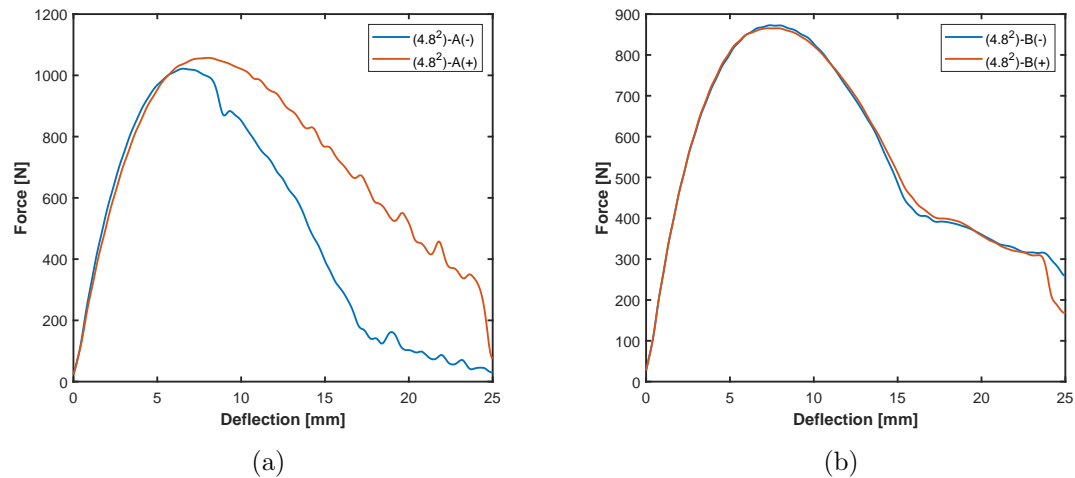


Figure 5.14. Reciprocity of force-deflection for assemblies based on the (4.8^2) tiling. (4.8^2) -A is non-reciprocal while (4.8^2) -B exhibits reciprocity. (a) (4.8^2) -A, (b) (4.8^2) -B.

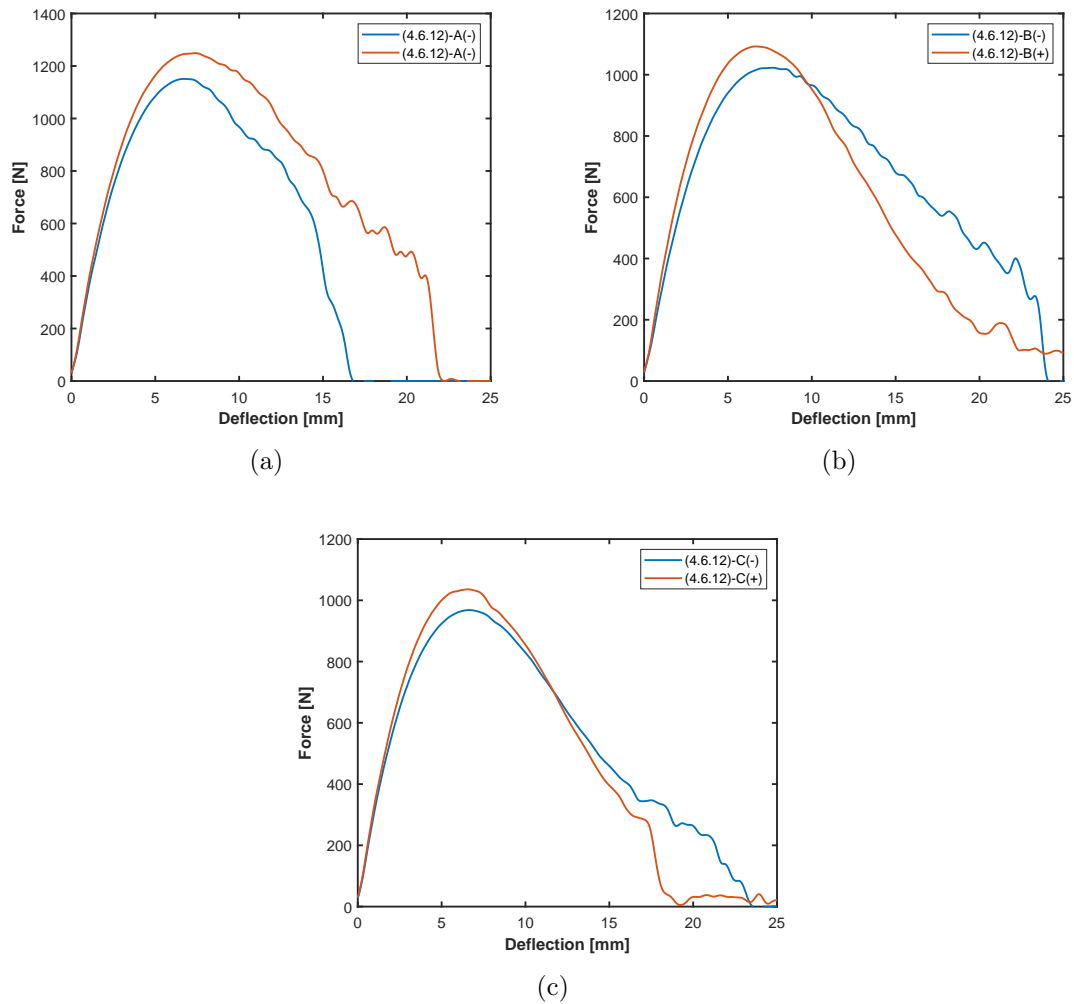


Figure 5.15. Reciprocity of force-deflection for assemblies based on the (4.6.12) tiling. All are non-reciprocal (a) (4.6.12)-A, (b) (4.6.12)-B, (c) (4.6.12)-C.

5.5 Effects of the Coefficient of Friction

In addition to the effects of architecture, the influence of the coefficient of friction on the load response of TIM systems was also considered. Detailed results are presented for a select few configurations, and aggregate results are shown for all configurations.

5.5.1 Detailed Effects of the Coefficient of Friction

This section looks at the effect of the coefficient of friction on the load response for four select configurations. The [3.4.6.4]-B, [3⁶]-B, (4.8²)-B, and (4.6.12)-A(+) configurations were chosen because they include the strongest, weakest, and mid-strength configurations. Additionally, both chiral and nonchiral configurations are represented, as well as at least one single-tile, dual-tile, and triple-tile configuration are included. The system energies and load response of each of these configurations with coefficients of friction $\mu = 0.2$, $\mu = 0.3$, and $\mu = 0.4$ are shown in Figures 5.16 - 5.23.

The influence of the friction coefficient on the [3.4.6.4]-B configuration is shown in Figures 5.16 and 5.17. This was the weakest configuration and was heavily sliding dominant with $\mu = 0.2$ as was evident from the sharp drops in the force-deflection curve and the high slip ratios throughout the simulations. Increasing the friction coefficient had a significant effect on this configuration. The reaction force values scale with the coefficient of friction approximately doubling from a maximum of about 450 N to a little over 900 N when μ changed from 0.2 to 0.4. Additionally, the sharp drops were smoothed out. The highest friction simulation was less sliding dominant as indicated by the lower slip ratios before the slip point. The reaction moments were affected even more increasing approximately six times in magnitude from $\mu = 0.2$ to $\mu = 0.4$. The increased friction also had the effect of somewhat delaying the onset of the reaction moment and thus delaying the peak in chiral length. The magnitude of the chiral length was increased significantly because the magnitude of the reaction moment increased more than that of the reaction force.

The friction results for the [3⁶]-B configuration are presented in Figures 5.18 and 5.19. This configuration was not as dependent on sliding as the [3.4.6.4]-B configuration was and this did not change with the increased friction. The system energies were essentially scaled replicas of each other. The magnitude of the reaction force did increase from about 900 N to 1100 N but this was not nearly the doubling that

was seen with [3.4.6.4]-B. It is worth noting that the [3⁶]-B configuration had significant sliding at a deflection of about 20 mm which led immediately to final failure when $\mu = 0.2$, but this sliding was arrested before final failure when the friction was increased. The reaction moment for this configuration was significantly affected. It approximately doubled with the increased friction, and its onset was delayed. This had the effect of increasing and delaying the maximum magnitude of the chiral length.

The double-tile (4.8²)-B configuration, Figures 5.20 and 5.21, and the triple-tile (4.6.12)-A(+) configuration which was the strongest configuration in this study, Figures 5.22 and 5.23, responded similarly to the increased friction. Both saw increases in the reaction force on the order of about 25% when the coefficient of friction was doubled to $\mu = 0.4$, similar to the [3⁶]-B configuration. Neither of these configurations exhibit chirality. The magnitude of the reaction moments did increase, but they remained trivial. Additionally, the relative magnitudes of the system energies were not significantly affected. It is interesting to note that the (4.6.12)-A(+) configuration reached final failure after a sudden slip at the same deflection regardless of the coefficient of friction. Unlike the [3⁶]-B configuration, the increased friction was not enough to arrest the sliding and delay the final failure.

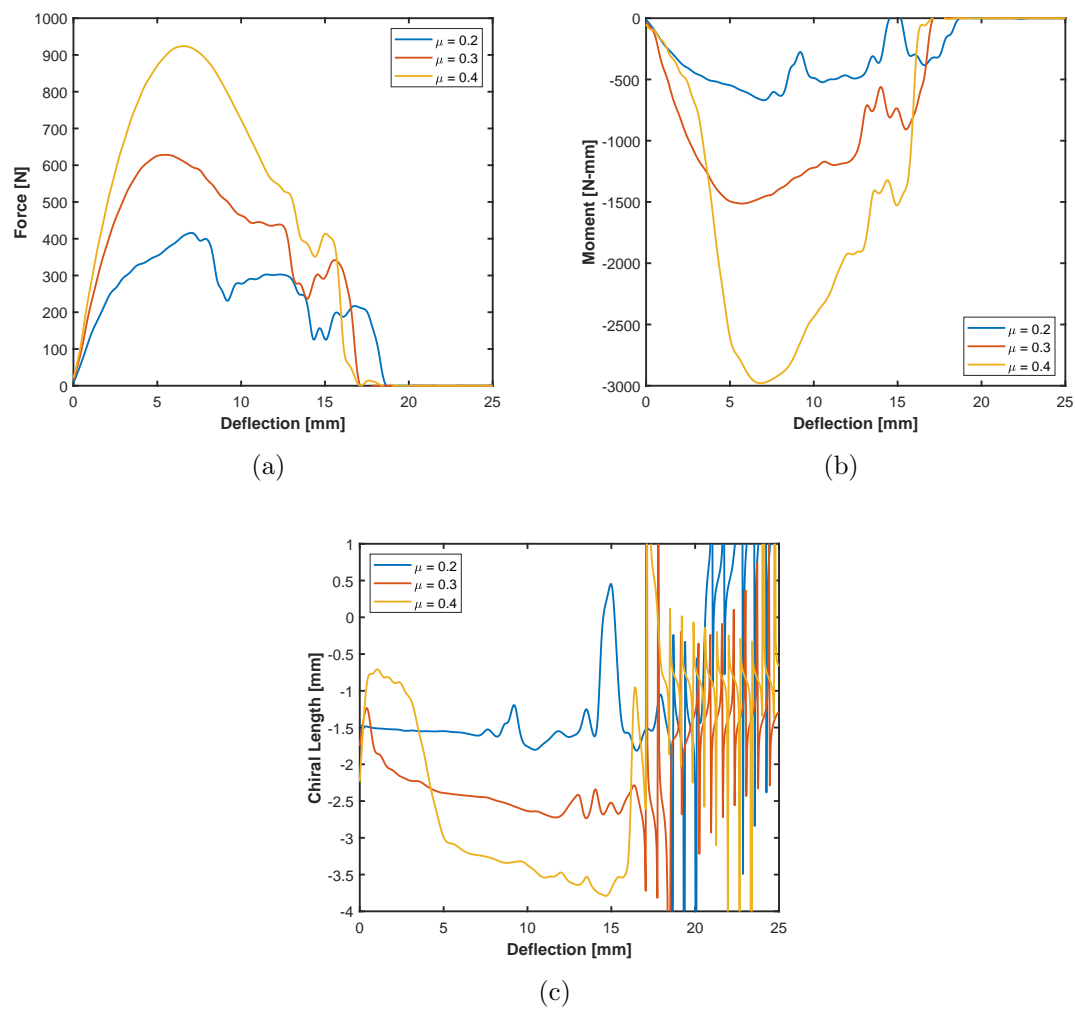


Figure 5.16. Effect of friction on [3.4.6.4]-B for (a) force-deflection, (b) moment-deflection, (c) chiral length.

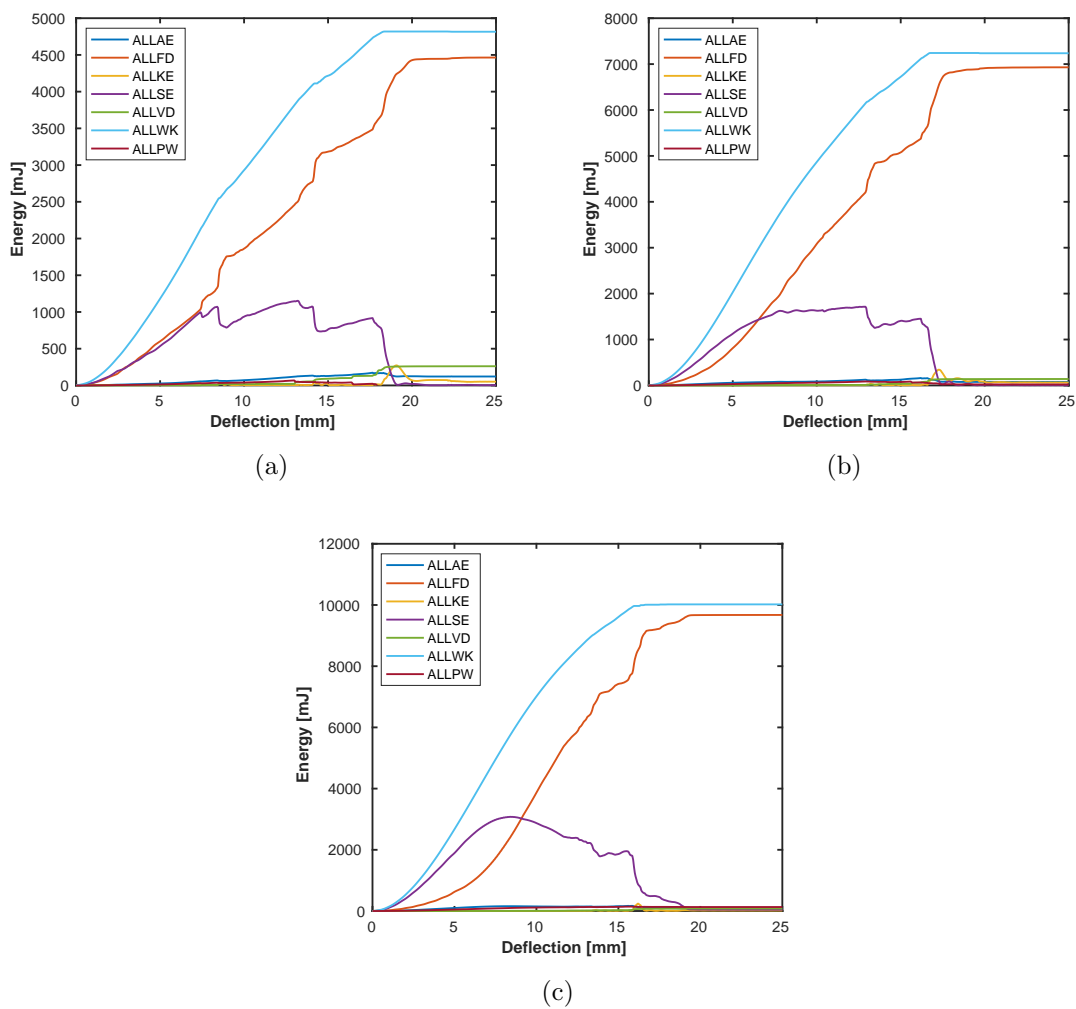


Figure 5.17. Effect of friction on system energies of [3.4.6.4]-B for (a) $\mu = 0.2$, (b) $\mu = 0.3$, (c) $\mu = 0.4$.

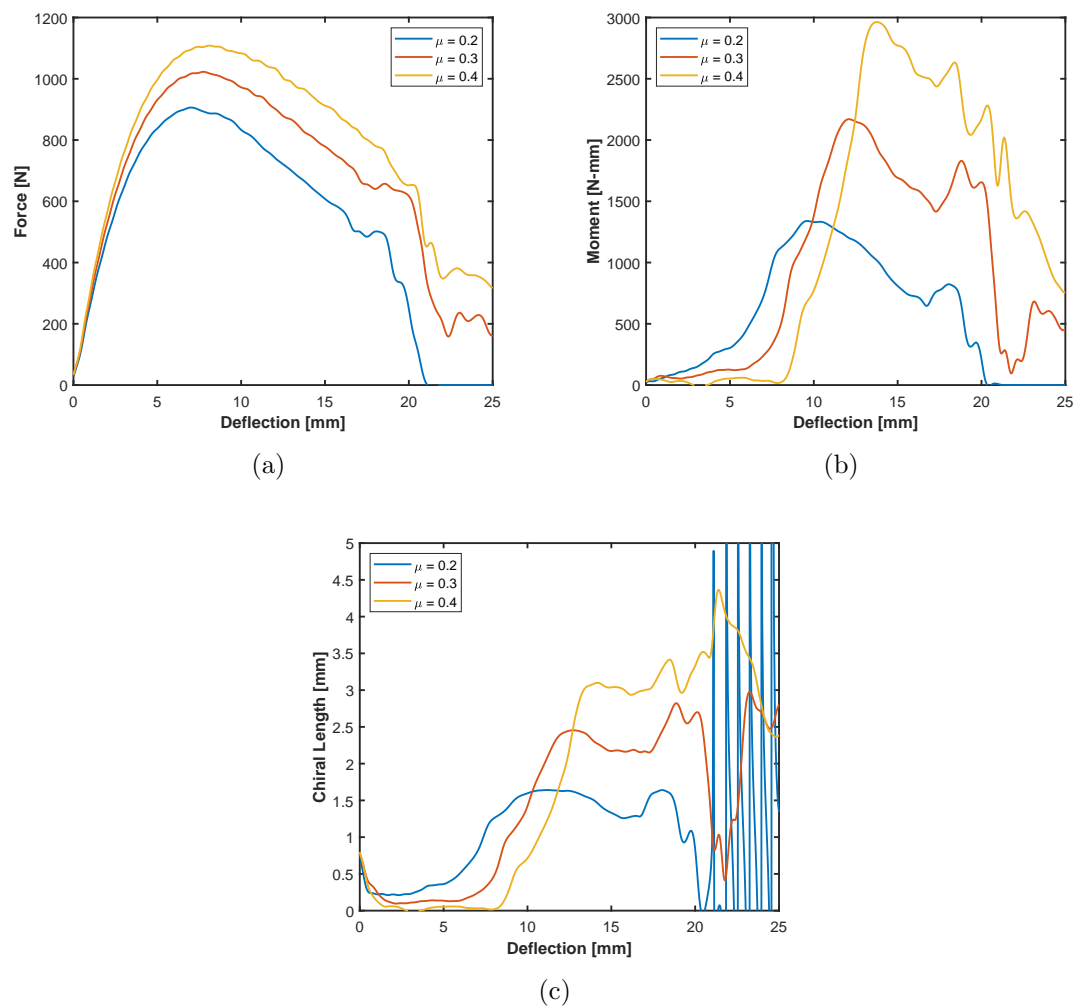


Figure 5.18. Effect of friction on $[3^6]$ -B for (a) force-deflection, (b) moment-deflection, (c) chiral length.

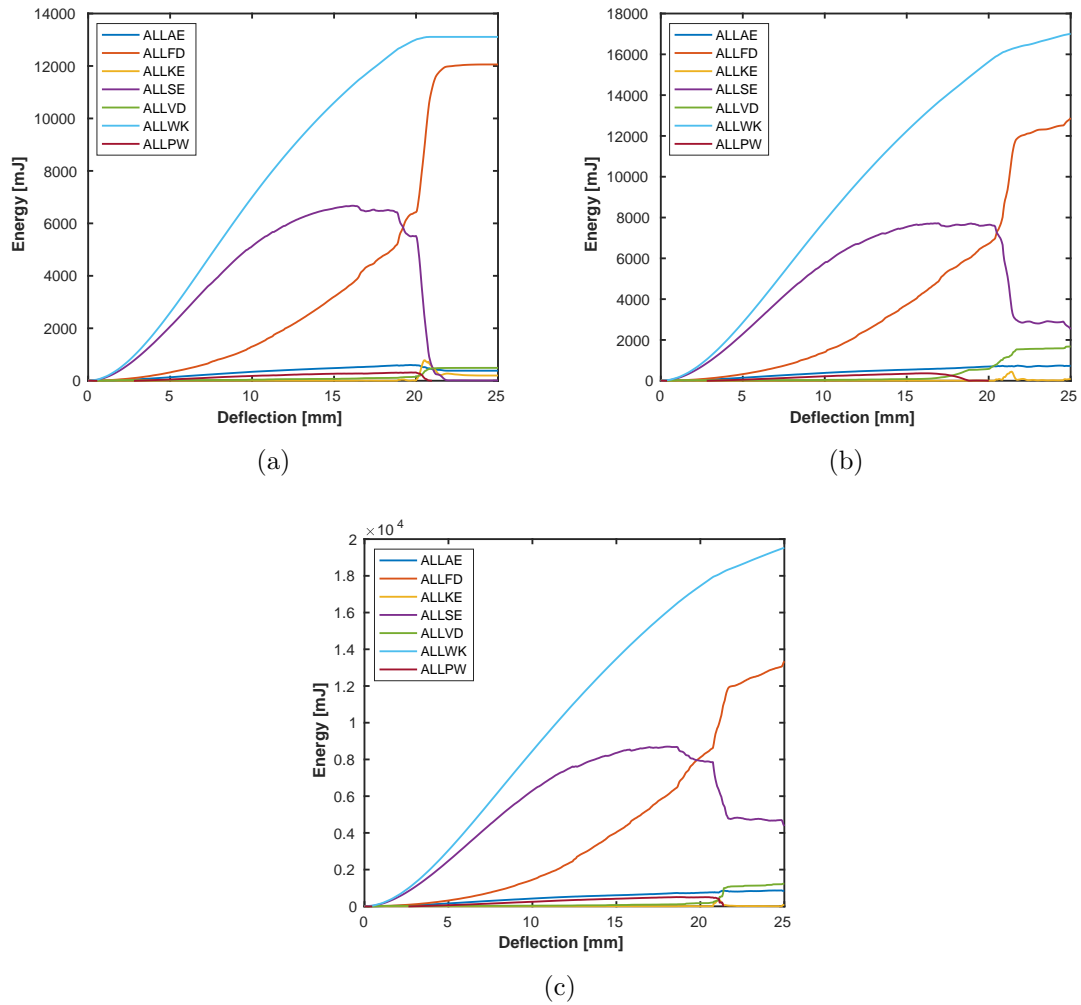


Figure 5.19. Effect of friction on system energies of $[3^6]$ -B for (a) $\mu = 0.2$, (b) $\mu = 0.3$, (c) $\mu = 0.4$.

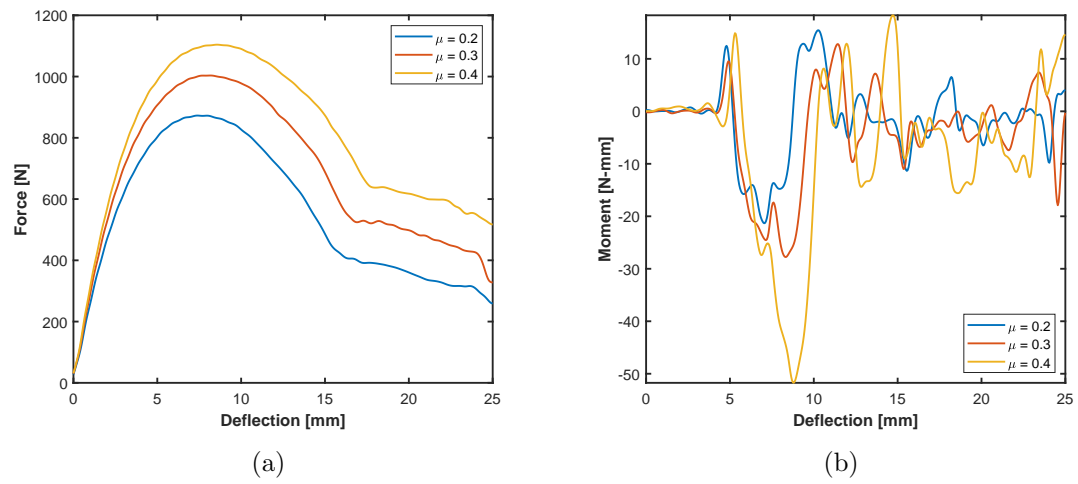


Figure 5.20. Effect of friction on (4.8^2) -B for (a) force-deflection, (b) moment-deflection.

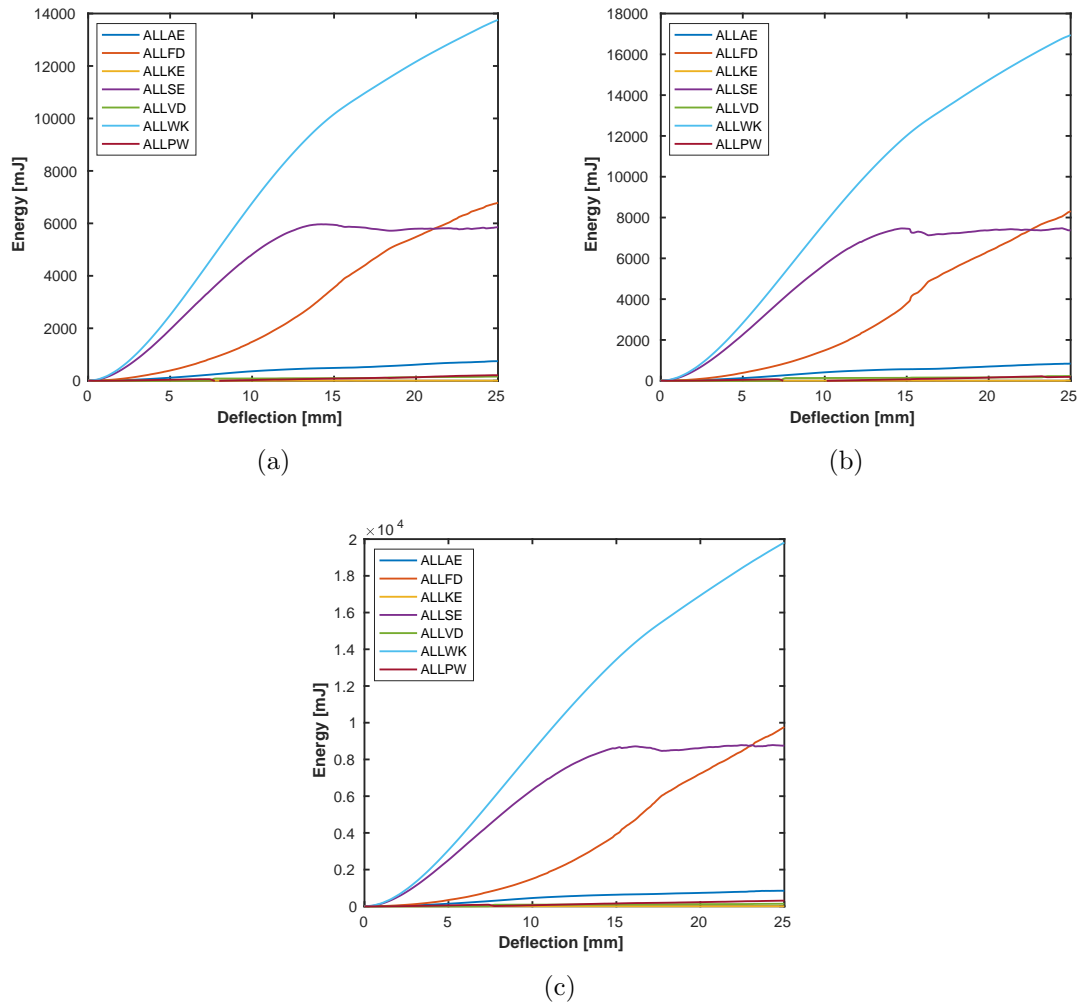


Figure 5.21. Effect of friction on system energies of (4.8²)-B for (a) $\mu = 0.2$, (b) $\mu = 0.3$, (c) $\mu = 0.4$.

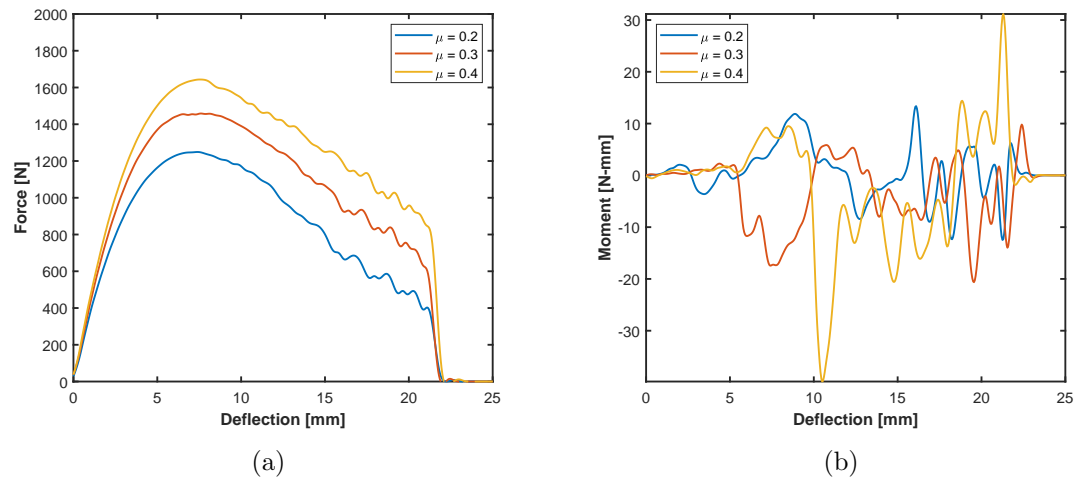


Figure 5.22. Effect of friction on (4.6.12)-A(+) for (a) force-deflection, (b) moment-deflection.

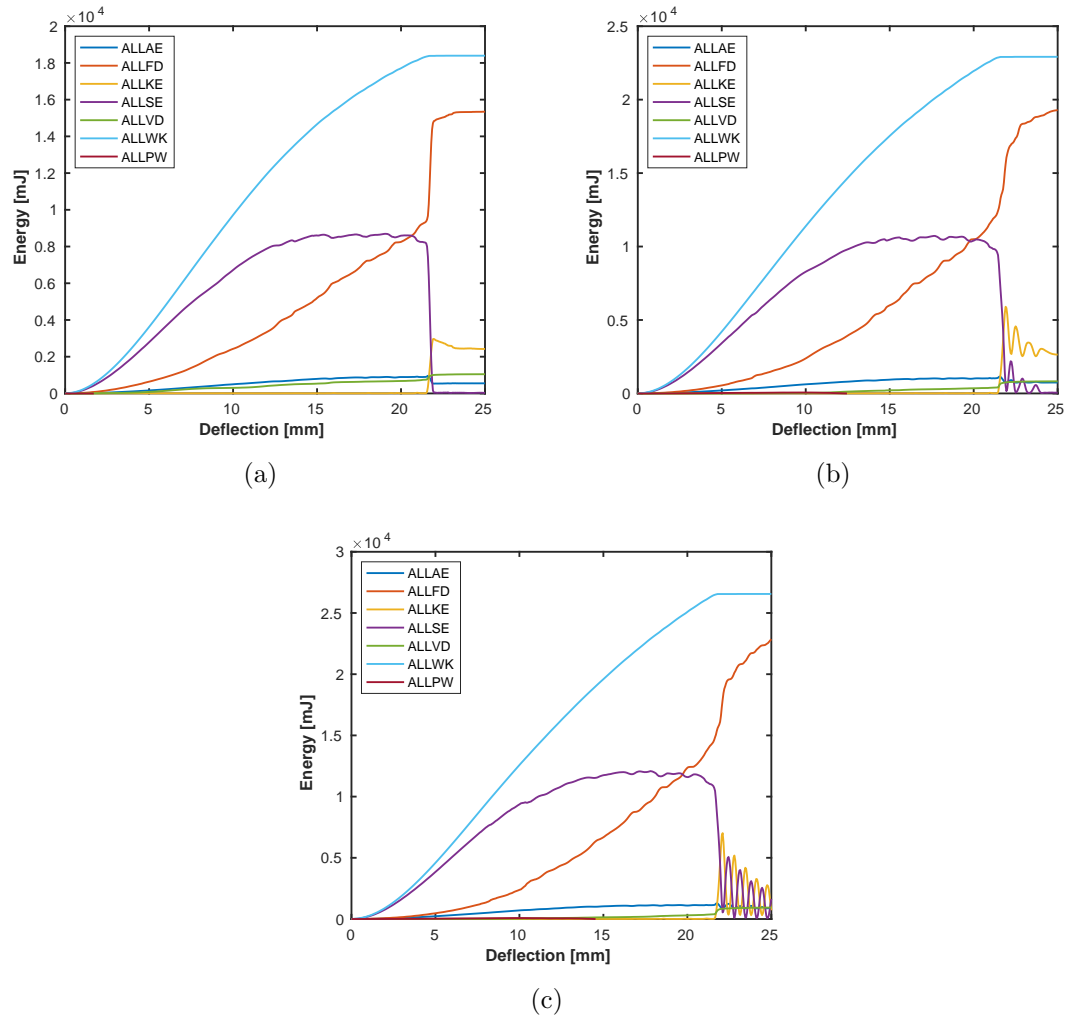


Figure 5.23. Effect of friction on system energies of (4.6.12)-A(+) for (a) $\mu = 0.2$, (b) $\mu = 0.3$, (c) $\mu = 0.4$.

5.5.2 Aggregate Effects of the Coefficient of Friction

All configurations were simulated with the coefficients of friction $\mu = 0.2$, $\mu = 0.3$, and $\mu = 0.4$. The aggregate results are shown in Figures 5.24 - 5.26 as cross property plots. The linear fit lines are shown for each data set representing the span of properties across all configurations for each coefficient of friction. In all cases, the span of each property was approximately the same, but the trend lines shifted as the friction changed. In the strength-stiffness correlation, increasing the friction moved the property sets along the slope of the strength-stiffness line towards increasing the strength and stiffness. Strength was increased very subtly to offset each property set above the previous one. The toughness-stiffness property sets also increased the magnitude of both properties as the friction was increased, and these also shifted up offsetting each trend line above the previous one toward increasing toughness. The toughness-strength property sets saw similar results, to the toughness-stiffness properties, but here the slope of the toughness-strength trends increased slightly.

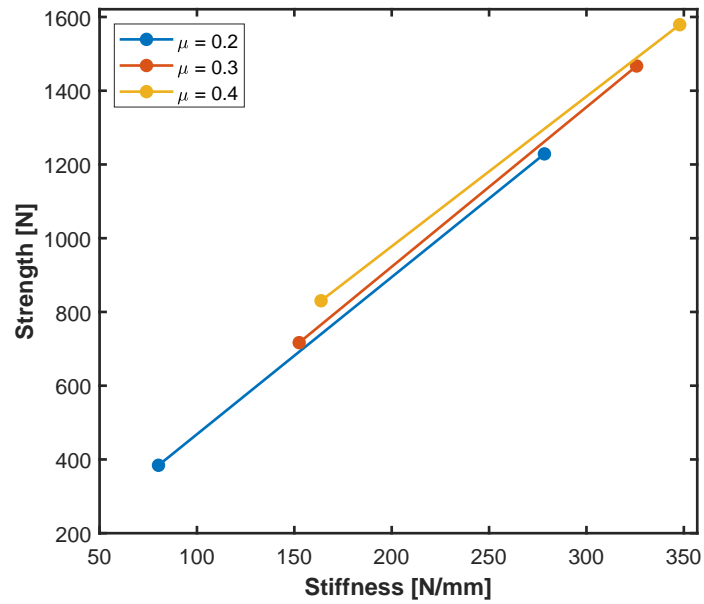


Figure 5.24. Strength and stiffness cross property correlation trends for $\mu = 0.2$, $\mu = 0.3$, and $\mu = 0.4$.

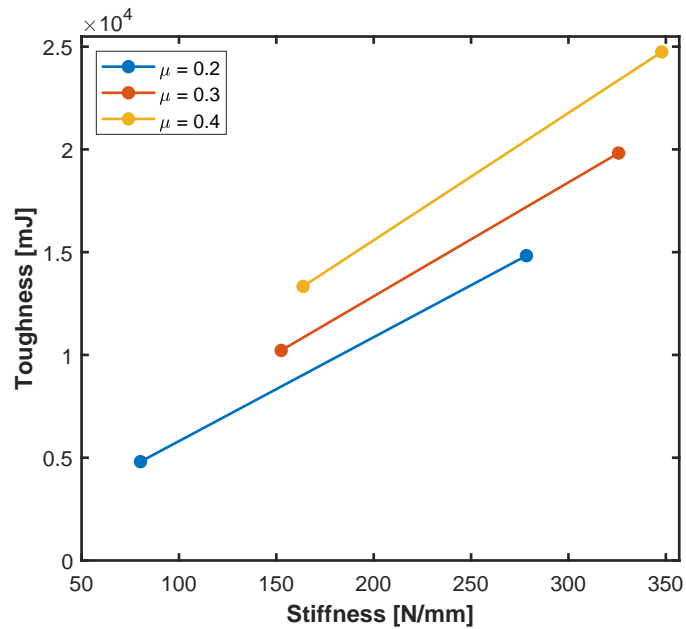


Figure 5.25. Toughness and stiffness cross property correlation trends for $\mu = 0.2$, $\mu = 0.3$, and $\mu = 0.4$.

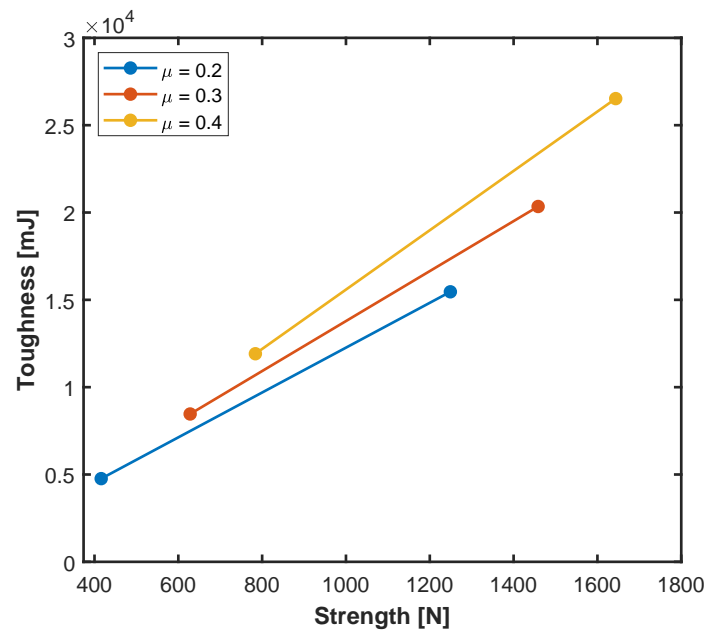


Figure 5.26. Toughness and strength cross property correlation trends for $\mu = 0.2$, $\mu = 0.3$, and $\mu = 0.4$.

5.6 Expansion of the Material Space

The results of this study have shown that the stiffness of a TIM system varies based on the segmentation pattern. This means a range of stiffnesses can be achieved for a segmented material system constructed with any single homogeneous material. Furthermore, the volume fractions of the TIM systems in this study were close to unity, so the density of the system did not vary significantly from that of the homogeneous material. Therefore, the effective material space can be expanded to include a wider range of stiffnesses without altering the density when considering segmented material systems consisting of any homogeneous material. Theoretical examples of this expansion are shown for ceramics and metals, Figure 5.27. Additionally, the coefficient of friction within a segmented system has been shown to alter its stiffness. This could be used to further adjust the stiffness of a segmented material system.

Segmentation enables the creation of material systems that are more ductile than the homogeneous material they are made from. This work has shown a strong correlation between the strength and stiffness of a TIM system, so increasing the ductility would also reduce the strength of a system. However, the local strength of the individual bodies in the system is not affected. The property space for a theoretical homogeneous material is shown in Figure 5.28 along with the expanded property space of a segmented system constructed from that material illustrating the potential combination of local strength and global ductility for a segmented material system. The direction of influence of the coefficient of friction is also shown which could be used to further adjust the properties of the system.

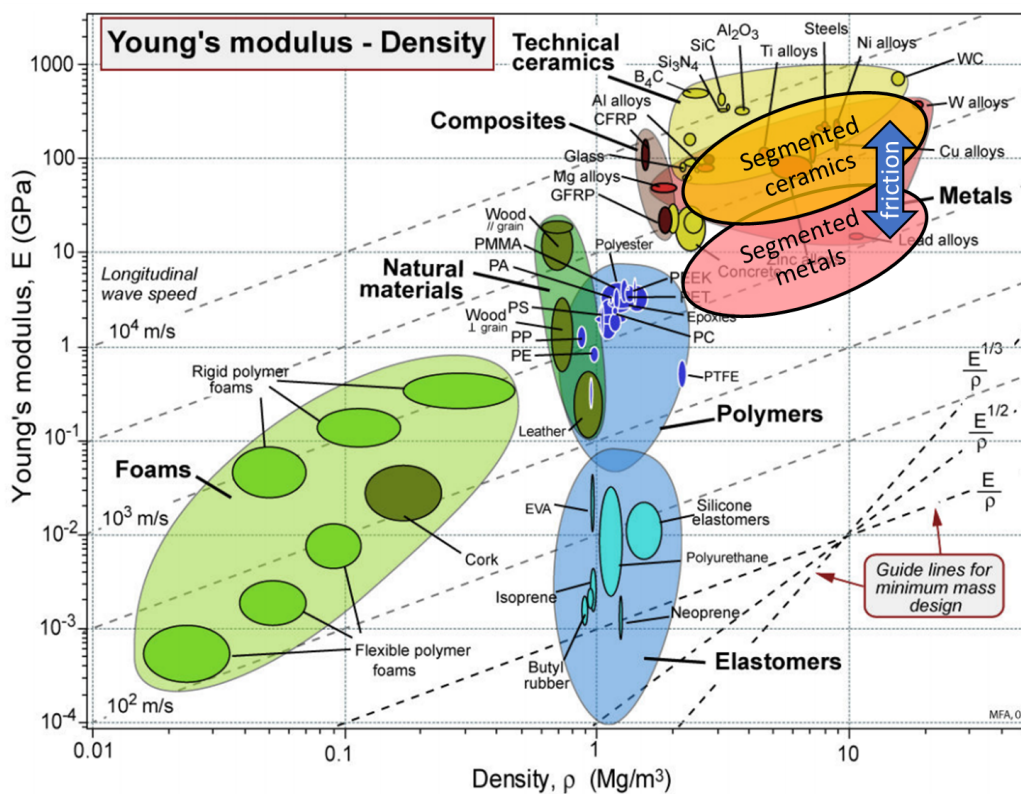


Figure 5.27. Material property chart of Young's modulus and density [19] with theoretical expansions of ceramic and metal material spaces resulting from segmentation. The direction of influence of friction on segmented systems is also marked.

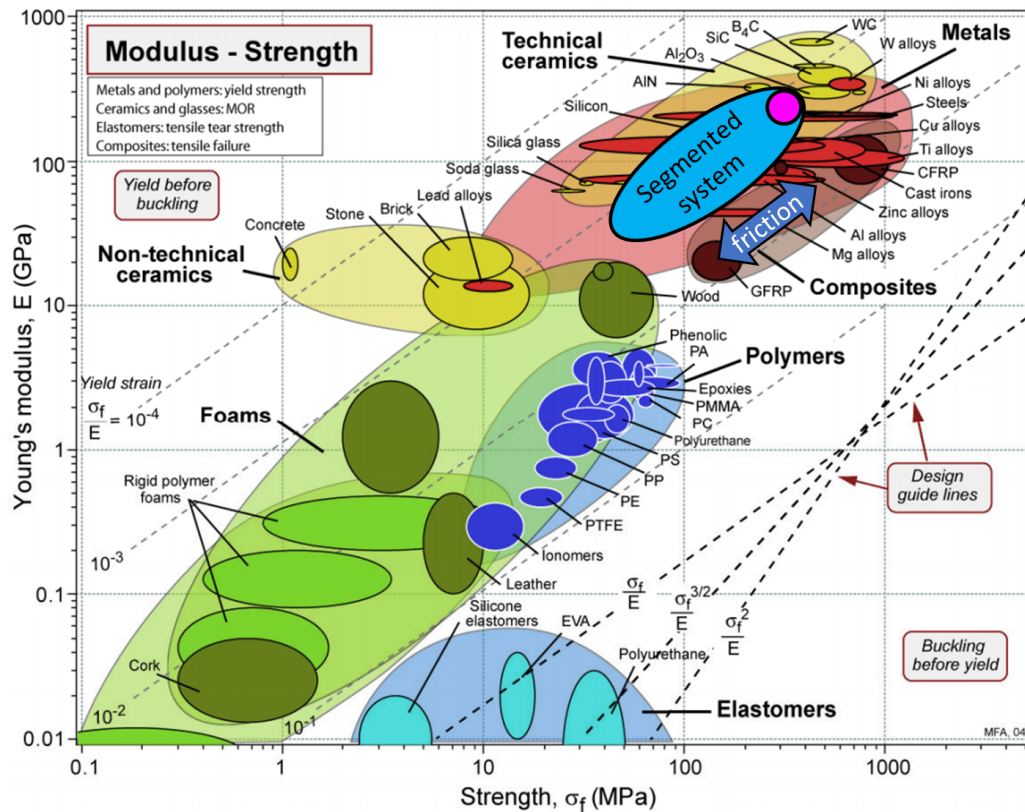


Figure 5.28. Material property chart of Young's modulus and strength [19] with a theoretical homogeneous material (magenta) and its corresponding segmented material system (blue). The direction of influence of friction on segmented systems is also marked.

6. CONCLUSIONS

TIM systems were constructed into 18 configurations based on six unique tilings and were simulated under both displacement control load and body force load. It was found that the load responses of all configurations were generally consistent with the typical skewed parabola that has been recorded in other TIM systems. Additionally, the attractive positive correlations of toughness-stiffness and toughness-strength were realized for all configurations.

There was significant variance in the performance of the TIM systems in this study. It was generally observed that the triple-tile (4.6.12) configurations were the strongest, followed but the double-tile (4.8²) configurations, the single hexagon tile [3⁶] configurations, and then all the single four-sided tile configurations. There was no single predictor of strength, but the strongest configurations tended to have the least total contact area between segmented bodies, the greatest number of contact interfaces, and the smallest tiles. It is postulated that this combination of features leads to more refined thrust lines through the system resulting in greater strength.

The unique characteristics of chirality and non-reciprocity in the load direction were explored. Configurations centered around a tile vertex rather than the middle of a tile exhibited chirality. This resulted in a tendency for the blocks within an assembly to collectively rotate as the assembly was displaced. It also caused a reaction moment on the system and was visible in the compressive stress fields. Non-reciprocity in the load direction occurred in all but one of the multi-tile assemblies. These assemblies had a different load response depending on the direction of the transverse load. This was a result of the assembly having geometric features such that the assembly could not exactly overlay its original position if it were flipped over and rotated by any amount.

The findings of this study allow for an expansion of the material space. When considering a segmented material system, a greater range of ductility is available as compared to homogeneous materials. The segmentation pattern can be chosen to achieve the desired ductility. Additionally, the coefficient of friction within the segmented system is readily modifiable with surface finishes, lubricants, or coatings and can be used to further refine the ductility. These methods can be used to design advantageous material systems that are ductile as a system while maintaining high strength within the individual components. Furthermore, chirality and non-reciprocity could be utilized to create unique material systems with functionality that is not achievable with monolithic materials.

Future work could explore the cause of chirality in more depth as well as investigate what geometric properties influence the chiral response. Additionally, more work could be done to explore how varying geometric properties affect the development of thrust lines within a segmented system and how this might affect the strength of the system.

REFERENCES

REFERENCES

- [1] Mohammad Mirkhalaf, Tao Zhou, and Francois Barthelat. Simultaneous improvements of strength and toughness in topologically interlocked ceramics. *Proceedings of the National Academy of Sciences*, 115(37):9128–9133, 2018.
- [2] Arcady V. Dyskin, Yuri Estrin, Elena Pasternak, Han C. Khor, and Alexei J. Kanel-Belov. Fracture resistant structures based on topological interlocking with non-planar contacts. *Advanced Engineering Materials*, 5(3):116–119, 2003.
- [3] Yuezhong Feng, Thomas Siegmund, Ed Habtour, and Jaret Riddick. Impact mechanics of topologically interlocked material assemblies. *International Journal of Impact Engineering*, 75:140–149, 2015.
- [4] Thomas Siegmund, Francois Barthelat, Raymond Cipra, Ed Habtour, and Jaret Riddick. Manufacture and Mechanics of Topologically Interlocked Material Assemblies. *Applied Mechanics Reviews*, 68(4):040803, 2016.
- [5] A. V. Dyskin, Y. Estrin, A. J. Kanel-Belov, and E. Pasternak. A new principle in design of composite materials: Reinforcement by interlocked elements. *Composites Science and Technology*, 63(3-4):483–491, 2003.
- [6] Maurizio Brocato. A continuum model of interlocking structural systems. *Atti della Accademia Nazionale dei Lincei, Classe di Scienze Fisiche, Matematiche e Naturali, Rendiconti Lincei Matematica e Applicazioni*, 29(1):63–83, 2018.
- [7] Jean-Gaffin Gallon. *Machines et inventions approuvées par l'Académie royale des sciences, depuis son établissement jusqu'à présent; avec leur description*. Gabriel Martin, Jean-Baptiste Coignard, Hippolyte-Louis Guerin, Paris, 1735.
- [8] Michael Glickman. The G-block system of vertically interlocking paving. In *Second International Conference on Concrete Block Paving*, Delft, Netherlands, 1984.
- [9] A.V Dyskin, Y. Estrin, A.J Kanel-Belov, and E. Pasternak. A new concept in design of materials and structures: assemblies of interlocked tetrahedron-shaped elements. *Scripta Materialia*, 44(12):2689–2694, 6 2001.
- [10] S. Khandelwal, T. Siegmund, R. J. Cipra, and J. S. Bolton. Transverse loading of cellular topologically interlocked materials. *International Journal of Solids and Structures*, 49(18):2394–2403, 2012.
- [11] S. Khandelwal, T. Siegmund, R. J. Cipra, and J. S. Bolton. Adaptive mechanical properties of topologically interlocking material systems. *Smart Materials and Structures*, 24(4):045037, 4 2015.

- [12] S. Khandelwal, T. Siegmund, R. J. Cipra, and J. S. Bolton. Scaling of the Elastic Behavior of Two-Dimensional Topologically Interlocked Materials Under Transverse Loading. *Journal of Applied Mechanics*, 81(3):031011, 2013.
- [13] M. Brocato and L. Mondardini. A new type of stone dome based on Abeille's bond. *International Journal of Solids and Structures*, 49(13):1786–1801, 2012.
- [14] M. Weizmann, O. Amir, and Y.J. Grobman. Topological interlocking in architectural design. *CAADRIA 2015 - 20th International Conference on Computer-Aided Architectural Design Research in Asia: Emerging Experiences in the Past, Present and Future of Digital Architecture*, 2015.
- [15] Michael Weizmann, Oded Amir, and Yasha Jacob Grobman. Topological interlocking in architecture: A new design method and computational tool for designing building floors. *International Journal of Architectural Computing*, 15(2):107–118, 2017.
- [16] Warren C. Young and Richard G. Budynas. *Roark's Formulas for Stress and Strain*. McGraw-Hill, New York, NY, seventh ed edition, 2002.
- [17] Mohammad Mirkhalaf, Amanul Sunesara, Behnam Ashrafi, and Francois Barthelat. Toughness by segmentation: Fabrication, testing and micromechanics of architected ceramic panels for impact applications. *International Journal of Solids and Structures*, 158:52–65, 2019.
- [18] Seyed M.ohammad Mirkhalaf Valashani and Francois Barthelat. A laser-engraved glass duplicating the structure, mechanics and performance of natural nacre. *Bioinspiration & Biomimetics*, 10(2):026005, 3 2015.
- [19] M. F. Ashby. Material and process selection charts. *The CES EduPack Resource Booklet 2*, page 42, 2010.
- [20] Wen Yang, Marc A. Meyers, and Robert O. Ritchie. Structural architectures with toughening mechanisms in Nature: A review of the materials science of Type-I collagenous materials, 6 2019.
- [21] Natasha Funk, Marc Vera, Lawrence J. Szewciw, Francois Barthelat, Mark P. Stoykovich, and Franck J. Vernerey. Bioinspired Fabrication and Characterization of a Synthetic Fish Skin for the Protection of Soft Materials. *ACS Applied Materials and Interfaces*, 7(10):5972–5983, 3 2015.
- [22] Bavarian Motor Works. BMW_Vision_Next_100_081_2.jpg.
- [23] Mikiko Inaki, Jingyang Liu, and Kenji Matsuno. Cell chirality: Its origin and roles in left-right asymmetric development. *Philosophical Transactions of the Royal Society B: Biological Sciences*, 371(1710), 2016.
- [24] Jumpei Sasabe and Masataka Suzuki. Distinctive roles of d-Amino acids in the homochiral world: Chirality of amino acids modulates mammalian physiology and pathology. *Keio Journal of Medicine*, 68(1):1–16, 2019.
- [25] Amanda S. Chin, Kathryn E. Worley, Poulomi Ray, Gurleen Kaur, Jie Fan, and Leo Q. Wan. Epithelial Cell Chirality Revealed by Three-Dimensional Spontaneous Rotation. *Proceedings of the National Academy of Sciences*, 115(48):12188–12193, 2018.

- [26] Tobias Frenzel, Muamer Kadic, and Martin Wegener. Three-dimensional mechanical metamaterials with a twist. *Science*, 358(6366):1072–1074, 11 2017.
- [27] D. Prall and R.S. Lakes. Properties of a chiral honeycomb with a poisson’s ratio of -1. *International Journal of Mechanical Sciences*, 39(3):305–314, 3 1997.
- [28] X. N. Liu, G. K. Hu, C. T. Sun, and G. L. Huang. Wave propagation characterization and design of two-dimensional elastic chiral metacomposite. *Journal of Sound and Vibration*, 330(11):2536–2553, 5 2011.
- [29] Corentin Coulais, Dimitrios Sounas, and Andrea Alù. Static non-reciprocity in mechanical metamaterials. *Nature*, 542(7642):461–464, 2 2017.
- [30] Y. Estrin, A. V. Dyskin, and E. Pasternak. Topological interlocking as a material design concept. *Materials Science and Engineering C*, 31(6):1189–1194, 2011.
- [31] A. J. Kanel-Belov, A. V. Dyskin, Y. Estrin, E. Pasternak, and I. A. Ivanov-Pogodaev. Interlocking of convex polyhedra: Towards a geometric theory of fragmented solids. *Moscow Mathematical Journal*, 10(2):337–342, 2010.
- [32] Branko Grünbaum and Geoffrey Colin Shephard. *Tilings & Patterns*. Dover Publications, Inc., Mineola, New York, second edition, 2016.
- [33] Andrew Williams. ABAQUS Python Code for the Simulation of Topologically Interlocked Material Systems Based on Archimedean and Laves Tilings, 1 2020. doi:10.4231/JBKY-JH21.

APPENDICES

A. CONVERGENCE

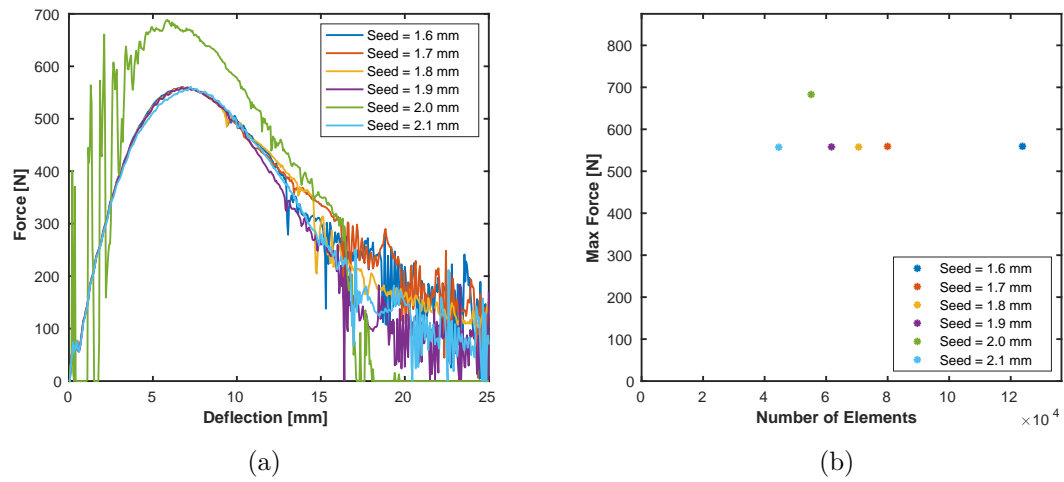


Figure A.1. Mesh convergence for $[4^4]$ -A configuration: (a) Force-deflection data. (b) Maximum force vs number of elements.

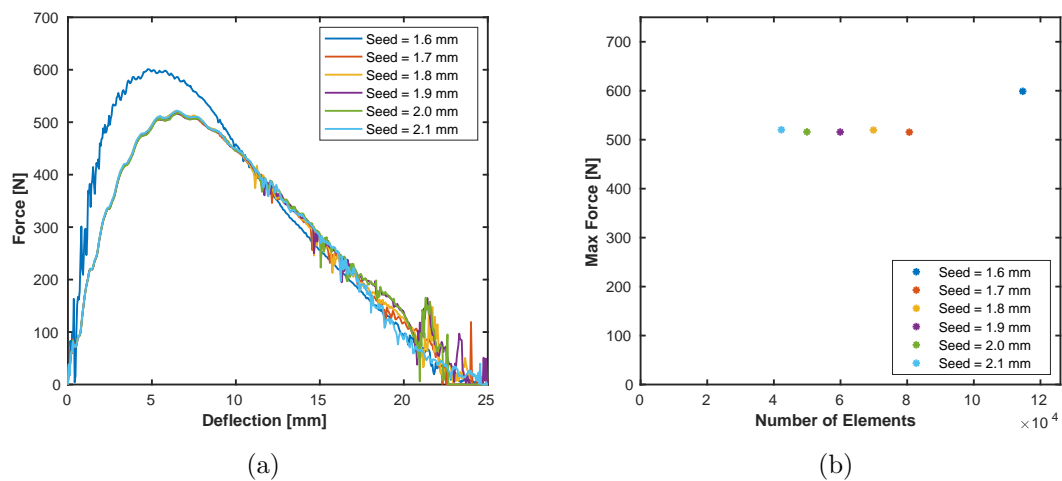


Figure A.2. Mesh convergence for $[4^4]$ -B configuration: (a) Force-deflection data. (b) Maximum force vs number of elements.

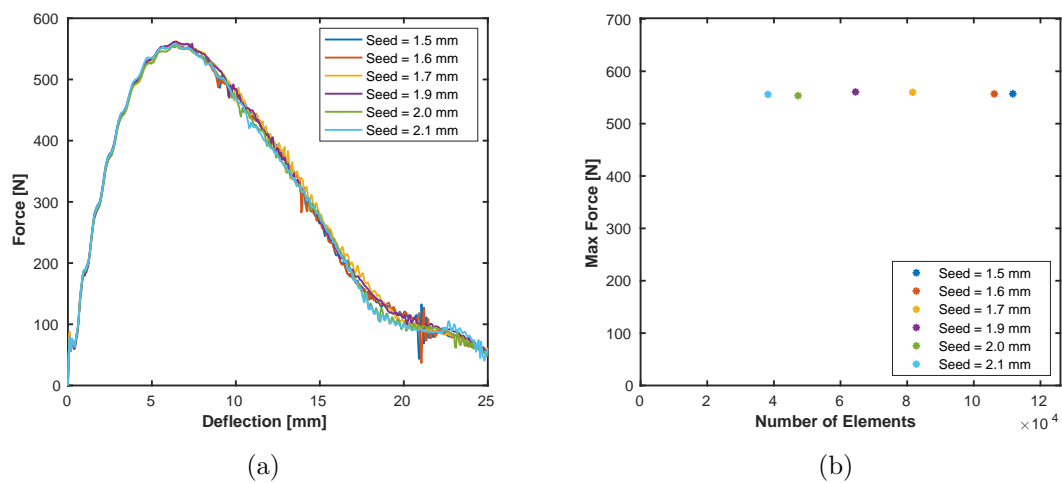


Figure A.3. Mesh convergence for $[3.6.3.6]$ -A configuration: (a) Force-deflection data. (b) Maximum force vs number of elements.

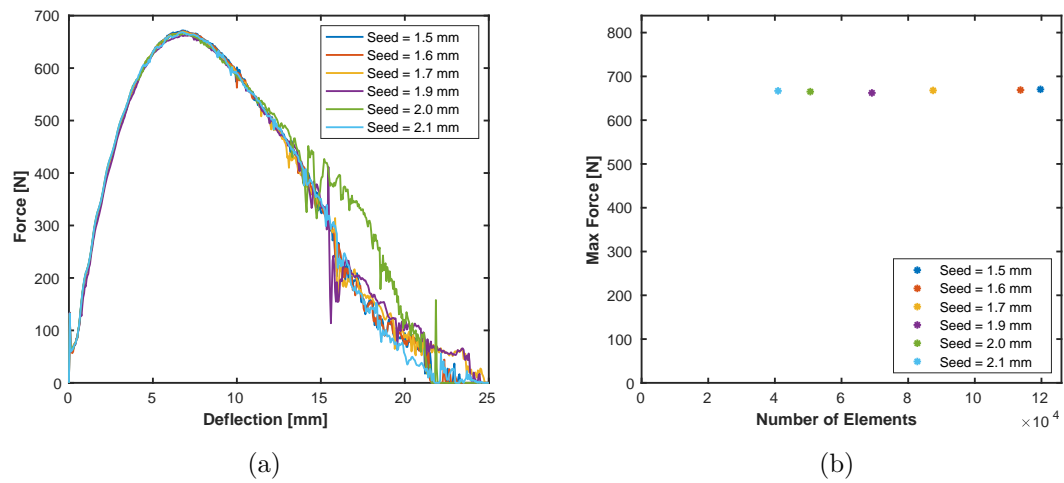


Figure A.4. Mesh convergence for [3.6.3.6]-B configuration: (a) Force-deflection data. (b) Maximum force vs number of elements.

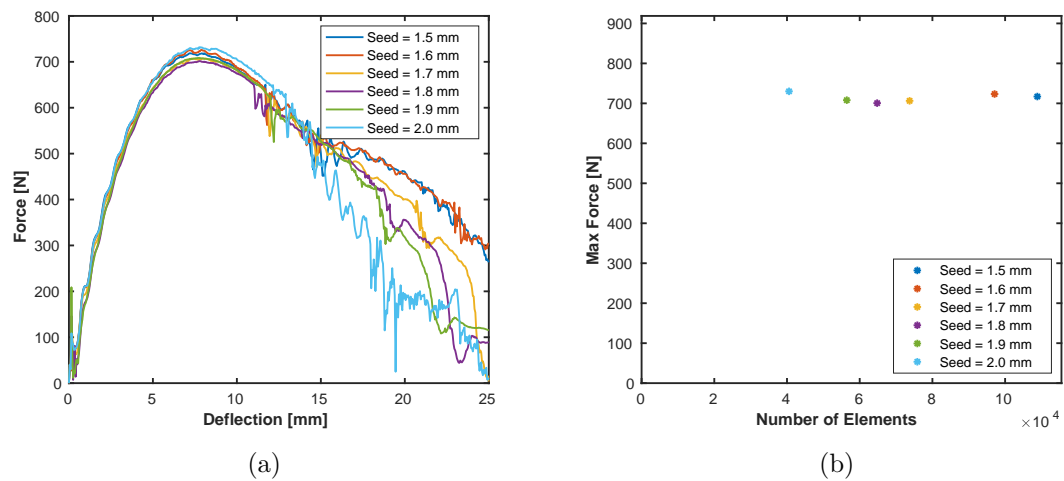


Figure A.5. Mesh convergence for [3.4.6.4]-A configuration: (a) Force-deflection data. (b) Maximum force vs number of elements.

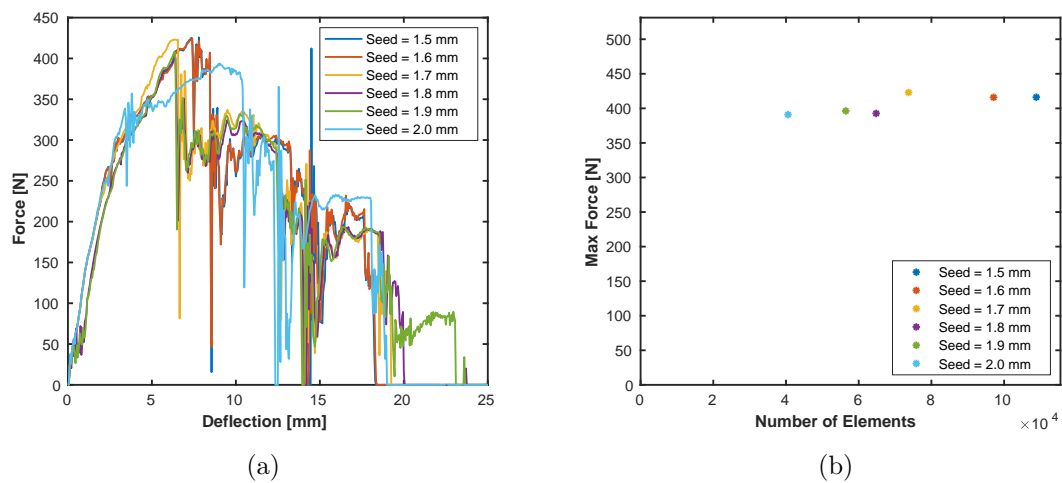


Figure A.6. Mesh convergence for [3.4.6.4]-B configuration: (a) Force-deflection data. (b) Maximum force vs number of elements.

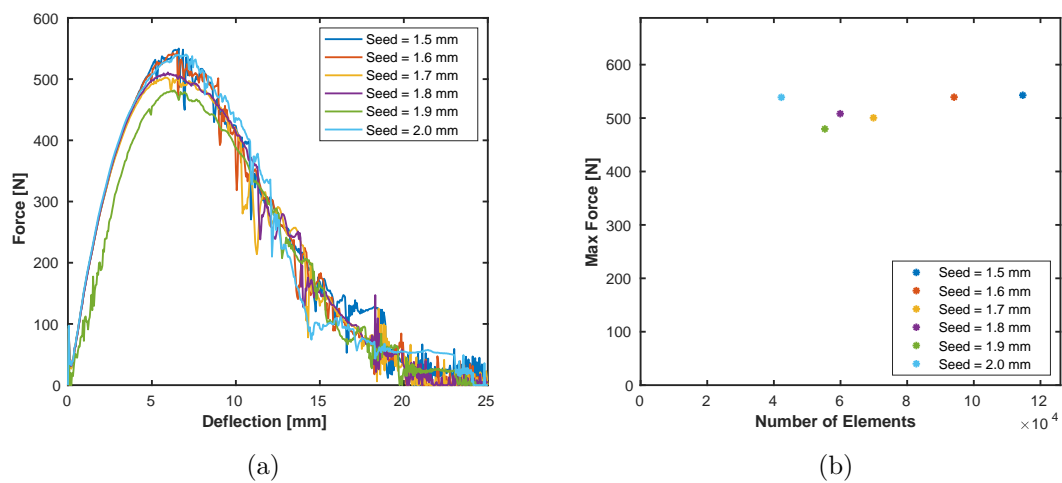


Figure A.7. Mesh convergence for [3.4.6.4]-C configuration: (a) Force-deflection data. (b) Maximum force vs number of elements.

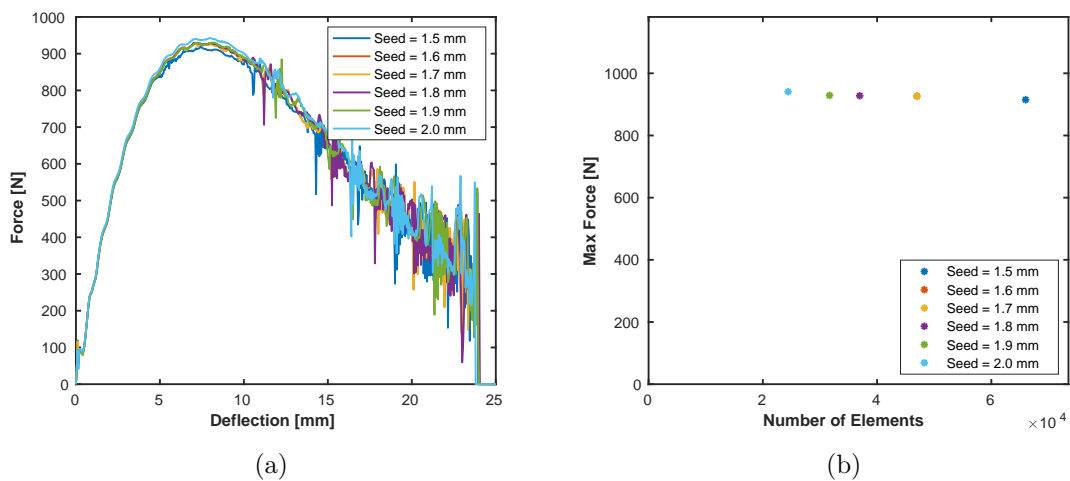


Figure A.8. Mesh convergence for $[3^6]$ -A configuration: (a) Force-deflection data. (b) Maximum force vs number of elements.

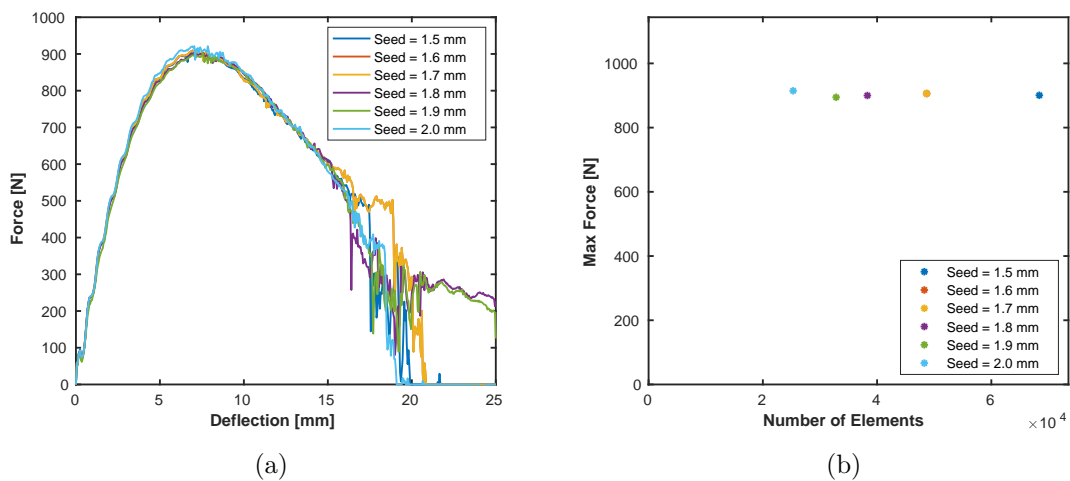


Figure A.9. Mesh convergence for $[3^6]$ -B configuration: (a) Force-deflection data. (b) Maximum force vs number of elements.

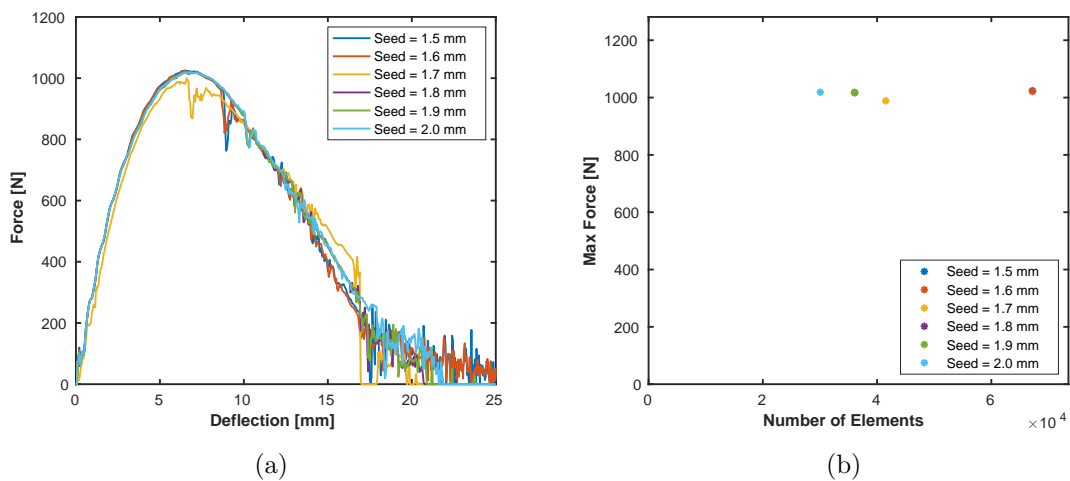


Figure A.10. Mesh convergence for (4.8^2) -A(-) configuration: (a) Force-deflection data. (b) Maximum force vs number of elements.

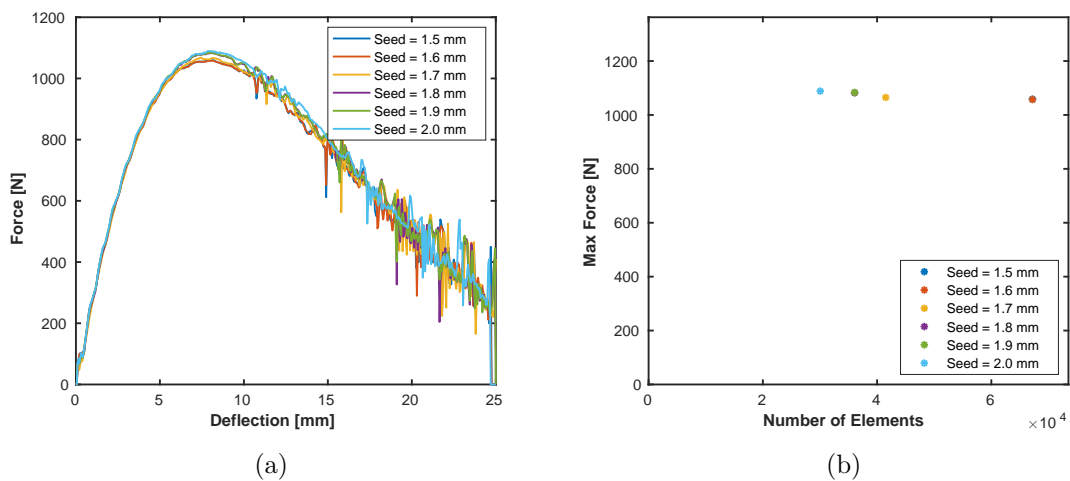


Figure A.11. Mesh convergence for (4.8^2) -A(+) configuration: (a) Force-deflection data. (b) Maximum force vs number of elements.

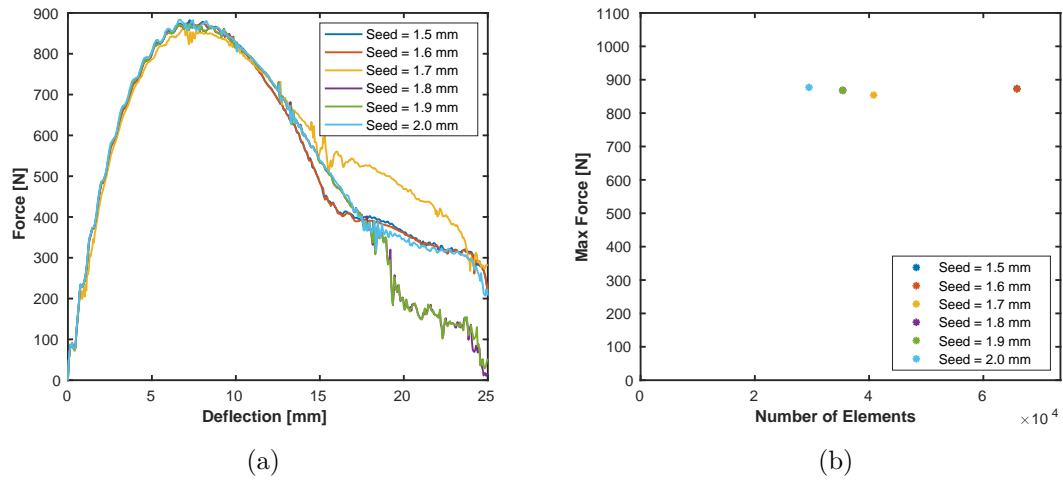


Figure A.12. Mesh convergence for (4.8^2) -B(-) configuration: (a) Force-deflection data. (b) Maximum force vs number of elements.

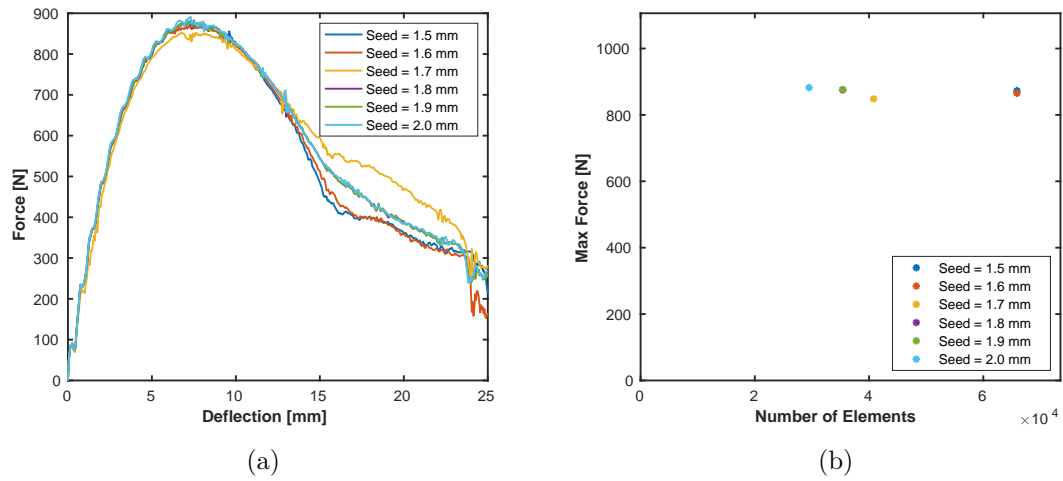


Figure A.13. Mesh convergence for (4.8^2) -B(+) configuration: (a) Force-deflection data. (b) Maximum force vs number of elements.

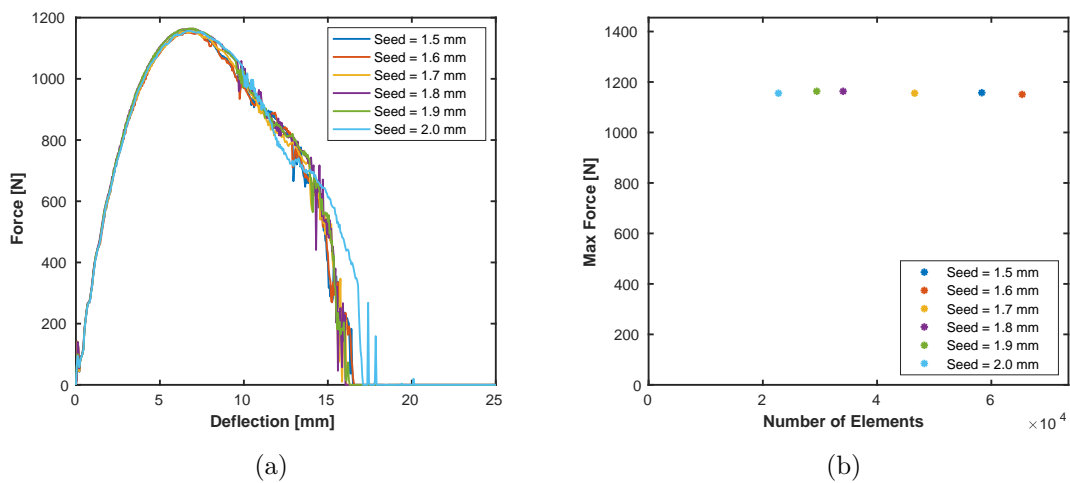


Figure A.14. Mesh convergence for (4.6.12)-A(-) configuration: (a) Force-deflection data. (b) Maximum force vs number of elements.

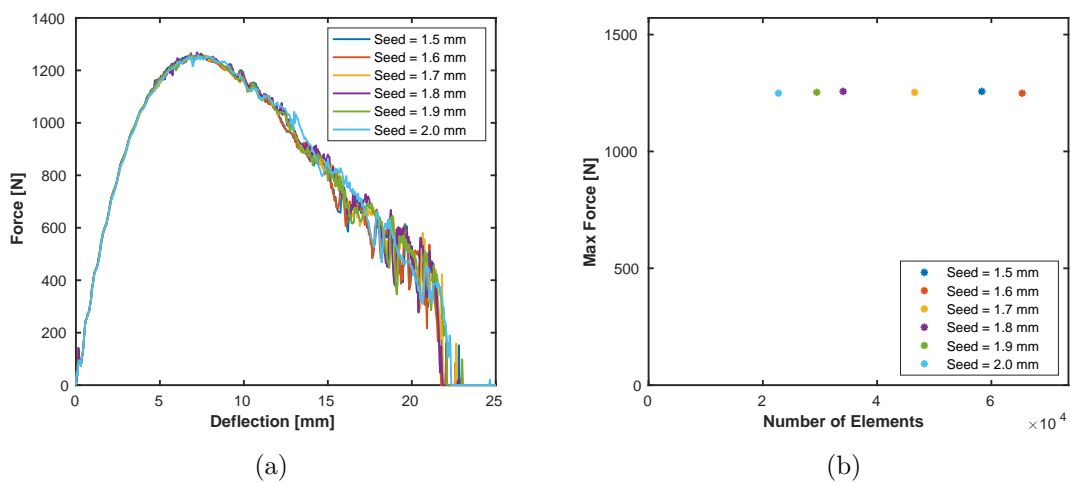


Figure A.15. Mesh convergence for (4.6.12)-A(+) configuration: (a) Force-deflection data. (b) Maximum force vs number of elements.

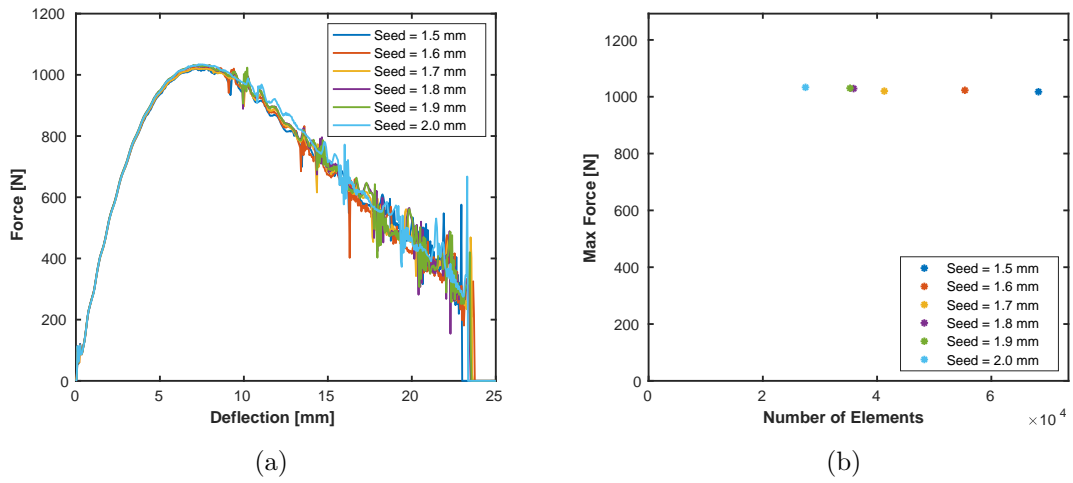


Figure A.16. Mesh convergence for (4.6.12)-B(-) configuration: (a) Force-deflection data. (b) Maximum force vs number of elements.

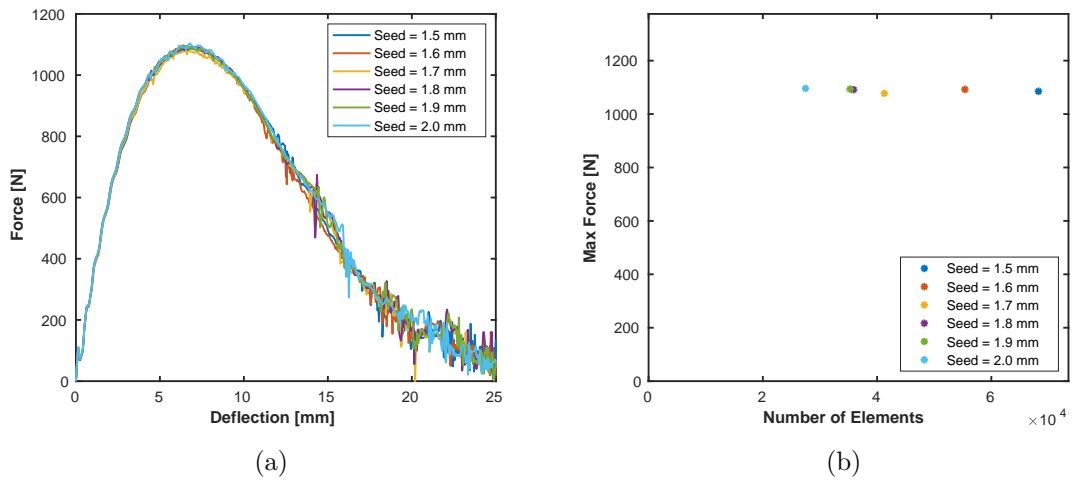


Figure A.17. Mesh convergence for (4.6.12)-B(+) configuration: (a) Force-deflection data. (b) Maximum force vs number of elements.

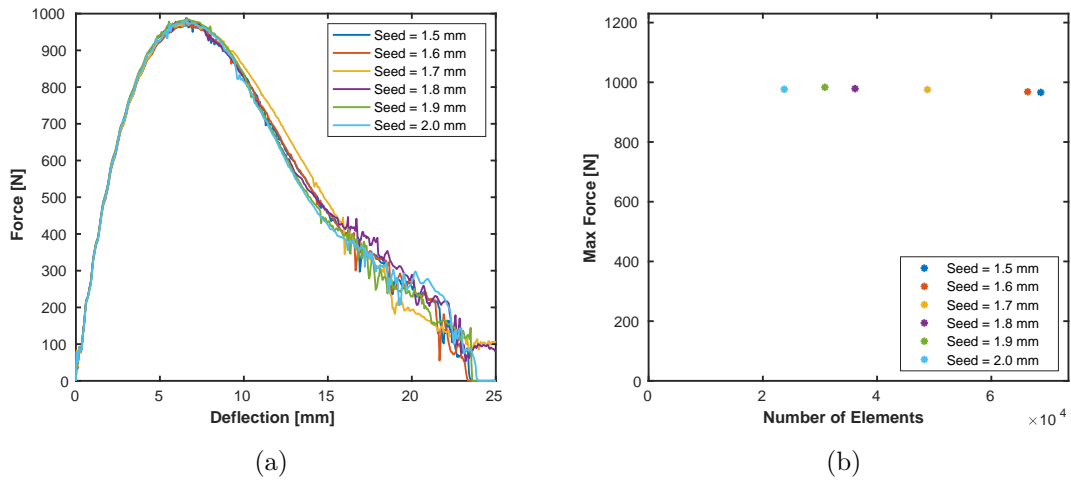


Figure A.18. Mesh convergence for (4.6.12)-C(-) configuration: (a) Force-deflection data. (b) Maximum force vs number of elements.

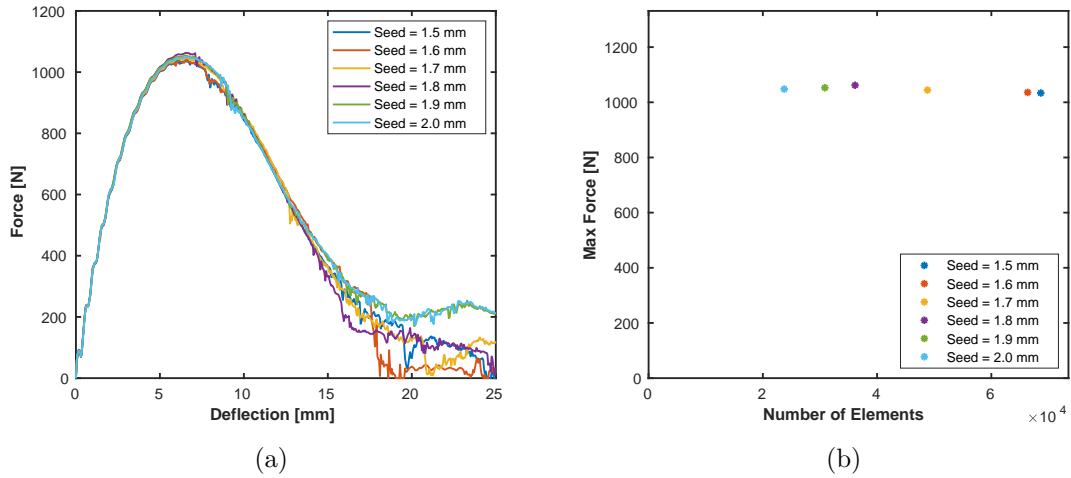


Figure A.19. Mesh convergence for (4.6.12)-C(+) configuration: (a) Force-deflection data. (b) Maximum force vs number of elements.

B. FALSE ENERGY

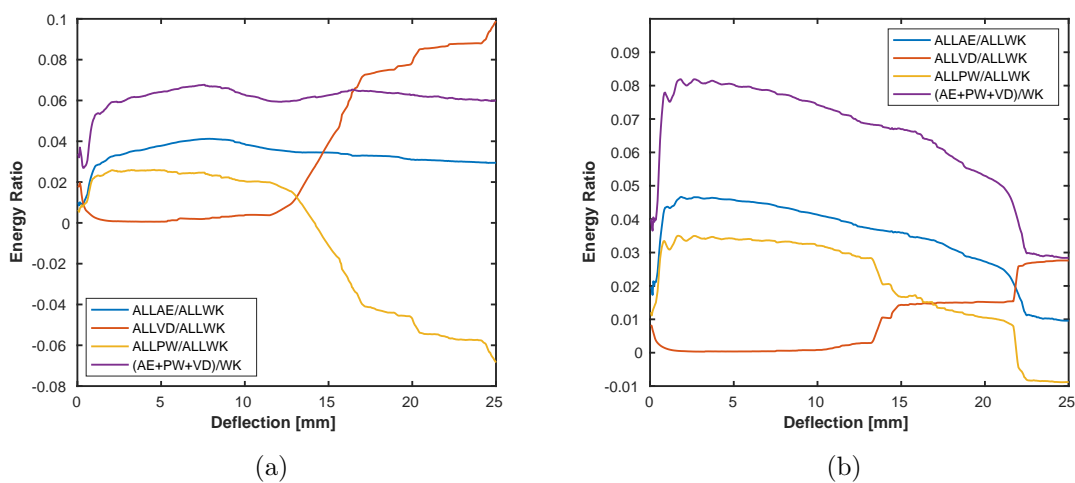
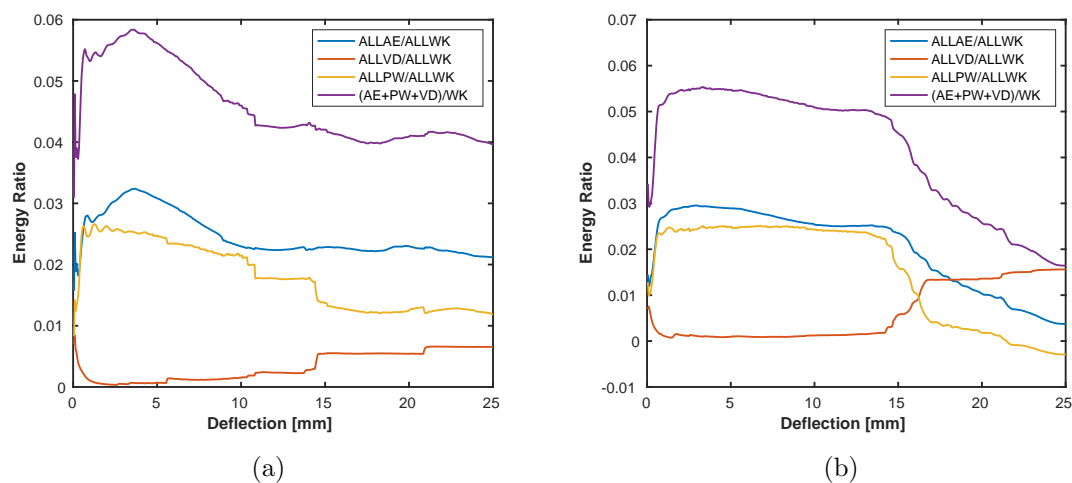
Figure B.1. False energies for (a) [4⁴]-A, (b) [4⁴]-B.

Figure B.2. False energies for (a) [3.6.3.6]-A, (b) [3.6.3.6]-B.

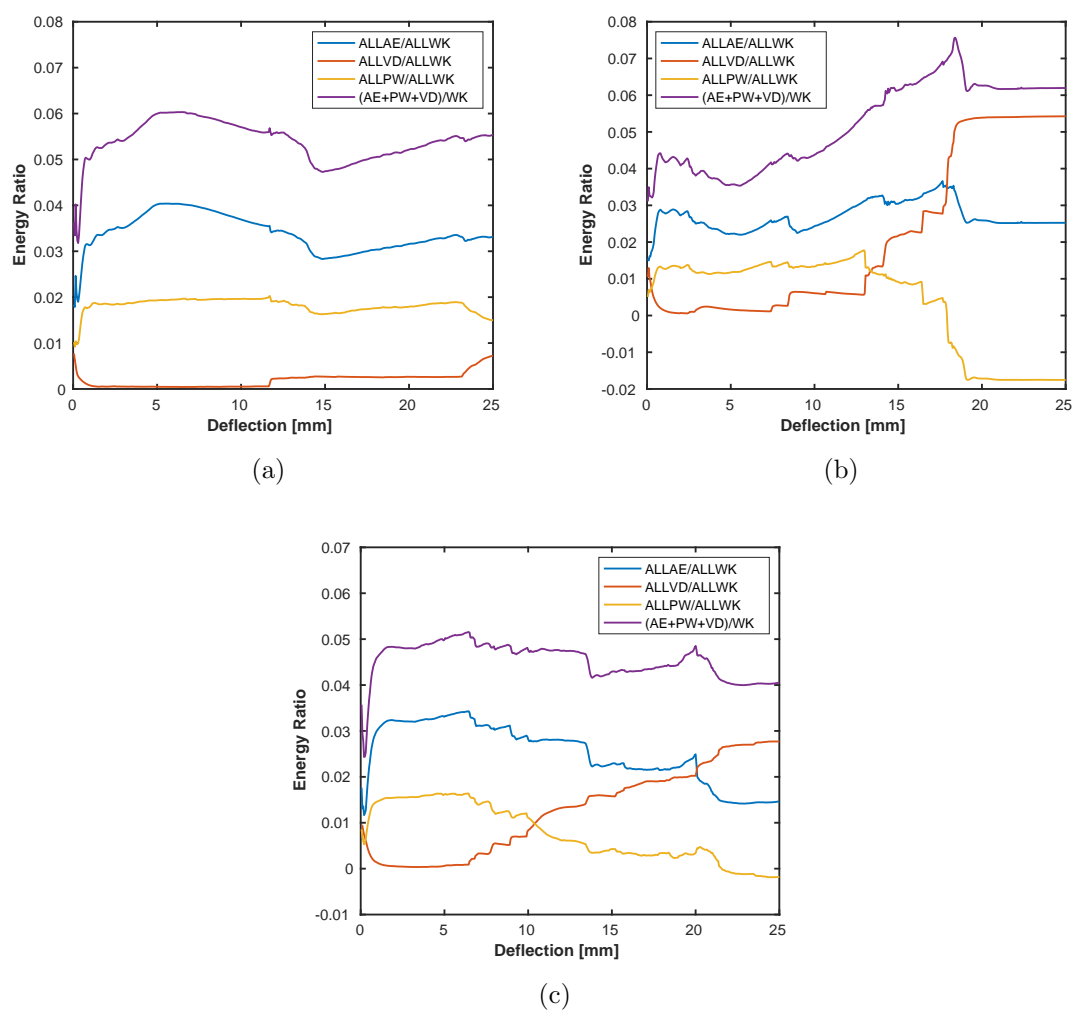


Figure B.3. False energies for (a) [3.4.6.4]-A, (b) [3.4.6.4]-B, (c) [3.4.6.4]-C.

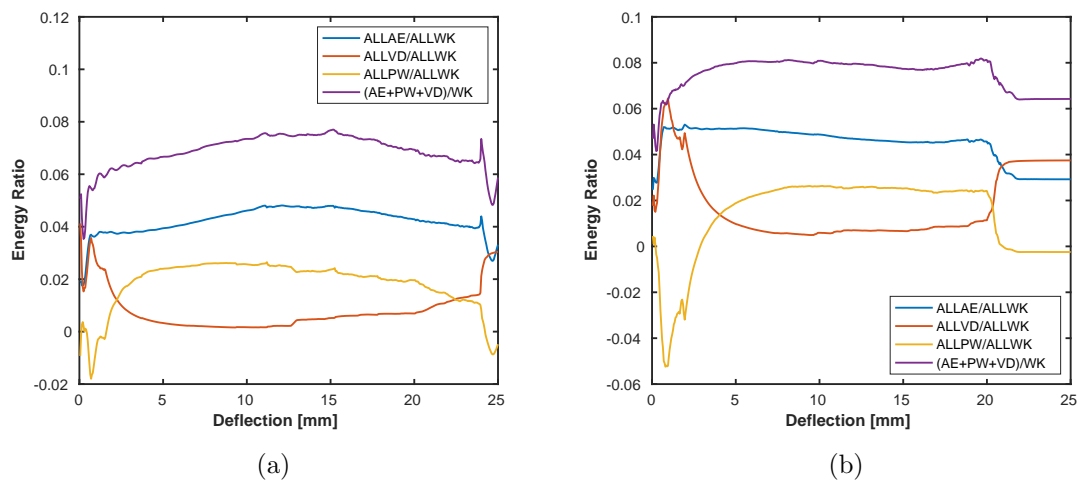
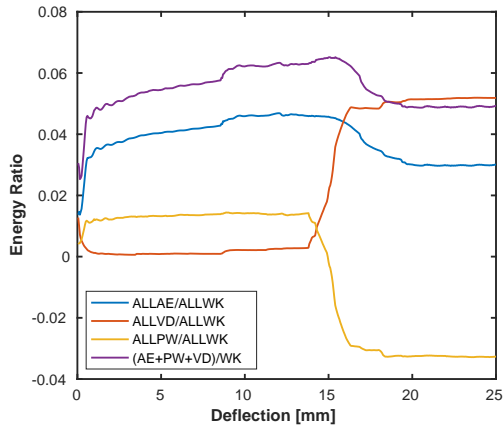
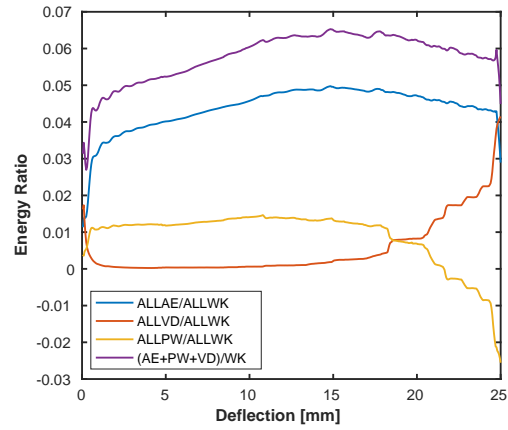


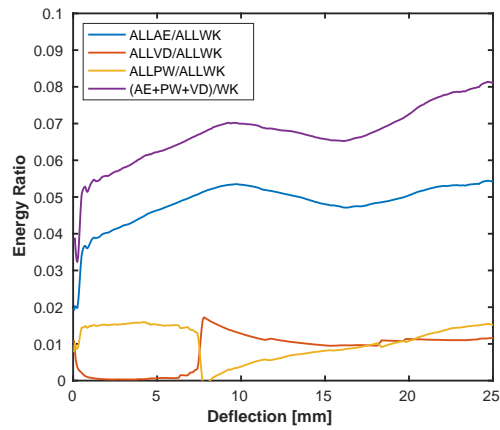
Figure B.4. False energies for (a) $[3^6]$ -A, (b) $[3^6]$ -B.



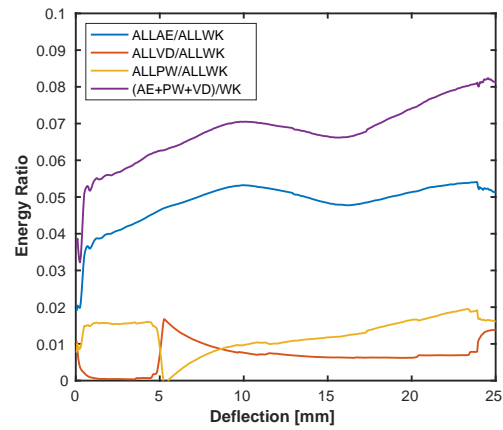
(a)



(b)



(c)



(d)

Figure B.5. False energies for (a) (4.8^2) -A(-), (b) (4.8^2) -A(+), (c) (4.8^2) -B(-), (d) (4.8^2) -B(+).

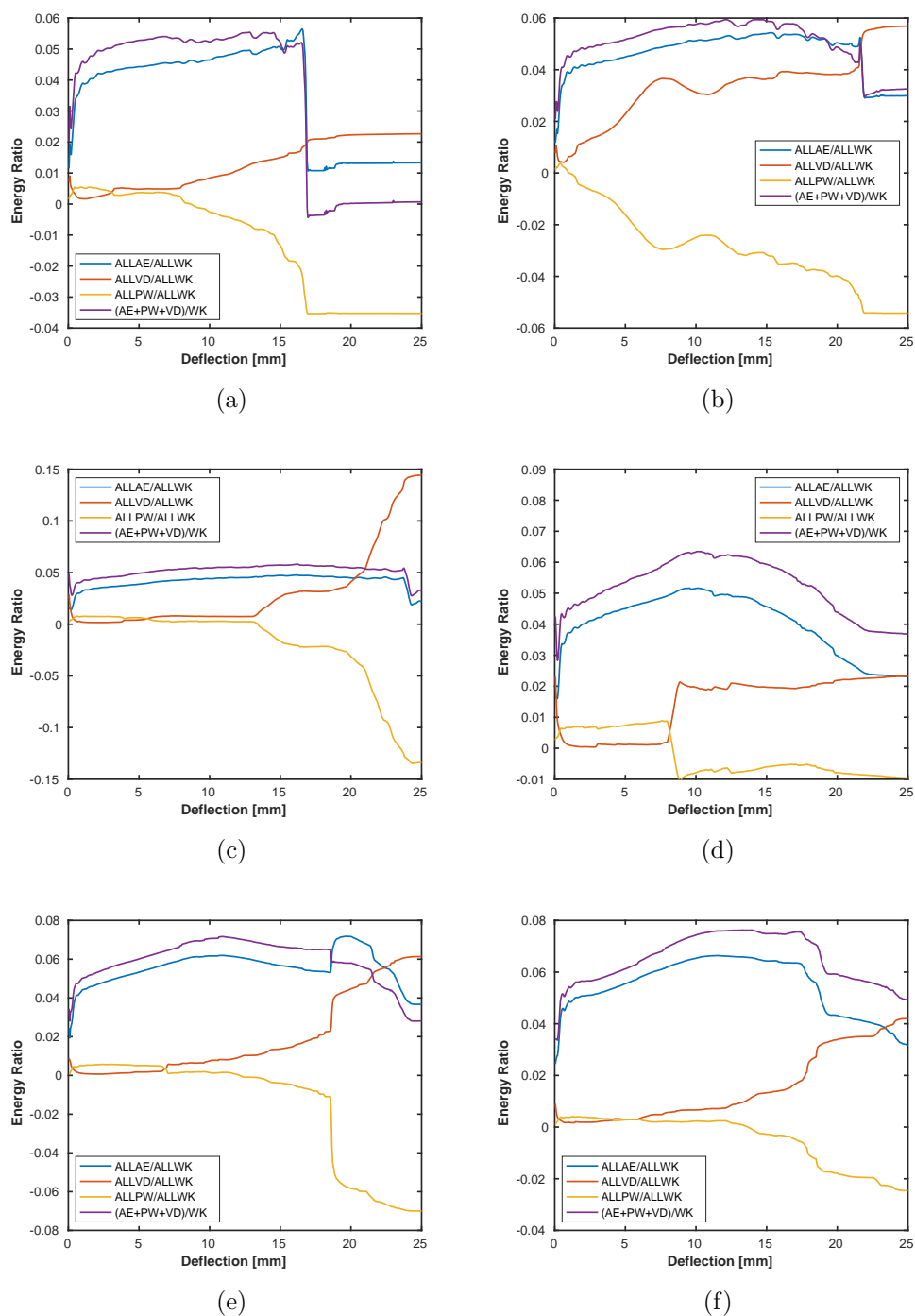


Figure B.6. False energies for (a) (4.6.12)-A(-), (b) (4.6.12)-A(+), (c) (4.6.12)-B(-), (d) (4.6.12)-B(+), (e) (4.6.12)-C(-), (f) (4.6.12)-C(+).

C. SELECT DATA

Table C.1.

Select data for all configurations with coefficient of friction $\mu = 0.2$.

Configuration	Stiffness [N/m]	Strength [N]	Toughness [mJ]	Slip Onset [mm]
[4 ⁴]-A	121.4	559.2	6667	10.65
[4 ⁴]-B	123.7	515.4	5976	13.35
[3.6.3.6]-A	135.6	556.8	6203	9.650
[3.6.3.6]-B	150.8	668.9	7585	13.05
[3.4.6.4]-A	147.5	723.4	12340	14.05
[3.4.6.4]-B	80.25	415.9	4073	3.450
[3.4.6.4]-C	123.3	539.1	4908	8.650
[3 ⁶]-A	200.5	926.2	13200	23.95
[3 ⁶]-B	198.7	906.1	12600	19.20
(4.8 ²)-A(-)	234.8	1022	10620	13.95
(4.8 ²)-A(+)	212.4	1057	15210	24.55
(4.8 ²)-B	187.6	872.7	10440	21.05
(4.6.12)-A(-)	261.0	1151	12610	15.30
(4.6.12)-A(+)	278.4	1249	16260	20.60
(4.6.12)-B(-)	216.7	1023	14300	20.45
(4.6.12)-B(+)	251.1	1092	11760	14.40
(4.6.12)-C(-)	231.8	968.2	10560	16.85
(4.6.12)-C(+)	252.2	1036	10540	16.60

Table C.2.
Select architectural aspects for all assemblies.

Assembly	Contact Area [mm ²]	Contact Interfaces	Largest Tile Area [mm ²]	Smallest Tile Area [mm ²]
[4 ⁴]-A	33340	112	881.4	881.4
[4 ⁴]-B	37220	144	674.8	674.8
[3.6.3.6]-A	28660	96	778.6	778.6
[3.6.3.6]-B	31340	105	778.6	778.6
[3.4.6.4]-A	30440	114	692.7	692.7
[3.4.6.4]-B	29870	111	692.7	692.7
[3.4.6.4]-C	34120	146	519.5	519.5
[3 ⁶]-A	25110	192	584.4	584.4
[3 ⁶]-B	25900	198	584.4	584.4
(4.8 ²)-A	25040	196	1118	231.6
(4.8 ²)-B	25080	196	1118	231.6
(4.6.12)-A	20340	204	1800	160.7
(4.6.12)-B	18010	150	2399	214.3
(4.6.12)-C	20870	212	1763	157.5

D. ABAQUS INPUT FILE

The following are key lines from an ABAQUS input file as used in this work. Note indentation indicates a continuation of the previous line.

```

** Units are Newton, millimeter, tonne, second
**
** Mesh frame with C3D4
*Element, type=C3D4
**
** Mesh blocks with C3D8R
*Element, type=C3D8R
**
** Section:  blockSection
*Solid Section, elset=blockSet, controls=elementControl,
    material=blockMaterial
**
** ELEMENT CONTROLS
**
*Section Controls, name=elementControl,
    hourglass=ENHANCED
1., 1., 1.
**
** MATERIALS
**
*Material, name=blockMaterial
*Density
9.5e-10,
*Elastic
1827., 0.35
**
** INTERACTION PROPERTIES
**
*Surface Interaction, name=interactionProperty-contact

```

```
*Friction
0.2,
*Surface Behavior, pressure-overclosure=HARD
*Contact Damping, definition=CRITICAL DAMPING FRACTION,
    tangent fraction=1.
0.3,
**
** INTERACTIONS
**
** Interaction:  interaction-contact
*Contact, op=NEW
*Contact Inclusions, ALL EXTERIOR
*Contact Property Assignment
, , interactionProperty-contact
*CONTACT CONTROLS ASSIGNMENT, TYPE=SCALE PENALTY
, , 5.0
** -----
**
** STEP: Step-1
**
*Step, name=Step-1, nlgeom=YES
*Dynamic, Explicit
, 0.5
*Bulk Viscosity
0.06, 1.2
** Mass Scaling:  Semi-Automatic
** Whole Model
*Fixed Mass Scaling, factor=100.
**
*End Step
```